ESTIMATION OF CHEMICAL INFORMATION IN SCATTERING MEDIA USING RADIATIVE TRANSFER THEORY TO REMOVE MULTIPLE SCATTERING EFFECTS

by

Raimundas Steponavičius

In Partial Fulfilment of the Requirements for the Degree of

Doctor of Philosophy

School of Chemical Engineering and Advanced Materials

Newcastle University, UK

August 2010

To Nick

Who was the best friend I have ever met
and from whom I learned so much ...
I will never forget You mate !

ABSTRACT

Two approaches for removing multiple light scattering effects using the radiative transfer theory in order to improve the performance of multivariate calibration models have been proposed namely: partial correction of multiple scattering effects and full correction of multiple scattering effects. The first approach is applicable for predicting the concentration of a scattering-absorbing (particulate) component as well as the concentration of an absorbing only species. The second approach is applicable only for estimation of the concentration of an absorbing only species. Application of the first approach to a simulated four component system showed that it will lead to calibration models which perform appreciably better than when empirically scatter corrected measurements of total transmittance or total reflectance are used. The validity of the method was tested experimentally using a two-component (polystyrene-water) and a four-component (polystyrene - ethanol - water - deuterated water) system. The proposed methodology of partial correction showed significantly better performance than the empirically pre-processed direct measurements (total transmittance, total reflectance and collimated transmittance) in all experiments. The results of applying the full correction approach showed that despite all errors the performance of PLS calibration model built on the corrected bulk absorption coefficient was marginally better than the performance of PLS model built on uncorrected bulk absorption coefficient. Finally, the benchmarking analysis revealed that there is still a significant potential for an improvement in the prediction performance in the quantitative analysis of turbid samples.

PUBLICATIONS

Journal articles:

1. Steponavicius, R. and S.N. Thennadil, *Extraction of Chemical Information of Suspensions Using Radiative Transfer Theory to Remove Multiple Scattering Effects: Application to a Model Two-Component System.* Analytical Chemistry, 2009. **81**(18): p. 7713-7723.
2. Steponavicius, R. and S.N. Thennadil, *Extraction of Chemical Information of Suspensions using Radiative Transfer Theory to Remove Multiple Scattering Effects: Application to a Model Multi-Component System*. Submitted to Analytical Chemistry, 2010-08.
3. Steponavicius, R. and S.N. Thennadil, *An Approach for a Full Correction of Multiple Scattering Effects in Prediction of Absorbing only Species Based on Radiative Transfer Theory*. To be submitted.

Conferences:

1. Steponavicius R., S.N. Thennadil, *Spectroscopic Monitoring of Emulsions and Latex Suspensions*, APACT 2007, Edinburgh, U.K.
2. Steponavicius R., S.N. Thennadil, *An Approach for Spectroscopic Monitoring of Latex Suspensions of Moderate Concentrations*, OPC 2007, Graz, Austria.
3. Steponavicius R., S.N. Thennadil, *Estimation of Polystyrene concentration in Latex using Light Transport Theory to Remove Multiple Scattering Effects*, FACSS 2007, Memphis, USA.
4. Steponavicius R., S.N. Thennadil, *Estimation of Chemical Information in Latex Suspensions using Light Transport Theory to Remove Multiple Scattering Effects*, CAC 2008, Montpellier, France. (P.S. The presented work was awarded with 'The Best Junior Chemometrician Award', the article is available in the book of extended abstracts, Vol. 1, p. 145-149, published by Cemagref-Montpellier SupAgro, France).

ACKNOWLEDGEMENTS

My journey to Newcastle University and this PhD has been undoubtedly the biggest venture in my life. It somewhat reminds me of Lomonosov's the Great Russian scientist's journey to Moscow to study. Driven by an unappeasable desire for knowledge that he was relentlessly seeking for at all costs he even travelled more than 1400 km on foot ! I too driven by that relentless quest for knowledge did everything to undertake this venture whatever the cost. I quit a good job, sold everything I had "pawned my parents" to the bank without having a clue how I was going to return the money borrowed and went overseas seeking for knowledge despite many saying: Are you crazy ?! There were some hard times on my way to this PhD, especially the year when I was doing the MSc course in Process Analytics and Quality Technology. I basically fed on buckwheat porridge, which I brought from my home country, since I could not afford buying food in U.K. But God blessed my journey and my efforts were rewarded plentifully. I got a chance to meet some eminent scientists and to touch a real science, but most importantly I met a lot of great friends from all over the world, who made this journey the most wonderful experience in my life. Thanks to Jamie, my first friend in U.K., for making me welcome to Newcastle and for a great time that I spent with you and your nice family that made me feel more like at home. A big thank you goes to my PAQT course mates: Philip, Chukwuma the big buddy, Debo (sorry mate for not putting all nine of your names), Zoe, Xue, Olusoga, Tunde, Dave and especially Nick who was the best friend I have ever met ! He was such a gifted person from whom I learned so much. I loved to discuss or argue with him, it was such a great pleasure ! The time seemed to stop then. It always baffled me how he was able to explain complicated things as Heisenberg uncertainty principle so simply and vividly. I will never forget those discussions. I pay a huge tribute to this man ! A big thank you for everything also goes to Maria (especially for patiently answering my annoying questions) Daniel (for cheering me up), Elitsa (for taking care of me and reminding me everything), Carlo (for nice Italian coffee and warm friendship), Par (for being a tough opponent in arguments), Cheng, Chris and Wouter. But this PhD would have been impossible without one great person – my supervisor dr. Suresh Thennadil, the best supervisor that I could have wished for by all means. I give 99 % of all merits for all that I have achieved during this PhD to him. A special thank you goes to prof. Elaine Martin for her support. Especially, for organising a refund of the tuition fee for the MSc course in PAQT, which was critically important for continuing this journey. Finally, I want to say thank You to my

beloved parents. This venture cost a lot of white hair to them, but they always stood by me no matter what and my gratitude to them is simply immeasurable. My father Pranas has always been a never ending source of wisdom to me. Also, to my sister and brother whose endless support and inspiration kept me always going. And the last but not the least person to whom I was I am and I will be grateful to the end of my days is my beloved wife Emilija. Thank You Darling for your support, patience and love. I love You so much !

This PhD was funded through Marie Curie FP6 (project INTROSPECT).

„Turėk kantrybės ir lauk galo“

(„Be patient and wait until the end“)

Pranas Steponavičius

Table of Contents

LIST OF FIGURES

LIST OF TABLES

NOMENCLATURE

$\mathbf{E}$ – electric field, [N/C]

$\mathbf{B}$ – magnetic induction, [T]

$\mathbf{H}$ – magnetic field, [A/m]

$\mathbf{D}$ – electric displacement, [C/m^2]

$\mathbf{E}_0$ – constant vector of electric field, [N/C]

$\mathbf{H}_0$ – constant vector of magnetic field, [A/m]

S – Poynting vector, [W/m^2]

I – light intensity, [W/m^2]

I_0 – intensity of incident light, [W/m^2]

T_t – total transmittance, [%]

R_t – total reflectance, [%]

T_c – collimated transmittance, [%]

$\mathbf{k}$ – wave vector, [1/m]

t – time, [s]

v – speed of electromagnetic wave, [m/s]

c – speed of light, [m/s]

c_i – concentration of species i, [%]

c_p – concentration of particles, [%]

N – complex refractive index

n – real part of complex refractive index

k – imaginary part of complex refractive index

m – ratio of complex refractive indices of particles and medium

p – phase function

g – anisotropy of light scattering or anisotropic factor

$\hat{g}$ – anisotropic factor estimate

x – size parameter

R – particle radius, [m]

F – differential cross-section, [m^2]

θ – scattered angle

ϕ – azimuth angle

S_{str} – static structure factor

V_T – energy of inter-particle interactions, [J]

N_p – number density of particles, [1/m^3]

P – probability density function

r – distance, [m]

s – directional vector

a – albedo

l – path length, [m]

A – absorbance

A – matrix of absorbances i.e. matrix of absorption spectra

a – vector of absorption spectrum

$\bar{\mathbf{a}}$ – mean spectrum

b – regression coefficients in empirical pre-processing

S – matrix of absorptivities or absorption cross-sections

s – vector of absorptivities or absorption cross-sections

C – matrix of concentrations

$\mathbf{A}_{\text{cal}}$ – matrix of absorption spectra of calibration dataset

$\mathbf{C}_{\text{cal}}$ – matrix of concentrations of calibration dataset

T – scores matrix

t – vector of scores of one principal component

P – loadings matrix

p – vector of loadings of one principal component

X – data matrix

y – predictor variable

w – weights

f – objective function

$\mathbf{P}_r$ – projection matrix

$\mathbf{p}_r$ – projection vector

e – error vector

$\mathbf{A}_p$ – spectra of mixtures of absorbing only species

M_R – mean of particle radius, [m]

d_R – standard deviation of particle radius, [m]

Greek letters:

λ – wavelength, [m]

$\boldsymbol{\lambda}$ – vector of wavelengths

ε_0 – electric permittivity of a free space, $8.8542 \cdot 10^{-12}$ [C^2/Nm]

μ_0 – magnetic permeability of a free space, $4\pi \cdot 10^{-7}$ [Tm/A]

ε – electric permittivity, [C^2/Nm]

μ – magnetic permeability, [Tm/A]

ω – angular frequency, [1/s]

σ_a – absorption cross-section, [m^2]

σ_{ap} – absorption cross-section of particles, [m^2]

σ_s – scattering cross-section, [m^2]

σ_{ext} – total extinction cross-section, [m^2]

$\sigma_s^{'}$ – average scattering cross-section of particles, [m^2]

μ_a – bulk absorption coefficient, [1/m]

$\mu_{a,corr}$ – corrected bulk absorption coefficient theoretical, [1/m]

$\hat{\mu}_{a,corr}$ – corrected bulk absorption coefficient estimate, [1/m]

μ_{ap} – bulk absorption coefficient of particles, [1/m]

μ_s – bulk scattering coefficient, [1/m]

$\hat{\mu}_s$ – bulk scattering coefficient estimate, [1/m]

μ_t – total extinction coefficient, [1/m]

Ω – solid angle

τ – optical depth, turbidity or total attenuation

Acronyms:

PAT – process analytical technologies

NIR – near infra-red

PCA – principal component analysis

PLS – partial least squares or projections to latent structures

LV – latent variable

MSC – multiplicative scatter or signal correction

EMSC – extended multiplicative signal or scatter correction

EMSCL	–	extended multiplicative scatter correction with wavelength dependent logarithmic term
SNV	–	standard normal variate
OSC	–	orthogonal signal correction
OPLS	–	orthogonal projections to latent structures
RTE	–	radiative transfer or transport equation
PY-HS	–	Percus-Yevick-Hard-Sphere approximation
PSD	–	particle size distribution
RMSECV	–	root mean square error of cross-validation
RMSEP	–	root mean square error of prediction
IAD	–	inverse adding doubling
SQP	–	sequential quadratic programming
BFGS	–	Broyden, Fletcher, Goldfarb, and Shanno formula for Hessian updating

CHAPTER I

INTRODUCTION

Accurate estimation of concentrations of chemical components in turbid samples (e.g. suspensions, emulsions) using spectroscopic techniques is still an open-end problem that challenges chemometricians and other applied scientists [1]. Effective solution to this problem is of tremendous practical importance since it is encountered in many areas such as monitoring polymerization reactions [2-5], fermentation processes [6-8] and pharmaceutical production [9-14]. Therefore, research and development of spectroscopy based process analytical technologies (PAT) for on-line analysis of particulate (heterogeneous, multiphase) streams is more vital than ever. In order to be competitive companies have to meet increasing requirements for processes in all aspects, namely, product quality, yield, process efficiency, safety and environment. All these aspects fall into the domain of process control an inherent part of which is PAT. Thus, in order to hit higher and higher process control targets and to stay on the competitive edge progress in process analytical technologies is indispensable. To achieve high level advanced process control in these processes on-line analytical techniques for accurate estimation of concentrations of chemical components in particulate streams are usually essential. Spectroscopic techniques are preferable, because they are fast, cheap, compatible with fibre optics and multifunctional and virtually no sample preparation is required, but, building accurate calibration models is an issue. Acquisition of accurate calibration models and thus applicability of spectroscopic methods to turbid samples is hindered by nonlinear multiple light scattering effects that degrade conventional calibration models designed for bilinear systems and make extraction of chemical information from such samples challenging.

The main problem, in the quantitative analysis of turbid samples using the Near-infrared (NIR) spectroscopy, is that multivariate calibration models built on conventional spectroscopic measurements such as transmittance or reflectance are adversely affected by variations arising from multiple light scattering, because these variations are not necessarily related to changes in chemical information i.e. concentrations of chemical components. There are essentially two ways to deal with undesirable scattering effects in NIR measurements: remove/minimize them by means of empirical pre-processing or separate scattering effects from absorption using first principles i.e. by invoking light propagation theory such as the radiative transfer theory. In either case, the goal is to obtain

a measure of absorption per unit length, which is independent from variations in path length of photons that occur due to multiple scattering and linearly proportional to concentrations of constituents. Although a considerable progress has been made in the empirical scatter correction techniques they are not expected to solve the problem of multiple light scattering completely because they are intrinsically approximate. And while they may be sufficient in some practical situations they may not be able to accommodate the whole complexity of nonlinear multiple scattering effects in many situations. Therefore, research and development for application of the second approach for scatter correction in PAT is gaining impetus though no actual industrial applications have been reported yet to the best of our knowledge.. The main measurement techniques currently used for deconvolution of absorption and scattering properties of a sample are time resolved, spatially resolved and integrating-sphere measurements.

1.2. AIM AND OBJECTIVES

The aim of this research was to develop new methodologies for estimation of chemical information in suspensions that gave better accuracy and robustness than the current methods based on empirical pre-processing techniques.

Objectives:

1. To show that the estimation of the concentration of a chemical species that (a) purely absorbs and (b) both absorbs and scatters light are two different types of problems from the point of view of multivariate calibration.
2. To consider two possible cases in estimation of concentrations of purely absorbing species: partial correction of multiple scattering effects and full correction of multiple scattering effects i.e. removing variations due to different path lengths of photons and removing variations due to different path lengths of photons as well as due to changes in particle size accordingly.
3. To separate multiple light scattering effects from absorption by means of the radiative transfer theory rather than empirical pre-processing:
    - To investigate the convergence conditions of the Inverse Adding-Doubling routine when the total transmittance, total reflectance and collimated transmittance measurements are used for the extraction of the optical properties of samples and to optimise it;
    - To investigate the sensitivity of the extracted scattering and absorption

properties of a sample to the error in the anisotropic factor *g* and hence the possibility of fixing it at a constant value and using just two measurements, namely, the total transmittance and reflectance, for the extraction of the absorption part thus simplifying the extraction procedure.

4. To test the partial correction method in estimation of concentrations of both types of species (i.e. absorbing only and scattering absorbing) on simulated data to show the maximum theoretical improvement in the prediction accuracy possible using the given methodology.
5. To validate the partial correction method for estimation of concentrations of both types of species by applying it on experimental data and benchmarking the results (i.e. the prediction accuracy) with the best ones achieved using empirical pre-processing for scatter correction.
6. To investigate the impact of nonlinear variations in the absorption coefficient of particles (those are due to the variation in the particle size) on the performance of multivariate calibration models.
7. To test the full correction method in estimation of concentrations of absorbing only species on simulated data to show the maximum theoretical improvement in the prediction accuracy possible using this methodology.
8. To validate the full correction method for estimation of concentrations of absorbing only species by applying it on experimental data and benchmarking the results (i.e. the prediction accuracy) with the ones achieved using empirical pre-processing and the partial correction method too.

1.3. CONTRIBUTION

- The state of the art in the field of spectroscopic analysis of turbid samples has been reviewed;
- Two new methodologies for estimation of chemical information in suspensions have been presented;
- Possible issues in the inversion of the Adding-Doubling algorithm using nonlinear optimisation have been pointed out and the strategies for initial guesses together with optimal settings for nonlinear optimisation have been suggested;
- The effect of absorption coefficient of particles, which varies nonlinearly with particle size, on the multivariate calibration results have been analysed.

CHAPTER II

LITERATURE REVIEW: THE STATE OF THE ART IN ESTIMATION OF CONCENTRATIONS OF CHEMICAL COMPONENTS IN TURBID SAMPLES USING SPECTROSCOPIC TECHNIQUES

Multivariate soft modelling techniques for extraction of quantitative information from spectral data such as principal component analysis (PCA), partial least squares (PLS), target transformation factor analysis and multivariate curve resolution have become an integral part of the quantitative analysis in NIR spectroscopy and are widely reported in the literature [15, 16]. While they have been very successful in the quantitative analysis of homogeneous (non-scattering) liquid mixtures their performance in the quantitative analysis of turbid samples, in many situations, is still comparatively worse in terms of the accuracy and robustness. The culprit is nonlinear effects of multiple scattering of light that are not completely accounted for by current methods and techniques in the pre-processing step which is crucial in the quantitative analysis of turbid samples. Successful elimination (removal, correction) of these effects in the pre-processing step would allow us to achieve the accuracy and robustness of multivariate calibration models as good as in the case of homogeneous liquid samples.

There were few attempts to overcome the scattering problem without pre-processing, but the calibration models were of moderate accuracy and of very limited use i.e. suitable only for a very narrow operational region and their robustness was a big question [17]. To remove systematic effects in NIR spectra that are unrelated to changes in chemical concentrations, including light scattering effects, various pre-processing methods and techniques have been suggested. First and second derivatives were among the first pre-processing techniques used for baseline correction in spectra [18, 19]. Frequency analysis methods such as wavelet and Fourier transforms have also been used for baseline subtraction by removing a low frequency component from a signal [20]. Although these techniques may be effective in correcting simple baseline artifacts such as offsets and angles they are not adequate for dealing with complex light scattering problems. For example, there have been repeated attempts to use single spectroscopic measurements such as transmittance or reflectance pre-processed with first or second derivatives for estimation of concentrations of chemical components in the field of emulsion polymerization, where the sampled reaction medium is very complex (i.e. multiphase) resulting in complicated scattering effects [4, 21-24]. The results of the subsequent multivariate calibration models

were clearly unsatisfactory indicating that light scattering effects were not adequately corrected by the derivatives. One of the pioneering works on empirical light scatter correction was done by Geladi et al. [25]. They proposed an empirical pre-processing technique called Multiplicative Scatter Correction (MSC), which became perhaps the most widely used pre-processing method for NIR spectra since its introduction to the chemistry literature in the 1980s. MSC is based on the assumption that light scattering has as an additive and a multiplicative or scaling effect on the measured spectrum. It is also assumed that the scattering effects do not depend on the wavelength. The limitations and drawbacks of the MSC are: the regression procedure should be applied to the part of the spectrum that does not contain chemical information, i.e., the part which is only influenced by multiplicative light scattering, otherwise some of the relevant chemical information might be removed, and, the second assumption is generally invalid since the light scattering phenomenon is strongly dependent on the wavelength λ. Standard normal variate (SNV) coupled with de-trending (DT) [26] is said to be an alternative to MSC, although Dhanoa et al. demonstrated that MSC and SNV-DT are, in fact, linearly related [27, 28]. Different implementations of MSC such as piecewise MSC and loopy MSC have also been presented [29, 30].

A group of pre-processing methods revolves around the MSC concept. An extended form of the multiplicative signal correction (EMSC) was first suggested by Martens and Stark [31], which addressed the first limitation of the original MSC, but the knowledge about the spectra of pure components was required. To address the second drawback of the MSC Martens et al. added the wavelength dependent terms to the equation of the EMSC [32]. They modelled wavelength dependency using the second order polynomial. However, strictly speaking, the wavelength dependency of the scattering effects is not quadratic and it depends on the particle size parameter (i.e. the ratio of the particle size and the wavelength) e.g. for particles small comparing to wavelength the scattered intensity is inversely proportional to the λ^4 (Rayleigh approximation). Therefore, Thennadil and Martin suggested a different wavelength-dependent term for the EMSC and showed that it works better [33]. Recently, Ottestad *et al*. demonstrated how a limited amount of *a priory* information about spectral variability can be used in EMSC to improve scatter correction [34]. Thennadil *et al*. also proposed a physics-based EMSC, where the physics of light transport is incorporated to further improve the removal of scattering effects [35]. Chen et al. proposed yet another version of EMSC called Optical Path-Length Estimation and Correction (OPLEC) by the authors [36]. The advantage of it is that it does not require

knowledge about spectra of pure components. The inverse forms of MSC and EMSC has also been investigated but no tangible differences noticed [37, 38]. All techniques that are rooted in MSC involve a transformation about a spectrum that is representative of the scattering in all samples. So far, they make the most popular group of pre-processing techniques for scatter correction used in many applications [39-41]. A good review of the most common pre-processing techniques for near-infrared spectra is given by Rinnan [42].

Other pre-processing methods for correction of scattering effects in NIR spectra have evolved from orthogonal signal correction (OSC), introduced in 1998 by Wold et al. [43]. OSC is based on removing the part of the spectral data which is unrelated to the concentrations of interest. This concept has led to methods such as direct orthogonalization [44], orthogonal projections to latent structures (OPLS) [45, 46] and net analyte pre-processing [47] and direct orthogonal signal correction [48]. Svensson et. al. investigated six variations of OSC and concluded that the use of these methods does not necessarily lead to better predictive ability [49]. The benefits of OSC lay in the reduction of the number of PLS factors necessary to generate an acceptable model and the improved interpretability of these factors for further qualitative analysis, as interfering information is removed from the significant factors [50]. These given methods make an implicit assumption, in the spectral domain, that effects from the light scattering are orthogonal (or at least, at a significant angle) to spectral effects from chemical concentration changes.

An excellent comparison study of performances of different pre-processing techniques in correcting multiple scattering effects is given by Thennadil and Martin [33]. The following pre-processing techniques were compared: first derivative, second derivative, SNV, MSC, three different forms of EMSC, inverse signal correction, OSC and OPLS [27]. According to the results, the best performance of PLS model was attained using EMSC with the logarithmic wavelength dependency for pre-processing of spectral data.

Miller and Naes proposed a path length correction method in which a PCA model is generated from calibration samples of the same path length, after which the unknown samples are corrected by projecting them back onto the PCA calibration space [51].

Instead of pre-processing (i.e. linearising the original data) nonlinear scattering effects can be alternatively dealt with using mathematical models capable of modelling nonlinear relationships [52]. Nonlinear multivariate calibration models have been explored in other works [53, 54] and will not be discussed here.

As mentioned in the introduction, there are essentially two ways to deal with

undesirable scattering effects in NIR measurements: remove/minimize them by means of empirical pre-processing or separate scattering effects from absorption using first principles i.e. by invoking light propagation theory such as the radiative transfer theory. The most frequently used approach for scatter correction has been empirical pre-processing because of its simplicity. The second approach of separating scattering from absorption using radiative transport theory has been primarily developed in the field of biomedical optics for biomedical applications where high multiple scattering makes it difficult to perform reliable measurements [55-57]. The state of the art measurement techniques used for deconvolution of scattering and absorption properties include time-resolved [58-60], spatially resolved [61, 62], and integrating sphere measurements [63-66]. While an appreciable progress is made on the second scatter correction approach in the field of biomedical physics, very little work has been done on the applicability of it in the field of Process Analytics mainly due to complex measurements and theory required to extract the absorption and scattering properties of a sample. One of the few applications of this scatter correction approach for development of Process Analytical Technologies was reported by Abrahamsson et al. [67]. They applied it on pharmaceutical tablets and showed a significant improvement in the accuracy of predictions in comparison with direct application of Partial Least Squares regression on transmittance measurements. The methodology they used has several shortcomings: two instruments are required (time resolved and conventional spectrometer), diffusion approximation assumptions have to be met and the reduced scattering coefficient could not be measured beyond 1100 nm using their time resolved system (whereas the overtones of the organic compounds appear in the NIR region above 1100 nm) and therefore it had to be extrapolated for the higher wavelength region. It is worth noting, that attempts to correlate various features of photon time-of-flight distribution with the concentration of chemical species of interest (e.g. by fitting the final slope) without explicitly separating absorption and scattering have also been reported [68-70]. Since the authors did not benchmark their methods against some empirical pre-processing techniques (they benchmarked it only against the direct PLS) it is difficult to evaluate their performance.

In the following, methods that do not explicitly use the radiative transport theory for the extraction of the absorbance are briefly reviewed. Crowe et al. derived a relationship between the attenuation and the absorption of a turbid sample using the temporal point-spread function [71]. Once determined from the calibration dataset this relationship can be used for finding the concentrations of chemical species from turbidity

measurements in unknown samples. But, this relationship holds only if the scattering properties of unknown samples are the same as in the calibration set. In other words, this method can be used when only absorption of the turbid samples varies. Stockford et al. proposed to remove light scattering effects using polarization techniques [72]. However, extensive sample dilution is required, because of a low signal of polarized light, and signal-to-noise ratio is an issue. Recently, a new approach for correction of nonlinear effects of multiple scattering (i.e. variation in the path length of photons), based on the extraction of the absorption part from the photon time-of-flight distribution and correlation of it to the measured turbidity, have been reported by Leger [73]. This photon path length distribution correction method does have an important limitation, as the path length distribution has to be assumed for each sample, whether it is measured or estimated. Therefore it is suitable only for samples that have similar scattering properties.

CHAPTER III

THEORY

3.1. LIGHT PROPAGATION IN TURBID MEDIA

Two processes govern propagation of light (i.e. electromagnetic waves) in turbid/particulate media, namely, absorption and scattering. The former attenuates the energy of an electromagnetic wave turning it into other forms of energy such as heat while the latter redistributes it in different directions. Since absorption takes place everywhere within the absorbing material/medium the total amount of absorbed energy depends on the distances travelled by the photons in different absorbing materials, in other words, it depends on what distances and in what materials the photons travelled. Scattering, on the other hand, occurs only at the interface of different materials that is where the speed of an electromagnetic wave changes as it passes from one material into the other. Therefore, scattering depends on the contrast between the speeds of propagation of electromagnetic waves in different materials and the spatial configuration of their boundaries. Absorptivity, that is capacity to absorb electromagnetic radiation, and the speed of propagation of electromagnetic waves are material dependent properties.

Fundamentally, propagation of electromagnetic waves in any sort of medium is described by the Maxwell equations. Here, the two material dependent properties related to absorption and scattering are defined by the complex refractive index i.e. by the imaginary and the real part of it correspondingly. If values of the complex refractive index are known at every point in the space one can find how the incident electromagnetic wave will be scattered by the sample and the intensity of the resulting electromagnetic field at any point in the space by solving the Maxwell partial differential equations with appropriate boundary conditions. Thus, in the case of suspensions with spherical particles, the complex refractive indices of the medium and the particles and the size and the position of every particle in the sample should be known. However, in the real samples of suspensions the positions of the particles are constantly and randomly changing due to Brownian and other motions. Although the configuration of the particles does not matter under single scattering conditions when the suspension is sufficiently dilute such that particle interactions are negligible, under multiple scattering it plays an important role because now one must explicitly take into account that each particle is illuminated by light scattered by other particles as well as the incident light [74]. Thus, to model the measurement of light

multiply scattered by a random collection of particles one would need to solve the Maxwell equations for many particle configurations to obtain a reliable statistical average. However, this approach requires enormous computations and becomes prohibitively time consuming hence impracticable for larger groups of particles. In this case, the use of the so-called radiative transfer equation (RTE) [75] for modelling light propagation is far more practical than attempting to solve the Maxwell equations for large particle collections and usually provides results accurate enough for many applications. To solve the RTE one needs to know the bulk optical properties of a sample, namely, the bulk scattering coefficient, the bulk absorption coefficient and the anisotropic factor that define the amount of light scattered and absorbed per unit distance travelled and the angular distribution of it at each scattering event. The treatment of multiple light scattering can then be partitioned into three consecutive steps [74]:

1. Computation of the far-field scattering and absorption properties of an individual particle by solving the Maxwell equations.
2. Computation of the scattering and absorption properties of a small volume element containing a tenuous particle collection by using the single scattering approximation i.e. computation of the bulk optical properties; and
3. Computation of multiple scattering by the entire particle group by solving the radiative transfer equation supplemented by appropriate boundary conditions.

In spectroscopic analysis of turbid samples one is more often interested in the inverse problem e.g. extraction of the bulk optical properties of a sample or the size of spherical particles or the optical constants of materials (i.e. the complex refractive index) from various measurements of the field intensities. To obtain the bulk optical properties from the measurements only one step back is needed i.e. to solve the inverse radiative transfer equation. To determine the size of the particles or their complex refractive index one needs to do one more step back and find the inverse of the Maxwell equations.

3.1.1. Maxwell equations, Mie solution

Propagation of light in classical electromagnetic theory is described by the set of Maxwell's equations, which for electromagnetic waves travelling in free space is as follows [76]:

$$\begin{cases} \nabla \times \mathbf{E} = -\dfrac{\partial \mathbf{B}}{\partial t} & (3.1) \\ \nabla \times \mathbf{B} = \varepsilon_0 \mu_0 \dfrac{\partial \mathbf{E}}{\partial t} & (3.2) \\ \nabla \cdot \mathbf{E} = 0 & (3.3) \\ \nabla \cdot \mathbf{B} = 0 & (3.4) \end{cases}$$

where **E** is the electric field, **B** the magnetic induction and constants ε_0 and μ_0 are the electric permittivity and magnetic permeability of a free space. Electric and magnetic fields are functions of time t and spatial coordinates. The first two are the key equations that explain how electromagnetic waves propagate i.e. the changing magnetic field induces the changing electric field and the changing electric field in turn induces the changing magnetic field, this way electromagnetic energy can be transmitted even in empty space. That light can indeed be considered as an electromagnetic *wave* phenomenon can be directly shown from the Maxwell equations by taking the curl of both sides of eq. (3.1). Then we have:

$$\nabla \times \left(\nabla \times \mathbf{E} \right) = -\frac{\partial}{\partial t} \left(\nabla \times \mathbf{B} \right) \tag{3.5}$$

Using vector identities we can write the curl of the curl of **E** as:

$$\nabla \times \left(\nabla \times \mathbf{E} \right) = \nabla \left(\nabla \cdot \mathbf{E} \right) - \nabla^2 \mathbf{E} \tag{3.6}$$

Now, because the divergence of **E** must be zero according to the eq. (3.3) the first term in the right hand side of eq. (3.6) vanishes, therefore substituting eq. (3.6) and (3.2) into the eq. (3.5) we obtain:

$$\nabla^2 \mathbf{E} = \varepsilon_0 \mu_0 \frac{\partial^2 E}{\partial t^2} \tag{3.7}$$

where $\nabla^2 \mathbf{E}$ is the Laplace operator of **E**, which denotes nothing but the second derivatives of **E** in all directions:

$$\nabla^2 \mathbf{E} = \frac{\partial^2 \mathbf{E}}{\partial x^2} + \frac{\partial^2 \mathbf{E}}{\partial y^2} + \frac{\partial^2 \mathbf{E}}{\partial z^2} \tag{3.8}$$

Equation (3.7) is the differential vector wave equation. The same equation which describes mechanical and sound waves and the general form of which for a plane wave travelling in x direction is:

$$\frac{\partial^2 y}{\partial x^2} = \frac{1}{v^2}\frac{\partial^2 y}{\partial t^2} \tag{3.9}$$

Where y is the displacement of the wave along the y axis, x is the distance and v is the speed of the wave. By comparing the eq. (3.7) with the eq. (3.9) we see that the speed of electromagnetic waves in vacuum, which is the speed of light c, is:

$$v = c = \frac{1}{\sqrt{\varepsilon_0 \mu_0}} \tag{3.10}$$

The analogous differential wave equation can be derived for **B** following the same steps. The fact that we can express the field of **E** and **B** in the form of the differential wave equation is very important meaning that the propagation of the electromagnetic field can indeed be described in terms of waves and so the solutions to the system of Maxwell's equations are generally wave functions. This fact is the key to solving all scattering problems including Lorenz-Mie solution for scattering by spherical particles [77]. However, only certain electromagnetic fields, those that satisfy the Maxwell equations, are physically realisable. To give the conditions that must be satisfied by electromagnetic fields we shall briefly discuss the plane-wave solution.

For electromagnetic waves in matter the Maxwell equations take the following form [76]:

$$\begin{cases} \nabla \times \mathbf{E} = -\dfrac{\partial \mathbf{B}}{\partial t} & (3.11) \\ \nabla \times \mathbf{H} = \dfrac{\partial \mathbf{D}}{\partial t} & (3.12) \\ \nabla \cdot \mathbf{D} = 0 & (3.13) \\ \nabla \cdot \mathbf{B} = 0 & (3.14) \end{cases}$$

where **H** is the magnetic field and **D** is the electric displacement. Only the first two equations (3.11) and (3.12) are independent, equations (3.13) and (3.14) can be derived from them. These two independent vector equations are equivalent to six scalar differential equations (due to their partial derivatives with respect to three coordinates), whereas the number of unknown scalar functions is 12 (i.e. partial derivatives of the four unknown field vectors **E**, **H**, **B** and **D** with respect to three coordinates). Consequently, the number of independent equations is insufficient to obtain the unique solution for the unknown field vectors, therefore, the system of equations (3.11)-(3.14) is known as the indefinite form of the Maxwell equations [78]. To allow a unique determination of the field vectors the

Maxwell equations must be supplemented by the relationships describing the effect of the material on the electric and magnetic fields. These constitutive relations are given by:

$$\mathbf{D} = \varepsilon \mathbf{E} \tag{3.15}$$

$$\mathbf{B} = \mu \mathbf{H} \tag{3.16}$$

where ε is the electric permittivity and μ is the magnetic permeability. They depend on the material. These relationships provide six additional scalar equations thus making the total number of equations equal to the number of unknowns. By substitution of **D** and **B** for their respective constitutive relations in (3.11) -(3.14) we get:

$$\begin{cases} \nabla \times \mathbf{E} = -\mu \dfrac{\partial \mathbf{H}}{\partial t} & (3.17) \\ \nabla \times \mathbf{H} = \varepsilon \dfrac{\partial \mathbf{E}}{\partial t} & (3.18) \\ \nabla \cdot \mathbf{E} = 0 & (3.19) \\ \nabla \cdot \mathbf{H} = 0 & (3.20) \end{cases}$$

Electric and magnetic fields in the form of the plane waves can be written as:

$$\mathbf{E} = \mathbf{E}_0 \cos\left(\mathbf{k} \cdot \mathbf{z} - \omega t\right) \tag{3.21}$$

$$\mathbf{H} = \mathbf{H}_0 \cos\left(\mathbf{k} \cdot \mathbf{z} - \omega t\right) \tag{3.22}$$

where $\mathbf{E}_0$ and $\mathbf{H}_0$ are constant vectors, $\mathbf{z}$ is the distance in z direction, ω is the angular frequency and $\mathbf{k}$ is the wave vector which may in general be complex:

$$\mathbf{k} = \mathbf{k}_r + i\mathbf{k}_i \tag{3.23}$$

Using Euler's formula time harmonic fields given in eq. (3.21) and (3.22) can be written as the real parts of their complex representations:

$$\mathbf{E}_c = \mathbf{E}_0 e^{i(\mathbf{k} \cdot \mathbf{z} - \omega t)} \tag{3.24}$$

$$\mathbf{H}_c = \mathbf{H}_0 e^{i(\mathbf{k} \cdot \mathbf{z} - \omega t)} \tag{3.25}$$

whereby $\mathbf{E} = \mathrm{Re}(\mathbf{E}_c)$ and $\mathbf{H} = \mathrm{Re}(\mathbf{H}_c)$ (the subscript c denotes the complex representation). If all operations on time harmonic fields are linear (e.g. addition, differentiation, integration) it is more convenient to work with the complex representation. Hence, equations (3.17)-(3.20) can be written in the following form:

$$\begin{cases} \nabla \times \mathbf{E}_c = i\omega\mu \mathbf{H}_c & (3.26) \\ \nabla \times \mathbf{H}_c = -i\omega\varepsilon \mathbf{E}_c & (3.27) \\ \nabla \cdot \mathbf{E}_c = 0 & (3.28) \\ \nabla \cdot \mathbf{H}_c = 0 & (3.29) \end{cases}$$

Substituting **k** for its complex representation given in (3.23) in the equations (3.24) and (3.25) we get the following form of the plane waves for **E** and **H**:

$$\mathbf{E}_c = \mathbf{E}_0 e^{-\mathbf{k}_i \cdot \mathbf{z}} e^{i(\mathbf{k}_r \cdot \mathbf{z} - \omega t)} \tag{3.30}$$

$$\mathbf{H}_c = \mathbf{H}_0 e^{-\mathbf{k}_i \cdot \mathbf{z}} e^{i(\mathbf{k}_r \cdot \mathbf{z} - \omega t)} \tag{3.31}$$

$\mathbf{E}_0 e^{-\mathbf{k}_i \cdot \mathbf{z}}$ and $\mathbf{H}_0 e^{-\mathbf{k}_i \cdot \mathbf{z}}$ are the amplitudes of the electric and magnetic waves and $\phi = \mathbf{k}_r \cdot \mathbf{z} - \omega t$ is the phase of the waves. The given electric and magnetic plane waves are compatible with the Maxwell equations if **k**, $\mathbf{E}_0$ and $\mathbf{H}_0$ are perpendicular to each other, that is:

$$\mathbf{k} \cdot \mathbf{E}_0 = \mathbf{k} \cdot \mathbf{H}_0 = \mathbf{E}_0 \cdot \mathbf{H}_0 = 0 \tag{3.32}$$

and the following condition is fulfilled :

$$\mathbf{k} = \mathbf{k}_r + i\mathbf{k}_i = \frac{\omega N}{c} \tag{3.33}$$

where N denotes the complex refractive index and is given by:

$$N = c\sqrt{\varepsilon\mu} = \sqrt{\frac{\varepsilon\mu}{\varepsilon_0 \mu_0}} \tag{3.34}$$

Since it is a complex number the following notation is used:

$$N = n + ik \tag{3.35}$$

where n and k are the real and the imaginary parts respectively. The free space wave number is $\omega/c = 2\pi/\lambda$ where λ is the wavelength in vacuum. The wave vector **k** in terms of the real and imaginary parts of the complex refractive index is:

$$\mathbf{k} = \mathbf{k}_r + i\mathbf{k}_i = \frac{\omega}{c} n + i\frac{\omega}{c} k \tag{3.36}$$

Substituting $\mathbf{k}_r$ and $\mathbf{k}_i$ for $\omega n/c$ and $\omega k/c$ in eq. (3.30) and (3.31) the plane homogeneous waves of the electric field and the associated magnetic field, that are solutions to the

Maxwell equations given the aforementioned conditions are satisfied, have the following form:

$$\mathbf{E}_c = \mathbf{E}_0 \, e^{-\frac{2\pi kz}{\lambda}} \, e^{i\left(\frac{2\pi nz}{\lambda} - \omega t\right)} \tag{3.37}$$

$$\mathbf{H}_c = \mathbf{H}_0 \, e^{-\frac{2\pi kz}{\lambda}} \, e^{i\left(\frac{2\pi nz}{\lambda} - \omega t\right)} \tag{3.38}$$

Thus the imaginary part of the complex refractive index determines the attenuation of the wave as it propagates through the medium whilst the real part determines the phase velocity $v = c/n$. n and k are often referred to as the optical constants of the material. The Poynting's vector, the magnitude of which is the intensity of the radiation usually denoted as I, for a plane wave is given by:

$$S = \frac{1}{2}\mathrm{Re}\left\{\sqrt{\frac{\varepsilon}{\mu}}\right\}\left|E_0\right|^2 e^{-\frac{4\pi kz}{\lambda}} \tag{3.39}$$

If we compare eq. (3.39) with Beer's law:

$$I = I_0 e^{\mu_a z} \tag{3.40}$$

we see that the absorption coefficient μ_a is:

$$\mu_a = \frac{4\pi k}{\lambda} \tag{3.41}$$

So the rate at which electromagnetic energy is removed from the wave as it propagates through the medium is determined by the imaginary part of the complex refractive index.

A problem which is of particular interest in this work is absorption and scattering of a plane electromagnetic wave by a single spherical particle. The analytical solution to this problem is given by Mie [77, 79]. It allows us to compute the absorption cross-section σ_{ap}, the scattering cross-section σ_s and the anisotropic factor g for a particle of a certain radius at a certain wavelength given the optical constants (i.e. complex refractive indices) of the particle and the medium. A program developed by C. F. Bohren and D. R. Huffman was used for computing these optical properties using Mie solution [76], though it was implemented in MATLAB programming language. The required inputs to the Mie code are the ratio of the complex refractive indices of the particle and the medium:

$$m = \frac{n_p + ik_p}{n_m + ik_m} \tag{3.42}$$

where the subscript p stands for particles and m for medium, and the size parameter x, which is equal to:

$$x = \frac{2\pi Rn}{\lambda} \tag{3.43}$$

where R is the radius of the particle. The absorption cross-section of a particle is found by integrating the scattered electromagnetic field **E** which is a function of m and x over the volume of the scatterer (i.e. particle) [80]:

$$\sigma_a = \int_{4\pi} \mathbf{k} \cdot 2nk \left| E\left(r'\right) \right|^2 d^3 r' \tag{3.44}$$

The scattering cross-section σ_s may be summarized with the following expression [80]:

$$\sigma_s = \int_0^{\infty} \int_0^{2\pi} \int_0^{\pi} f\left(R\right) \cdot F\left(\theta, \phi, R, m, \lambda\right) \cdot S_{str}\left(\theta, V_T, \lambda\right) \cdot \sin\theta \cdot d\theta \cdot d\phi \cdot dR \tag{3.45}$$

where f is the fraction of particles of radius R, which is a function of the particle size distribution, F is the differential cross-section which is a function of R and the complex refractive index m, θ is the scattered angle and ϕ is the azimuth angle. Here F is computed using Mie solution. And finally S_{str} is the static structure factor; this factor is a function of the energy of inter-particle interactions V_T and represents the microstructure of suspension. For highly diluted systems the inter-particle interactions are negligible, and S is equal to 1. In the case in which these interactions are not negligible (e.g. dense particulate systems), S has to be taken into account. It can be described using the Percus-Yevick-Hard-Sphere approximation (PY-HS) or using the Twersky's theory based on multiple light scattering theory [80]. The computed absorption and scattering cross-sections of individual particles can then be used to calculate the respective optical properties for a bulk of particles i.e. the absorption and scattering coefficients μ_{ap} and μ_s. The bulk scattering coefficient is just the sum of the scattering cross-sections of the particles in a unit volume of a sample and so is μ_{ap}. Thus, for particles of the same size we have:

$$\mu_{ap} = \sigma_{ap} N_p \tag{3.46}$$

$$\mu_s = \sigma_s N_p \tag{3.47}$$

where N_p is the number density of the particles i.e. the number of particles per unit volume. If particles have different sizes then the bulk scattering (or absorption) coefficient is given by:

$$\mu_s = \sigma_s^{'} N_p = \sigma_{s,1} N_{p,1} + \sigma_{s,2} N_{p,2} + \sigma_{s,3} N_{p,3} + ... + \sigma_{s,n} N_{p,n} \tag{3.48}$$

where $\sigma_s^{'}$ is the average scattering cross-section of particles. To get it in the explicit form let us divide both sides of the equation (3.48) by N_p:

$$\frac{\sigma_s^{'} N_p}{N_p} = \frac{\sigma_{s,1} N_{p,1} + \sigma_{s,2} N_{p,2} + \sigma_{s,3} N_{p,3} + ... + \sigma_{s,n} N_{p,n}}{N_p} \tag{3.49}$$

where $N_{p,i}/N_p$ is a fraction of particles with radius R_i which depends on the particle size distribution (PSD). Equation (3.49) may be written in terms of the probability density function P:

$$\sigma_s^{'} = \left(\sigma_{s,1} P_1 + \sigma_{s,2} P_2 + \sigma_{s,3} P_3 + ... + \sigma_{s,n} P_n \right) dR = \sum_{i=1}^{n} \sigma_{s,i} P_i \, dR \tag{3.50}$$

Therefore, if the PSD is known the average scattering cross-section for poly-disperse particles can be determined from the following integral:

$$\sigma_s^{'} = \int_o^{\infty} \sigma_s P \, dR \tag{3.51}$$

In the program for computing the optical properties of poly-disperse particles Gauss-Laguerre quadrature was used to find the given integral. This quadrature was chosen because it is designed to integrate functions from zero to infinity and thus naturally suits our problem.

The computed bulk optical properties of the particles μ_{ap}, μ_s and g can in turn be used for modelling light propagation in the sample under multiple scattering using RTE to obtain the intensities of the transmitted and reflected fields. By following the reverse order one should be able to determine the particle size distribution and/or the complex refractive indices of the particles and the medium from the measured intensities of the transmitted and reflected light.

3.1.2. Radiative transfer theory

If the bulk optical properties of a sample are known light propagation in turbid media, neglecting any wave phenomena associated with light (e.g. diffraction, interference), can be modelled using the heuristic radiative transfer theory, where, light propagation is modelled by solving the full radiative transport equation [75, 81] given by:

$$\frac{d\mathbf{I}(\mathbf{r},\mathbf{s})}{d\mathbf{s}} = -\mu_t \cdot \mathbf{I}(\mathbf{r},\mathbf{s}) + \frac{\mu_s}{4\cdot\pi}\int_{4\pi} p(\mathbf{s},\hat{\mathbf{s}})\cdot \mathbf{I}(\mathbf{r},\hat{\mathbf{s}})\cdot d\Omega \tag{3.52}$$

where $\mathbf{I}(\mathbf{r},\mathbf{s})$ is the specific intensity at the distance *r* from the source along the directional vector **s** [W/m^2], μ_a is the bulk absorption coefficient [m^{-1}], μ_s is the bulk scattering coefficient [m^{-1}], $\mu_t = \mu_a + \mu_s$ is the total extinction coefficient, $p(\mathbf{s},\hat{\mathbf{s}})$ is the phase function, which is a measure of the angular distribution of scattered light and Ω is the solid angle. The radiative transfer equation describes the change in the intensity of light of a given wavelength as it travels through a sample in a certain direction.

The bulk absorption and scattering coefficients are proportional to concentrations of absorbing and scattering components respectively. For samples with multiple absorbing and scattering components the bulk absorption and scattering coefficients are the sums of the respective coefficients of individual components:

$$\mu_a = \sum_{i=1}^{n}\mu_{a,i} = \sum_{j=1}^{n_p}\mu_{ap,j} + \sum_{k=1}^{n_a}\mu_{a,k} = \sum_{j=1}^{n_p}\sigma_{ap,j}\cdot c_{p,j} + \sum_{k=1}^{n_a}\sigma_{a,k}\cdot c_k \tag{3.53}$$

$$\mu_s = \sum_{i=1}^{n_p}\mu_{s,i} = \sum_{j=1}^{n_p}\sigma_{s,j}\cdot c_{p,j} \tag{3.54}$$

where $\sigma_{ap,j}$ and $\sigma_{s,j}$ are the absorption and scattering cross-sections (m^2) of the particulate species *j*, $c_{p,j}$ is the concentration of the particulate species *j* expressed as number density i.e. number of particles per unit volume (m^{-3}) and n_p is the number of different particulate species present in the sample. $\sigma_{a,k}$ represents the absorptivity (m^2/kg) of the purely absorbing species *k*, c_k is the concentration (kg/m^3) of the absorbing species *k* and n_a is the number of purely absorbing species present in the sample. It should be noted that the bulk absorption and scattering coefficients as well as the absorption and scattering cross-sections of the particles and the absorptivity of the purely absorbing species are all wavelength dependent. In equation (3.53) μ_a has been split into two terms. The first summation represents the contribution from the particulate species and the second summation represents the contribution from the purely absorbing species.

The phase function *p* describes the angular distribution of scattered light at a particular wavelength. There are several phase functions that have been used among which the most common is the Henyey-Greenstein phase function:

$$p(\theta, g) = \frac{1 - g^2}{\sqrt{\left(1 + g^2 - 2 \cdot g \cdot \cos\theta\right)^3}} \tag{3.55}$$

where θ – is an angle between incident and scattered directions and g is the anisotropy factor. As we can see from the equations (3.52-3.55), at each wavelength, the RTE is defined by three variables μ_a, μ_s and g referred to as the bulk optical properties.

There is no analytical solution to the radiative transfer equation, but it can be solved numerically using the following methods: Monte Carlo [82, 83], adding-doubling [64, 65], discrete ordinates [84] and Chandrasekhar's X and Y functions [85]. Monte Carlo techniques have no limitations and so are valid for any radiative transport problem, but they are slow because of the statistical nature. The other methods are valid numerical solutions of the RTE under certain assumptions and therefore yield accurate results if those assumptions are satisfactorily met. Hence, the choice of the numerical method depends on the type of the problem. In this research work, the light propagation model which simulates samples with arbitrary scattering to absorption ratios, anisotropic scattering and mismatched boundaries (air-glass-sample) accurately and relatively fast was needed. The most suitable candidate in this case is Adding-Doubling. It works naturally with layered media and yields the total reflection and transmission of a sample readily. The total reflectance and transmittance can be accurately measured with a simple integrating sphere setup therefore the use of these measurements for the extraction of the optical properties of a sample is practical [65]. There are also a number of approximations to the radiative transfer like the diffusion equation [86, 87], Kubelka-Munk [88] or successive orders [89] that are easier to solve but they place restrictions on the values of one or more of the optical properties or are not sufficiently flexible in incorporating the necessary boundary conditions needed for turbid samples with mismatched boundaries [64].

3.1.2.1. Adding-doubling

The Doubling method was introduced by Van de Hulst for solving the radiative transport equation in a slab geometry [89]. The advantages of the adding-doubling method are that only integrations over angle are required, physical interpretation of results can be made at each step, the method is equivalent for isotropic and anisotropic scattering, and results are obtained for all angles of incidence used in the integration [90]. The disadvantages are that it is (a) slow and awkward to calculate internal fluences, (b) suited only to a layered geometry with uniform irradiation, and (c) necessary that each layer has

homogeneous optical properties. For determining optical properties using only reflection and transmission, internal fluences are not needed so (a) is not a problem. Items (b) and (c) place restrictions on the sample geometry i.e. the samples must be uniformly illuminated, homogeneous slabs of sufficient width so that light does not "leak" from the sides of the sample. The adding-doubling method is well-suited to iterative problems because it provides accurate total reflection and transmission calculations with relatively few quadrature points. The method is very fast for small numbers of quadrature points, and consequently iteration is practical.

In Adding-Doubling the following assumptions are made: the distribution of light is independent of time, samples have homogeneous optical properties, the sample geometry is an infinite plane-parallel slab of finite thickness, the sample has a uniform index of refraction, internal reflection at boundaries is governed by Fresnel's law, and the light is unpolarized. A non-absorbing layer with a different index of refraction may be present at the boundaries (e.g. glass slide).

The doubling method assumes that the reflection $R(\nu,\nu')$ and transmission $T(\nu,\nu')$ of light incident at an angle ν and exiting at an angle ν' is known for one layer. The reflection and transmission of a slab twice as thick is found by juxtaposing two identical slabs and adding the reflection and transmission contributions from each slab. The reflection and transmission for a slab of an arbitrary thickness are calculated by first finding the reflection and transmission for a thin starting slab with the same optical properties and then repeatedly doubling the thickness of the thin slab until the desired thickness is reached. The starting/initial layer should be thin enough so that single scattering conditions can be applied. The reflection and transmission for the initial layer can then be found using diamond initialisation which is the best method according to Wiscombe's results [91]. The required inputs are a (albedo), τ (optical depth, turbidity or total attenuation) and the scattering anisotropy g if Henyey-Greenstein phase function is used eq. (3.55). Albedo is the following dimensionless quantity:

$$a = \frac{\mu_s}{\mu_t} = \frac{\mu_s}{\mu_a + \mu_s} \tag{3.56}$$

which tells us what fraction of the attenuated light is due to scattering or in other words which extinction mechanism is predominant absorption or scattering. The optical depth is also a dimensionless quantity showing how much of light is attenuated in a certain distance l travelled within the sample:

$$\tau = \left(\mu_a + \mu_s\right) l \tag{3.57}$$

The Adding method extends the Doubling method to dissimilar slabs. Thus, slabs with different optical properties can be placed adjacent to one another to simulate layered media or internal reflection caused by differences in the index of refraction.

The implementation of the Adding-Doubling method for calculating the reflection and transmission of a turbid slab in a medium with a different index of refraction consists of the following steps

- Choose quadrature scheme [64]
- Generate starting layer [92]
- Generate boundary layers [93]
- Double starting layer until desired thickness is reached [89]
- Add boundary layers to this [90]
- Calculate reflection and transmission [90]

A full guide on implementing Adding-Doubling method for solving the radiative transfer problem is given by Prahl [65].

3.2. MULTIVARIATE CALIBRATION

Multivariate calibration is the main tool in quantitative spectroscopic analysis i.e. in the prediction of concentrations of chemical components from spectral measurements. It is based on the fact that the measured absorbance of the sample is directly proportional to the concentration of the absorber (i.e. absorbing species), given by the Beer-Lambert's law:

$$A = -\ln\left(\frac{I}{I_0}\right) = \sigma_a \cdot c \cdot \ell = \mu_a \cdot \ell \tag{3.58}$$

where A is the absorbance at a particular wavelength (it is a dimensionless quantity), I_0 and I are the intensities of the incident and the attenuated light [W/m^2] and ℓ is the path length travelled by the photons. Note, that σ_a and hence A are wavelength dependent. It is also assumed in multivariate calibration that the total absorbance for a sample with multiple absorbing species is the sum of the absorbances of those species:

$$A = \ell \sum_{i=1}^{n} \mu_{a,i} = \ell \sum_{i=1}^{n} \sigma_{ai} \cdot c_i = \left(\sigma_{a1} \cdot c_1 + \sigma_{a2} \cdot c_2 + \sigma_{a3} \cdot c_3 + \cdots + \sigma_{an} \cdot c_n\right) \cdot \ell \tag{3.59}$$

The same assumption is made in equation (3.53). If this assumption is satisfied then each absorption spectrum represents a system of linear equations. For example, an absorption spectrum of a sample containing three absorbing species consisting of m wavelengths can be mathematically represented as given by:

$$\begin{cases} \sigma_{a1,1} \cdot c_1 + \sigma_{a2,1} \cdot c_2 + \sigma_{a3,1} \cdot c_3 = \mu_{a,1} \\ \sigma_{a1,2} \cdot c_1 + \sigma_{a2,2} \cdot c_2 + \sigma_{a3,2} \cdot c_3 = \mu_{a,2} \\ \sigma_{a1,3} \cdot c_1 + \sigma_{a2,3} \cdot c_2 + \sigma_{a3,3} \cdot c_3 = \mu_{a,3} \\ \vdots \\ \sigma_{a1,m} \cdot c_1 + \sigma_{a2,m} \cdot c_2 + \sigma_{a3,m} \cdot c_3 = \mu_{a,m} \end{cases} \tag{3.60}$$

$$\underset{m \text{ wavelengths}}{\mathbf{S}} \begin{bmatrix} \sigma_{a1,1} & \sigma_{a2,1} & \sigma_{a3,1} \\ \sigma_{a1,2} & \sigma_{a2,2} & \sigma_{a3,2} \\ \sigma_{a1,3} & \sigma_{a2,3} & \sigma_{a3,3} \\ \vdots & \vdots & \vdots \\ \sigma_{a1,m} & \sigma_{a2,m} & \sigma_{a3,m} \end{bmatrix} \cdot \underset{k \text{ samples}}{\mathbf{C}} \begin{bmatrix} c_{1,1} & c_{1,2} & c_{1,3} & \cdots & c_{1,k} \\ c_{2,1} & c_{2,2} & c_{2,3} & \cdots & c_{2,k} \\ c_{p,1} & c_{p,2} & c_{p,3} & \cdots & c_{p,k} \end{bmatrix} = \underset{\mu_a \text{ spectrum of sample } k}{\mathbf{A}} \begin{bmatrix} \mu_{a,11} & \mu_{a,12} & \mu_{a,13} & \cdots & \mu_{a,1k} \\ \mu_{a,21} & \mu_{a,22} & \mu_{a,23} & \cdots & \mu_{a,2k} \\ \mu_{a,31} & \mu_{a,32} & \mu_{a,33} & \cdots & \mu_{a,3k} \\ \vdots & \vdots & \vdots & \ddots & \vdots \\ \mu_{a,m1} & \mu_{a,m2} & \mu_{a,m3} & \cdots & \mu_{a,mk} \end{bmatrix} \tag{3.61}$$

species 1 | species 2 | species 3 | μ_a spectrum of sample 1 | μ_a spectrum of sample 2 | μ_a spectrum of sample 3

For multiple samples this can be conveniently written in the matrix form as given in eq. (3.61). Therefore, the general problem in matrix notation is written as:

$$\mathbf{A} = \mathbf{S} \cdot \mathbf{C} \tag{3.62}$$

where **A** is the matrix of absorbance measurements, **S** is the matrix of absorption cross-sections (absorptivities) of pure chemical species and **C** is the concentration matrix. Now, we could find the concentrations of the species from the measured absorbances using ordinary least squares:

$$\mathbf{C} = \left(\mathbf{S}^{\mathsf{T}} \cdot \mathbf{S}\right)^{-1} \cdot \mathbf{S}^{\mathsf{T}} \cdot \mathbf{A} \tag{3.63}$$

if the absorptivities of pure components were known. Finding the matrix **S** requires the calibration step, which consists of collecting the absorbance measurements for a set of samples with known concentrations of species i.e. the calibration dataset, and then finding **S** via least squares:

$$\mathbf{S} = \mathbf{A}_{cal} \cdot \mathbf{C}_{cal}^{\mathsf{T}} \cdot \left(\mathbf{C}_{cal} \cdot \mathbf{C}_{cal}^{\mathsf{T}}\right)^{-1} \tag{3.64}$$

However, in order to obtain **S** the concentrations of all absorbing species must be known in the calibration samples. Often the concentration of only one or few components is of interest to us and so the determination of concentrations of the rest of the species in the calibration samples requires additional work which may be costly and sometimes impossible (e.g. in the quantitative analysis of oil which consists of millions of organic species). Alternatively, we can rewrite equation (3.63) as:

$$\mathbf{c} = \mathbf{F} \cdot \mathbf{A} \tag{3.65}$$

where matrix **F** stands for $\left(\mathbf{S}^{\mathbf{T}} \cdot \mathbf{S}\right)^{-1} \cdot \mathbf{S}^{\mathbf{T}}$ and the small **c** denotes the concentration of one species, which is of interest. Now the objective is to find the matrix **F**. But, in this case, we can calibrate it for just one germane component:

$$\mathbf{F} = \mathbf{c}_{cal} \cdot \mathbf{A}_{cal}^{\mathsf{T}} \left(\mathbf{A}_{cal} \cdot \mathbf{A}_{cal}^{\mathsf{T}}\right)^{-1} \tag{3.66}$$

Once the calibration step is done i.e. the matrix **F** is known, the concentration of the species of interest in the unknown samples can be found from the measurements using eq. (3.65).

This classic way of multivariate calibration is however often not applicable, because usually the spectra in the matrix **A** are highly correlated and therefore the

inversion of the matrix $\mathbf{A} \cdot \mathbf{A}^{\mathrm{T}}$ is a problem. Calibration results are very sensitive to noise in the measurements consequently the calibration model is not robust. To overcome this problem multivariate modelling techniques such as Principal Component Regression or Partial Least Squares Regression are usually applied that decompose the matrix of measurements A into orthogonal components called principal components or latent variables that can then be used for building the regression model.

3.2.1. Partial least squares

The whole idea is to transform the measurement matrix **A**, the columns of which are correlated, into a new matrix **T** (called the matrix of scores) with orthogonal (independent) columns that represent new uncorrelated variables (called principal components or latent variables) using the following linear transformation:

$$\mathbf{A} = \mathbf{T} \cdot \mathbf{P}^{\mathrm{T}} \tag{3.67}$$

The matrix **P** is called loadings and it represents a set of independent vectors. Equation (3.67) can be alternatively written as:

$$\mathbf{T} = \mathbf{A} \cdot \mathbf{P} \tag{3.68}$$

The dot product means that scores are basically projections of the rows of matrix **A** onto the vectors given in **P** (taking into account that these vectors have unit lengths). Note, that the convention is to have the rows of **A** as samples and the columns as wavelengths (variables) i.e. the transpose of what have been used in eq. (3.61-3.66). Thus scores can be thought of as lengths of the projections of the samples onto the independent vectors given in the matrix **P**.

In PLS directions of the orthonormal vectors of **P** are chosen such that the covariance between **A** and **c** is maximised i.e. the scores of the first latent variable have maximum correlation with concentrations. If we express the vector of scores as some unknown linear combination of **A**:

$$\mathbf{t}_1 = \mathbf{A} \cdot \mathbf{w}_1 \tag{3.69}$$

where $\mathbf{t}_1$ is the scores vector of the first latent variable and $\mathbf{w}_1$ is the unknown vector called the vector of weights, then the optimisation problem can be formulated as find $\mathbf{w}_1$ such that the covariance $\mathbf{c}^{\mathrm{T}} \cdot \mathbf{t}_1$ is maximised. Mathematically this can be written as:

$$\max\left(\left(\mathbf{c}^{\intercal}\cdot\mathbf{t}_1\right)^{T}\cdot\left(\mathbf{c}^{\intercal}\cdot\mathbf{t}_1\right)\right)=\max\left(\mathbf{t}_1^{\intercal}\cdot\mathbf{c}\cdot\mathbf{c}^{\intercal}\cdot\mathbf{t}_1\right)=\max\left(\mathbf{w}_1^{\intercal}\cdot\mathbf{A}^{\intercal}\cdot\mathbf{c}\cdot\mathbf{c}^{\intercal}\cdot\mathbf{A}\cdot\mathbf{w}_1\right)$$
$$\text{subject to the constraint } \mathbf{w}_1^{\intercal}\cdot\mathbf{w}_1=1 \tag{3.70}$$

This constrained optimisation problem can be solved using Lagrange's method of undetermined multipliers:

$$\frac{\partial}{\partial\mathbf{w}_1}\left(\mathbf{w}_1^{\intercal}\cdot\mathbf{A}^{\intercal}\cdot\mathbf{c}\cdot\mathbf{c}^{\intercal}\cdot\mathbf{A}\cdot\mathbf{w}_1-\boldsymbol{\lambda}\left(\mathbf{w}_1^{\intercal}\cdot\mathbf{w}_1-1\right)\right)=0 \tag{3.71}$$

$$\left(\mathbf{A}^{\intercal}\cdot\mathbf{c}\cdot\mathbf{c}^{\intercal}\cdot\mathbf{A}\right)\cdot\mathbf{w}_1=\boldsymbol{\lambda}\cdot\mathbf{w}_1 \tag{3.72}$$

As one can notice from the eq. (3.72), $\mathbf{w}_1$ appears to be the eigenvector of the matrix $\mathbf{A}^{\intercal}\cdot\mathbf{c}\cdot\mathbf{c}^{\intercal}\cdot\mathbf{A}$ and $\boldsymbol{\lambda}$ is the eigenvalue of it. The first eigenvector will have the largest eigenvalue meaning that the first latent variable will explain the most of the covariance between **A** and **c**. Having obtained $\mathbf{t}_1$ we find the first loadings vector $\mathbf{p}_1$ from the least squares solution:

$$\mathbf{p}_1=\left(\mathbf{t}_1^{\intercal}\cdot\mathbf{t}_1\right)^{-1}\cdot\mathbf{t}_1^{\intercal}\cdot\mathbf{A} \tag{3.73}$$

The next step is to find the relationship between the scores $\mathbf{t}_1$ of the matrix **A** and the concentrations i.e. solve $\mathbf{c}=\mathbf{t}_1\cdot\alpha_1$ for α_1 again using regression:

$$\alpha_1=\left(\mathbf{t}_1^{\intercal}\cdot\mathbf{t}_1\right)^{-1}\cdot\mathbf{t}_1^{\intercal}\cdot\mathbf{c} \tag{3.74}$$

And finally compute the prediction errors in **A** and **c**:

$$\mathbf{E}_{\mathbf{A}}=\mathbf{A}-\mathbf{t}_1\cdot\mathbf{p}_1^{\intercal} \tag{3.75}$$

$$\mathbf{E}_{\mathbf{c}}=\mathbf{c}-\mathbf{t}_1\cdot\alpha_1 \tag{3.76}$$

Substitute **A** and **c** for $\mathbf{E}_A$ and $\mathbf{F}_c$ and repeat the iteration to find the next latent variable. The iterations are continued for as many latent variables as we need. The eigenvalues of the subsequent latent variables will gradually decrease explaining less and less of the covariance between the measured absorbances and the corresponding concentrations. How many latent variables we need to include into the calibration model is determined via the cross-validation procedure. The general objective of the cross-validation is to find the number of latent variables that gives the best prediction accuracy, which is evaluated using the root mean square error of cross-validation (RMSECV) statistical metrics. RMSECV is based on the prediction of the unknown samples to avoid the over-fitting. There are many

methodologies for cross-validation such as leave-one-out, random subsets, venetian blinds, contiguous block or boot strapping. The one used in this work was leave-one-out. To obtain a completely unbiased estimate of prediction error another set of totally 'unseen' data i.e. a test set, is used for prediction (if available), in which case the error metrics is called the root mean square error of prediction (RMSEP). Thereby, conventionally, the data is divided/split into the calibration set and the test set, but only if the number of samples (i.e. data points) in each set is sufficient (rule of thumb – more than 30). If the calibration set represents the whole population of samples well then RMSECV and RMSEP values should be statistically the same.

Partial least squares algorithm was originally proposed by Wold [94]. A detailed description of it and its statistical properties are also given by Geladi and Kowalski [95] and Höskuldsson [96].

3.2.2. Empirical pre-processing techniques

The pre-processing step is critical in the quantitative analysis of suspensions and turbid samples in general. This is because the nonlinear effects of multiple light scattering degrade the performance of the conventional multivariate calibration models such as PLS significantly since they are designed for bilinear systems. The objective of the pre-processing step is therefore to remove the nonlinear effects of multiple scattering and linearise the measurement matrix **A**.

A number of different empirical pre-processing techniques have been designed for removing various artifacts from the spectral data and they have been briefly discussed in the literature review. According to S. N. Thennadil's extensive study on the performance of different pre-processing techniques [33] EMSC with logarithmic wavelength dependency did the best in correcting multiple scattering effects. Therefore, it was used as a benchmark in this work when evaluating the results obtained using the proposed new methodologies. Hence, a brief description of the basic MSC and two different forms of EMSC techniques is given here.

Multiplicative Scatter Correction. The basis of the Multiplicative Scatter/Signal Correction is the fact that the wavelength dependency of light scattering effects is different from that of chemically based light absorption. Therefore, following this heuristic argument, it should be possible to distinguish between absorption and scattering using data from many wavelengths. In MSC it is assumed that light scattering has an additive and a

multiplicative or scaling effect on the measured spectrum i.e. it moves the baseline and scales the spectrum. Accordingly, the spectrum of each sample can be written in a simple linear model of the following form:

$$\mathbf{a}_i = b_{0,i} + b_{1,i}\bar{\mathbf{a}} + \mathbf{e}_i \tag{3.77}$$

where $\mathbf{a}_i$ is the spectrum of the i^{th} sample and $\bar{\mathbf{a}}$ is the reference spectrum, which is usually taken as the mean spectrum of all samples. For each sample coefficients $b_{0,i}$ and $b_{1,i}$ are estimated by ordinary least squares regression. Coefficient b_0 represents the additive effect and coefficient b_1 represents the multiplicative or scaling effect of light scattering to the measurement. The residual spectrum $\mathbf{e}_i$ ideally represents the chemical information in $\mathbf{a}_i$. After the coefficients have been found the corrected spectrum for each sample is calculated as follows:

$$\mathbf{a}_{i,corr} = \frac{\mathbf{a}_i - b_{0,i}}{b_{1,i}} = \bar{\mathbf{a}} + \frac{\mathbf{e}_i}{b_{1,i}} \tag{3.78}$$

In summary, the scattering for each sample is estimated relative to that of the reference sample, and the spectrum of each sample is then corrected so that all samples have approximately the same scattering level as the reference sample. However, this technique for correcting for multiplicative light scattering is only reliable if the chemical variation between the spectra to be corrected and the reference spectrum is negligible, or alternatively, the regression procedure is only applied to that part of the spectrum that does not contain chemical information, i.e., the part that is only influenced by multiplicative light scattering. If the above conditions are not satisfied, then the estimated intercept and slope may contain information relating to the analyte of interest and hence this will be lost during the implementation of the correction procedure. A more detailed discussion about the limitations and the drawbacks of the MSC can be found in [31].

Extended Multiplicative Signal Correction. The aforementioned limitation of MSC can be addressed by adding the summation of absorptivities of the pure species present in the sample to the MSC equation as first proposed by Martens and Stark [31] if such information is available. Then, the variation in chemical information does not influence the coefficients b_0 and b_1 representing the scattering effects. Another drawback of the MSC is the assumption that light scattering effects are independent of the wavelength for a given sample. However, light scattering is a highly nonlinear function of the wavelength e.g. for small particles the scattered intensity is inversely proportional to the λ^4 (Rayleigh

approximation). Therefore, the basic form of EMSC [31] was further extended to account for the wavelength dependency of light scattering effects. Martens modelled wavelength dependency using the second order polynomial [32]. Thus, the measured spectrum is decomposed into the following terms:

$$\mathbf{a}_i = b_{0,i} + b_{1,i}\bar{\mathbf{a}} + \sum_{k=1}^{n} d_{k,i}\boldsymbol{\sigma}_k + b_{2,i}\boldsymbol{\lambda} + b_{3,i}\boldsymbol{\lambda}^2 + \mathbf{e}_i \tag{3.79}$$

where $\boldsymbol{\sigma}_k$ is the absorptivity of the k^{th} pure chemical species and the term $b_2\boldsymbol{\lambda} + b_3\boldsymbol{\lambda}^2$ is used for modelling the wavelength dependency of the scattering effects. The coefficients of this linear equation $b_{0,i}$, $b_{1,i}$, $b_{2,i}$, $b_{3,i}$ and $d_{k,i}$ are estimated by ordinary least squares regression. The corrected spectrum for each sample is then calculated as:

$$\mathbf{a}_{i,corr} = \frac{\mathbf{a}_i - b_{0,i} - b_{2,i}\boldsymbol{\lambda} - b_{3,i}\boldsymbol{\lambda}^2}{b_{1,i}} \tag{3.80}$$

Strictly speaking the wavelength dependency of the scattering effects is not quadratic; it is a complex nonlinear function in the case of scattering by spherical particles given by Mie solution. Therefore, Thennadil and Martin used a different wavelength-dependent term for the EMSC [33]:

$$\mathbf{a}_i = b_{0,i} + b_{1,i}\bar{\mathbf{a}} + \sum_{k=1}^{n} d_{k,i}\boldsymbol{\sigma}_k + b_{2,i}\log\boldsymbol{\lambda} + \mathbf{e}_i \tag{3.81}$$

The reasoning behind using the logarithmic term is based on the aforementioned fact that for small particles the scattered intensity is inversely proportional to λ^4. In general, it is plausible that the scattering by particles can be expected to be approximately of the form $\alpha\lambda^{\beta}$. Taking the logarithm of this term, since absorbance units are the basis of the analysis, leads to the 'log' term in equation (3.81). The correction in this case is given by:

$$\mathbf{a}_{i,corr} = \frac{\mathbf{a}_i - b_{0,i} - b_{2,i}\log\boldsymbol{\lambda}}{b_{1,i}} \tag{3.82}$$

As one can notice in eq. (3.79) and (3.81), the available information about the pure chemical species i.e. spectra of pure components can be included in both EMSC forms.

3.3. THE PROBLEM OF QUANTITATIVE NIR ANALYSIS OF TURBID SAMPLES

A turbid sample is a heterogeneous sample that scatters light e.g. particles suspended in water. The problem in obtaining a good calibration model for turbid samples using conventional chemometrics stems from the fact that the measured change in absorbance or optical depth cannot be effectively correlated with changes in concentrations of chemical components because it is confounded with changes caused by light scattering. The problem is illustrated in figure 3.1. Figure 3.1 (a) represents case (a) where light passes through a homogenous liquid mixture. In this case, the photons only undergo absorption. Figure 3.1 (b) represents case (b) where light passes through a turbid sample (particles suspended in liquid) with particle concentration sufficiently low that the photons passing through the sample encounter a particle only once (single scattering).

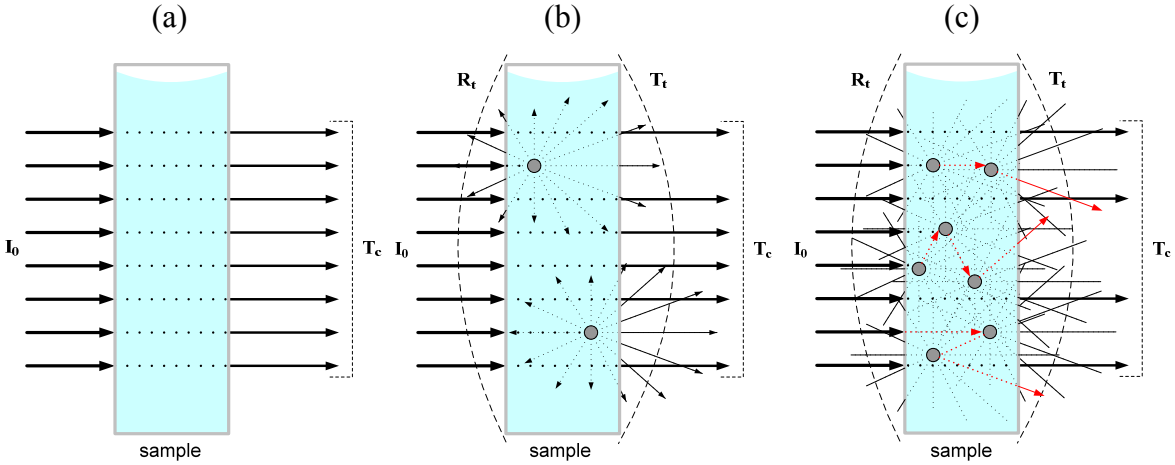

Figure 3.1. a.) Homogeneous sample (e.g. liquid mixture), absorption only; b.) Turbid sample with very low concentration of scatterers (particles), absorption + single scattering; c.) Turbid sample with a high concentration of scatterers, absorption + multiple scattering.

Figure 3.1 (c) represents case (c) where the particle concentration is sufficiently high such that the photons encounter several particles i.e. undergo multiple scattering events before exiting the sample. Since the direction of the photons change during each scattering event, the total path length travelled by the photon before exiting the sample will be different from (greater than or equal to) the sample thickness. From the point of making measurements for estimating the concentrations of chemical components, it is desirable to choose a configuration that provides measurements proportional to the concentrations of the chemical components. In the absence of scattering, that is in case (a), since the attenuation of light passing through a sample is linearly related to the concentrations of chemical species via the Lambert-Beer law eq. (3.58), which for a sample containing *n*

absorbing chemical species is given by eq. (3.59), we can simply measure what fraction of the incident collimated beam of light is axially transmitted through the sample (this measurement is referred to as collimated transmittance T_c in this work). The path length travelled by the photons in this case is the sample thickness ℓ. In the presence of scattering, the total attenuation of the incident light is still linearly related to the concentrations of species via the modified Lambert-Beer equation:

$$\tau = -\ln\left(\frac{I}{I_0}\right) = \ell \cdot \sum_{i=1}^{n} \sigma_{ext,i} \cdot c_i = \left(\mu_a + \mu_s\right) \cdot \ell \tag{3.83}$$

where $\sigma_{ext,i} = \sigma_{a,i} + \sigma_{s,i}$ is the extinction cross-section with the scattering cross-section being non-zero for those species which are particles. But, measuring it (i.e. the optical depth τ) in this case may not be trivial, because one needs to measure only the unscattered fraction of the transmitted light i.e. light that went straight through the sample. In case (b), $\ln(1/T_c)$ is usually a very good estimate of τ since T_c normally has only a very small component of the multiply scattered (diffuse) light in it. In case (c), measuring those ballistic photons that were neither absorbed nor scattered is a much bigger problem, because only a small fraction of light goes through the sample without being absorbed or scattered and it is difficult to separate them from the scattered photons. The accuracy of τ approximated by simply using T_c measurement, in this case, strongly depends on the measurement set-up. Theoretically, there will always be a fraction of diffusely scattered light included in the T_c measurement. However, it depends very much on the distance between the detector and the sample and the size (i.e. the cross-sectional area) of the irradiating collimated beam. As the distance between the detector and the sample increases the amount of diffuse light reaching the detector is quickly decreasing (according to the inverse square law), whereas the intensity of the unscattered light, which remains collimated, ideally should not change. If the detector was placed in infinity only a very small part of the diffuse light would reach the detector i.e. only those few scattered photons that happened to exit the sample exactly along the axis of illumination i.e. in the direction of the detector. Hence, transmitted collimated light measured along the axis of illumination may have a relatively small diffuse component depending on the distance between the detector and the sample and the size of the illuminated area. Note that as the amount of scattering increases, an increasing amount of forward scattered light will be included in the T_c measurement. In cases (b) and (c), even though Beer's law still applies and a sufficiently

accurate measurement for the total attenuation can be obtained, the situation is complicated by the presence of nonlinear scattering effects. The scattering cross-section of particles is a highly non-linear function of particle size and shape. Thus for the same concentration of the scattering species, two different particle sizes would lead to changes in the absorbance which need to be corrected when building multivariate calibration models.

In the first case, multivariate calibration is straight-forward because absorption varies only with concentrations of chemical components (the other two terms, the absorption cross section and the path length, are constant) and this relationship is linear (see eq. 3.59). Therefore partial least squares models, that are based on the assumption of linear relationship between the absorbance and concentrations of the species, usually give very good results. In the second case, however, two terms in equation 3.83 can vary: the concentrations and the extinction cross-section of particles (the path length of light is constant). In the third case, the concentrations, the extinction cross-section of particles and the path length of light can all vary. This leads to confounding effects in the estimation of concentration of chemical components in turbid samples which arise because different combination of values of concentration, path length and extinction cross-section can lead to the same measurement value of A in equation (3.83). From the point of inverting the measurement value to obtain the concentration of species, since the contribution from these 3 parameters due to changes in particle size, shape and concentration cannot be distinguished from each other, it could cause potentially large errors in the estimated concentrations and thus will result in lack of robustness. In addition, these variations are nonlinear and therefore they degrade linear calibration models. This is true for any direct measurement since none of them is free from multiple light scattering effects. For instance, total reflectance or total transmittance measurements schematically shown in figure 3.1 (b) and (c). Since these measurements involve collection of light exiting from the sample in all directions, the average path length travelled by the photons is no longer equal to the sample thickness and it is not constant from sample to sample with the variation depending on the variation in the scattering properties of the sample which in turn depend on the particle size, shape and concentration. Thus, to obtain accurate calibration models for turbid samples, variations due to the path length and the absorption cross section of particles have to be corrected.

One can notice that a suitable quantity for multivariate calibration when dealing with turbid samples is μ_a, which is a measure of absorption per unit length [cm^{-1}] and so it is independent of the path length travelled by photons. It can be extracted by solving the

RTE. However, it is still not free from nonlinear effects because of changes in absorption cross section of particles σ_{ap}, which is a nonlinear function of particle size and shape. Thus, μ_a has one nonlinear term μ_{ap} in the equation (3.53), which is related to and contains quantitative information about particles that absorb light. Therefore, estimation of concentrations of absorbing only species and estimation of the concentration of the scattering absorbing species i.e. particles, are two different problems from the point of view of multivariate calibration. In the first case, the quantitative information to be extracted from μ_a using multivariate techniques is in the linear term whilst in the second case it is contained in the nonlinear term. Therefore, the number of latent variables needed and the accuracy of the calibration models may differ depending on the case. Hence, the problem of extracting concentration of chemical species in a particulate system (suspensions or powder mixtures) can be classified into two groups, viz.: the extraction of information of a chemical species that (a) purely absorbs and (b) both absorbs and scatters light. Furthermore, in the case of absorbing only species, we could obtain a completely linear system, which would be perfectly suitable for multivariate calibration, if we subtracted the absorption coefficient of particles μ_{ap} from μ_a. That is, theoretically, we could do one further step and remove/correct the nonlinear multiple scattering effects completely in that case. In the first step (extraction of μ_a) we get rid of photon path length variations that predominate in all measurements in highly scattering media and in the second step (subtraction of μ_{ap} from μ_a) we get rid of nonlinear variations in μ_a because of μ_{ap}. So in this case, there are two options: to do the first step only, which we will call partial correction of multiple scattering effects or to do both steps, which we will call full correction of multiple scattering effects. Both approaches have been researched for the case of estimation of concentrations of absorbing only species in this work, one dealing with partial correction the other one with full correction of multiple scattering effects.

CHAPTER IV

METHODOLOGIES FOR REMOVING MULTIPLE SCATTERING EFFECTS

Since conceptually there are two possible approaches for removing multiple light scattering effects using the radiative transfer theory (RTE) in order to improve the performance of multivariate calibration models two methodologies have been proposed and experimentally verified in this work, namely: partial correction of multiple scattering effects and full correction of multiple scattering effects. The first methodology is applicable for predicting the concentration of a scattering-absorbing component as well as the concentration of an absorbing only species. The second methodology is applicable only for estimation of the concentration of an absorbing only species.

4.1. THE CONCEPT

4.1.1. Partial correction of multiple scattering effects: removing variations due to path length

As discussed in the previous chapter, the main source of variation in measured intensities in the multiple scattering regime is the path length of photons, see fig. 3.1 c.). In principle, this variation can be eliminated by extracting a measure of absorption per unit length i.e. the bulk absorption coefficient μ_a, which is independent of the path length, using the radiative transfer theory. The concept of partial correction of multiple scattering effects for estimation of concentrations of chemical components in suspensions is presented in fig. 4.1. It is essentially a two step procedure: acquisition of the bulk optical properties and then extraction of pertinent chemical information from the bulk absorption coefficient.

At least three different measurements are needed to find the three unknown optical properties. The three measurements that were used for extraction of the optical properties were: total transmittance T_t, total reflectance R_t and collimated transmittance T_c. To obtain the bulk optical properties from these measurements we need to solve the inverse radiative transfer problem. Although the single scattering approximation is easier to solve sample preparation requires extensive dilution, which may introduce significant errors and change the state of the sample. Therefore, it is preferable to use samples with higher concentration of particles in which case multiple scattering effects become significant and the full radiative transfer equation has to be solved. In this work the adding-doubling method was used to solve the RTE, which is an exact and relatively fast numerical solution well suited

for this type of the problem, as described in chapter 3. Successful applications of it to similar problems have been reported in a number of works [6, 66, 97-99]. The optical properties were obtained via nonlinear optimisation i.e. by repeatedly solving the radiative transfer equation using the adding-doubling method until the solution matched the measured reflection and transmission values. The details of the inversion procedure are given in chapter 5. A discussion on the inverse adding-doubling (IAD) can also be found in Prahl's paper [64]. Before the data is fed to the IAD routine pre-screening and pre-processing steps may be done. These steps usually involve standard procedures such as detection and removal of outliers and filtering of noise i.e. smoothing.

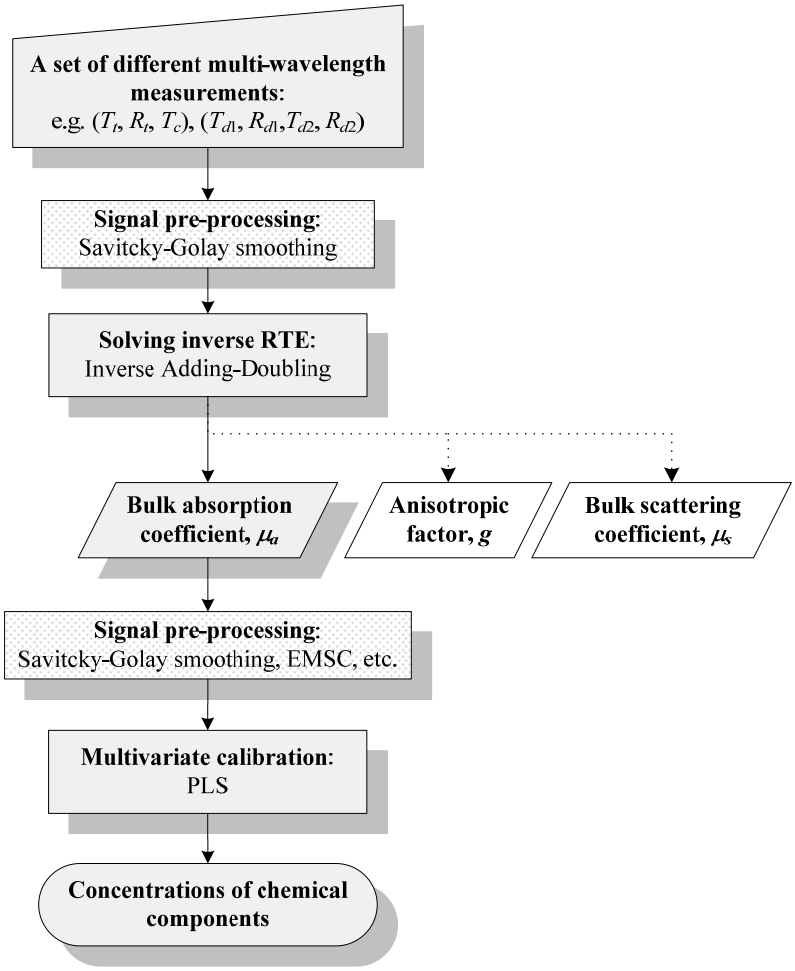

Figure 4.1. Methodology for partial correction of multiple scattering effects.

Once the bulk absorption coefficient has been extracted one can proceed to multivariate calibration. An intermediate step, which may improve calibration results, is again data pre-screening and signal pre-processing. In this step, empirical pre-processing techniques such as extended multiplicative scatter correction, that transform the data, can be applied on μ_a. They may improve calibration results i.e. the accuracy of predictions,

because μ_a may be subject to all sorts of baseline variations stemming from light losses, instrument drift etc. Although different multivariate calibration techniques could be used here for building a multivariate calibration model on the pre-processed bulk absorption coefficient PLS was chosen in this work as it is the most popular multivariate technique at present. Outliers may occur at this stage if IAD fails to converge to the right solution.

The same methodology can be applied to both cases i.e. estimation of the concentrations of non-scattering components and estimation of the concentration of the scattering absorbing component (i.e. particles). But, as discussed in chapter 3.3., the required number of latent variables in the PLS model and the accuracy of predicted concentrations may differ, because these two cases are different in principle from the point of view of multivariate calibration.

4.1.2. Full correction of multiple scattering effects: removing variations due to path length and particle size

The problem of quantitative analysis of absorbing only species in turbid samples can be further divided into two sub-problems: estimation of their concentrations when the scatterer (particles in our case) does not absorb and when it does absorb. In the first case, the absorption part is completely independent from changes in the physical properties of particles and medium such as size and real refractive index that change only the scattering part in this case and thus perfectly suitable for multivariate calibration since it varies only with concentrations of absorbing only species and this variation is linear. Therefore, only the first correction step, i.e. separation of absorption from scattering by extracting μ_a and μ_s, is needed in this case. The second case is more complex because absorbing particles affect not only scattering but also absorption of a sample. And these effects are nonlinear functions of the particle morphology (size, shape and etc.) and the refractive index of a medium since they change both absorption and scattering cross-sections of particles (σ_s and σ_{ap}) nonlinearly. When the number density and the size distribution of particles vary significantly variations in spectroscopic measurements of turbid samples are often dominated by the scattering. Extraction of μ_a allows us to circumvent the nonlinear scattering effects, but we are still left with some nonlinear effects in absorption due to nonlinear changes in the absorption cross-section of particles in this case. Therefore, in order to remove the nonlinear effects completely one should do one more correction step, that is, subtract the nonlinear μ_{ap} term from μ_a. This would make μ_a linear with

concentrations of absorbing only species, which are of interest in this case. The full correction is actually the same as taking particles away from the medium, but using calculations based on light propagation theory rather than doing that physically.

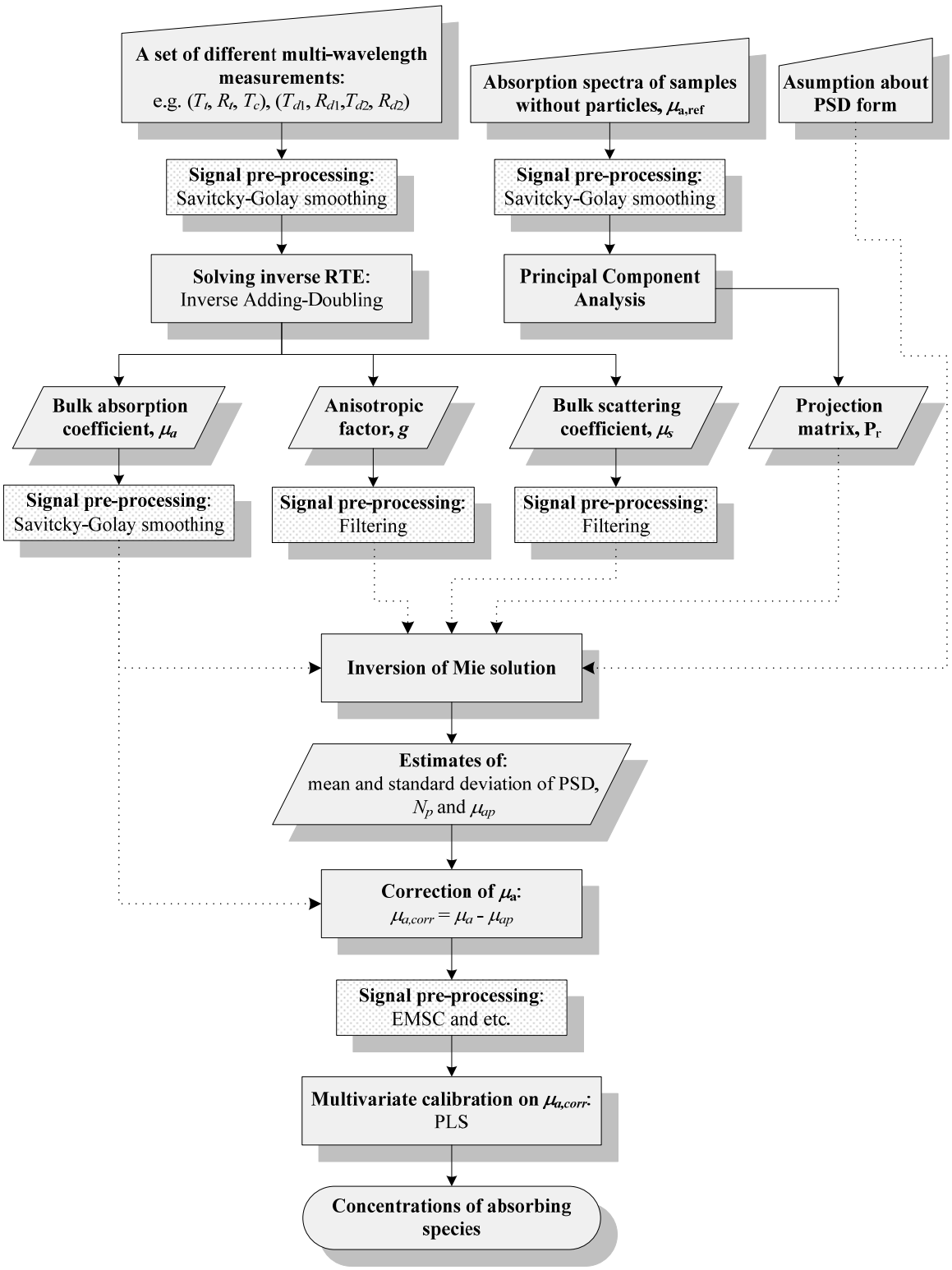

Figure 4.2. Methodology for full correction of multiple scattering effects.

It is not a trivial task to get an estimate of μ_{ap}. The two other optical properties of particles namely μ_s and g are directly obtained using IAD (if we have just one scattering species), but μ_{ap} is an implicit part of the bulk absorption coefficient and so cannot be extracted directly. For spherical particles, μ_{ap} as well as μ_s and g can be computed using Mie solution given the particle size distribution and number density (concentration) and complex refractive index. Since PSD and N_p are unknown one has to find them first, by inverting Mie solution using the known optical properties, to be able to compute μ_{ap}. Inversion of Mie solution is a renowned problem [100-113]. The fact which simplifies this problem in our case is that the goal is not to obtain an accurate particle size distribution. Even an approximate estimate of μ_{ap} and a subsequent correction may partly linearise μ_a and that may improve calibration results, which is our ultimate goal. The proposed concept of full correction of nonlinear scattering effects for estimation of concentrations of absorbing only species in suspensions is presented in figure 4.2.

Conventionally, values of μ_s at multiple wavelengths have been used for the inversion of Mie solution and acquisition of PSD [112, 113]. The objective function used in the nonlinear optimisation being the length of the error vector of μ_s, see eq. (4.1). Where μ_s is the actual measurement and $\hat{\mu}_s$ is its estimated value. The scattering coefficient is usually measured in single scattering regime so the other optical properties are not available.

$$f = \sqrt{\sum_{i=1}^{n} \left(\mu_{s,i} - \hat{\mu}_{s,i} \right)^2} \tag{4.1}$$

The advantage of working with multiple scattering is that we can extract all three optical properties and they can be used as inputs to the inverse Mie. There are several possible objective functions. For example, one could use just g or μ_s and g (at multiple wavelengths) instead of μ_s in which case the objective function would be:

$$f = \sqrt{\sum_{i=1}^{n} \left(\mu_{s,i} - \hat{\mu}_{s,i} \right)^2} + \sqrt{\sum_{i=1}^{n} \left(g_i - \hat{g}_i \right)^2} \tag{4.2}$$

Although to extract accurate values of g using IAD is a difficult challenge it is still worthwhile adding the length of the error in g vector to the objective function. The logic is the same as in the least squares method, the more points we have to fit the better the estimated constants are likely to be. Nobody has reported the use of g in the objective

function yet to the best of our knowledge.

In this work, a new way of including μ_a into the objective function, in order to maximise the use of the available information, is also described. This method is applicable when the absorbing only species that constitute the medium are known. Then, one can form a matrix $\mathbf{A}_p$ made up of the spectra of pure components (i.e. absorbing only species) or mixtures of these components:

$$\mathbf{A}_p = \begin{matrix} \\ \\ \\ \\ \\ \\ \end{matrix} \begin{matrix} \text{spectrum 1} & \text{spectrum 2} & \text{spectrum 3} & & \text{spectrum } n \end{matrix} \\ \begin{bmatrix} \mu_{a,11} & \mu_{a,12} & \mu_{a,13} & \cdots & \mu_{a,1n} \\ \mu_{a,21} & \mu_{a,22} & \mu_{a,23} & \cdots & \mu_{a,2n} \\ \mu_{a,31} & \mu_{a,32} & \mu_{a,33} & \cdots & \mu_{a,3n} \\ \vdots & \vdots & \vdots & \ddots & \vdots \\ \mu_{a,m1} & \mu_{a,m2} & \mu_{a,m3} & \cdots & \mu_{a,mn} \end{bmatrix} \begin{matrix} \\ \\ \\ \\ \\ \\ \end{matrix} \begin{matrix} \\ \\ \\ \\ \\ m \text{ wavelengths} \end{matrix} \tag{4.3}$$

Columns of $\mathbf{A}_p$**,** corresponding to spectra of pure components for instance, can be considered as vectors. These independent vectors span *n* dimensional subspace, where *n* is the number of pure components, in *m* dimensional space, where *m* is the number of wavelengths. Every spectrum of a mixture of these components must be in that subspace since they are all some linear combination of the columns of $\mathbf{A}_p$ that form the basis of that subspace. For example, any spectrum of a binary mixture **a** can be expressed as:

$$\mathbf{a} = \mathbf{S} \cdot \mathbf{c} = \begin{matrix} \\ \\ \\ \\ \\ \\ \end{matrix} \begin{matrix} \text{pure comp 1} & \text{pure comp 2} \end{matrix} \\ \begin{bmatrix} \sigma_{a1,1} & \sigma_{a2,1} \\ \sigma_{a1,2} & \sigma_{a2,2} \\ \sigma_{a1,3} & \sigma_{a2,3} \\ \vdots & \vdots \\ \sigma_{a1,m} & \sigma_{a2,m} \end{bmatrix} \cdot \begin{bmatrix} c_1 \\ c_2 \end{bmatrix} = \begin{bmatrix} \sigma_{a1,1} \\ \sigma_{a1,2} \\ \sigma_{a1,3} \\ \vdots \\ \sigma_{a1,m} \end{bmatrix} \cdot c_1 + \begin{bmatrix} \sigma_{a2,1} \\ \sigma_{a2,2} \\ \sigma_{a2,3} \\ \vdots \\ \sigma_{a2,m} \end{bmatrix} \cdot c_2 = \boldsymbol{\mu}_{a1} + \boldsymbol{\mu}_{a2} \tag{4.4}$$

Where, **c** is the vector of volumetric fractions of pure components. Note that $\mu_a = \sigma_a \cdot 1$ in case of pure components. Lower case bold fonts denote vectors and upper case bold fonts

denote matrices. Here, the subspace that the two column vectors form is obviously a plane and the spectra of all possible mixtures of these two components lie in this plane too. Now, if we put some particles into that mixture then the dimensionality of the measured absorption **a** would increase due to the nonlinear μ_{ap} component, since **a** would be equal to $\mathbf{a} = \boldsymbol{\mu}_{a1} + \boldsymbol{\mu}_{a2} + \boldsymbol{\mu}_{ap}$, and so its vector would be sticking out of the plane defined by the two absorbing only components, see illustration in fig. 4.3.

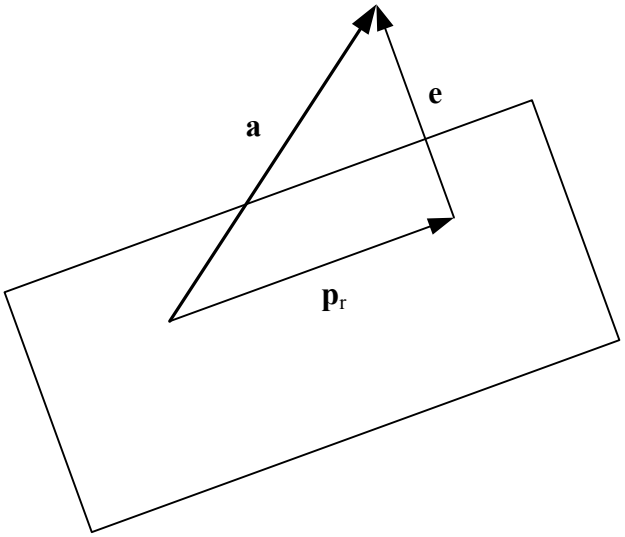

Figure 4.3. Projection on to the plane defined by absorbing only components.

The distance from the vector **a** to the plane represents the error due to uncorrected μ_{ap}. It is equal to the length of the error vector **e**, which can be calculated as:

$$\mathbf{e} = \mathbf{a} - \mathbf{p}_r \tag{4.5}$$

Where, the vector $\mathbf{p}_r$ is the projection of the vector **a** onto the plane. The projection of the vector **a** onto the column space can be found using the projection matrix $\mathbf{P}_r$:

$$\mathbf{p}_r = \mathbf{P}_r \cdot \mathbf{a} \tag{4.6}$$

$$\mathbf{P}_r = \mathbf{S} \cdot \left(\mathbf{S}^{\intercal} \cdot \mathbf{S}\right)^{-1} \cdot \mathbf{S}^{\intercal} \tag{4.7}$$

For full derivation of the projection matrix refer to [114]. This error can be included into the objective function of the inverse Mie solution as a measure of how accurate the estimated μ_{ap} and consequently the corrected μ_a are at each iteration of nonlinear optimisation. The more accurate the estimated μ_{ap} the more accurate the corrected μ_a and the smaller the error is. When μ_{ap} is determined accurately it is been completely removed from μ_a and the error should be equal to zero (i.e. vector **a** should lie in the plane in the

given example). Note that spectra that are already in the column space of $\mathbf{A}_p$ i.e. spectra of mixtures of absorbing only species, will stay unchanged by the projection matrix $\mathbf{P}_r$, that is $\mathbf{P}_r \cdot \mathbf{a} = \mathbf{a}$ in the given example since the projection of the vector which is already in the plane onto the same plane is the same vector, which means that all vectors in that subspace are actually the eigenvectors of $\mathbf{P}_r$. This is a convenient way to measure the accuracy of the correction. Neither Mahalanobis distance nor some Euclidean distance is suitable for this purpose i.e. for measuring how close the corrected μ_a is from the subspace of absorbing only samples, because even if the estimate of the corrected bulk absorption coefficient $\hat{\mu}_{a,corr}$ was in that subspace the distance from the centre of mass would not necessarily be equal to zero, which it should be in this case. Thereby, in the proposed methodology, the error in the corrected μ_a is calculated as follows:

$$\mathbf{e} = \hat{\boldsymbol{\mu}}_{a,corr} - \mathbf{P}_r \cdot \hat{\boldsymbol{\mu}}_{a,corr} \tag{4.8}$$

Note, that not only the spectra of pure components can be used in the matrix $\mathbf{A}_p$, which would be equal to using the matrix $\mathbf{S}$, but spectra of mixtures of pure components too. The subspace of the pure components in both cases will be the same. We might well have the case when the absorption coefficients of pure species are not linearly additive at some absorption bands as will be seen in the four component experiment discussed in the chapters 6.2.2 and 7.4. Then the matrix of just pure components is not sufficient, because they do not span/define the whole subspace of spectra of all possible mixtures. In such cases, we can use methods like Principal Component Analysis to model approximately the variation in absorption spectra. But for that we need to collect absorption spectra of different mixtures. The extracted principal components, that are actually eigenvectors of the matrix of the spectra of mixtures, can then be used as columns in the matrix $\mathbf{A}_p$.

If we add the error vector $\mathbf{e}$ to the objective function (4.2) we get the following:

$$f = w_1 \sqrt{\sum_{i=1}^{n} \left(\mu_{s,i} - \hat{\mu}_{s,i} \right)^2} + w_2 \sqrt{\sum_{i=1}^{n} \left(g_i - \hat{g}_i \right)^2} + w_3 \sqrt{\sum_{i=1}^{n} e_i^{\,2}} \tag{4.9}$$

where, w_1, w_2 and w_3 are the weights. In this way, all available information is used and so there is a higher likelihood to get a better defined global minimum than using just μ_s, because the nonlinear optimisation will now have to fit all three optical properties of particles namely μ_s, g and μ_{ap} (indirectly). Values of μ_s and g may be in a very different scale, therefore they were normalised to unit length so that they had equal weights in the

objective function. The length of the error vector **e** was about the same scale as of μ_s and g. If needed the weight of each term in the objective function can be adjusted using additional multipliers w_1, w_2 and w_3. It is particularly useful when the extracted optical properties are of different accuracy. For example in our experiments, the accuracy of the extracted g was significantly lower than the accuracy of μ_s therefore a lower weight was used on g.

To further simplify the inversion of Mie solution we assumed that the form of the particle size distribution was also known. In many practical situations this assumption may be reasonable because approximate distributions are often known. The size of the latex particles that were used in the experiments followed the normal distribution. Thus, there were three unknown variables in the inversion, namely, mean and standard deviation of PSD and N_p.

The first and the most crucial step in both methodologies is the extraction of the optical properties of a sample through the inversion of the radiative transfer equation using an appropriate set of measurements. Acquisition of accurate estimates of μ_a, μ_s and g is not a trivial task. It requires specific measurements and inversion of a complex theory. The accuracy of predictions of concentrations of chemical species depends highly on the accuracy of this step. Hence, this is discussed in detail in the next chapter.

CHAPTER V

EXTRACTION OF OPTICAL PROPERTIES OF SAMPLES

5.1. INVERSE ADDING-DOUBLING ROUTINE

The three unknown properties that we are looking for in the inverse adding-doubling are albedo a eq. (3.56), anisotropic factor g and turbidity or optical depth τ eq. (3.57). Two of them τ and g can in principal be measured directly. Optical depth τ can be approximately estimated by simply measuring the collimated transmittance $\tau = \ln(1/T_c)$. Anisotropy of scattering of light g is a more complicated property to measure, because we need to measure the amount of scattered light at all angles, but it can be done with a special instrument such as a goniometer.

There are many possible sets of three or more different measurements for inversion of RTE using adding-doubling method, for example:

- Total transmittance T_t, total reflectance R_t and g;
- Total transmittance T_t, total reflectance R_t and τ;
- Diffuse transmittance T_d and diffuse reflectance R_d measurements collected from different solid angles;
- Total transmittance T_t and total reflectance R_t measurements at different path lengths (i.e. T_{t1}, R_{t1}, T_{t2}, R_{t2} and so on);

Theoretically, any set of at least three different measurements should give a unique solution. We have chosen the following set of measurements T_t, R_t and τ, because it is the simplest one to implement in practical situations e.g. all three of them can be measured in one go with a double integrating sphere [64].

In this case, by extracting μ_a and μ_s we determine how much of the measured total attenuation (i.e. turbidity), which is nothing but $\tau = \mu_t = \mu_a + \mu_s$ in the case of the unit path length, was due to absorption and how much due to scattering.

Because the adding-doubling method is not an analytical solution to the radiative transfer equation (it is an iterative numerical solution) calculating the inverse is not straightforward. One ought to resort to nonlinear optimisation in this case. The iterative procedure of the IAD consists of the following steps:

1.) Guess a set of optical properties, namely, μ_a, μ_s and g;
2.) Calculate the total reflection and transmission using the adding-doubling method;

3.) Compare the calculated total reflection and transmission values with the measured ones;

4.) Change the values of μ_a, μ_s and g so that the error between the measured and calculated R_t and T_t is decreased (using nonlinear optimisation), and, repeat until they match.

Graphically this can be illustrated as shown in figure 5.1.

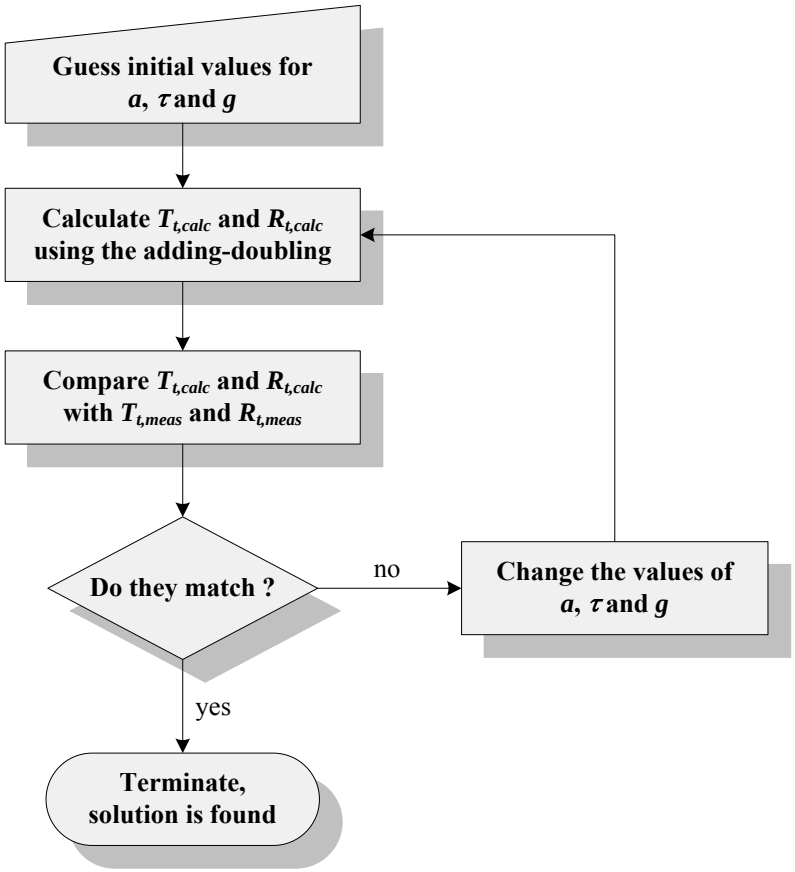

Figure 5.1. Inverse adding-doubling routine.

Constrained nonlinear optimisation was carried out using '*fmincon*' function from the Optimisation Toolbox (the 4th release) in MATLAB software (version 7.3.0.267). '*fmincon*' offers two different optimisation algorithms: the subspace trust region algorithm based on the interior-reflective Newton method where each iteration involves the approximate solution of a large linear system using the method of preconditioned conjugate gradients, which is designed for large scale problems, and the Sequential Quadratic Programming (SQP) algorithm designed for standard medium scale problems [115]. The SQP method was opted for our inverse problem. SQP was originally developed by Han [116] and Powell [117] and is generally considered the most reliable and efficient

algorithm for nonlinear programming currently available.

In general, there are two main steps in optimisation: calculating the search direction and the length of the step (called the line search). In SQP, the search direction is determined using quasi-Newton method, which is based on finding the extreme of the quadratic function. A quadratic approximation (fit) for any function around some point **x** is obtained using Taylor series i.e. by taking the first three terms of it:

$$y = f(\mathbf{x}) + \mathbf{J}(\mathbf{x})^{\mathsf{T}} \cdot \boldsymbol{\Delta} + \frac{1}{2}\boldsymbol{\Delta}^{\mathsf{T}} \cdot \mathbf{H}(\mathbf{x}) \cdot \boldsymbol{\Delta} \tag{5.1}$$

where, **x** is the vector of current values of variables, **J** is the vector of first order partial derivatives of **x** i.e. the gradient of **x** (also known as the Jacobian), **H** is the matrix of second order partial derivatives of **x** (known as the Hessian) and **Δ** is the following vector of differences of *x*:

$$\boldsymbol{\Delta} = \begin{bmatrix} \dot{x}_1 - x_1 \\ \dot{x}_2 - x_2 \\ \vdots \\ \dot{x}_n - x_n \end{bmatrix} \tag{5.2}$$

where, $\dot{\mathbf{x}}$ is the optimal solution that we are looking for. Having obtained gradients **J** and **H** through differentiation it is straightforward to find **Δ** and hence the optimal solution $\dot{\mathbf{x}}$ from eq. (5.1) provided the initial solution **x** is known. Differentiating eq. (5.1) gives:

$$\frac{d\mathbf{y}}{d\mathbf{x}} = \mathbf{J}(\mathbf{x}) + \mathbf{H}(\mathbf{x}) \cdot \boldsymbol{\Delta} \tag{5.3}$$

and setting it to zero and solving gives:

$$\boldsymbol{\Delta} = \begin{bmatrix} \dot{x}_1 - x_1 \\ \dot{x}_2 - x_2 \\ \vdots \\ \dot{x}_n - x_n \end{bmatrix} = -\mathbf{H}(\mathbf{x})^{-1} \cdot \mathbf{J}(\mathbf{x}) \tag{5.4}$$

Thus, if the objective function is strictly quadratic the solution is found in one step. But if it is not then more iterations is required to find the solution. The vector **Δ** points to the direction of the steepest descent in the value of the objective function (the same direction the negative gradient is pointing to). Newton-type methods (as opposed to quasi-Newton methods) calculate **H** directly and proceed in the direction of descent to locate the minimum after a number of iterations. Calculating **H** numerically involves a large amount

of computation. Quasi-Newton methods avoid this by using the observed behaviour of $f(x)$ and the gradient of it to build up curvature information to make an approximation to **H** using an appropriate updating technique. A large number of Hessian updating methods have been developed. However, the formula of Broyden, Fletcher, Goldfarb, and Shanno (BFGS) is thought to be the most effective [115]. The formula given by BFGS is:

$$\mathbf{H}_{k+1} = \mathbf{H}_k + \frac{\mathbf{q}_k \cdot \mathbf{q}_k^{\intercal}}{\mathbf{q}_k^{\intercal} \cdot \mathbf{s}_k} - \frac{\mathbf{H}_k^{\intercal} \cdot \mathbf{s}_k^{\intercal} \cdot \mathbf{s}_k \cdot \mathbf{H}_k}{\mathbf{s}_k^{\intercal} \cdot \mathbf{H}_k \cdot \mathbf{s}_k} \tag{5.5}$$

where,

$$\mathbf{s}_k = \mathbf{x}_{k+1} - \mathbf{x}_k$$

$$\mathbf{q}_k = \mathbf{J}\left(\mathbf{x}_{k+1}\right) - \mathbf{J}\left(\mathbf{x}_k\right)$$

The Hessian, **H**, is always maintained to be positive definite so that the direction of search is always in a descent direction.

The options and settings available in '*fmincon*' nonlinear constrained optimiser are listed in the following table 5.1.

Table 5.1. Options and settings for medium scale optimisation in '*fmincon*' optimiser, MATLAB software.

Option name	Description
DerivativeCheck	Compare user-supplied derivatives (gradients of the objective function and constraints) to finite-differencing derivatives
Diagnostics	Display diagnostic information about the function to be minimized
DiffMaxChange	Maximum change in variables for finite differencing
DiffMinChange	Minimum change in variables for finite differencing
Display	Level of display, e.g. displays output at each iteration
FunValCheck	Check whether objective function values are valid e.g. displays an error when the objective function returns a value that is complex, infinity or not a number.
GradObj	Gradient for the objective function defined by the user (optional)
MaxFunEvals	Maximum number of function evaluations allowed
MaxIter	Maximum number of iterations allowed
OutputFcn	Specify one or more user-defined functions that an optimization function calls at each iteration
PlotFcns	Plots various measures of progress while the algorithm executes, e.g. the current point, the function count, the function value, the

	step size or the first-order of optimality
TolFun	Termination tolerance on the function value
TolCon	Termination tolerance on the constraint violation
TolX	Termination tolerance on x
TypicalX	Typical x values
MaxSQPIter	Maximum number of SQP iterations allowed
RelLineSrchBnd	Relative bound (a real nonnegative scalar value) on the line search step length such that the total displacement in x satisfies. This option provides control over the magnitude of the displacements in x for cases in which the solver takes steps that are considered too large
RelLineSrchBndDuration	Number of iterations for which the bound specified in *RelLineSrchBnd* should be active

Some of these settings such as termination tolerances may have a significant effect on optimisation in terms of accuracy and convergence therefore the choice of the optimal values that depend on the problem is quite important.

5.1.1. Analysis of convergence and optimisation error

As Prahl mentioned in his paper [64], IAD may not always converge to the right solution giving us a large error in the extracted values of *albedo* and *g*. There has been no reasoning given as to why and when this may happen. A rigorous analysis of the convergence and optimisation error would provide us with a better insight into this and may aid in handling the related issues in the future.

Since we have only two unknowns (*albedo* and *g*), in the case when the turbidity τ is measured directly, the objective function as well as the two measurements can be visualised in three dimensions, which can be very useful for understanding of what is happening in nonlinear optimisation. The surfaces of the total transmittance and the total reflectance as functions of *a* and *g* are plotted in figures 5.2 and 5.3. In the illustrated example, the values of T_t and R_t were calculated for the *a*-*g* grid of resolution of 0.01 (i.e. 101×101 points) and the optical depth of $\tau = 5$ using the forward adding-doubling with matched boundaries [65] i.e. it was assumed that the real refractive indices of the sample and the outer medium from which the incident irradiation comes were the same and there was no light reflection at their boundary for simulation purposes. As we can see from the plots, the surfaces of T_t and R_t are distinct hence for every pair of *a* and *g* values there is a distinct pair of T_t and R_t values.

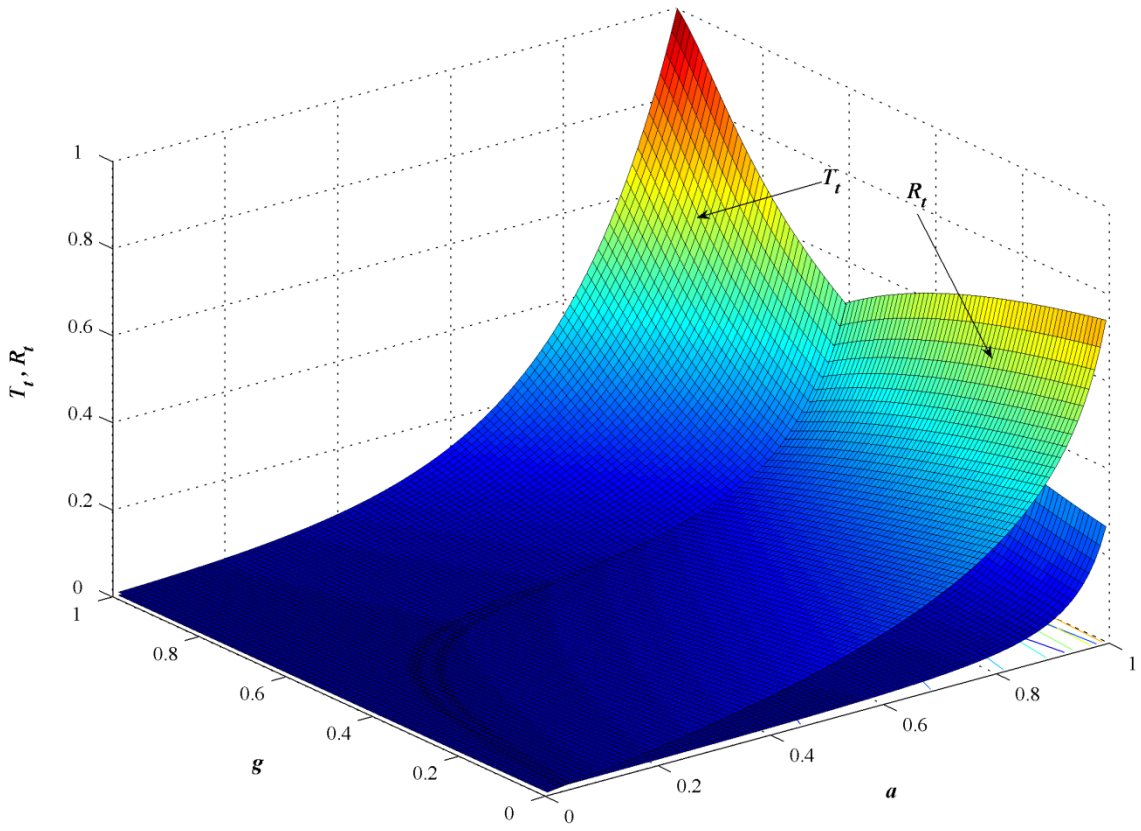

Figure 5.2. T_t and R_t surfaces as functions of a and g, at the optical depth of 5, view 1.

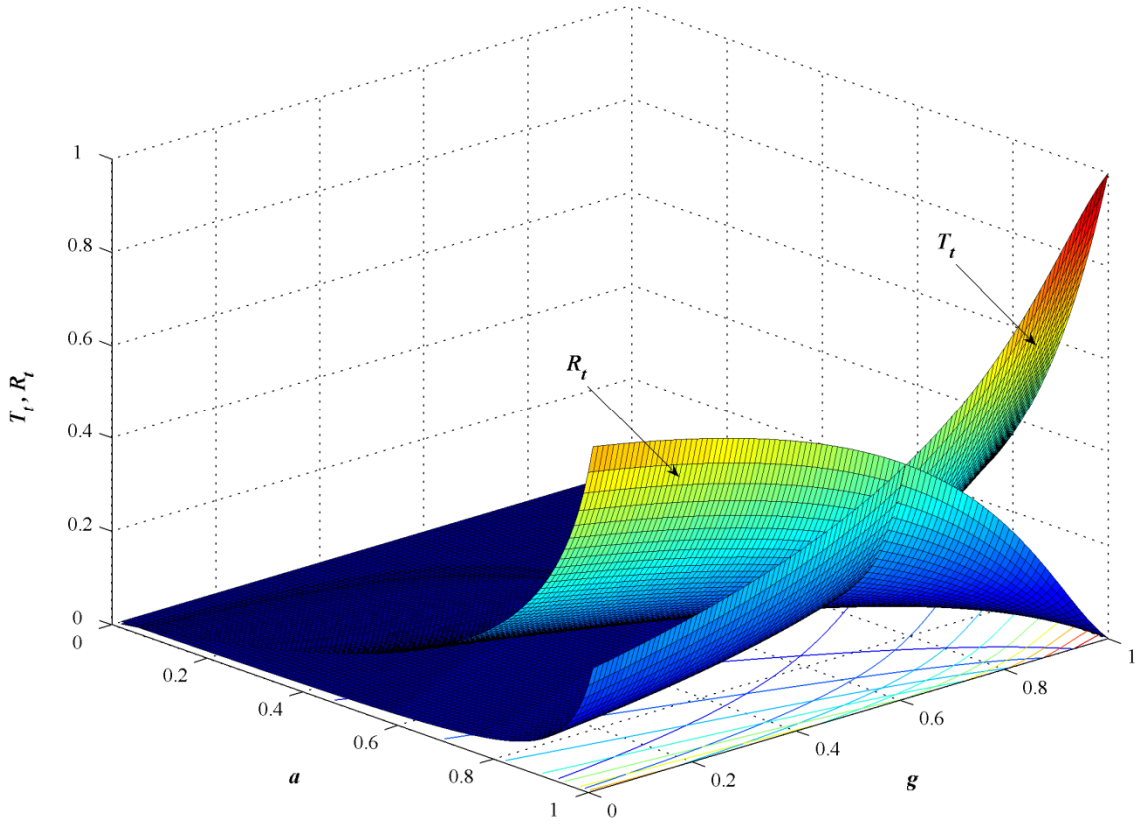

Figure 5.3. T_t and R_t surfaces as functions of a and g, at the optical depth of 5, view 2.

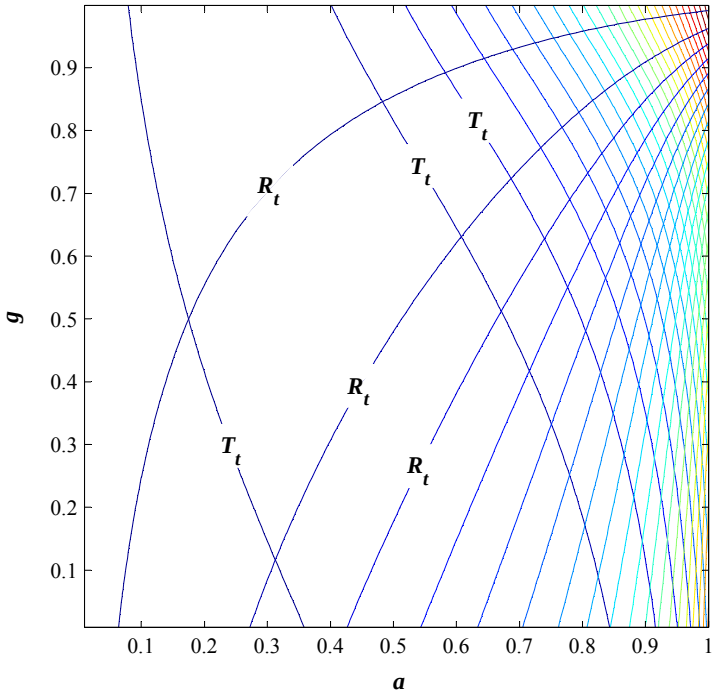

Figure 5.4. The isolines of T_t and R_t surfaces projected on a-g plane, calculated at $\tau = 5$.

That this is the case i.e. that the solution is unique, can be easily verified by looking at the contour lines of these surfaces (also called the isolines i.e. the lines connecting the points of the same value or height) on the a-g plane, fig. 5.3 and 5.4. Since every pair of isolines cross only once the solution is indeed unique. One can also notice in the contour plot that the isolines of T_t and R_t are quite perpendicular, which means that nonlinear optimisation can solve the IAD problem effectively.

It is important to note that de Vries et al. demonstrated that the IAD solution may become not unique as a result of light losses using the double integrating sphere setup [118], the same setup that Prahl used in his experiments [63, 64]. This is especially relevant when the values of g and a are close to one i.e. when the scattering is dominant and very forward directed, then, the loss of light, mainly through the exit port in the transmittance sphere (required for capturing the non-scattered light), is significant. This is one of the advantages of using a single integrating sphere setup and measuring the collimated transmittance separately, because then the exit port of the integrating sphere is closed when taking the total transmittance measurement. Another detailed discussion on light losses in the double integrating sphere setup and the region of the validity of this method is given by Zhu et al. [119].

There are several possible objective functions that we can use for minimisation, e.g.: one can take the sum of the absolute or relative errors in T_t and R_t, the sum of the

squared errors or the root of the sum of the squared errors i.e. the length of the error vector. However, no significant difference has been noticed in optimisation results using different objective functions. In this work, the length of the error vector given by:

$$f = \sqrt{\left(T_t - \hat{T}_t\right)^2 + \left(R_t - \hat{R}_t\right)^2} \tag{5.6}$$

was chosen as the objective function to minimise, where T_t and R_t are the measured values of the total transmittance and reflectance and $\hat{T}_t$ and $\hat{R}_t$ are their estimates respectively. The surface of it (corresponding to T_t and R_t depicted in fig. 5.2-5.4) as a function of *albedo* and g is illustrated from different views in fig. 5.5 and 5.6, the actual solution is at $a = 0.8$ and $g = 0.8$. One can notice that there are no other minima except for the global one in the objective function therefore, given the measurements are accurate and a feasible solution exists, IAD should always converge to it. Also, that the global minimum at such *albedo* and g values and the optical depth of 5 is well expressed i.e. the gradient downwards is sufficiently large at any point in the field except for the global minimum.

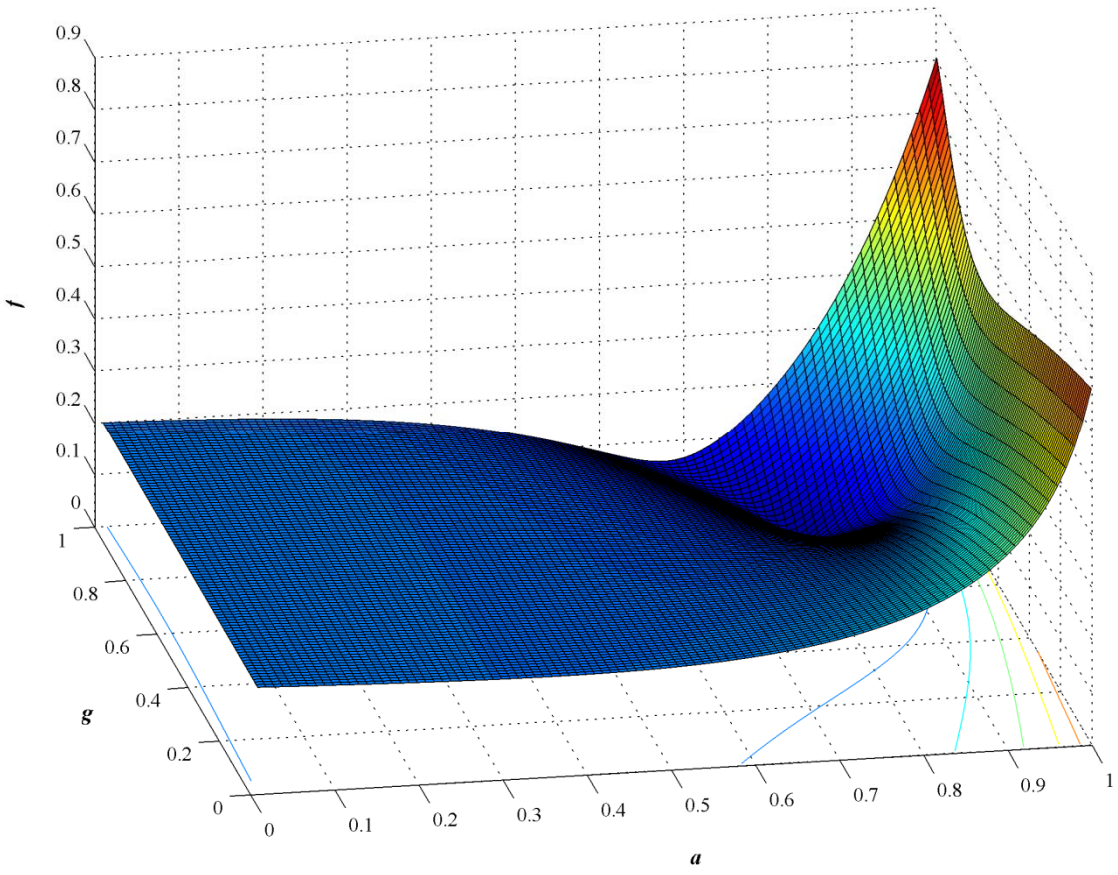

Figure 5.5. The surface of the objective function of IAD calculated at $\tau = 5$, the actual solution is at $a = 0.8$ and $g = 0.8$.

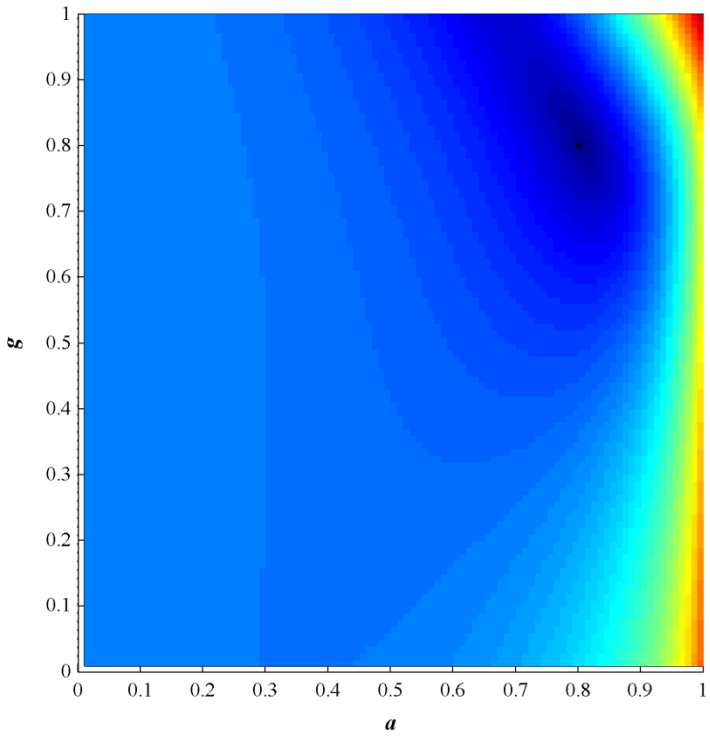

Figure 5.6. The surface of the objective function of IAD calculated at $\tau = 5$, the actual solution is at $a = 0.8$ and $g = 0.8$, view from top.

This leads to a fast and accurate solution. However, the geometry of the surface of the objective function (especially around the global minimum) may change significantly, depending on the values of the optical properties being extracted, and so may the performance of nonlinear optimisation. For example, at high optical depths the transmitted signal may become very low (in most of the *a*-*g* area) resulting in a big flat region (plateau) illustrated in figure 5.7. The value of the objective function along the isolines of R_t will change very little in the flat region of T_t since neither R_t nor basically T_t is changing in this direction. Consequently, for a global minimum anywhere in that area we see a long valley there in the objective function, fig. 5.8, which stretches along the isoline of the actual R_t, instead of a well defined global minimum considered previously in fig. 5.5. The global minimum in the example illustrated in fig. 5.8 and 5.9 is at $a = 0.5$ and $g = 0.5$, that is where the white ball is placed. The value of f at the bottom of the whole valley can be very close to zero in such cases. And so the change in f along the bottom of the valley can be extremely small too. Optimisation terminates when the change in the value of the objective function in the direction of the steepest descent i.e. its directional derivative, or the magnitude of the gradient is smaller than a predefined tolerance (determined by *TolFun* in '*fmincon*').

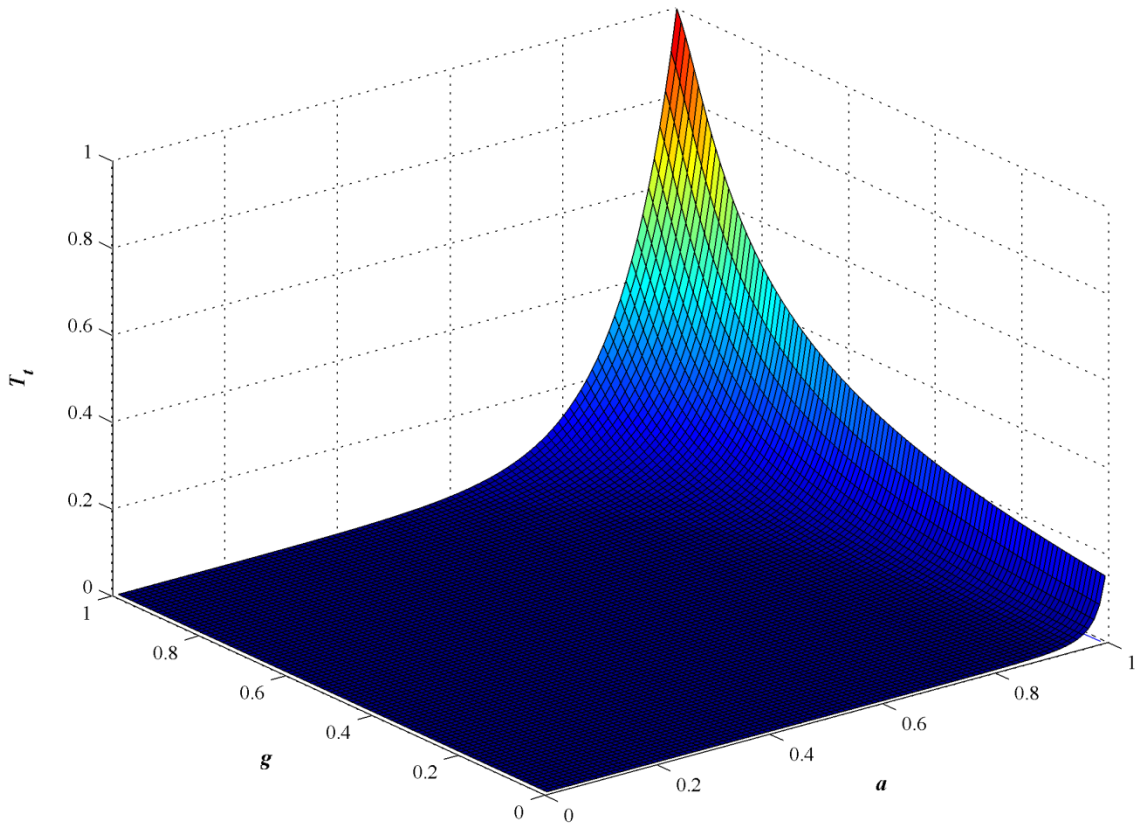

Figure 5.7. T_t surface as a function of a and g calculated at $\tau = 10$.

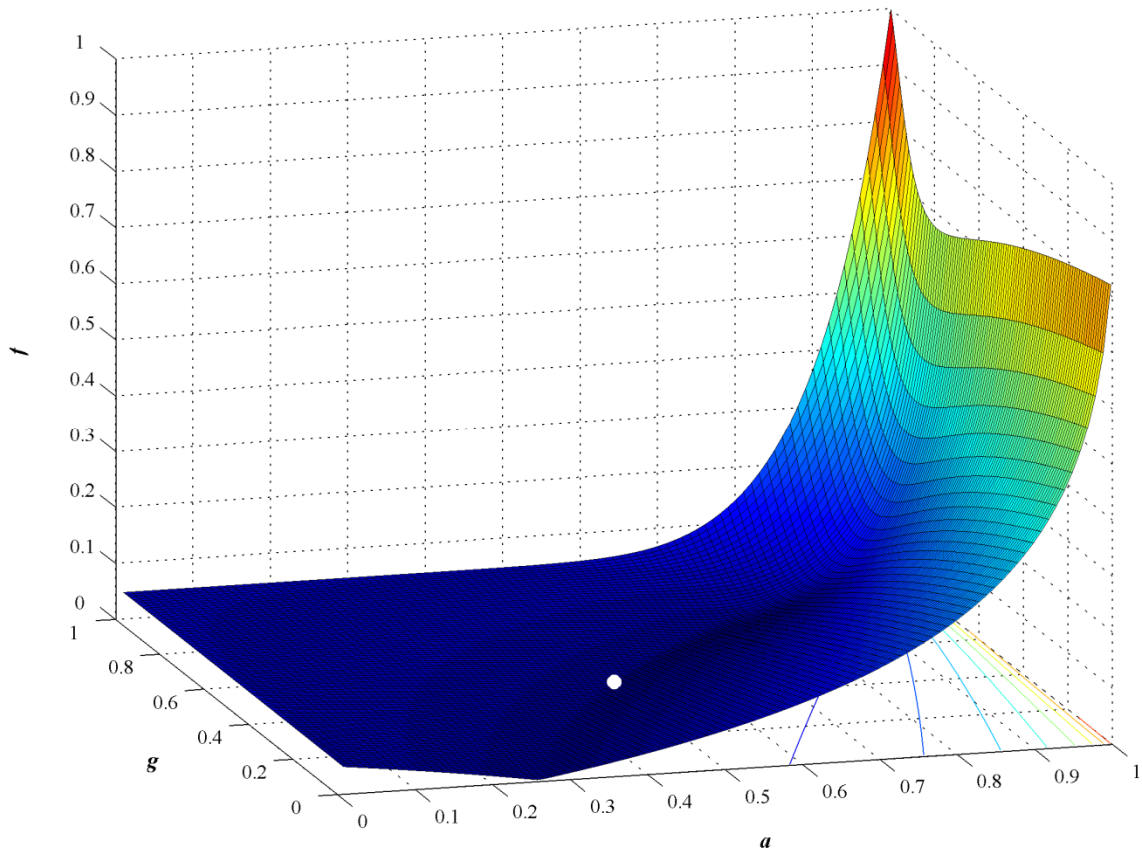

Figure 5.8. The surface of the objective function of IAD calculated at $\tau = 10$.

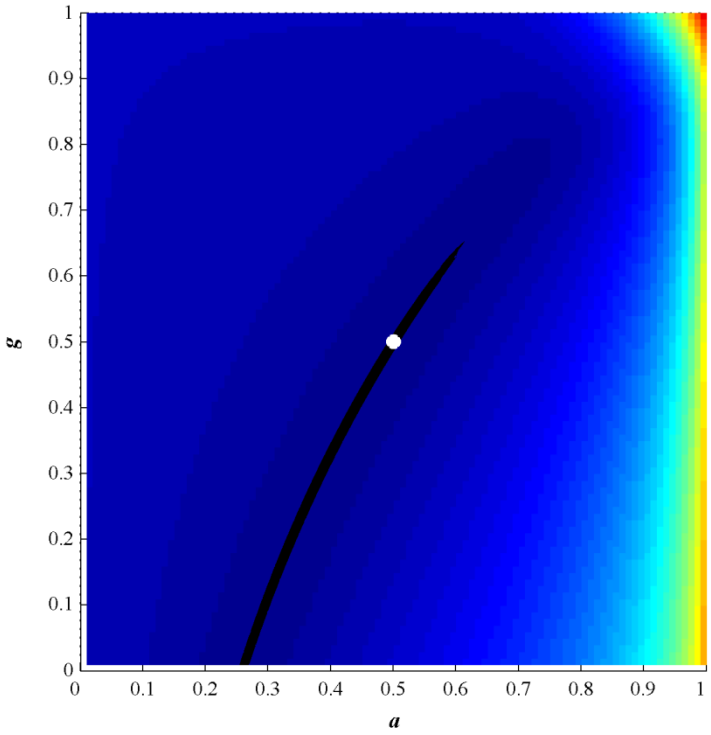

Figure 5.9. The surface of the objective function of IAD calculated at $\tau = 10$, the actual solution is at $a = 0.5$ and $g = 0.5$, view from top.

Therefore, in such cases, very low termination tolerances (as low as $1 \cdot 10^{-12}$) may be required in order to force optimisation to move along the shallow valley, that is to continue the search, otherwise it may terminate somewhere in the valley far from the solution giving us a large error. In general case, the error of optimisation depends on how far the zone with the gradient values smaller than the predefined termination tolerance stretches from the actual minimum, since optimisation can terminate anywhere in that zone i.e. any point in that zone is basically a minimum at the given tolerance. The further it stretches the further away from the actual minimum optimisation may terminate and the larger the optimisation error may accordingly be. In figures 5.6 and 5.9 the black areas around the global minima mark the zones where the gradient values are smaller than $1 \cdot 10^{-7}$. As one can notice, this area is much larger and it stretches much further away from the actual minimum in the second case (fig. 5.9) than in the first case where it is just a small spot. As a result, the accuracy in the estimated values of the optical properties at the given tolerance will be high in the first case and may be significantly lower in the second case e.g. if optimisation terminates at the far end of the black zone. Hence, termination tolerances that might be sufficient for the first case in terms of the accuracy of the solution may be insufficient for the second case. In conclusion, the error of optimisation varies with the values of a, τ and g

(especially with the first two), therefore it may be needed to adjust the termination tolerances accordingly in order to keep the optimisation error at the same level. It is important to note that in the second case the error also depends on where in the valley the optimisation lands, which mainly depends on the initial guessing values of a and g i.e. the departure point (as will be later illustrated in fig. 5.12).

Prahl showed how the accuracy of the optical properties extracted using IAD depends on their values and also the values of the total transmittance and the total reflectance and deduced that this variation in the accuracy is due to different accuracy in numerical integration of the phase function [64]. However, some error is introduced by nonlinear optimisation, not just the adding-doubling. And this error also depends on the values of a, τ and g as it has been shown. Furthermore, the optimisation error increases with increasing turbidity as does the error of the adding-doubling.

Another zone which may cause convergence problems is located at $a = 0$ limit. The directional derivative of the objective function is extremely low there for any τ. The plots in fig. 5.10 and 5.11 show how the magnitude of the gradient of the objective function (calculated using eq. (5.6) with estimates of T_t and R_t set to zero) varies with all three optical properties i.e. how the scalar field of the gradient looks like.

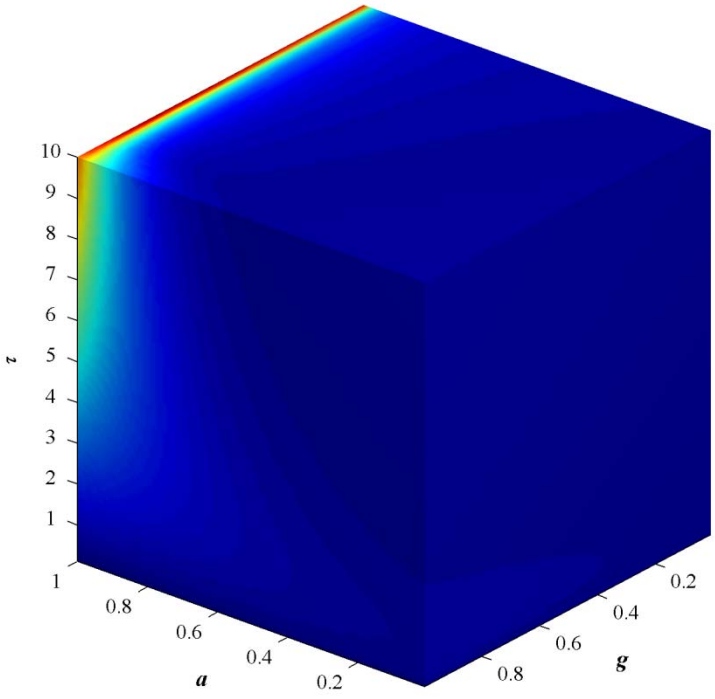

Figure 5.10. Values of the gradient of the objective function of IAD in a, τ and g space given in a colour scale, the red end of the colour scale indicating a high gradient and the blue end on the contrary, view 1.

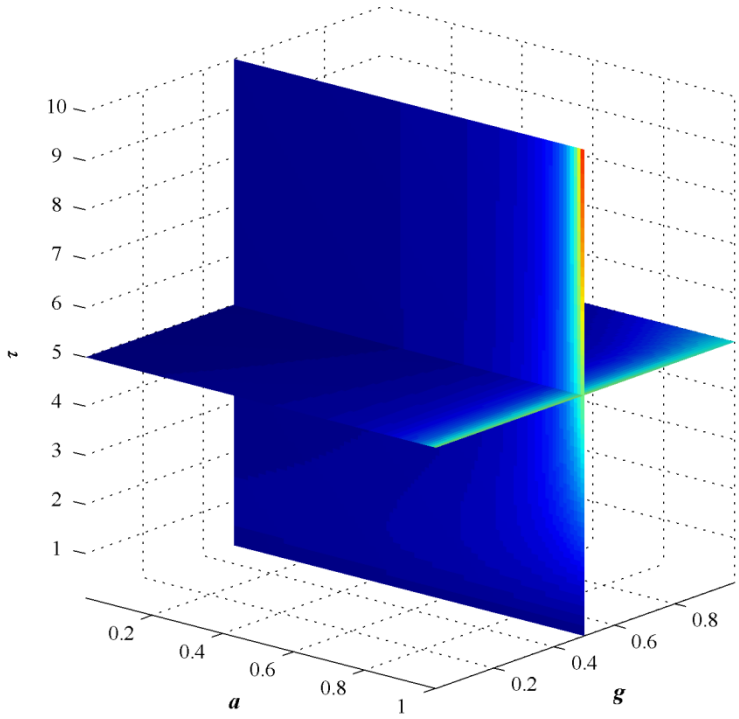

Figure 5.11. Values of the gradient of the objective function of IAD in a, τ and g space expressed in a colour scale, the red end of the colour scale indicating a high gradient and the blue end on the contrary, view 2.

The red end of the colour scale is indicating a high magnitude of the gradient i.e. a steep change in the objective function in the a, τ, g space, and the dark blue colour is indicating a low magnitude of the gradient accordingly.

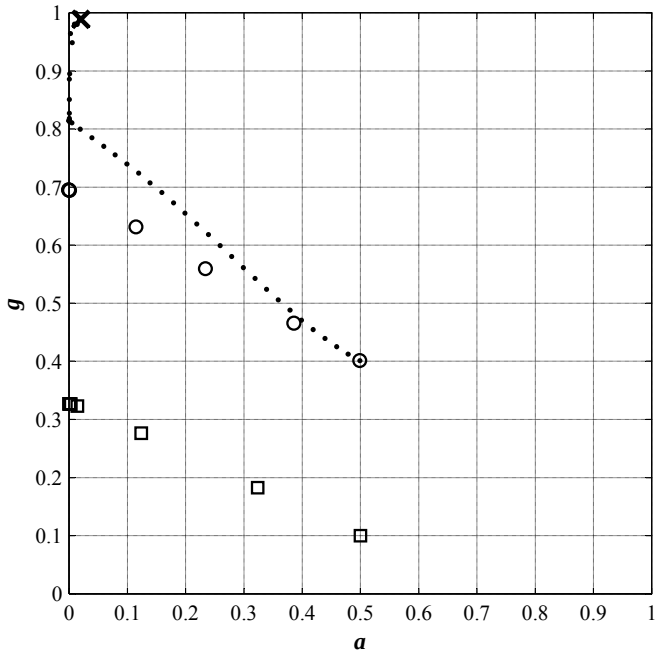

Figure 5.12. Optimisation steps at each iteration (the cross marks the global minimum).

One can notice that the magnitude of the gradient is generally (i.e. at any level of τ) getting smaller with *albedo* decreasing, reaching the smallest value in the limit $a = 0$. If the search step gets there optimisation usually terminates. 'The ball does not roll if placed on a flat surface' since there is no gradient downwards. An example is given in figure 5.12. It shows three runs. The actual solution was at $a = 0.02$, $\tau = 10$ and $g = 0.989$, marked with the cross. The first and the second run differ only in the starting guess, the rest of the optimisation parameters were the same, namely, the algorithm (SQP) and the termination tolerances ($TolFun = 1 \cdot 10^{-12}$, $TolX = 1 \cdot 10^{-12}$, $TolCon = 1 \cdot 10^{-12}$). In both cases, optimisation terminated prematurely, because it got into that zone where the directional derivative was smaller than the predefined tolerance *TolFun*. The output from each iteration of the first run is given in table 5.2. We can see that the value of the directional derivative at the termination point was extremely small of the order of $1 \cdot 10^{-15}$ easily satisfying the termination tolerances.

Table 5.2. The output from each iteration of the first IAD run.

Iter	F-count	f(x)	max constraint	Line search steplength	Directional derivative	First-order optimality	Procedure
0	4	0.04886	0				
1	8	0.0206995	0	1	-0.0202	0.0937	
2	12	0.00480048	0	1	-0.0102	0.0453	
3	16	9.11451e-006	1.102e-017	1	0.000771	0.0195	
4	20	0.000412671	0	1	0.000427	0.0302	
5	24	6.74021e-005	0	1	-0.000334	0.0287	Hessian modified
6	28	9.11498e-006	1.762e-019	1	1.48e-005	0.0347	Hessian modified
7	32	1.35511e-005	0	1	9.21e-006	0.0217	Hessian modified
8	36	8.92887e-006	0	1	-7.87e-007	0.00239	Hessian modified
9	40	8.90834e-006	0	1	5.65e-008	0.00139	Hessian modified
10	44	8.89798e-006	0	1	2.74e-011	1.82e-006	Hessian modified
11	48	8.89798e-006	0	1	-5.32e-015	7.12e-008	Hessian modified

```
Optimization terminated: magnitude of directional derivative in search
 direction less than 2*options.TolFun and maximum constraint violation
  is less than options.TolCon.
Active inequalities (to within options.TolCon = 1e-012):
  lower      upper     ineqlin   ineqnonlin
    2          2


x| =

    0.0002   10.0000    0.3272
```

To get out of this region one has to lower the termination tolerances. But, how low one can go depends on the numerical accuracy/precision of the adding-doubling method and the way the directional derivative is calculated with finite differences in optimisation. For instance, if we make a differential change in g equal to $1 \cdot 10^{-12}$ (at $a = 0.0001$, $\tau = 1$, $g = 0.001$) the calculated differential change in T_t using our adding-doubling code (with 64 quadrature points) will be equal to zero, i.e. $\partial T / \partial g = 0$ although theoretically it is not zero. This means that if MATLAB optimiser '*fmincon*' makes a differential change $dg \le 1 \cdot 10^{-12}$ at that point, when using finite differencing to find the derivative of f in the direction of the negative gradient, the directional derivative ∂f will be equal to zero at the given precision

and the optimisation will terminate. It is worth noting that using 64 quadrature points for integration the calculated values of the total transmittance and reflectance are of high precision. The less quadrature points we use the more insensitive to small changes (perturbations) in *albedo* and *g* the calculated T_t and R_t are. Using 4 or 8 quadrature points is a common practice because fast computation is usually required. The third run in the figure 5.12 demonstrates that limiting the maximum step size (option *RelLineSrchBnd* in table 5.1) may sometimes aid '*fmincon*' in finding the global minimum.

It is important to emphasis however that the computational error of the IAD, which consists of the adding-doubling error and the optimisation error, at the current level of errors in T_t and R_t measurements (obtained with currently available instrumentation), is insignificant (e.g. Prahl demonstrated that the latter is approximately an order of magnitude larger than the former [64]). The sensitivity of the extracted values of *albedo* and *g* to the error in the measured total transmittance and total reflectance is different for different values of a, τ and g. The high sensitivity is where a small change in T_t or R_t brings a significant change in a and g. This corresponds to the points of the low gradient in the objective function. Therefore, the spatial distribution of the gradient values in a,g,τ coordinates presented in figures 5.10 and 5.11 also tells us a lot about the distribution of the sensitivity of the optical properties to the error in the measurements.

Conclusions:

- There is always a unique global minimum in the objective function of the IAD. But, at high turbidity and low *albedo* we have a long valley with a very low gradient going through the actual minimum in the objective function. Thus, if the termination tolerances are not sufficiently low optimisation can terminate somewhere in the valley far from the actual solution giving us a large error.
- Nonlinear optimisation may also have convergence issues, when searching for inverse adding-doubling solution using T_t, R_t and τ as inputs, if it hits $a = 0$ limit where the gradient of the objective function is also extremely small. Lowering termination tolerances can help to get rid of this problem, but this will not have an effect if termination tolerances get lower than the numerical accuracy/precision of the adding-doubling. Also, lower tolerances mean longer search time. Thus, in practical situations, one has to look for the optimum.
- The error of optimisation varies with the values of a, τ and g, especially with the first two. The error becomes larger as the turbidity increases and *albedo* decreases.

Therefore, it may be needed to adjust the termination tolerances accordingly in order to keep the optimisation error at the same level.

The first and the second conclusions explain why in Prahl's reported work IAD sometimes did not converge to the accurate solution and it had to be repeated with different guessing values until a good solution was reached.

Hints for improving optimisation performance:

To avoid the problem of '*fmincon*' ending up somewhere in the shallow valley or at the limit of $a = 0$, we have to make sure that optimisation does not get to the proximity of that limit or far from the actual solution. This can be done by:

- Choosing the right strategy for guessing the initial values. Two possible solutions:
  1. Choose the current solution as the next guessing point (i.e. for the next wavelength). Because the optical properties are functions of wavelength, their values at neighbouring wavelengths are close, therefore the location of the next minimum is close to the current minimum. This may not work if we have sharp changes in absorption spectrum or measurements are far from each other in terms of wavelengths.
  2. Form the look up table for a and g values that correspond to the respective T_t and R_t values. The starting guess values for a and g that have T_t and R_t values closest to the actual measurements are then chosen from the look up table at each iteration.
- Constraining the step size in search direction.
- Raising the lower bound for *albedo*.

The strategy of the guessing values also directly influences the speed of the IAD.

5.1.2. Sensitivity of extracted optical properties to the error in scattering anisotropy

Measuring the true collimated transmittance i.e. the intensity of light that went through the sample unscattered, at higher turbidity is not trivial because the contribution of diffuse light i.e. light that has undergone scattering, to the T_c measurement becomes significant thus making its value erroneous. Therefore an attractive alternative would be to take g value as constant then the third measurement i.e. collimated transmittance, would not be needed. Hence how the error in g influences the value of the absorption coefficient μ_a is of interest. For this purpose we can plot and examine the values of μ_a in R_t, T_t, g

coordinates (see figure 5.13).

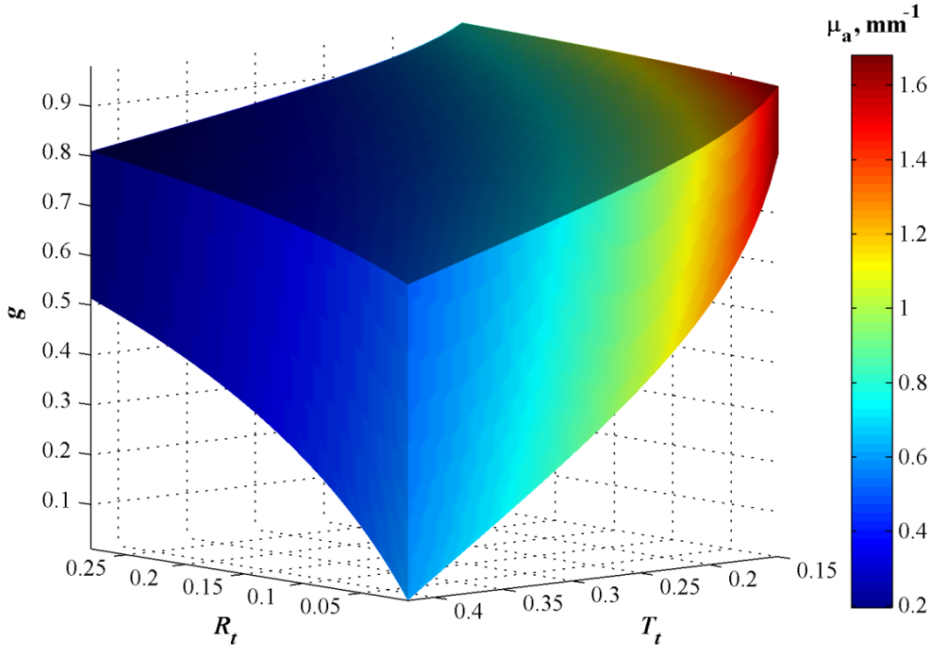

Figure 5.13. Shows how μ_a changes along the g axis for any value of T_t and R_t.

As one can notice, values of μ_a along the g axis change little. However they do change as shown in figure 5.14 where values of μ_a are plotted against g at fixed values of $T_t = 0.35$ and $R_t = 0.05$. This suggests that it may be possible to use constant g without introducing much error in μ_a if variation in g is small. Errors in g mainly go into μ_s since these two optical properties are highly correlated as can be seen in fig. 5.15. Consequently, if a fixed value of g is used μ_s information cannot be utilised for the full correction of scattering effects described in chapter 4.1.2.

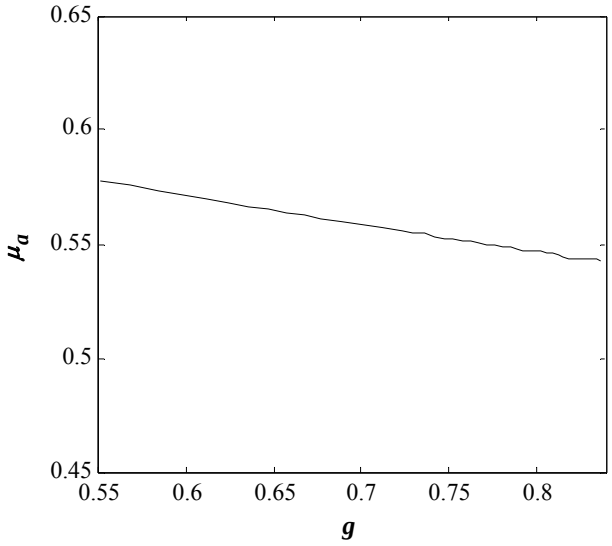

Figure 5.14. Change in μ_a with g at fixed values of $T_t = 0.35$ and $R_t = 0.05$.

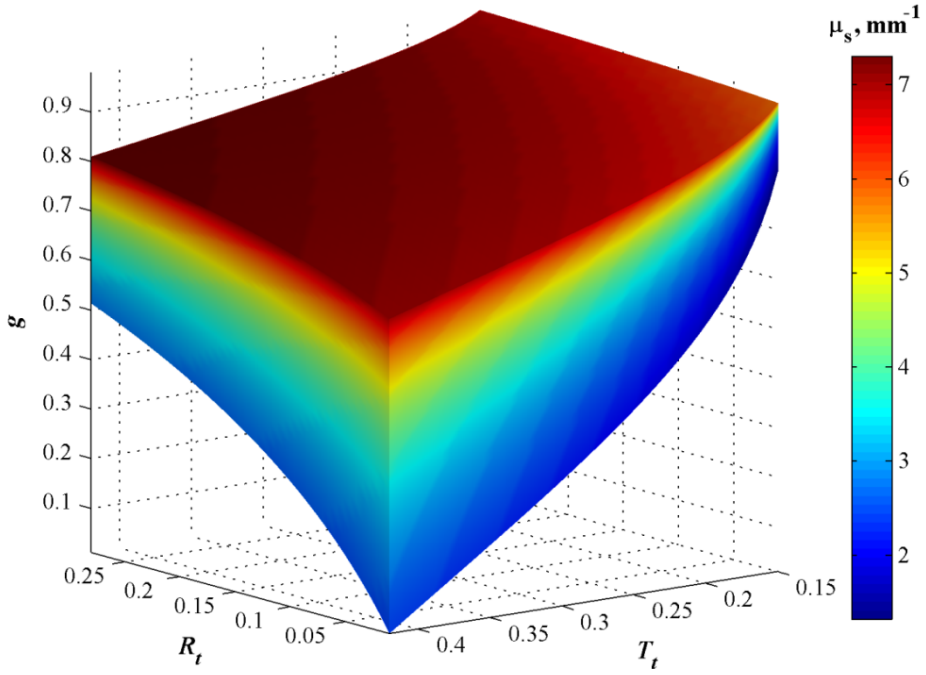

Figure 5.15. Shows how μ_s changes along the g axis for any value of T_t and R_t.

CHAPTER VI

APPLICATION OF PARTIAL CORRECTION METHOD

6.1. SIMULATION

The proposed approach of partial correction of multiple scattering effects was applied to a simulated dataset of spectra of turbid samples (considered previously by Thennadil and Martin [33]) to test the extent of improvement in model performance that can be theoretically obtained compared to the performance that would be obtained using empirical scatter-correction approaches.

6.1.1. Design of experiment

In their work, Thennadil and Martin modelled the turbid system as a four component system comprising one scattering component (i.e. polystyrene particles) and three non-scattering components which were simulated using the optical properties of toluene (species 2), deuterated water (species 3) and water (species 4). The volume fraction of particles varied between 0.01 and 0.1 and the radius of particles spanned the range 100 nm to 500 nm. The volume fraction of species 2 and 3 spanned the ranges 0-0.0115 and 0.2-0.4 respectively. The spectra of the total transmittance and the total reflectance were simulated using the radiative transfer equation. Noise was then added to the spectra to resemble the real measurements. Thennadil and Martin used the dataset so created to study the effectiveness of various pre-processing techniques on calibration models built for predicting the concentration of a non-scattering component. In the current study this dataset consisting of 50 calibration samples and 391 test set samples was used to compare the proposed approach of using the extracted bulk absorption spectra for building calibration models with those obtained using the traditional approach of using total reflectance or transmittance measurements with empirical pre-processing to remove scattering effects. Their performances were compared in prediction of both the scattering component (polystyrene) and the non-scattering component (toluene).

6.1.2. Results and discussion

The simulated spectra of the total transmittance and the total reflectance and the corresponding bulk absorption coefficient for the turbid system toluene-polystyrene-water-heavy water are shown in figure 6.1. All graphs are provided in the same scale so that the

magnitudes of variation in different measurements in each case can be visually compared.

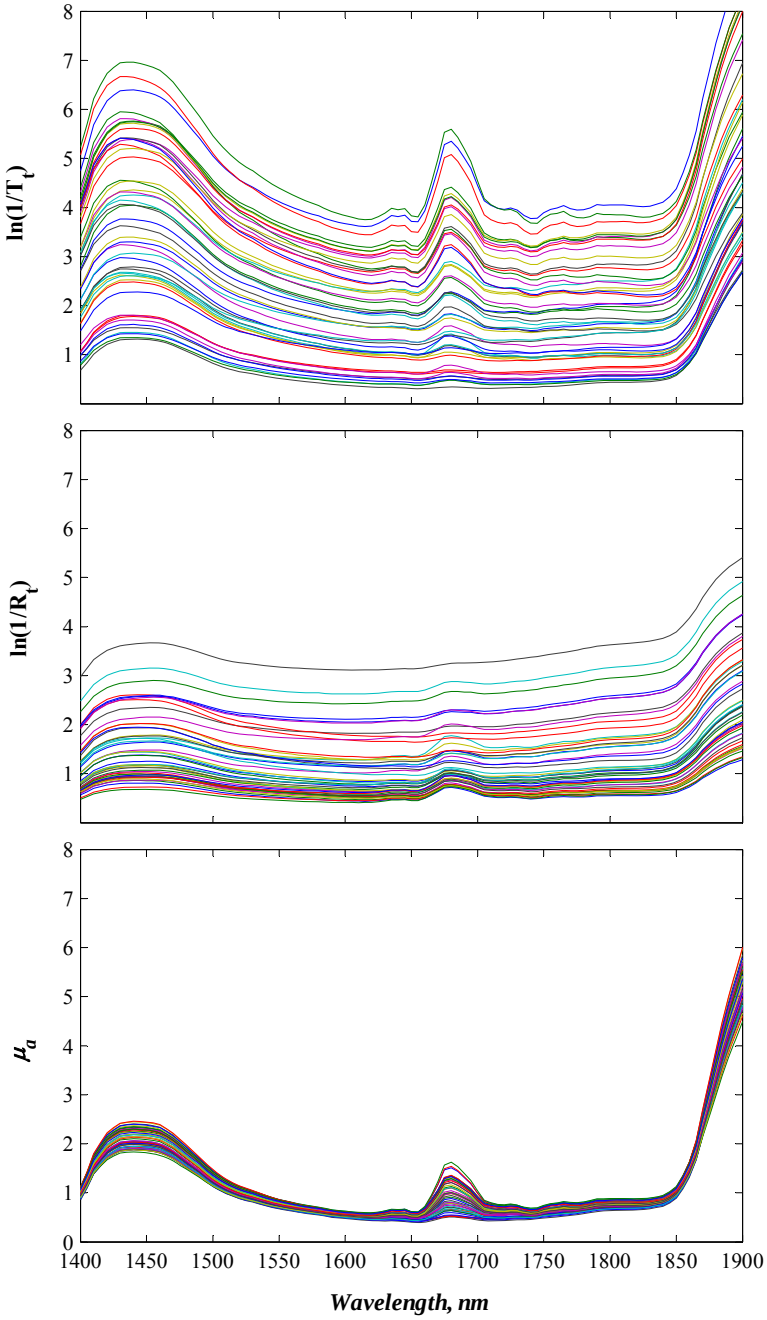

Figure 6.1. Total transmittance, total reflectance and bulk absorption coefficient μ_a, calibration data set (simulations).

It can be seen that (baseline) variation in μ_a is much smaller than in the two direct measurements: approximately five times smaller than in total transmittance and four times smaller than in total reflectance. Variation in T_t and R_t measurements is due to changes in both chemical and physical properties of the sample, whereas variation in μ_a is predominantly due to changes in chemical information (i.e. concentrations). It is apparent

from this comparison that the variation in the path length travelled by photons, which is subject to number, size and shape of particles is the main contributor to the variation in spectroscopic measurements of a turbid sample in this case. Not only is the magnitude of variation due to changes in physical properties much larger than due to changes in concentrations, but it is also nonlinear, which makes it a serious problem for the bilinear multivariate calibration models such as PLS.

Table 6.1 summarizes the results of the performances of PLS calibration models built on the total reflectance and the total transmittance data and the results obtained when the spectra of the bulk absorption coefficient μ_a were used to predict the concentration of the scattering-absorbing species (i.e. polystyrene) in the simulated four component system. For the case where spectra of the total reflectance were used for building calibrations, it was found that pre-processing by any of the techniques considered in [33] did not improve the performance of PLS calibration models in terms of the accuracy. The EMSCL (Extended Multiplicative Scatter Correction with wavelength dependent logarithmic term) method, which was found in [33] to be the best performing scatter correction technique for predicting the concentrations of non-scattering species, in the present case, needed fewer number of latent variables (LVs) and therefore was used for the benchmarking representing the best results that can be achieved with empirically pre-processed R_t. When total transmission measurements were used pre-processing with EMSCL provided a slight improvement and was again marginally better than the other pre-processing methods thus it was also used for the benchmarking representing the best results that can be achieved with empirically pre-processed T_t.

Table 6.1. Performance of calibration models for estimating concentration of scattering-absorbing component (polystyrene) in the simulated data-set of a four-component system.

Dataset which PLS was built on	Pre-processing	LVs	Calibration	Test
			RMSECV (g/l)	RMSEP (g/l)
Calibration models built on total reflectance	none	12	3.26	3.3
	EMSCL	12	2.17	2.5
Calibration models built on total transmittance	none	8	5.35	4.48
	EMSCL	8	4.04	3.14
Calibration model built on μ_a	None	6	1.38	1.42

From the table 6.1, it is seen that PLS model built on μ_a for estimation of the concentration of the scattering component yielded much better prediction results than those built on the empirically pre-processed total reflectance or total transmittance spectra, the latter exhibiting the worst performance. The RMSEP value obtained by using μ_a was more than 1.7 times lower than that obtained using the total reflectance and was achieved with half the number of latent variables.

There are two points to be noted in the table 6.1. Firstly, even for the theoretical situation, the prediction error in particle concentration when using μ_a, while better than using reflectance spectra coupled with pre-processing, is appreciable. Secondly, since there are only 4 components in the system, taking closure condition into consideration, if scattering effects were completely eliminated, we would have needed only 3 latent variables in the model. Instead the best model needs 6 LVs. Figure 6.2 shows a plot of actual vs. predicted concentration of polystyrene using the model based on μ_a. One can notice that the accuracy of predictions drops with the increasing concentration of particles.

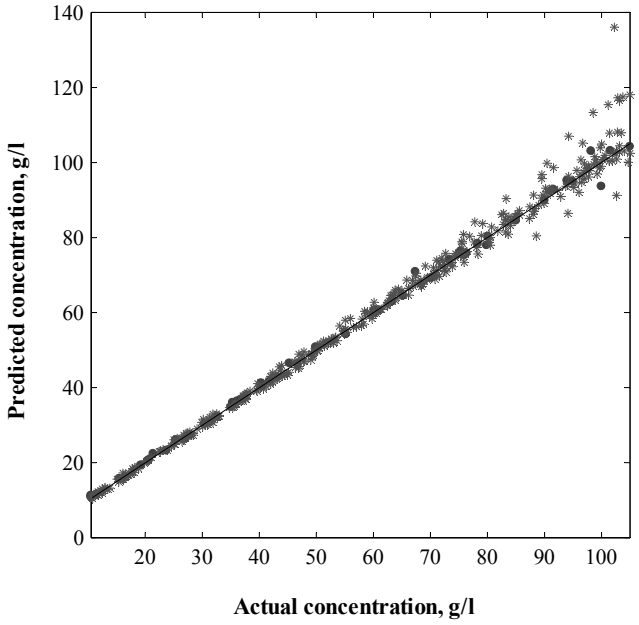

Figure 6.2. Predicted vs. actual values of concentration of scattering-absorbing component (polystyrene) for training (●) and validation (*) data sets (simulations).

These observations could be explained by the insight provided by taking a closer look at the bulk absorption coefficient given by eq. (3.53). Although μ_a is free from nonlinear photon path length variations, it still has some intrinsic variation not related to the chemical information. The information about the concentration of the scattering

component is contained in the term $\mu_{ap} = \sigma_{ap}c_p$ in eq. (3.53). It is the only problematic term in μ_a from the point of view of multivariate calibration, because it varies not only with volumetric concentration of particles but also with their morphology (i.e. size and shape). To examine this term further, for spherical particles it can be rewritten as:

$$\mu_{ap} = \sigma_{ap} \cdot N_p = \frac{\sigma_{ap}}{V_p} \cdot c_p = \frac{3 \cdot \sigma_{ap}}{4 \cdot \pi \cdot R^3} \cdot c_p = K \cdot c_p \tag{6.1}$$

V_p is the volume of a single particle (m^3), N_p is the concentration of particles expressed as number density (m^{-3}), c_p is the volumetric concentration of particles (m^3/m^3) and R is the particle radius (m). The term separated from c_p is denoted as K. The parameter K is a function of particle radius both explicitly as well as implicitly due to σ_{ap} also being a function of particle radius [76]. While it does not explicitly contain concentration information, due to its dependence on particle size, it will be correlated to the concentration of particles. This is because particle concentration can be changed in 3 different ways: by keeping the number density of the particles the same and changing their size (radius), keeping the particle size the same and changing the number density or by a combination of both. From eq. (6.1), looking at the first right-hand-side relation, it can be seen that the effect due to particle number density is a baseline offset of the absorption cross-section of the particle, whereas the effect due to particle size is manifested by a wavelength dependent change in the particle absorption cross-section. When both vary simultaneously, the fact that the number density is implicitly related to the particle size and thus indirectly to the absorption cross-section and the multiplicative (confounding) effect on one another means that only a portion of the concentration information can be extracted from the combined effect. Thus variations arising from this term can have an adverse affect on calibration model performance when the models are built for predicting the concentration of a particulate species (i.e. species that both absorbs and scatters light). The fact that we need three extra latent variables to predict the particle concentration may be due to requiring extra LVs to describe the effects described above.

Further, the accuracy of multivariate calibration models in predicting the concentration of the scattering-absorbing component will depend on the magnitude of variation in K. Since for the same particle concentration, K can take on different values due to changes in particle size, it introduces an error due to the confounding effect arising from the multiplicative nature of this parameter with respect to the particle concentration. The higher the concentration of particles, the larger will be the effect on μ_{ap} due to variations in

K. Since variations in *K* degrade the performance of a calibration model due to the confounding effect it induces, this translates into higher levels of uncertainty in the concentration estimates with increasing concentrations. This would explain the larger spread in the data in fig. 6.2 at higher concentrations.

Table 6.2. Performance of calibration models for estimating concentration of purely absorbing component (toluene) in the simulated data-set of a four-component system.

Dataset which PLS was built on	Pre-processing	LVs	Calibration	Test
			RMSECV (g/l)	RMSEP (g/l)
Calibration models built on total reflectance	none	10	1.13	0.88
	EMSCL+1st der.	9	0.33	0.33
Calibration models built on total transmittance	none	10	1.78	1.33
	EMSCL+1st der.	7	0.50	0.53
Calibration model built on μ_a	none	6	0.11	0.12

Performance of PLS calibration models built on the empirically pre-processed measurements and the bulk absorption coefficient in estimation of the concentration of the purely absorbing component (i.e. toluene) is summarised in table 6.2. Where, results obtained applying the methodology of partial correction of multiple scattering effects are benchmarked against the best results from the empirical pre-processing of T_t and R_t taken from [33]. According to [33], the best calibration results with the total reflectance as well as the total transmittance were achieved using EMSCL followed by the first derivative for pre-processing, therefore, the respective RMSECV and RMSEP values were taken from there for benchmarking. For a full list of results of performance of different empirical pre-processing techniques the reader is referred to the original work [33].

As in the case of estimating the scattering-absorbing component, PLS model built on μ_a for estimation of the concentration of the purely absorbing component yielded considerably better prediction results than those built on the empirically pre-processed total reflectance or total transmittance spectra. Calibration model built on empirically pre-processed T_t again exhibited the worst performance. In this case, the RMSEP value obtained by using μ_a was nearly three times lower than the best result from the empirical pre-processing, which belongs to the total reflectance pre-processed with EMSCL followed by the first derivative, and was achieved with three latent variables less. Figure 6.3 shows a

plot of the actual concentration of toluene versus the concentration of toluene predicted using the model based on μ_a. Notice, that in this case, the error is independent from the concentration i.e. it has approximately constant variance throughout the concentration range, because it is not affected by the confounding effect between the concentration and the particle size discussed previously, which affects the prediction of the scattering component.

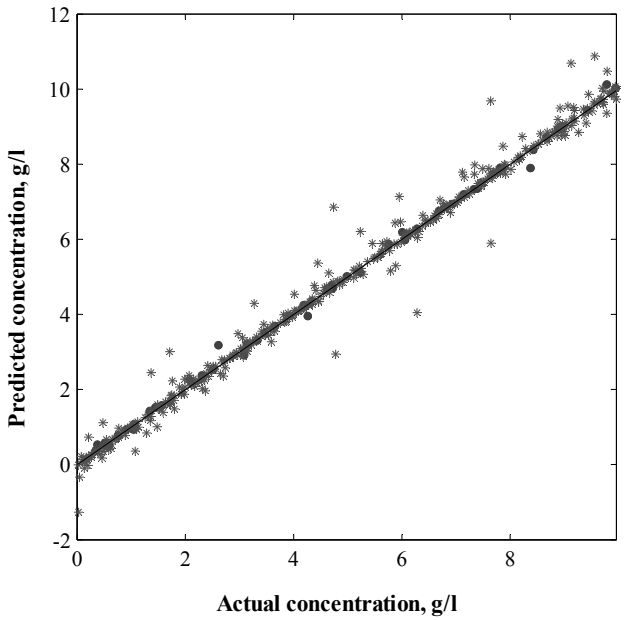

Figure 6.3. Predicted vs. actual values of concentration of purely absorbing component (toluene) for training (●) and validation (*) data sets (simulations).

Simulation results indicate that applying the proposed methodology of partial correction of multiple scattering effects an appreciable improvement in the prediction performance can be obtained compared to applying empirical scatter correction techniques to single measurements. It should be emphasised however that the estimation of the concentration of scattering-absorbing species and the estimation of the concentration of absorbing only species are two distinct cases (problems) in the spectroscopic quantitative analysis of turbid samples. Therefore, in the following chapters these two types of species will be treated separately.

6.2. EXPERIMENTS

6.2.1. Two component model system

The methodology of partial correction of multiple scattering effects was first tested on the experimental (spectral) data of a simple two component turbid system, namely, polystyrene particles suspended in deionised water. The concentration of the scattering-absorbing component i.e. polystyrene particles was the target in this case. The objectives of this initial experiment were: to analyse the feasibility of this methodology under given experimental conditions, to find out in what range of the optical properties of a sample it succeeds (i.e. the errors in the measurements are acceptable) under given experimental conditions, to identify the issues that might preclude its successful implementation and to aid in designing further more complex experiments.

6.2.1.1. Design of experiment

The samples were prepared according to the following experimental design – five particle sizes i.e. diameters: Ø 100 nm, 200 nm, 300 nm, 430 nm and 500 nm, seven concentrations (in wt. %) for each particle size: 0.1 %, 0.5 %, 0.9 %, 1.23 %, 1.6 %, 1.95 and 2.3 %, giving a total of 35 samples.

It should be noted that there are two major differences between the system studied using simulations and the two component model system used to generate the experimental dataset. The first is the number of components, in the simulation a 4 component system was considered whereas the experimental model system has only 2 components. Secondly, the simulation dataset spans a much larger range of concentrations of the scattering component (1-10 %). Thus the highest particle concentration in the simulated dataset is almost 5 times larger than that used in the two component experimental system. The implication of the latter point is that multiple scattering effects are much more dominant in the simulated system. Since the maximum particle concentration in the experimental system is only 2.3 %, the multiple scattering effects will be comparatively small. As a result, in this regime (two component samples with low multiple scattering) we would expect calibration models based on single measurements (total reflectance or transmittance) with empirical scatter correction approaches to work reasonably well. Such a relatively simple system was chosen since it would allow us to examine the accuracy of the complex inversion steps and the instrumentation setup involved in the extraction of the bulk optical properties. If the bulk absorption coefficient is extracted with sufficient

accuracy, then the calibration model built using the proposed approach should perform as well as or better than the single measurement approaches. This would validate the given concept of the partial correction of multiple scattering effects in terms of the accuracy as well as highlight any problems in the inversion methodology that need to be addressed for the successful implementation of this method for more complex systems.

6.2.1.2. Experimental set-up

Three spectroscopic measurements T_c, T_t and R_t were taken for each sample at multiple wavelengths using a scanning spectrophotometer (CARY 5000, Varian Inc.) with a diffuse reflectance accessory shown in fig. 6.4.

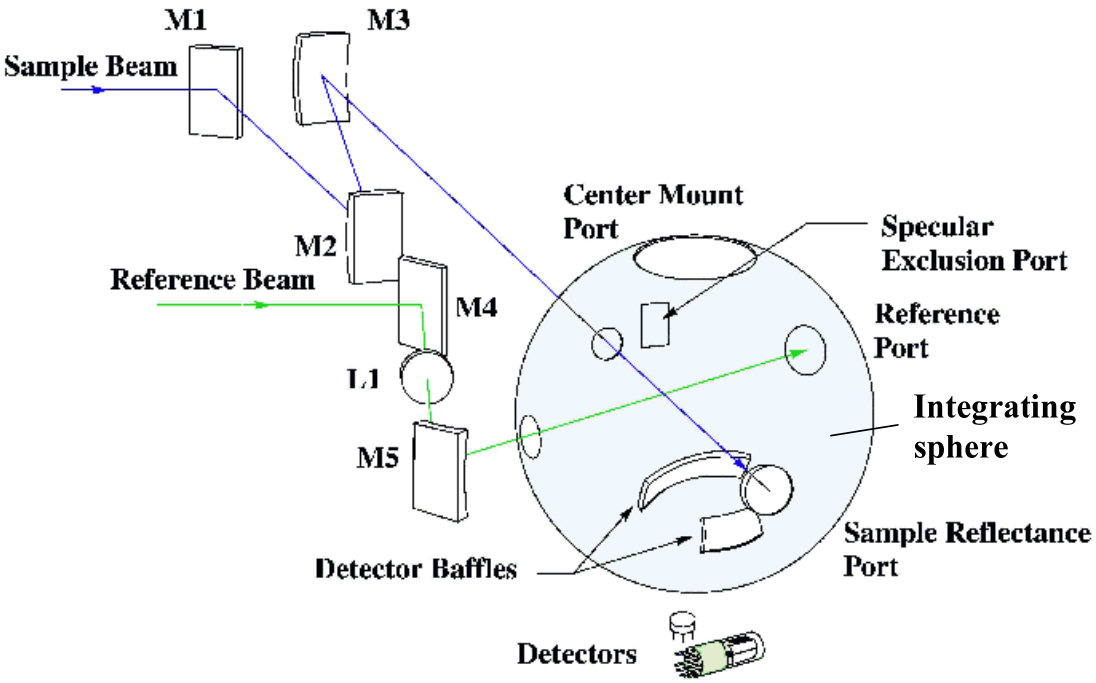

Figure 6.4. The optical design of the external DRA.

Spectral data was collected in the wavelength range 1600-1848 nm at 4 nm intervals resulting in the measurements at 63 discrete wavelengths per spectrum. This region was chosen because the first overtone peaks of polystyrene due to C–H stretching vibrations appear around 1680 nm. The Peltier (TE) cooled PbS detector was used for this wavelength region. An average integration time was set to 0.4 s, the bandwidth and the energy level were automatically adjusted by the instrument software to maintain a good signal-to-noise ratio throughout the entire wavelength region. The collimated transmittance (T_c) was measured with the instrument's standard configuration. For the total reflectance (R_t) and total transmittance (T_t) measurements the external diffuse reflectance accessory

(DRA-2500, Varian Inc.) was mounted, see fig. 6.4. It consists of a 150 mm diameter integrating sphere (manufactured by Labsphere), which has a port-to-sphere area ratio of less than 10%. The sphere is coated with "Spectralon" material, which acts as an almost perfect Lambertian surface. A schematic representation of the different measurement configurations is shown in figure 6.5.

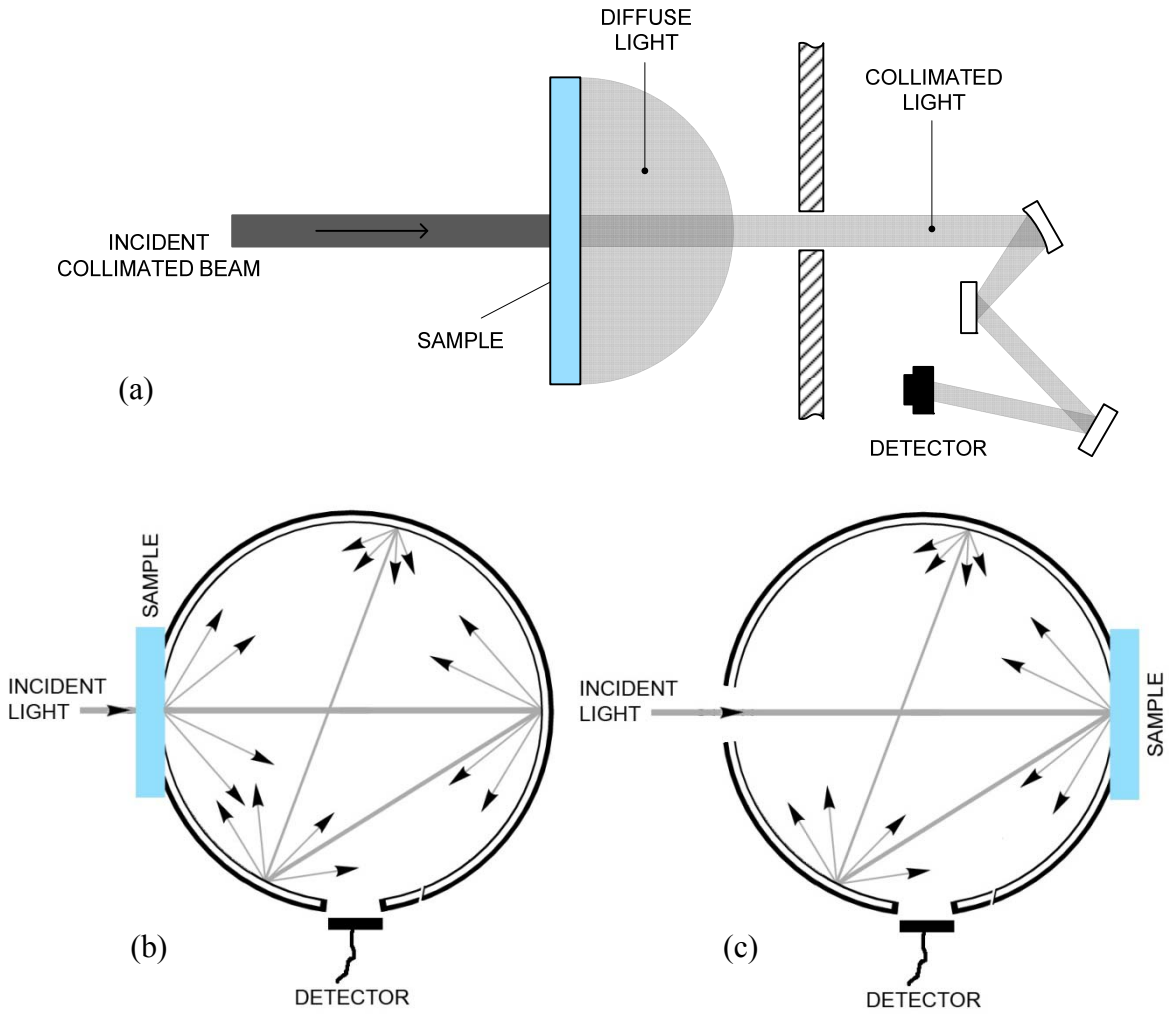

Figure 6.5. a.) Collimated transmittance measurement, b.) Total transmittance measurement, c.) Total reflectance measurement.

The collimated transmittance was used for measuring (estimating) the optical depth τ. The drawback of using this measurement for acquisition of τ estimate is that although it captures mostly the unscattered part of the light it is partly "contaminated" by the diffuse light as discussed earlier in section 3.3. The error depends on the measurement setup and the scattering levels i.e. turbidity. Hence, the results of this research work could serve as some yardstick for up to which scattering levels this simple measurement could be used for estimation of τ with a similar measurement setup without deteriorating the final prediction

performance significantly. For the total transmittance measurement, the sample is placed at the entrance port of the sphere, while the exit port is blocked with "Spectralon" reflectance standard. In this way, both collimated and diffusely transmitted light is collected by the detector. For the total reflectance measurement, the sample is placed at the exit port of the sphere, so that all light reflected by the sample is collected in the sphere. To obtain similar irradiation conditions for transmittance and reflectance measurements (i.e. illumination area and angle) different focusing lenses were used. A 1 mm path length measurement cell made out of special optical glass (100.099-OS, Hellma) was used for this experiment.

6.2.1.3. Results and discussion

Simulation results showed that a significant improvement in prediction accuracy can be achieved if PLS models are built on the bulk absorption coefficient rather than directly on reflectance or transmittance measurements, which are subject to nonlinear variations due to different path lengths travelled by photons. To validate the concept, the proposed approach was applied to a simple turbid system comprising polystyrene particles suspended in water. The collected spectra of the three measurements (i.e. total reflectance, total transmittance and collimated transmittance) and the extracted bulk absorption coefficient are presented in figure 6.6. The wavelength region considered here (1600-1848 nm) contains the first overtones of O–H stretching, bending and libration vibrations of water at around 1790 nm and the tail part (below 1848 nm) of the peak due to O–H stretching and bending vibrations at around 1900 nm [120]. The spectrum of water below the 1790 nm absorption band has also non-zero absorbance (within the wavelength range considered) even though it is relatively a flat and featureless "baseline". The main absorption band of polystyrene in this region is around 1680 nm, which is due to the first overtone of the C–H stretching vibrations.

The level of noise in T_t and R_t measurements at low levels of signal was significant (especially in R_t). Therefore, the raw spectra of T_t and R_t were smoothed using Savitsky-Golay filter with the window width 9 and the polynomial order 3 to remove noise in the measurements before feeding them to the IAD. The effect of applying this filter on the spectral data, for some of the noisiest T_t and R_t measurements, is shown in fig. 6.7. The noise in the collected T_c measurements was negligible therefore filtering was not applied to the T_c spectral data. Collimated transmittance is less noisy than T_t and R_t measurements with CARY 5000 spectrophotometer because there is more power available in the irradiating beam in its standard configuration than when using the DRA accessory.

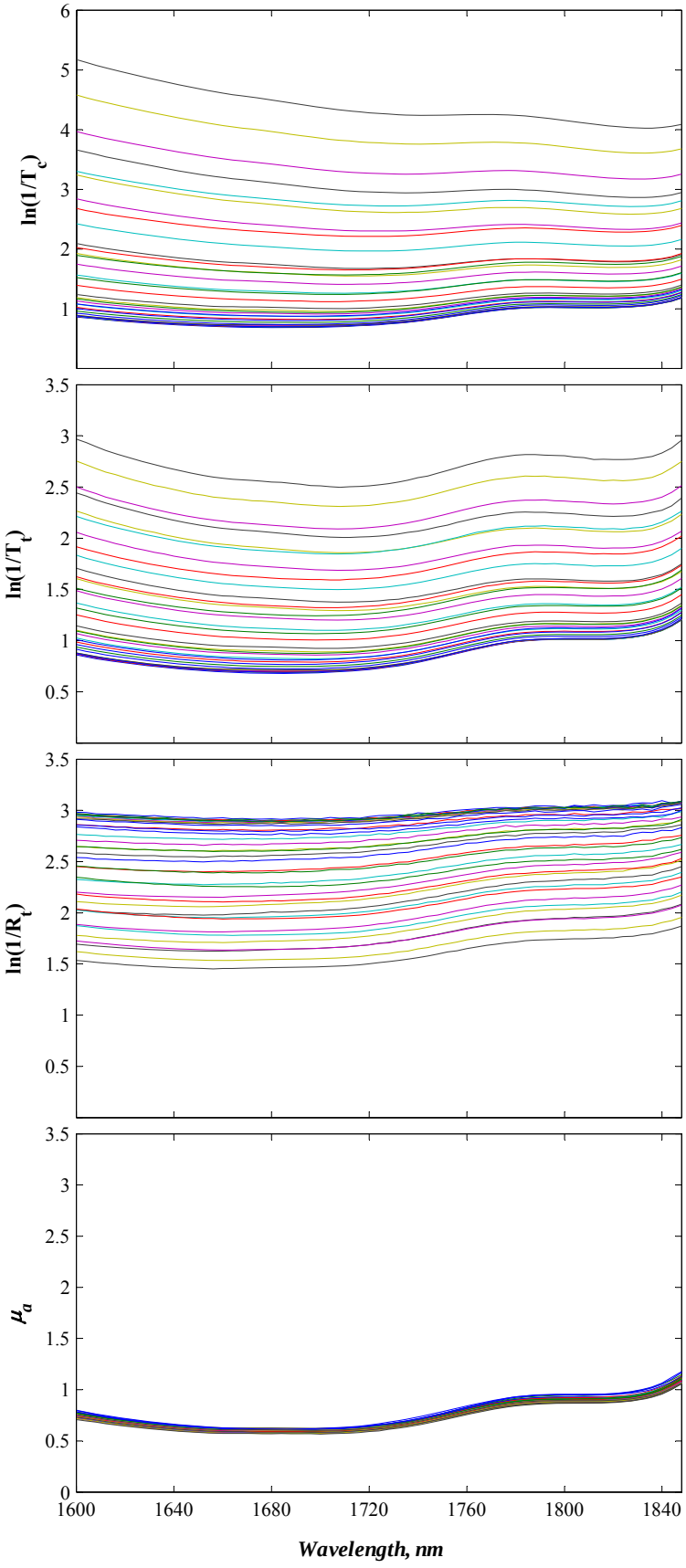

Figure 6.6. Experimental polystyrene-water data set: collimated transmittance, total transmittance, total reflectance and bulk absorption coefficient μ_a, (T_t and R_t filtered).

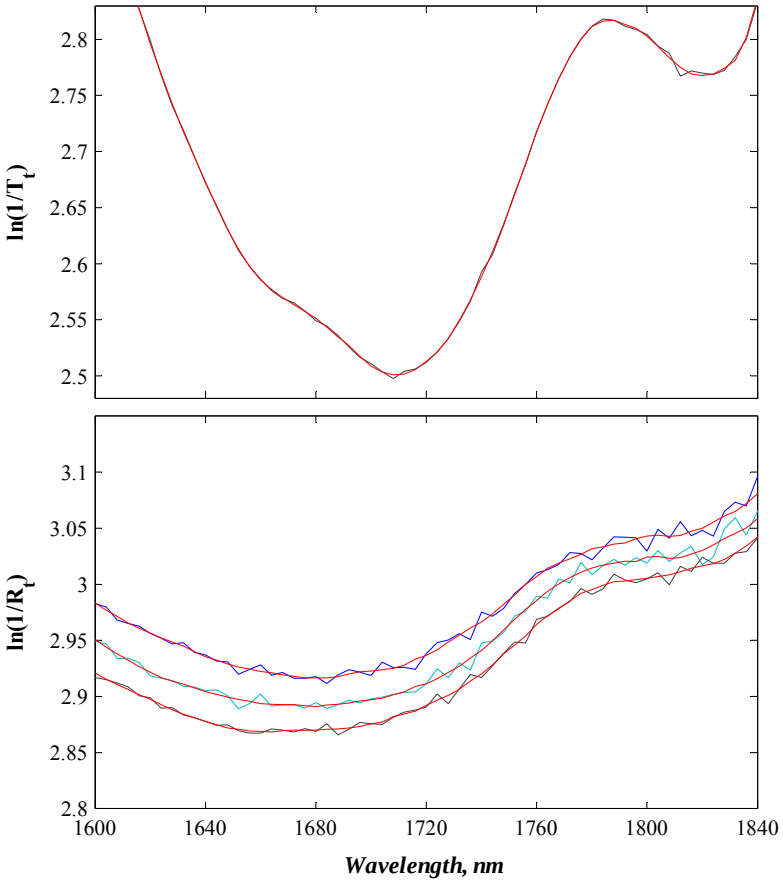

Figure 6.7. Examples of raw and filtered measurements of T_t and R_t (noise was filtered using Savitsky-Golay smoothing method), red lines denote smoothed spectra.

The required inputs/constants in the IAD alongside the three measurements were the path length of the measurement cell and the real refractive indices of air, the glass of the measurement cell, and the sample. The real refractive indices were needed to compute reflections at the air-glass-sample and sample-glass-air interfaces using Fresnel equations. The real refractive index of the measurement cell for the required wavelength region was provided by the manufacturer (Hellma). The real refractive index of the polystyrene was taken from Velazco-Roa and Thennadil [121]. However, the values were available only up to 1400 nm. Therefore, the values at higher wavelengths were obtained by extrapolation using the model given by the Cauchy dispersion formula [76]:

$$n = A + \frac{B}{\lambda^2} + \frac{C}{\lambda^4} \tag{6.2}$$

Where, empirical coefficients $A = 1.5478$, $B = 0.01796$ and $C = 0.00031$ were determined via nonlinear least squares fitting procedure. The real refractive index of water was taken from Segelstein [122] and the real refractive index of a sample was calculated simply as a

sum of real refractive indices of water and polystyrene multiplied by their respective volume fractions. The real refractive index of air was taken as equal to one across the entire wavelength range.

As it was seen with simulations (fig. 6.1), the magnitudes of variation are much larger in the measurements than in the extracted μ_a (fig. 6.6.), meaning that the majority of undesirable variation occurring due to physical effects has been successfully removed by extracting the bulk absorption coefficient μ_a under experimental conditions too. To check the consistency in the extracted μ_a, its profiles (spectra) for all seven concentrations were closely examined for each particle size separately. Figure 6.8 shows the spectra of μ_a for seven samples with different concentrations of polystyrene but the same particle size (430 nm in diameter).

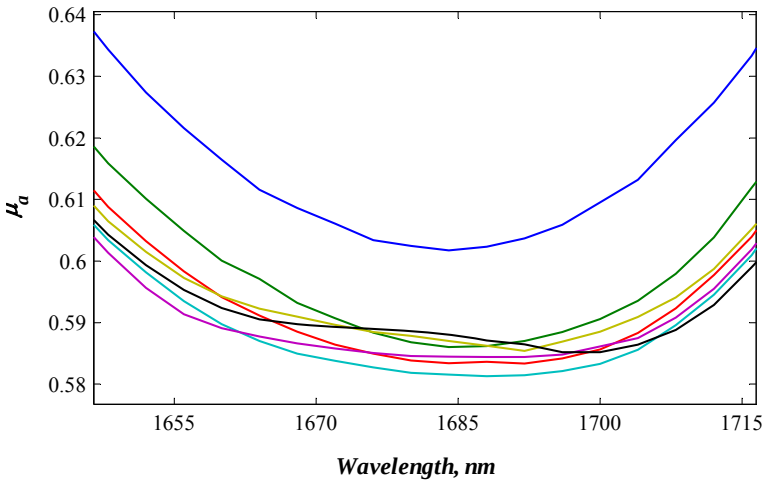

Figure 6.8. μ_a profiles for different concentrations for 430 nm diameter polystyrene particles: 0.1 % wt., 0.5 % wt., 0.9 % wt., 1.23 %wt., 1.6 % wt., 1.95 % wt., 2.3 % wt.

The differences in μ_a of the seven samples were only due to changes in polystyrene concentration. If the extraction step was carried out effectively, the peak where polystyrene absorbs should systematically increase with the concentration of polystyrene. While this was true with the 100 nm particles, for samples with particle sizes larger than 100 nm the bulk absorption spectra for the lowest two concentrations of polystyrene did not fall in the right order. In figure 6.8, this can be seen for the samples with polystyrene particles with the mean diameter of 430 nm. This is likely due to the increased losses of light in the integrating sphere measurement setup. The adding-doubling method does not take into account the light lost through the sides of the measurement cell.

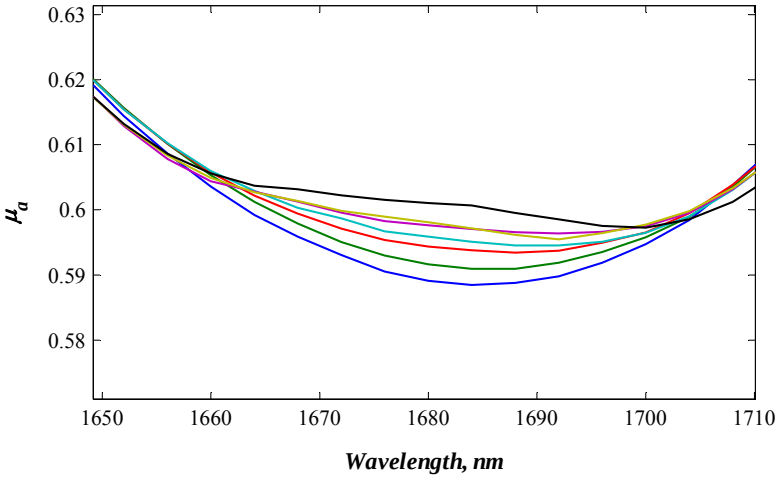

Figure 6.9. μ_a profiles for different concentrations after EMSCL: — 0.1 % wt., — 0.5 % wt., — 0.9 % wt., — 1.23 %wt., — 1.6 % wt., — 1.95 % wt., — 2.3 % wt.

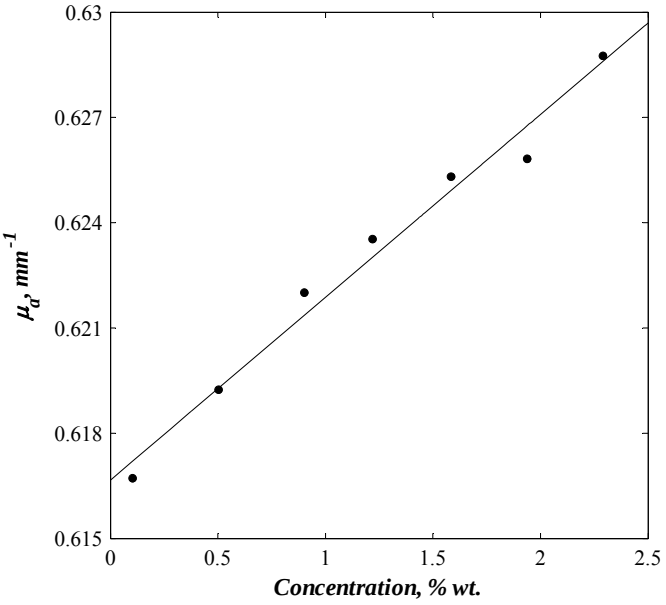

Figure 6.10. Values of μ_a at 1680 nm wavelength versus polystyrene concentration.

When the particle number density is low, the mean free path of the photons becomes high. As a result a photon that is scattered sideways has a greater probability of reaching the side walls of the measurement cell since the probability of it getting scattered again before it reaches the wall becomes lower. Since the adding-doubling method assumes that the breadth of the measurement cell is infinite, any loss through the side walls is manifested as absorption. When this effect becomes significant, the bulk absorption coefficient extracted using the adding-doubling method is overestimated. The reason it is evident for the larger particles is because for the same volumetric concentration of particles, there are much fewer large particles. This is due to the fact the number of particles is related to the cube of

the particle radius when the total particle volume is kept constant. This explains why the absorption (μ_a) spectra for the lowest concentrations were shifted up and had higher values. To correct these offsets in μ_a, that are not related to chemical information, an empirical data processing step was carried out.

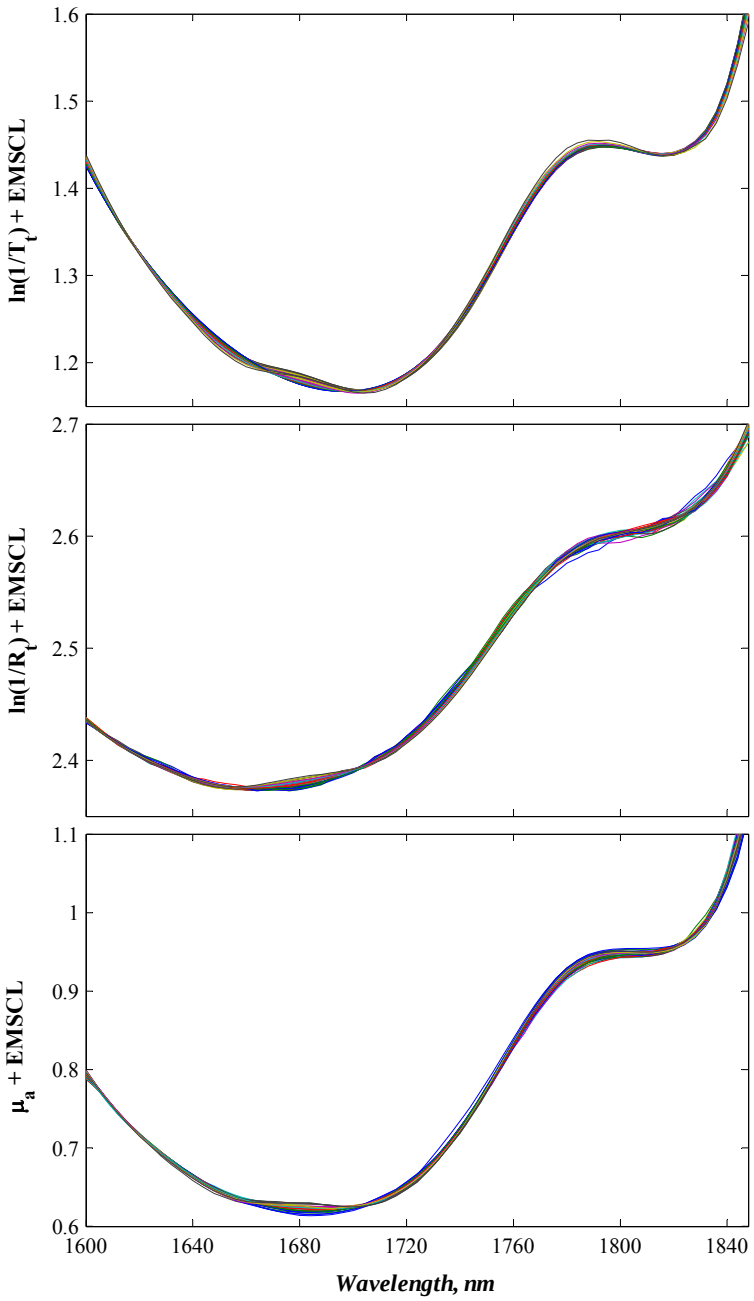

Figure 6.11. EMSCL transformed spectra of total transmittance, total reflectance and bulk absorption coefficient μ_a.

It was found that the application of EMSCL in this case successfully corrected the baseline variations in μ_a introduced by light loss from the sides of the measurement cell. This is evident from the figure 6.9 where one can notice that in the region of polystyrene

absorption the EMSCL corrected absorption spectra now shows an increase in μ_a with increasing concentration of polystyrene latex particles. And this relationship is linear as demonstrated in fig. 6.10. Normally, if μ_a is extracted accurately, this additional data processing step should not be required since the variation in μ_a will be only due to changes in chemical information (i.e. concentrations of species) then. But, if the absorption and scattering of light are not completely separated by inverting the RTE, because of inaccurate measurements or extraction procedure, and the extracted μ_a still carries a significant amount of scattering information an additional empirical data processing step may be needed, as it was in this case.

Having obtained consistent estimates of bulk absorption coefficient, after pre-processing with EMSCL, we proceeded to the next step of building PLS calibration models. Since in all three cases the best (or the same level of) prediction performance was achieved with the spectral data pre-processed using the EMSCL technique only PLS models built on μ_a, R_t and T_t pre-processed with EMSCL are reported. The pre-processed spectral datasets of the total transmittance, the total reflectance and the bulk absorption coefficient that were used for building the calibration models are given in figure 6.11. The RMSECV curves of calibration models that gave the lowest prediction errors are given in figure 6.12. The results are summarized in table 6.3.

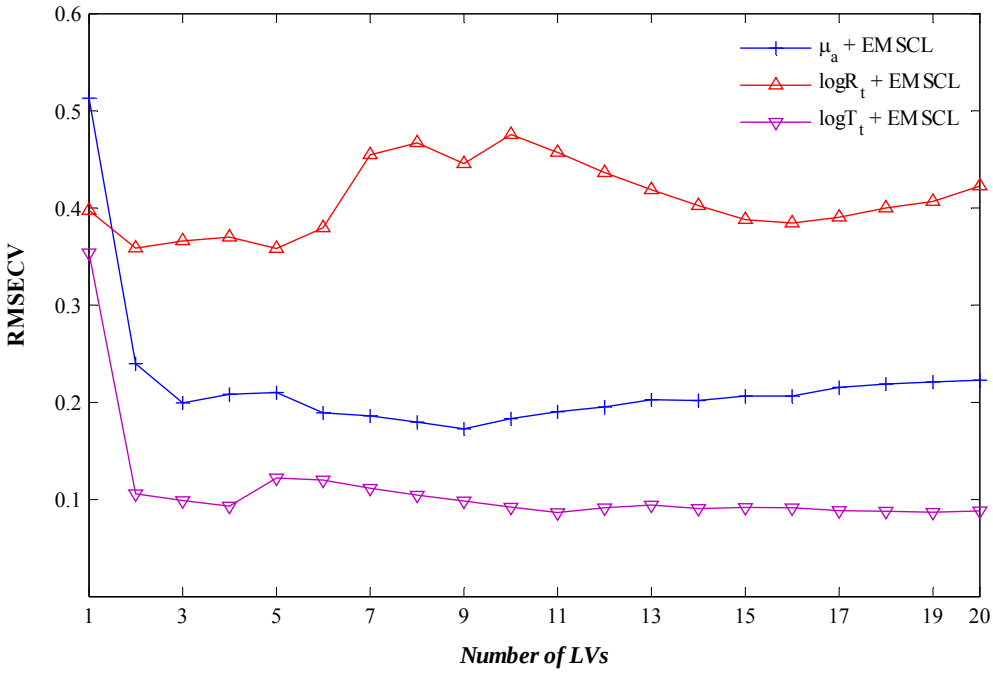

Figure 6.12. RMSECV curves of different PLS calibration models built using: R_t pre-processed with EMSCL, T_t pre-processed with EMSCL and μ_a with EMSCL.

Table 6.3. Performance of calibration models for estimating polystyrene concentration in the experimental data-set of a two-component (polystyrene-water) system.

Dataset which PLS was built on	Pre-processing	LVs	Calibration
			RMSECV
Calibration models built on total reflectance	None	5	0.41
	EMSCL	2	0.36
Calibration models built on total transmittance	None	4	0.12
	EMSCL	4	0.09
Calibration model built on μ_a	None	6	0.19
	EMSCL	3	0.20

The system considered here consisted of two components. Therefore, theoretically, one latent variable should have been sufficient to model it. However, it is apparent from the RMSECV curve built on μ_a that three latent variables are needed to describe variation in it. This result agrees with the conclusion drawn from the analysis of simulated data that extra LVs are needed to describe the nonlinear variation in absorption coefficient of particles. The other important finding in the analysis of simulated data that the prediction accuracy drops with increasing particle concentration is not so clear from the predicted versus actual values plot for experimental data, fig. 6.13, probably due to a much narrower concentration range used.

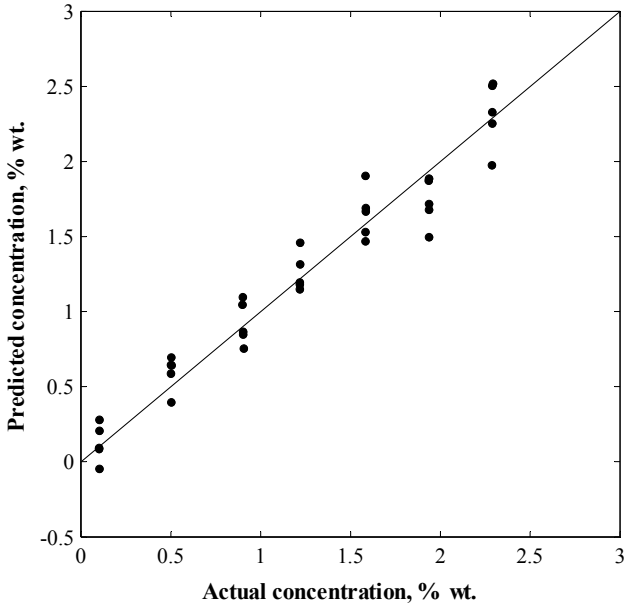

Figure 6.13. Predicted concentration of polystyrene versus the actual for calibration model built on μ_a pre-processed with EMSCL data.

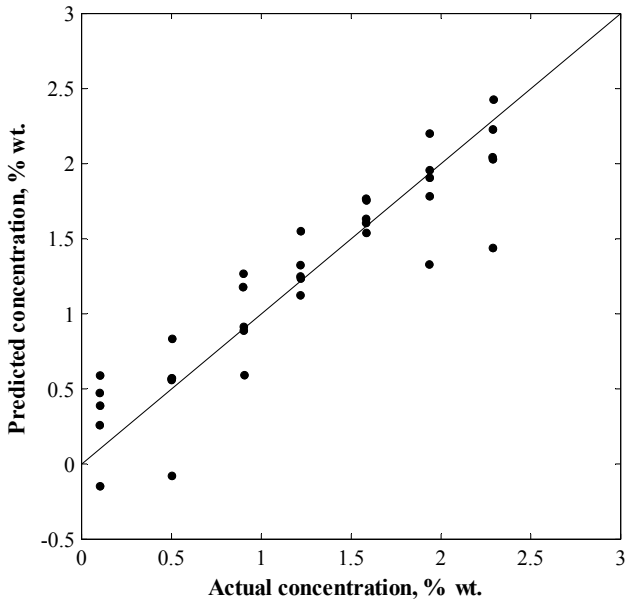

Figure 6.14. Predicted concentration of polystyrene versus the actual for calibration model built on R_t pre-processed with EMSCL data.

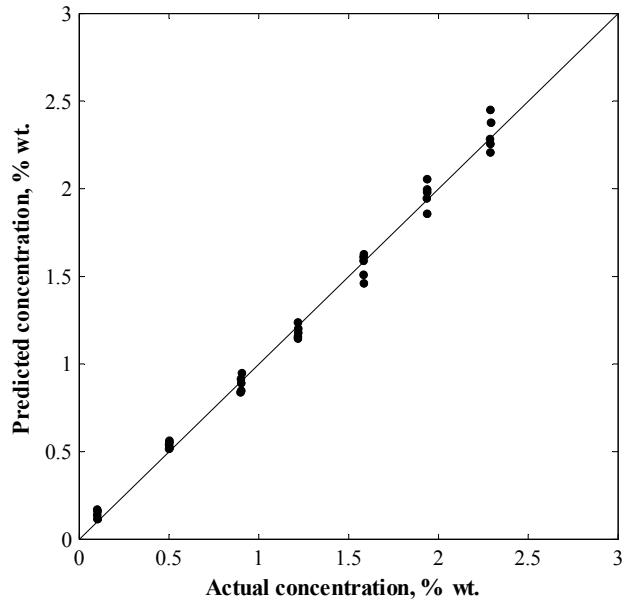

Figure 6.15. Predicted concentration of polystyrene versus the actual for calibration model built on T_t pre-processed with EMSCL data.

The plots of predicted vs. actual values for R_t and T_t are given in fig. 6.14 and 6.15. In fig. 6.14, one can notice a non-uniform somewhat nonlinear pattern in the sample distribution, which implies that EMSCL did not correct the nonlinear effects of multiple light scattering in R_t completely though it did the best job out of all other empirical pre-processing techniques. The same inference could be made from the error vs. the actual values plot or other types of graphical analysis of residuals and their normality however some of them

such as a histogram are not suitable in this case because of a small number of samples.

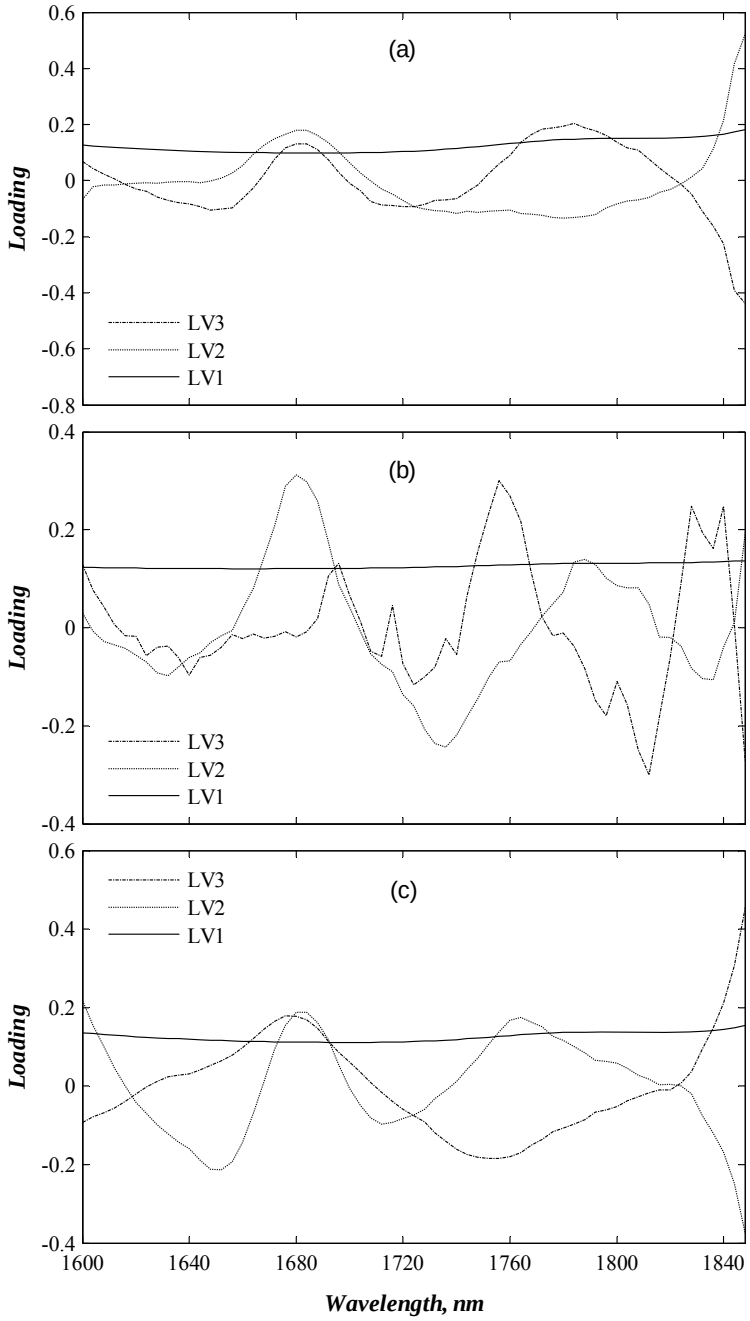

Figure 6.16. (a), (b) and (c) – loadings of the first 3 latent variables from the PLS models obtained using μ_a, R_t and T_t respectively.

While the proposed approach considerably outperformed the model obtained from spectra of total reflectance with EMSCL applied to it, very surprisingly PLS model built on the total transmittance performed much better than the proposed approach. From physical considerations and the results from simulated data with 4 components this appears to be contradictory.

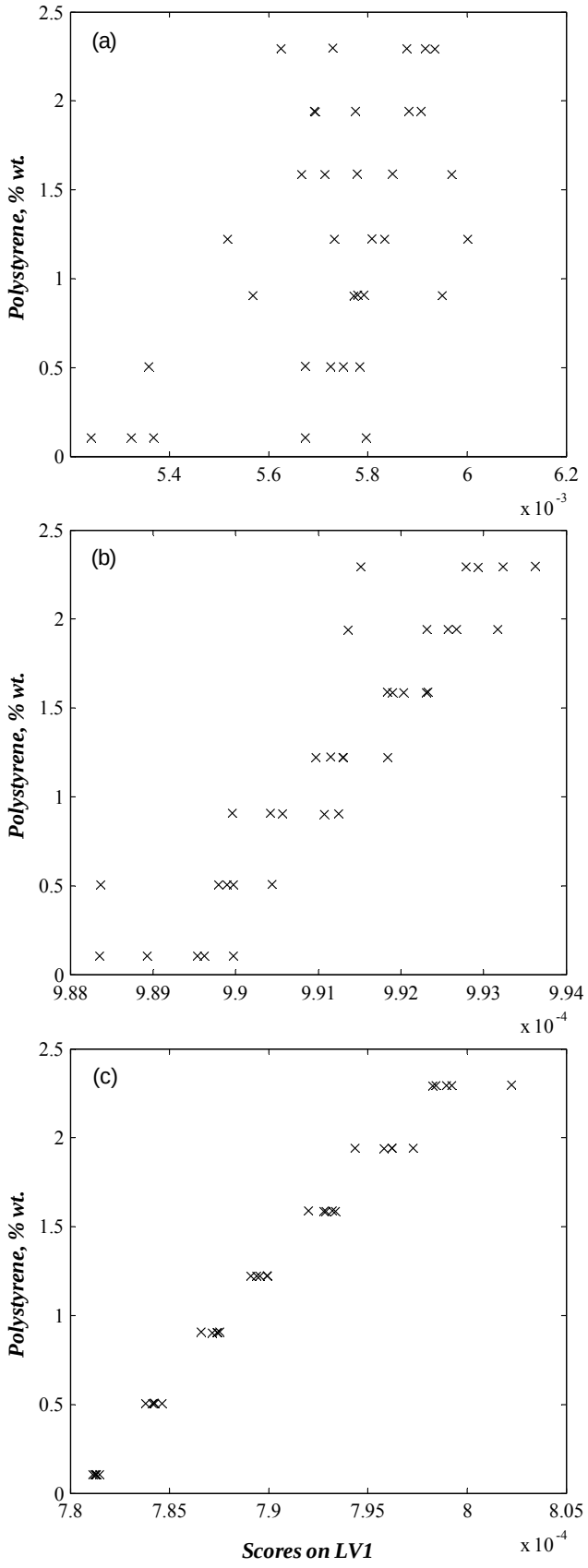

Figure 6.17. (a), (b) and (c) – scores of LV1 vs. particle concentrations for the PLS models obtained using μ_a, R_t and T_t respectively.

This apparently contradictory result can be explained by examining the scores and loadings plots of PLS models built on μ_a, R_t and T_t pre-processed with EMSCL (calibration data is shown in fig. 6.11). Figures 6.16 (a), (b) and (c) show the PLS loadings for the first three latent variables for models built using μ_a, R_t and T_t, and figures 6.17 (a), (b) and (c) show the corresponding scores of the first latent variable (LV1) plotted versus the particle concentration. For all three cases, it is seen that the first LV is essentially modelling the water absorbance, which is the largest source of variation in the spectra after the scattering effects have been removed (empirically in the case of T_t and R_t and fundamentally in the case of μ_a). While the second LV captures the variation in the polystyrene peak at 1680 nm. The third LV represents the remaining nonlinear scattering effects that have not been removed. If the correction was perfect the third LV would not be needed i.e. it would represent just noise. For the models built on R_t and T_t pre-processed with EMSCL, there is a significant correlation between the scores on the first LV and the particle concentrations. The correlation is the strongest for T_t. For μ_a this correlation is very weak and it could be argued that it is almost insignificant. Thus, the models built using R_t and T_t benefit from the correlation of particle concentration with the water absorption in the first LV, whereas this secondary correlation, which is due to the use of a two-component system, is not available for the model built using μ_a.

In a two component system, the concentrations of the two components are inversely correlated due to the closure condition. Therefore, if the first LV was representing water absorption, then the scores of the first LV should have shown a negative correlation with the polystyrene concentration, because increasing the concentration of particles would result in the decrease of water concentration (due to volume displacement). However, it is seen that the correlation is positive. This positive correlation can be explained if we consider path length variations occurring due to changes in the particle concentrations. When the particle concentration increases, multiple scattering increases which in turn increases the path length travelled by the photons. This increase in path length means that the photons will travel longer distances through the medium (which is predominantly water) resulting in the absorption due to water increasing with increasing particle concentrations and thereby leading to a positive correlation of particle concentration with water absorption which is represented by the first LV. The fact that the volume displacement effect which would have manifested as a negative correlation is not evident indicates that this effect is much smaller than the effect due to path length variation which

generates a positive correlation. It appears that this effect is the largest in the total transmittance measurements and to a smaller degree in the total reflectance measurements for the range of concentrations considered in this study. Naturally, in the case where the extracted bulk absorption spectra μ_a are used for building the PLS model, since the path length effect is removed by applying the RTE, this secondary correlation is mostly eliminated. As a result, the scores of LV1 show almost no correlation with polystyrene concentration.

From this discussion it can be concluded that the model built using μ_a is almost fully based on the actual polystyrene signal whereas those built on the direct measurements have a significant contribution from the path length effect which only for a two-component system gives rise to additional correlation with the particle concentrations and which in turn leads to an apparent advantage. It should be noted that even with this advantage the model based on R_t does not outperform the proposed approach probably due to the fact that the path length correlation is not as strong as is the case with T_t. The analysis presented shows that the extraction algorithm using the RTE to obtain the bulk absorption spectra is successful in effectively removing path length variations and providing essentially a path length normalised absorption spectra. The discussion presented here also suggests that the models based on the direct measurements will lead to much larger errors when applied to a multi-component system where the secondary correlation will not exist. On the other hand, a model based on μ_a can be expected to have less deterioration when applied to multiple component systems provided the bulk absorption spectra could be extracted with similar levels of accuracy as in the present study.

In this experiment, the methodology of partial correction of multiple scattering effects was applied to develop models for estimating the concentration of a particulate species that both absorbs and scatters light. The other common situation where the species of interest is purely absorbing and is dissolved in a matrix containing a mixture of absorbing and scattering components e.g. glucose in blood, will be investigated in the following experiment. Another possible case of interest, which was not mentioned, is when the species of interest (purely absorbing) is adsorbed on the surface of scattering particles. This methodology is applicable to such cases too. From the point of view of removing multiple scattering effects through the extraction of μ_a, the procedure is unaffected regardless of which of the three cases is being considered. The difference in each of the cases is how the species of interest contributes to μ_a and thus affects the calibration model

built using this extracted property. In theory, situations where the species of interest is purely absorbing and dissolved in a medium containing scatterers represent a comparatively simpler problem. Examining eq. (3.53), if for example the purely absorbing species of interest is component 1, then the term $\sigma_{a,1} c_1$ varies only with concentration of species 1 as there is no particle size contribution to the absorptivity $\sigma_{a,1}$. The effect of particle size only occurs indirectly through the term representing the particulate species which is an additive term. When the (purely absorbing) species of interest is adsorbed on the particle, the situation could be expected to be slightly more complicated since the adsorbed species will modify the value of absorption cross-section σ_{ap} of the particle, the extent of which will depend on level of adsorption of the species. As a result, the number of latent variables required may be more than that indicated by the additive relationship given by eq. (3.53).

6.2.2. Four component model system

6.2.2.1. Design of experiment

The results of the two component experiment showed that the proposed methodology of partial correction of multiple scattering effects gives better prediction accuracy than the multivariate calibration models built on empirically pre-processed total reflectance despite all experimental errors. But, the calibration model built on T_t pre-processed using EMSCL outperformed the proposed method and that contradicts with our simulation results. According to the above given reasoning and deductions this should not be happening with multi-component samples. To test this hypothesis an experiment with a multi-component system was designed. There were two species of interest in this experiment, namely, the scattering-absorbing and the absorbing, thus the least number of components needed to break the correlation between the two components of interest and the rest of the components was four. The following components were chosen for the experiment: polystyrene particles, ethanol, heavy water and deionised water. They are readily available chemicals of high purity: ethanol 99.8 % vol. (Fisher Scientific), heavy water 99.9 % vol. (Qmx Laboratories). Polystyrene latex of different particle sizes was bought from Duke Scientific. Particle size distributions in the latex samples were checked by taking SEM (scanning electron microscopy) pictures that are shown in the appendix C. The three absorbing components ethanol, water and heavy water are fully miscible and they do not dilute or swell polystyrene particles at moderate concentrations (this is

concerning ethanol in particular). To get zero correlation between any pair of components in this case is not possible because of a closure condition ($\sum c_i = 100\ \%$) i.e. if one concentration is changed some other concentration must change. Here c_i is the weight concentration of species i. But we can get sufficiently small correlation between the components of interest and the rest by moving that correlation to between the components that we are not interested in, in this case water and heavy water. There were three variables from the point of view of experimental design, namely, ethanol concentration, polystyrene concentration and particle size, for which the value range had to be defined. Ideally, we would like to test a wide range of particle sizes and concentrations. The wider the range the more nonlinear and complex multiple scattering effects are and the more advantageous the proposed method would in principle be in comparison with empirical pre-processing. However, the range of particle size and concentration had to be such that the following conditions were satisfied: stable suspension, multiple scattering and sufficient signal in all three measurements. Given our experimental setup, i.e. static (not flow-through) measurement cell, the first condition sets the limit for the maximum size of particles i.e. particles should be small enough to avoid settlement. A simple stability test, during which the change in transmittance was observed in time, revealed that the rate of settlement for polystyrene particles larger than 500 nm is appreciable (note that particle sizes are everywhere given in diameter). Therefore 500 nm particle diameter was chosen as the upper limit. The highest concentration of particles was set to 5 % wt., because beyond that the transmission gets too low for samples with 500 nm diameter particles i.e. we get unacceptably noisy measurements (unexplained variance in subsequently extracted μ_a is more than 5 % of the total variance which should be mainly due to changes in chemical information) and nonlinear detector response. When choosing the lower limit for particle size and concentration we have to make sure that multiple scattering condition is met and light losses in the given experimental setup are acceptable. Decreasing μ_s at fixed μ_a decreases the number of scattering events per photon thus getting the sample closer to single scattering regime and increases light losses in the holder (relative to the amount of scattered light). As one can see from eq. (3.47) lowering of any of the two parameters, namely, particle size and/or concentration, reduces μ_s. Extraction problems (i.e. IAD was failing to converge) when extracting optical properties of samples with particles of 100 nm diameter and concentration range 0.1-2.3 % wt. in the previous experiment indicated significant light losses in our cuvette holder at such particle size and concentrations. The

extraction results were particularly unsatisfactory for the two lowest concentrations 0.1 %wt. and 0.5 %wt. With these samples we were on the edge of multiple scattering regime too. This was tested by plotting the area of the total transmittance spectra versus the concentration of particles. In fig. 6.18 one can see these plots for samples with different particle sizes. The coefficient of determination R^2, which shows the goodness of the linear fit, was 0.983, 0.939, 0.873 and 0.840 for samples with 100, 200, 300 and 430 nm diameter particles respectively.

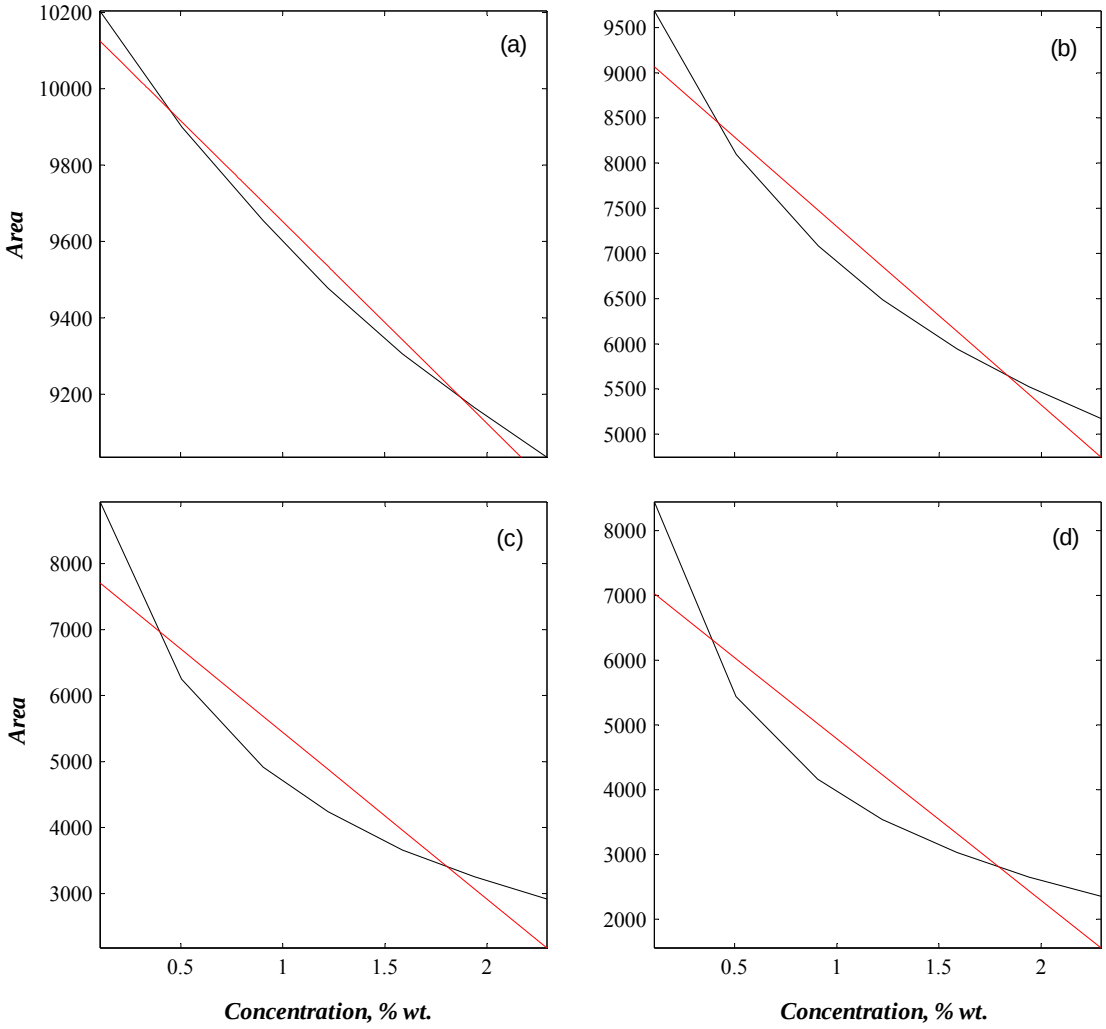

Figure 6.18. Plots of area under the spectrum versus concentration of polystyrene particles for samples with particle size of (a) 100 nm, (b) 200 nm, (c) 300 nm and (d) 430 nm.

If the relationship is linear we have single scattering [123]. As we can notice from the given plots in fig. 6.18, this relationship is close to linear for samples with particles of 100 nm size, but, with particles getting larger the relationship between the area and the concentration becomes more and more nonlinear. A nice criterion for evaluating the scattering regime (i.e. determining if the scattering is single or multiple) was proposed by

Mokhtari and Sorensen [124], but it is only valid for the case of non-absorbing particles and medium. If we would like to go lower than 100 nm with the particle size then we should increase the particle concentration substantially in order to stay in multiple scattering regime. But at these concentrations samples with large particles, for instance 500 nm, would be nearly opaque and so the transmission would be insufficient.

Table 6.4. Design of the four component experiment

No.	Concentrations, % wt.				Particle size, Ø nm
	H_2O	D_2O	C_2H_5OH	Polystyrene	
1	63.60	25.40	10.00	1.00	100
2	55.14	41.86	2.00	1.00	100
3	59.02	34.98	4.00	2.00	100
4	32.61	57.39	8.00	2.00	100
5	34.03	56.97	6.00	3.00	100
6	44.32	43.68	8.00	4.00	100
7	63.50	28.50	4.00	4.00	100
8	55.79	29.21	10.00	5.00	100
9	68.96	24.04	2.00	5.00	100
10	38.85	58.15	2.00	1.00	200
11	37.80	51.20	10.00	1.00	200
12	38.63	51.37	8.00	2.00	200
13	69.72	24.28	4.00	2.00	200
14	34.27	56.73	6.00	3.00	200
15	59.96	32.04	4.00	4.00	200
16	42.47	45.53	8.00	4.00	200
17	45.69	47.31	2.00	5.00	200
18	63.51	21.49	10.00	5.00	200
19	66.74	22.26	10.00	1.00	300
20	50.41	46.59	2.00	1.00	300
21	69.59	24.41	4.00	2.00	300
22	38.91	51.09	8.00	2.00	300
23	41.07	49.93	6.00	3.00	300
24	61.51	30.49	4.00	4.00	300
25	55.75	32.25	8.00	4.00	300
26	50.75	42.25	2.00	5.00	300
27	47.39	37.61	10.00	5.00	300
28	61.68	27.32	10.00	1.00	430
29	73.83	23.17	2.00	1.00	430
30	50.22	43.78	4.00	2.00	430
31	60.83	29.17	8.00	2.00	430
32	55.37	35.63	6.00	3.00	430
33	38.29	53.71	4.00	4.00	430
34	58.78	29.22	8.00	4.00	430
35	66.41	26.59	2.00	5.00	430
36	61.94	23.06	10.00	5.00	430
37	76.94	20.06	2.00	1.00	500
38	66.32	22.68	10.00	1.00	500
39	51.11	38.89	8.00	2.00	500
40	63.30	30.70	4.00	2.00	500
41	54.34	36.66	6.00	3.00	500
42	63.28	24.72	8.00	4.00	500
43	48.36	43.64	4.00	4.00	500
44	49.64	43.36	2.00	5.00	500
45	46.81	38.19	10.00	5.00	500

Based on this analysis it was decided to set the smallest particle diameter to 100 nm and to set the lower limit of particle concentration to 1 % wt. in the design of experiment which is given in table 6.4. Ethanol was chosen as the target absorbing only analyte. Its concentration was varied from 2 to 10 % wt. in this experiment. Thereby, five particle sizes (diameters): 100, 200, 300, 430 and 500 nm; five particle concentrations: 1, 2, 3, 4 and 5 % wt. and five concentrations of ethanol: 2, 4, 6, 8 and 10 % wt. were chosen for the design of experiment (DoE). Hence, for a full factorial design we would need 125 samples. However, in this case, a fractional factorial design comprising 45 samples was found to be sufficient considering the quality of extracted information and thus optimal in terms of the cost of the experiment. The given design of experiment was selected from a large number of randomly generated DoEs, where the concentration of deuterium was varied randomly within the predefined range and the concentration of water was closing the mass balance, as the one having the lowest correlation between each species of interest and the rest of the species. The correlations obtained between the concentrations of the target analytes, namely ethanol and polystyrene, and the rest of the variables are provided in table 6.5.

Table 6.5. Table of correlations between variables

Variable	Ethanol	Polystyrene	Particle Ø	Water	D_2O
Ethanol	**1.00**	0	0	0.14	0.12
Polystyrene	0	**1.00**	0	0.09	0.04
Particle Ø	0	0	**1.00**	0.26	0.26
Water	0.14	0.09	0.26	**1.00**	0.96
D_2O	0.12	0.04	0.26	0.96	**1.00**

Samples were prepared by weighing the actual masses of species added and then calculating the actual concentrations. Before the measurements samples were mildly shaken to ensure that polystyrene particles were uniformly distributed in the sample/suspension. Samples were randomised to avoid any possible correlations with experimental conditions (ambient temperature, instrument wear and so on).

6.2.2.2. Experimental set-up

The same experimental setup as in the previous experiment was used except for the settings of the spectrophotometer. Some adjustments were made in the shape of the irradiating beam using different optical lenses in both the total transmittance and the total

reflectance measurements making the two shapes match better thus making the irradiation conditions closer in the two measurements (it is one of the drawbacks of using a single integrating sphere setup; they are identical in a double integrating sphere set up). Then, a fixed spectral bandwidth of 7 nm was used in the whole wavelength region. The detector sensitivity was automatically adjusted by the instrument. The narrower bandwidth allowed us to get more spectral features, but measurements had more noise, which had to be filtered out in the pre-processing stage. To reduce the noise the integration time of 5 to 10 seconds was used (significantly longer than in the two component experiment). For the baselines the integration time was increased even more as this did not prolong the duration of experiment much since they are not taken before every measurement. The narrower bandwidth also yielded a smaller irradiating spot, which in turn might have reduced light losses a little since the distance from the irradiation point to the edge of the holder increased a little bit. Spectral data was collected in the wavelength region 1500-1880 nm at 2 nm intervals resulting in measurements at 191 discrete wavelengths per spectrum. This region was chosen because the first overtone peaks of polystyrene and ethanol due to C–H stretching vibrations are present there.

6.2.2.3. Results and discussion

As discussed earlier on in chapter 3, we have to provide the real refractive indices of air, the glass of the measurement cell and the sample among other inputs to IAD method in order to extract the optical properties of that sample. It is not trivial to determine a bulk refractive index of a sample exactly as opposed to the refractive indices of air and glass, because it is a heterogeneous system i.e. suspension. However, since the contact area of spherical particles with glass is much smaller than the contact area of liquid medium with glass its contribution to the bulk refractive index of a sample was neglected and it was assumed that the real refractive index of the sample was equal to the real refractive index of the medium in the calculations. In the two-component experiment the real refractive index of the medium was known and it was constant for every sample because the medium consisted of only one liquid component – water. But, in the multi-component experiments real refractive indices of media of samples are not known *a-priori* because the media consist of several liquid components the concentrations of which would be unknown except for the calibration dataset. In such cases, there are two possible ways, to actually measure the real refractive index of the medium with the refractometer, but one has to be

able to sample the medium first (e.g. by filtering), or to choose some average value based on prior knowledge about ranges in which concentrations of components forming the medium vary. The second option is not rigorous and introduces some error, but for practical purposes it may be sufficient as it was shown in this experiment where both options were tested and compared. Given the refractive indices of pure components and their respective concentrations the bulk refractive index of the medium can be accurately calculated using Lorentz-Lorenz mixing rule [125], which for a two component medium is:

$$\frac{n^2-1}{n^2+2}=\left(\frac{n_1^2-1}{n_1^2+2}\right)\cdot c_{vol,1}+\left(\frac{n_2^2-1}{n_2^2+2}\right)\cdot c_{vol,2} \tag{6.2}$$

Where n_1, n_2 and n are the real refractive indices of the first component, the second component and their mixture respectively, $c_{vol,1}$ and $c_{vol,2}$ are volume fractions of these components. However, the simplest mixing rule (Arago-Biot) [126] i.e. the resulting refractive index of the mixture of components is equal to a linear sum of fractions of refractive indices of all components constituting the medium eq. (6.3), is an approximation which was accurate enough for our simulation purposes.

$$n=\sum_{i=1}^{n} n_i\cdot c_{vol,i} \tag{6.3}$$

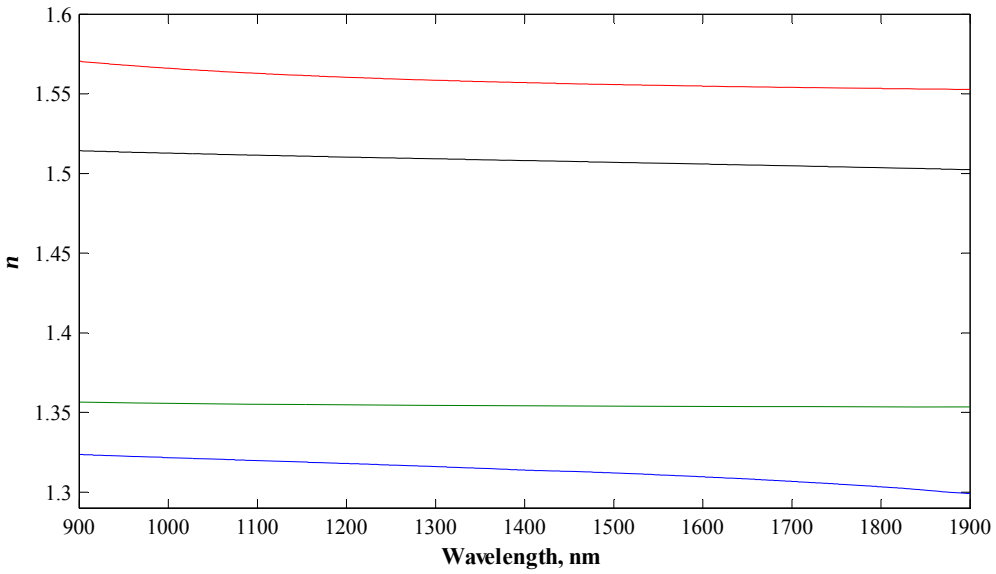

Figure 6.19. Real refractive indices of water (blue), ethanol (green), polystyrene (red) and the glass of the measurement cell (black).

In the first case, the actual refractive indices of the samples, calculated using the given approximation, were used assuming that they were known. In the second case, the

refractive index of water was used as the refractive index of the medium for all samples. The real refractive indices of water, ethanol, polystyrene and the glass of the measurement cell in the chosen wavelength range are given in fig. 6.19. The refractive indices of ethanol and heavy water were taken from the refractive index database available at [127] (values of the refractive indices beyond the given wavelength region were extrapolated using the given dispersion formulae). The refractive index of heavy water is very close to the refractive index of water therefore it was not shown in fig. 6.19.

As in the previous experiment, the collected spectra of T_t and R_t were smoothed using the Savitsky-Golay filter with the window width 9 and polynomial order 3 to remove noise from the spectral data. Figure 6.20 shows the raw spectra of T_t and R_t at lower level of signal where we have the highest noise levels in the measurements. T_c data, as in the previous case, did not require filtering.

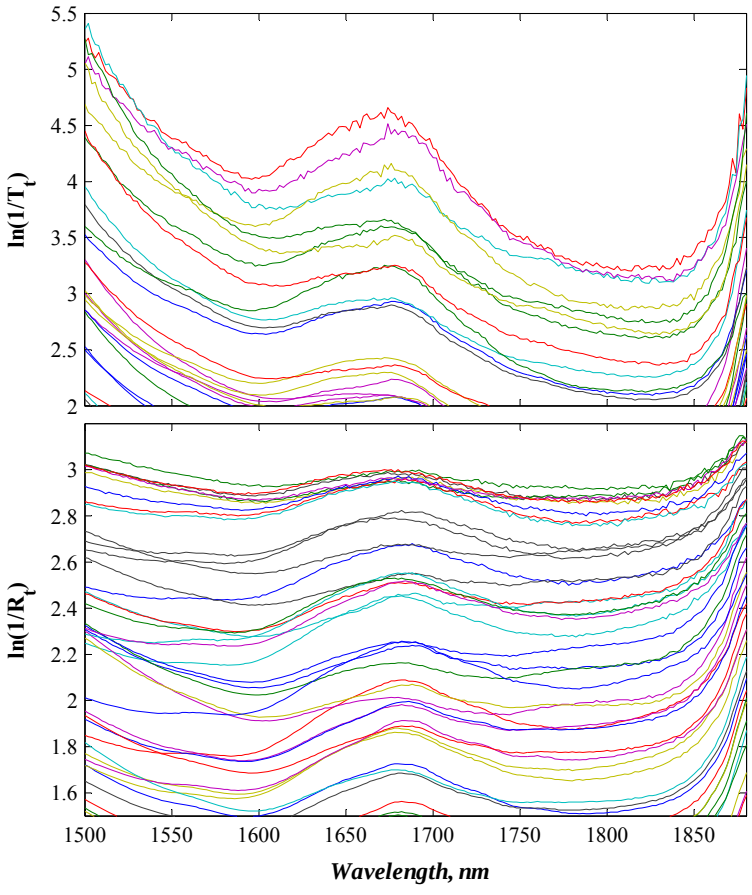

Figure 6.20. Raw spectra of total transmittance and total reflectance, four-component experiment.

The processed (filtered) spectral data and the extracted bulk absorption coefficient μ_a for all 45 samples are shown in figure 6.21.

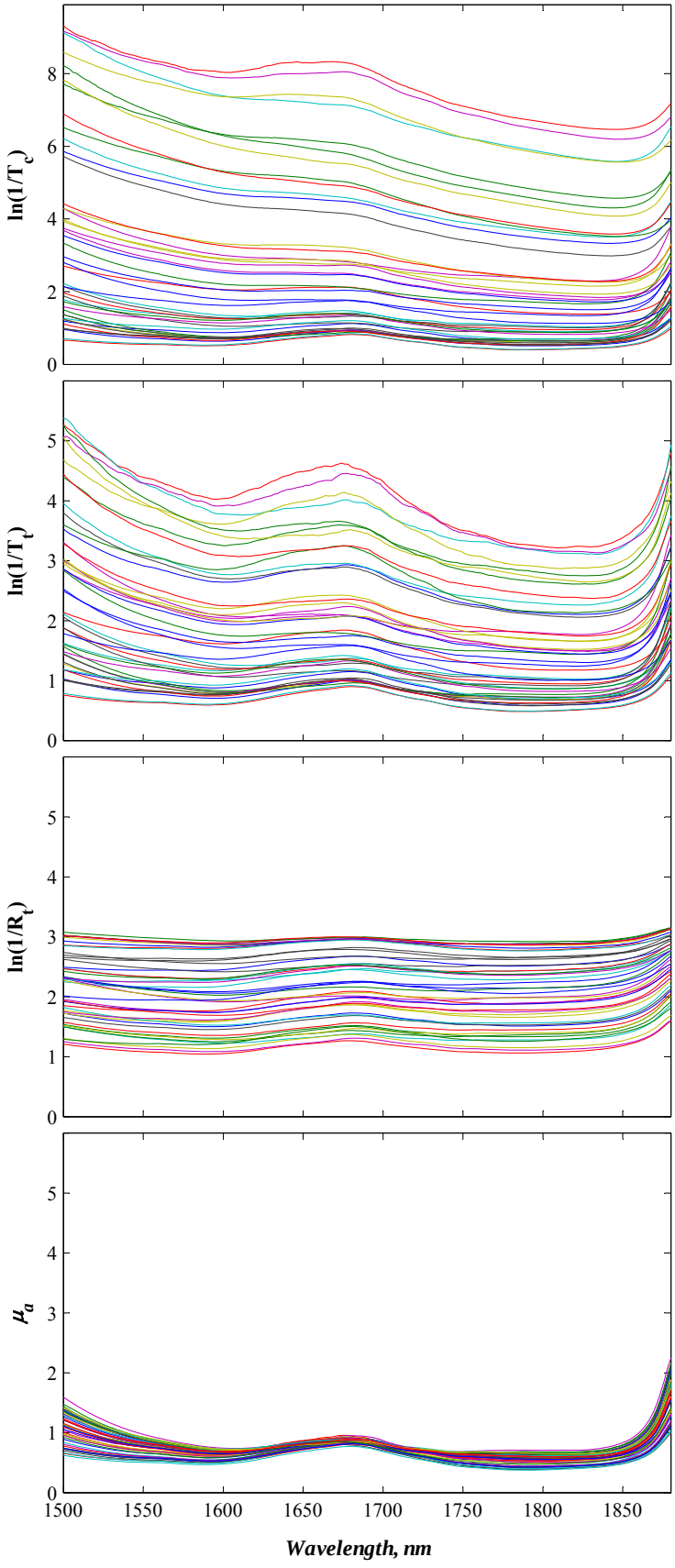

Figure 6.21. Data set of four-component experiment: collimated transmittance, total transmittance, total reflectance and bulk absorption coefficient μ_a, (T_t and R_t filtered).

All plots in fig. 6.21 are provided in the same scale so that the magnitudes of variation can be visually compared. If we compare figure 6.6 (two-component dataset) with figure 6.21 (four-component dataset) we can notice that variation in the measurements is significantly higher in the four-component experiment, because, the range of the particle concentration used in this experiment was nearly twice that of the previous experiment with the two component system. Hence, in the four-component experiment, the magnitude of the undesirable variation occurring due to physical effects is higher and it has been successfully removed by extracting the bulk absorption coefficient.

Another important point in figure 6.21 is this pronounced broad peak in the wavelength region 1600-1750 nm, which, if we have a close look at figure 6.22, does not appear in the absorption spectra of pure components (note that the shapes of polystyrene and ethanol peaks are different from it). The absorption spectrum of polystyrene was obtained by measuring the collimated transmission through the polystyrene film.

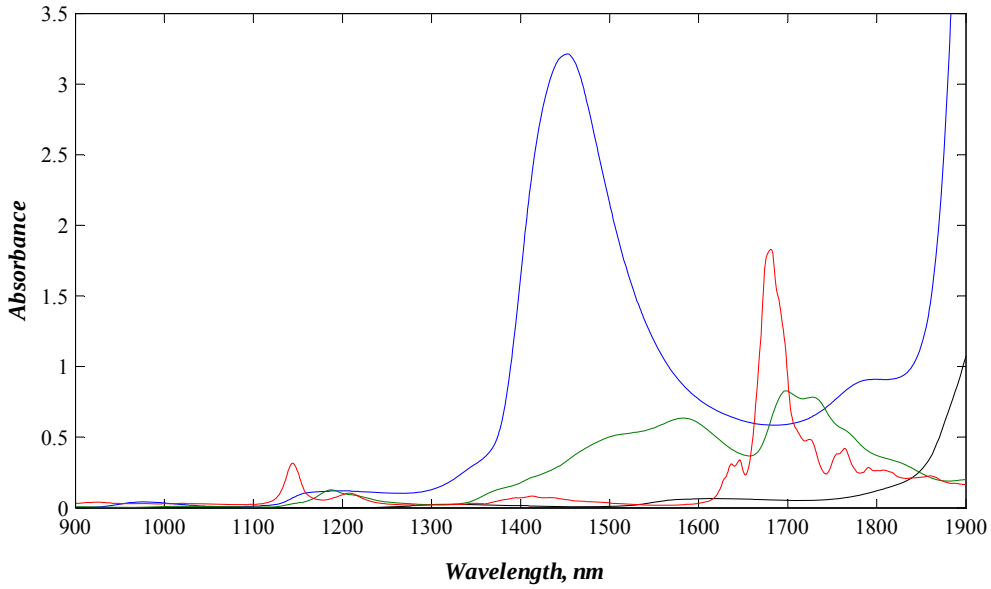

Figure 6.22. Absorption spectra of pure components: water (blue), heavy water (black), ethanol (green) and polystyrene (red).

The new absorption peak is due to some bonding between the molecules of the components that caused new vibrations, hence absorption in this wavelength region. To find out which components form new bonds in the system different binary mixtures, namely, ethanol-water, ethanol-heavy water and water-heavy water were examined. The concentrations of the binary mixtures were varied and the absorption was measured. If two components do not form additional bonds there should be only two variables in their binary mixture which the absorption varies with i.e. the two concentrations. But because the concentrations

would be fully correlated in such a case, giving us essentially one variable, the relationship between the absorbance and either of the concentrations should be linear at any chosen wavelength. Ethanol-water and ethanol-heavy water mixtures had no signs of new absorption features and consequently a linear relationship was observed at all wavelengths, i.e. the resulting spectra of the mixtures were basically the sum of the spectra of pure components with respect to their volumetric fractions, indicating that there was no additional bonding between the components. But spectral results of water-heavy water mixtures gave the answer as to what caused this unidentified absorption peak in the four component system. The same peak can be clearly seen in figure 6.23, absorption band 1600-1750 nm. It appears neither in the absorption spectrum of pure water nor in the absorption spectrum of deuterium oxide (fig. 6.22).

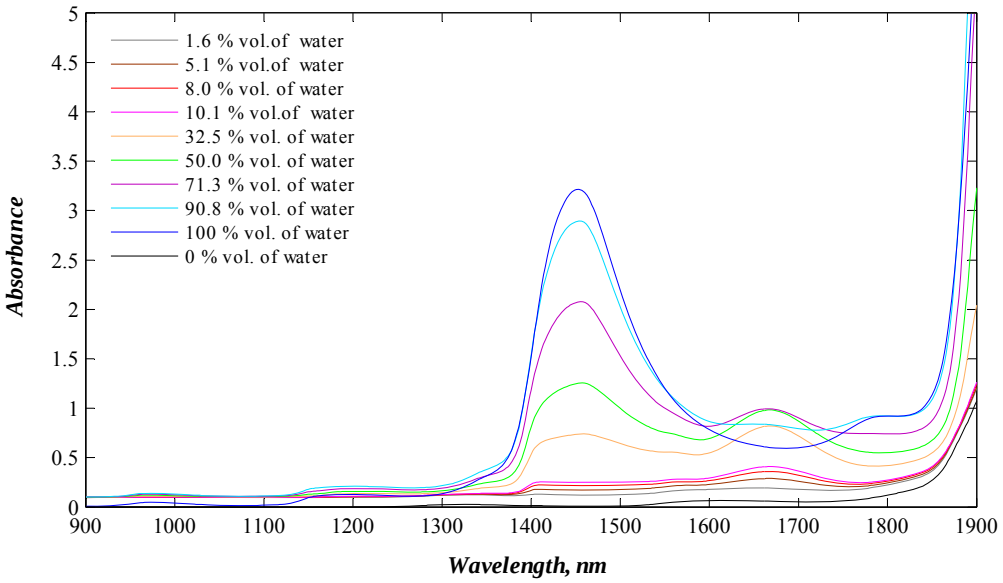

Figure 6.23. Absorption spectra of water-heavy water mixtures.

This suggests that the peak is probably due to the formation of H_2O–D_2O dimers. Studies of water, D_2O and HDO dimers have been carried out in the past by researchers using infrared spectroscopy which have shown that dimers with H_2O.DOD and D_2O.HOH structures are formed with the dimer preferring the former structure [128-130]. According to the figure 6.23, as the concentration of water increases this absorption peak increases too, but only up to a certain point (≈ 60 % vol.) after which it starts decreasing until it vanishes when the concentration of deuterium oxide reaches 100 % vol. Hence, this effect is nonlinear with respect to the concentrations of water and D_2O at the wavelengths where the dimers of H_20 and D_2O absorb and it is linear everywhere else in the region considered as shown in fig. 6.24.

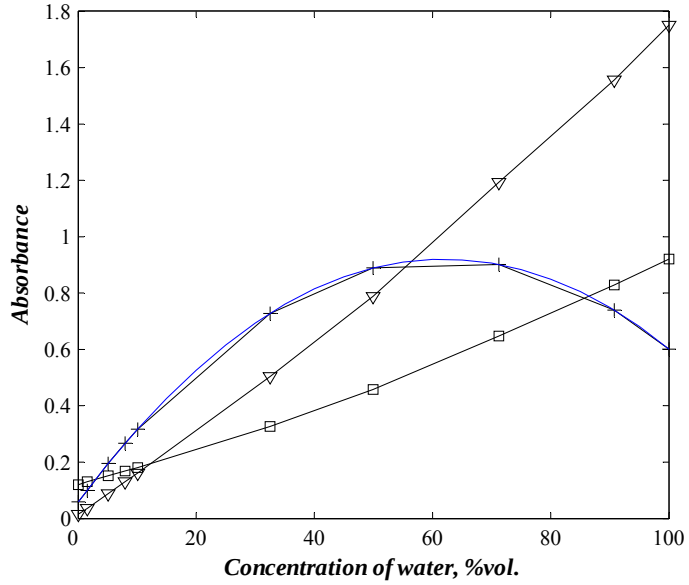

Figure 6.24. Dependency of absorption on concentration for water-heavy water system at: 1500 nm (triangle), 1880 nm (square) and 1670 nm (cross); the blue line is the fit.

This will influence our calibration results in terms of the number of latent variables required to describe the system since there is an additional variable i.e. the concentration of H_2O D_2O dimers that absorb in the given wavelength range too. Taking particle size into account there will be effectively six variables in total varying in this dataset. Therefore, theoretically (discarding experimental errors), if nonlinear scattering effects were completely removed six latent variables should explain the variation in the samples.

Analysis on the accuracy of the measurements

The performance of multivariate calibration models ultimately depends on the accuracy of the extracted optical properties which in turn is highly dependent on the accuracy of the measurements, in this case, total transmittance, total reflectance and collimated transmittance. Therefore, the accuracy of the measurements and the resulting optical properties will be discussed in detail in this paragraph.

To inspect the accuracy of the measurements they were compared with the simulated spectra. The total transmittance and the total reflectance spectra of the samples were simulated using the adding-doubling method (details can be found in the chapter III section 3.1.2.1). The extinction coefficients of water, heavy water and ethanol were obtained by measuring their absorptivity. Although they were also readily available in the literature experimental values were used because they differ slightly depending on the instrument and its settings e.g. spectral bandwidth. The scattering cross-section σ_s, the

absorption cross-section σ_a and the anisotropic factor g of poly-disperse particles were calculated using Mie solution. The inputs for the Mie solution, namely, the complex refractive index of particles and sample medium and particle size distribution, were known for each sample. However, there was a considerable uncertainty in the values of the complex refractive index of polystyrene especially concerning the imaginary part of it. The values reported in the literature by different authors differ significantly [121]. Therefore, the imaginary part of the complex refractive index of polystyrene used for the simulations was obtained by appropriately scaling the measured absorption spectrum of polystyrene film i.e. it was scaled so that the magnitude of the main polystyrene peak at 1680 nm in the simulated μ_a matched the one in the extracted μ_a for samples with Ø 500 nm particles that have the highest absorption cross-section. Having the extinction coefficients of the liquid components forming the media, absorption and scattering cross-sections of the particles and the concentrations of the chemical species the bulk absorption and scattering coefficients were calculated from the equations (3.53) and (3.54) given in the chapter III section 3.1.2.

A detailed comparison of the actual spectral data with the simulated values for the three measurements is presented in appendix A, figures A1-A15. The data is presented for each particle size separately for convenience, thereby giving us nine plots per case, which go in the order of increasing concentration of particles (1 %, 1 %, 2 %, 2 %, 3 %, 4 %, 4 %, 5 %, 5 %). The mismatch between the actual and theoretical values might be due to the following reasons: errors in the measurements (e.g. light losses in the holder and the integrating sphere, inaccurate baselines and etc.), errors in the measured concentrations, errors in the constants (namely, refractive indices, particle size distribution and the path length of the measurement cell) and errors in the computations (viz. not everything was taken into consideration, for instance structure factor i.e. particle interactions, not all assumptions were perfectly right, numerical precision of Mie and adding-doubling programs). The origin of the mismatch in each case will be discussed in the light of the aforementioned reasons.

First of all, we can notice one tendency, the actual measurement of total transmittance is moving up and total reflectance is moving down relative to their simulated values as the concentration of particles increases. This is most likely due to particle interactions that get stronger with increasing concentration. Interactions hinder free movement of particles. As a result, some structures are being formed and the distribution of particles is not random any more. Light scattered by structured particles is subject to

interference effects, though in light transport theory it is assumed that scatterers are distributed randomly thus no interference effects are present. This translates into a smaller scattering cross-section, in other words, a particle in a structure can be considered as having a smaller scattering cross-section than an independent particle. Consequently, the bulk scattering coefficient of structured suspensions is smaller too. To account for this a structure factor is introduced to eq. (3.45), but in the simulations carried out in this part it was assumed there were no particle interactions. Therefore, as the concentration of particles went up the effect of particle interactions became progressively significant and the actual bulk scattering coefficient got progressively smaller than the theoretical value i.e. the mismatch between the two increased with the concentration of particles. Consequently, the mismatch in the total transmittance and the total reflectance increased too as they are directly related to the bulk scattering coefficient i.e. smaller bulk scattering coefficient yields higher transmission since the turbidity is smaller and lower reflectance since less light is scattered.

Light losses in the cell holder depend on the photon free path length. The longer the free path length the higher is the chance of losing some photons in the holder. This is because under real experimental conditions the exit area of light is finite and photons travelling away from the exit have a small probability of being re-scattered towards the exit area. The photon free path length is related to the bulk absorption and scattering coefficients that can be considered as probabilities for a photon to be absorbed and/or scattered per unit distance. Thus, light losses increase with decreasing μ_s and μ_a.

The mismatch in the total reflectance for the samples with small particles (100 nm and 200 nm) and low particle concentrations may be explained by significant light losses since they had small values of μ_s. The corresponding total transmittances showed a good match because their signal was much higher and so the relative impact of lost light was small. However, as the particle size got larger the signal of R_t increased while the signal of T_t decreased, therefore the relative weight of light losses was getting larger in T_t. This may explain why T_t is larger than the simulated values for 100, 200 and 300 nm particle sizes (due to particle interactions), but smaller than the simulated values for 430 and 500 nm particles. The reason why R_t was larger than the simulated values for 300, 430 and 500 nm particles may be attributed to the flaw in the design of the holder of the measurement cell. The irradiating spot at spectral bandwidth equal to 7 nm was a little bit wider than the opening of the holder. Therefore a fraction of light was reflected of the edges of the holder. This was largely accounted by the zero baseline, but at high scattering this might have

yielded a tangible error. Finally, the mismatch in the optical depth τ, which increased with increasing particle size i.e. with increasing multiple scattering of light, was mainly due to the error in the collimated transmittance measurement, which was because some of the multiply scattered light was reaching the detector.

Extraction results

The extracted optical properties and their simulated values are given in appendix B, figures B1-B15. μ_s profiles of the samples with the same particle size were plotted in the same figure together with theoretically simulated values; the same with g. As we can see from the results in figure B6, IAD was failing to converge to the right solution for all nine samples with particles of 100 nm size i.e. values of g often terminated at one of the constraints (1 or 0). This was happening because due to the errors in the measurements the global minimum did not exist. In this case, the highest error was in the total reflectance, as discussed before. Therefore, we can draw a conclusion that the error in R_t for 100 nm samples in the given range of particle concentration was too high. However, interestingly enough, this did not influence the values of μ_a and μ_s much. This is probably because of the hard equality constraint on τ the values of which were accurate for 100 nm samples. IAD converged to the solution in all other cases where the particle sizes were higher and light losses were less significant. The extracted values of μ_s match the theoretical ones well at the lowest concentrations, figures B1-B5, but as the concentration of particles increases the extracted values are getting progressively lower than the simulated. This is in agreement with the above given reasoning regarding the effect of particle interactions. The same is true with the extracted values of g. They were smaller at higher concentration of and hence stronger interactions between particles. These results support the conclusion that the effect of particle interactions is equal to that of reducing the particle size. As Prahl showed in his paper [64] the variation in g with turbidity, hence particle concentration too, is due to the error in the collimated transmittance measurement. This error is in particular evident at large particle sizes and high particle concentrations where we have the strongest multiple scattering, compare figures A3, A6, A9, A12 and A15. Because of this reason, IAD failed to converge for one of the 500 nm samples having the highest particle concentration at the lower end of the wavelength region, figure B10 (red line), where the scattering is the highest and thus the mismatch is the largest, see figure A15. In spite of some mismatches between the extracted and theoretical values in μ_s and g the extracted values of μ_a matched the theoretical ones sufficiently well, see figures B11-B15. This

means that the experimental errors influenced μ_s and g mostly whereas μ_a was relatively less sensitive to them.

It can be concluded from the analysis of the accuracy of the measurements and the extracted optical properties that for the given experiment (i.e. the measurement setup and the samples) the optimal range of particle size was approximately from 200 to 400 nm (in diameter) and concentration from 1 to 3 % wt. That is for these samples the extracted optical properties matched the theoretical values very well.

The case when the real refractive index of water was taken as the refractive index of the sample for every sample when extracting the optical properties was also analysed. The difference in the extracted optical properties shown in figures B16-B18 represents the maximum difference i.e. the real refractive index of that sample was most different from the real refractive index of water. As one can notice it is not significant especially in μ_a suggesting that fixing the real refractive index of the medium at some constant average value, in this case the real refractive index of water, may still give us sufficiently accurate values of the extracted bulk absorption coefficient for a good prediction performance of multivariate calibration models.

6.2.2.3.1. Case of absorbing species

During the standard data pre-screening (check) procedure for outliers and leverages carried out before multivariate calibration one leverage point corresponding to the eighth sample (indicating a significant error either in the measurement or in the concentration) was identified and removed from the dataset. Hence, the final dataset comprised 44 samples in total.

The RMSECV curves for multivariate calibration models (PLS) built on the different datasets are presented in fig. 6.25. As we can see, the best performance was achieved with PLS model built on the extracted bulk absorption coefficient. It required six latent variables, which conforms to the effective number of variables in the designed experimental system. The performance of the calibration models in estimation of the concentration of ethanol (i.e. absorbing species) is summarised in table 6.6. μ_a^w is the bulk absorption coefficient extracted using the real refractive index of water as the refractive index of the medium for all samples. According to the results, PLS model built on μ_a gave the best accuracy with the least number of latent variables i.e. with the simplest calibration model. It is worth noting that different pre-processings of μ_a were also tried, but the best

performance was achieved without pre-processing, which should be the case theoretically if the bulk absorption coefficient is determined sufficiently accurately. Whilst applying EMSCL on the total reflectance and transmittance yielded an appreciable improvement in the performance of PLS model.

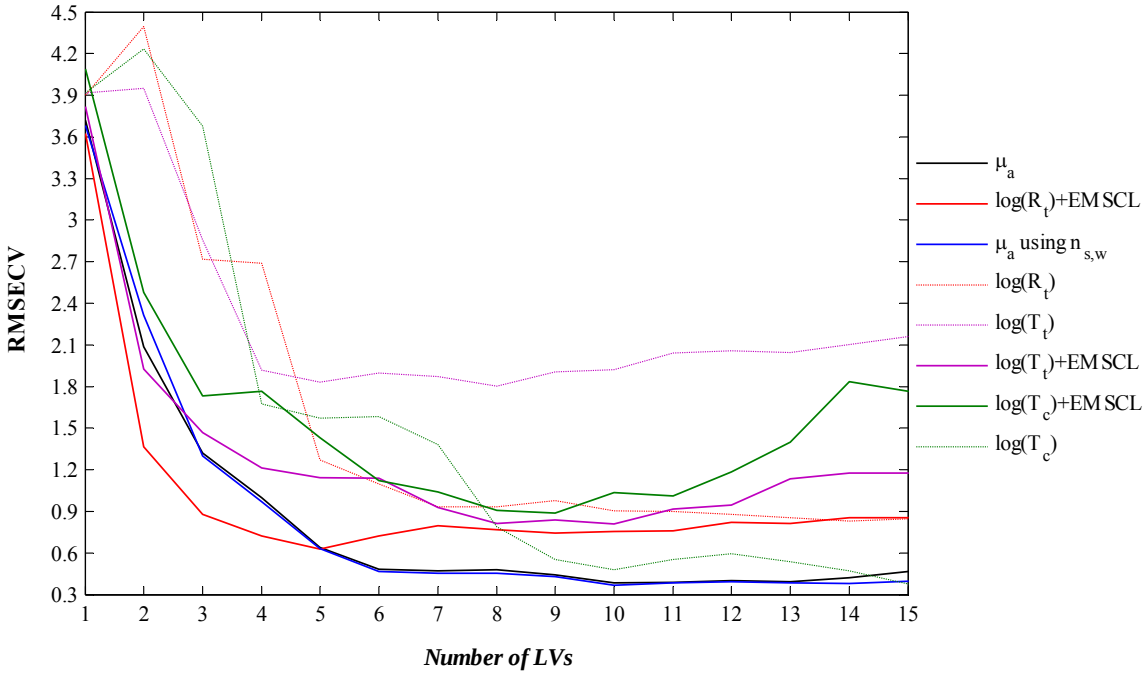

Figure 6.25. RMSECV curves for prediction of ethanol concentration in four-component system, benchmarking methodology of partial correction of multiple scattering effects.

Table 6.6. Performance of calibration models for estimating concentration of absorbing only species (ethanol) in the four-component system.

Data	Pre-processing	LVs	RMSECV (% vol.)
R_t	None	7	0.94
	EMSCL	5	0.63
T_t	None	5	1.83
	EMSCL	8	0.81
T_c	None	10	0.48
	EMSCL	9	0.88
μ_a	None	6	0.48
μ_a^w	None	6	0.47

An important result is that basically the same predicting performance was achieved with μ_a^w extracted using the refractive index of water as the refractive index of the medium for all samples. It can be concluded thus that fixing the real refractive index of the medium at a constant value in analogical situations should not deteriorate the performance of the calibration model significantly.

It is interesting to notice that the same accuracy was also achieved by building PLS calibration model on the turbidity measurement ($-\log T_c$), but that required nearly twice as much LVs than for μ_a. The reason why a higher accuracy could be achieved with T_c than with T_t or R_t by adding extra LVs to the calibration model is a lower noise in the T_c measurement than in the T_t and R_t measurements (and subsequently in the extracted μ_a) obtained with the given instrument. Consequently, more of the nonlinear variation due to multiple scattering could be modelled (i.e. explained) in the T_c measurement than in the T_t or R_t measurements at the expense of extra LVs.

6.2.2.3.2. Case of scattering-absorbing species

The RMSECV curves for PLS calibration models built on the empirically pre-processed direct measurements and on the extracted bulk absorption coefficient for estimation of the concentration of the scattering-absorbing component (i.e. polystyrene particles) are presented in figure 6.26. The results of the performances are summarised in table 6.7. As in the case with absorbing only species, the best predictive performance was achieved with PLS calibration model built on the extracted bulk absorption coefficient. However, in this case, it was achieved with one latent variable more i.e. 7 LVs. This time, PLS model built on the empirically pre-processed total transmittance performed considerably worse than when built on μ_a as opposed to the results from the two-component experiment where it could benefit from the secondary correlation, which confirmed the anticipated outcome with a multi-component system.

Again, no significant difference is observed between using μ_a^w and μ_a for calibration, thus approving the use of the fixed refractive index for a medium when extracting the optical properties of samples in similar cases. Comparing the results in predicting the two types of species i.e. the absorbing and the scattering-absorbing, using the empirically pre-processed measurements, one can notice that in the first case a better performance was obtained using $-\log R_t$ + EMSCL and in the second case using $-\log T_t$ + EMSCL, see figures 6.25 and 6.26 and tables 6.6 and 6.7.

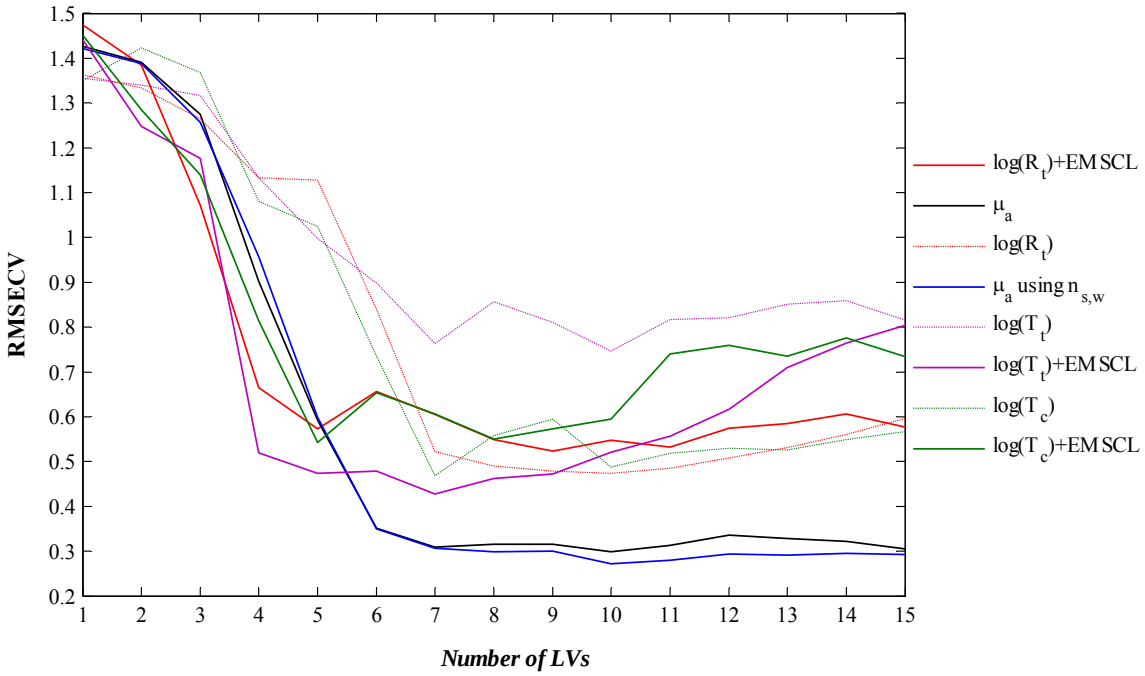

Figure 6.26. RMSECV curves for prediction of concentration of polystyrene particles in four-component system, benchmarking methodology of partial correction of multiple scattering effects.

Table 6.7. Performance of calibration models for estimating concentration of scattering-absorbing species (polystyrene) in the four-component system.

Data	Pre-processing	LVs	RMSECV (% vol.)
R_t	None	7	0.52
	EMSCL	5	0.57
T_t	None	7	0.76
	EMSCL	7	0.43
T_c	None	7	0.47
	EMSCL	5	0.54
μ_a	None	7	0.31
μ_a^w	None	7	0.31

CHAPTER VII

APPLICATION OF FULL CORRECTION METHOD

From the point of view of multivariate calibration, we want a quantity (measured or extracted) which varies with concentrations of chemical species linearly, because then the quantitative information can be effectively extracted using multivariate techniques such as PLS. In the case of quantitative analysis of non-scattering samples total absorbance is a suitable quantity for multivariate calibration since it varies linearly with concentrations of absorbing species eq. (3.59), absorptivities (i.e. absorption cross-sections) of chemical species and the path length of light are constant in this case. However, in turbid samples the path length of photons is not constant and the absorption cross-section of particles may not be constant either depending on whether particles absorb or not. If particles only scatter light then the path length normalised μ_a is a suitable quantity for multivariate calibration and therefore partial correction approach is the most appropriate in this case. When particles not only scatter but also absorb light, the extracted μ_a is still nonlinearly related to the physical properties of particles such as size through μ_{ap} eq. (3.53) (a more detailed discussion on the problem of quantitative analysis of turbid samples can be found in chapter 3.3). In such cases, the bulk absorption of the absorbing only species, represented by the $\sum_{k=1}^{n_a} \mu_{a,k}$ term in eq. (3.53), is theoretically the most suitable quantity for multivariate calibration. To obtain this quantity two pre-processing steps are required, first to extract the bulk absorption coefficient μ_a and second to subtract μ_{ap} from it. And this is referred to as the full correction of multiple scattering effects in this work.

7.1. IMPACT OF NONLINEAR ABSORPTION COEFFICIENT OF PARTICLES ON MULTIVARIATE CALIBRATION

The analysis of the impact of the nonlinear absorption coefficient of particles on calibration was carried out to investigate the conditions under which it would be necessary to apply the full correction method. The justification for application of the full correction of multiple scattering effects may differ depending on the situation that is it depends on how much the particle size varies and how broad the wavelength range used is.

To illustrate that, let us consider a turbid system comprising two absorbing and one scattering absorbing species which is mono-disperse particles. The values of μ_a for one sample at m wavelengths can be represented by the following system of equations:

$$\begin{cases} \sigma_{a1,1}\cdot c_1+\sigma_{a2,1}\cdot c_2+\sigma_{ap,1}\cdot N_p=\mu_{a,1} \\ \sigma_{a1,2}\cdot c_1+\sigma_{a2,2}\cdot c_2+\sigma_{ap,2}\cdot N_p=\mu_{a,2} \\ \sigma_{a1,3}\cdot c_1+\sigma_{a2,3}\cdot c_2+\sigma_{ap,3}\cdot N_p=\mu_{a,3} \\ \vdots \\ \sigma_{a1,m}\cdot c_1+\sigma_{a2,m}\cdot c_2+\sigma_{ap,m}\cdot N_p=\mu_{a,m} \end{cases} \tag{7.1}$$

As opposed to absorbing only species, the absorption cross-sections of which are constant at particular wavelength, the absorption cross-section of particles is a variable quantity which depends on particle size i.e. radius R. Thus, μ_{ap} is a function of two independent variables c_p (mass or volume concentration of particles) and R. The interpretation of μ_{ap} term in the given form i.e. as a product of σ_{ap} and N_p, is not convenient because both quantities are nonlinear functions of R. To make the analysis more convenient R can be separated from c_p into a separate nonlinear term as given in the section 6.1.2 eq. (6.1). Then the nonlinear effects of R can be investigated separately. The system of equations would then look like:

$$\begin{cases} \sigma_{a1,1}\cdot c_1+\sigma_{a2,1}\cdot c_2+K_1\cdot c_p=\mu_{a,1} \\ \sigma_{a1,2}\cdot c_1+\sigma_{a2,2}\cdot c_2+K_2\cdot c_p=\mu_{a,2} \\ \sigma_{a1,3}\cdot c_1+\sigma_{a2,3}\cdot c_2+K_3\cdot c_p=\mu_{a,3} \\ \vdots \\ \sigma_{a1,m}\cdot c_1+\sigma_{a2,m}\cdot c_2+K_m\cdot c_p=\mu_{a,m} \end{cases} \tag{7.2}$$

Where, K is a nonlinear function of R only. The absorption cross-section of particles, which is in K, is a function of the size parameter which changes with the particle radius and with the wavelength too, eq. (3.43). The relationship between K and the size parameter x, simulated using Mie code for mono-disperse particles, is depicted in fig. 7.1.

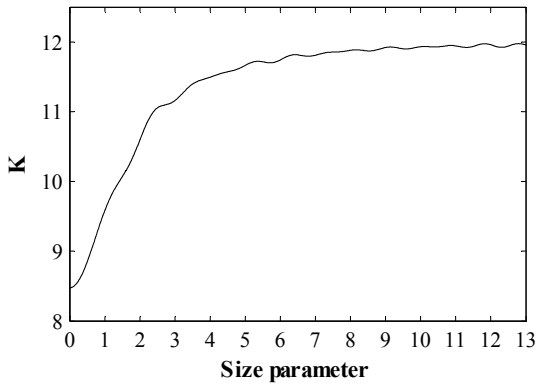

Figure 7.1. The plot of the function $K(x)$ for a mono-disperse suspension.

One can notice some ripples on the curve that are due to interference effects. For poly-disperse particles these interference ripples may not appear because of the averaging over many particle sizes [74]. As we can see the function is highly nonlinear.

To explain the nonlinear effects of K on the measurement matrix (and so the covariance matrix, which is used in multivariate calibration, too) let us model this nonlinear function of R, λ and m as $\log(u+R/\lambda)$, since an explicit analytical form of it does not exist (Mie solution is an iterative solution). Where, u is some wavelength dependent parameter representing the changes in the ratio of the complex refractive indices m and R/λ represents the size parameter x (λ is the wavelength). Then we have:

$$\begin{cases} \sigma_{a1,1}\cdot c_1+\sigma_{a2,1}\cdot c_2+\log\left(u_1+R_k/\lambda_1\right)\cdot c_p=\mu_{a,1} \\ \sigma_{a1,2}\cdot c_1+\sigma_{a2,2}\cdot c_2+\log\left(u_2+R_k/\lambda_2\right)\cdot c_p=\mu_{a,2} \\ \sigma_{a1,3}\cdot c_1+\sigma_{a2,3}\cdot c_2+\log\left(u_3+R_k/\lambda_3\right)\cdot c_p=\mu_{a,3} \\ \vdots \\ \sigma_{a1,m}\cdot c_1+\sigma_{a2,m}\cdot c_2+\log\left(u_m+R_k/\lambda_m\right)\cdot c_p=\mu_{a,m} \end{cases} \tag{7.3}$$

For multiple samples this can be written in the matrix form as:

$$\underset{\text{species 1}}{\overset{\mathbf{S}}{\begin{bmatrix} \sigma_{a1,1} & \sigma_{a2,1} & \log\left(u_1+R_k/\lambda_1\right) \\ \sigma_{a1,2} & \sigma_{a2,2} & \log\left(u_2+R_k/\lambda_2\right) \\ \sigma_{a1,3} & \sigma_{a2,3} & \log\left(u_3+R_k/\lambda_3\right) \\ \vdots & \vdots & \vdots \\ \sigma_{a1,m} & \sigma_{a2,m} & \log\left(u_m+R_k/\lambda_m\right) \end{bmatrix}}}_{\text{species 2}} \cdot \underset{k\text{ samples}}{\overset{\mathbf{C}}{\begin{bmatrix} c_{1,1} & c_{1,2} & c_{1,3} & \cdots & c_{1,k} \\ c_{2,1} & c_{2,2} & c_{2,3} & \cdots & c_{2,k} \\ c_{p,1} & c_{p,2} & c_{p,3} & \cdots & c_{p,k} \end{bmatrix}}} = \underset{\mu_a\text{ spectrum of sample 1}}{\overset{\mathbf{A}}{\begin{bmatrix} \mu_{a,11} & \mu_{a,12} & \mu_{a,13} & \cdots & \mu_{a,1k} \\ \mu_{a,21} & \mu_{a,22} & \mu_{a,23} & \cdots & \mu_{a,2k} \\ \mu_{a,31} & \mu_{a,32} & \mu_{a,33} & \cdots & \mu_{a,3k} \\ \vdots & \vdots & \vdots & \ddots & \vdots \\ \mu_{a,m1} & \mu_{a,m2} & \mu_{a,m3} & \cdots & \mu_{a,mk} \end{bmatrix}}}_{\mu_a\text{ spectrum of sample 2}}{}^{\mu_a\text{ spectrum of sample 3}}{}^{\mu_a\text{ spectrum of sample }k} \tag{7.4}$$

$$\underset{\text{particles}}{}$$

Where, R_k is the size of the particles in the k^{th} sample. For the matrix **A**, which represents the set of the extracted μ_a spectra, to be linear means that its columns should be some linear combination of the columns of **S** and its rows should be some linear combination of the rows of **C**, since, the columns of **A** can be expressed as (example is given only for the

first column of **A** i.e. for the first sample):

$$\begin{bmatrix} \sigma_{a1,1} \\ \sigma_{a1,2} \\ \sigma_{a1,3} \\ \vdots \\ \sigma_{a1,m} \end{bmatrix} \cdot c_{1,1} + \begin{bmatrix} \sigma_{a2,1} \\ \sigma_{a2,2} \\ \sigma_{a2,3} \\ \vdots \\ \sigma_{a2,m} \end{bmatrix} \cdot c_{2,1} + \begin{bmatrix} \log\left(u_1 + R_1/\lambda_1\right) \\ \log\left(u_2 + R_1/\lambda_2\right) \\ \log\left(u_3 + R_1/\lambda_3\right) \\ \vdots \\ \log\left(u_m + R_1/\lambda_m\right) \end{bmatrix} \cdot c_{p,1} = \underbrace{\begin{bmatrix} \mu_{a1,1} \\ \mu_{a1,2} \\ \mu_{a1,3} \\ \vdots \\ \mu_{a1,m} \end{bmatrix}}_{\boldsymbol{\mu_{a1}} \text{ spectrum of species 1}} + \underbrace{\begin{bmatrix} \mu_{a2,1} \\ \mu_{a2,2} \\ \mu_{a2,3} \\ \vdots \\ \mu_{a2,m} \end{bmatrix}}_{\boldsymbol{\mu_{a2}} \text{ spectrum of species 2}} + \underbrace{\begin{bmatrix} \mu_{ap,1} \\ \mu_{ap,2} \\ \mu_{ap,3} \\ \vdots \\ \mu_{ap,m} \end{bmatrix}}_{\boldsymbol{\mu_{ap}} \text{ spectrum of particles}} = \begin{bmatrix} \mu_{a,11} \\ \mu_{a,21} \\ \mu_{a,31} \\ \vdots \\ \mu_{a,m1} \end{bmatrix} \tag{7.5}$$

and the rows of A can be expressed as (example is given only for the first row of **A**):

$$\begin{aligned} &\begin{bmatrix} c_{1,1} & c_{1,2} & c_{1,3} & \cdots & c_{1,k} \end{bmatrix} \cdot \sigma_{a1,1} \quad \begin{bmatrix} \mu_{a1,1} & \mu_{a1,2} & \mu_{a1,3} & \cdots & \mu_{a1,k} \end{bmatrix} \\ &\qquad\qquad + \qquad\qquad\qquad\qquad + \\ &\begin{bmatrix} c_{2,1} & c_{2,2} & c_{2,3} & \cdots & c_{2,k} \end{bmatrix} \cdot \sigma_{a2,1} = \begin{bmatrix} \mu_{a2,1} & \mu_{a2,2} & \mu_{a2,3} & \cdots & \mu_{a2,k} \end{bmatrix} = \begin{bmatrix} \mu_{a,11} & \mu_{a,12} & \mu_{a,13} & \cdots & \mu_{a,1k} \end{bmatrix} \\ &\qquad\qquad + \qquad\qquad\qquad\qquad + \\ &\begin{bmatrix} c_{p,1} & c_{p,2} & c_{p,3} & \cdots & c_{p,k} \end{bmatrix} \cdot K_{p,1} \quad \begin{bmatrix} \mu_{ap,1} & \mu_{ap,2} & \mu_{ap,3} & \cdots & \mu_{ap,k} \end{bmatrix} \end{aligned} \tag{7.6}$$

This in turn means that the number of independent columns or rows in **A** i.e. the rank of **A**, is equal to the number of independent columns in **S**.

If the particle size is not varying the matrix of μ_a spectra **A** obviously fulfils all linearity conditions, since the absorption cross-sections of particles are constants at given wavelengths, and so it is suitable for multivariate calibration. If R is varying the nature and the effect of the resulting nonlinearities depends not only on R and the range of its values, but also on the variables that are related to the absorption cross-section of particles i.e. the wavelength and the contrast between the refractive indices of particles and medium which in this case is represented by u. Generally, the closer the wavelengths which the measurements are taken at (i.e. the narrower the wavelength range) the closer the values of the aforementioned variables are. In the limit, where the values of these variables can be considered to be the same (in the given example the values of u and λ), all equations in (7.3), which represents measurements for a single sample, would have the same nonlinear μ_{ap} term, which would mean that all of them would basically represent the same function with just different linear coefficients. That is if we plotted μ_{ap} of two very close

wavelengths one against the other we should get a line, because they both vary with R in the same way. In such case, although there is a strong nonlinearity between μ_a and μ_{ap} the column space and the row space of **A** would still have the same dimension i.e. **A** would have the same rank. These types of nonlinearities are classified as univariate. For those species that are linear with μ_a (i.e. absorbing only species) univariate nonlinearities do not pose a problem since their concentrations (row vectors) can still be expressed as some linear combination of the row vectors of **A**. This implies that if the measurements are taken in the narrow wavelength range the effect of nonlinearities may be negligible and so the full correction may not be needed. However, the difference in nonlinear μ_{ap} term may become significant as the difference in wavelengths increases i.e. when the variables u and λ start to differ significantly. Consequently, the relationship between the variations in μ_{ap} with R at different wavelengths may not be linear any more. That is, it may not be possible to express the rows of **A** in terms of the same independent vectors. Which means, that the rows of the μ_a matrix **A** are not linearly related anymore and neither are the columns and so we are dealing with the multivariate type of nonlinearities. In this case, the dimensionality (i.e. the rank) of the matrix **A** increases because there are many more independent vectors (strictly speaking each row is an independent vector since it cannot be expressed in terms of the other rows) than just the number of chemical components. This leads to a higher number of latent variables needed to model the system using PLS. In principle, any other nonlinear function of R, λ and u could be used for modelling K for explaining the possible effects on the multivariate calibration.

To evaluate the impact of the absorption coefficient of particles, which varies nonlinearly with the particle size, on the calibration simulations using Mie code for mono-disperse particles were carried out. The refractive indices of the same four chemical components as those used in the experiments (water, deuterium oxide, ethanol and polystyrene particles) were taken for the model system, and the same wavelength range was used 1500-1880 nm. The concentrations of ethanol, polystyrene and deuterium oxide were varied from 0 to 0.1, from 0 to 0.2 and from 0 to 0.5 in fractions of mass respectively. The concentration of water was taken such that the closure condition was satisfied i.e. $c_w + c_{hw} + c_{eth} + c_{pst} = 1$. Two cases were simulated, in the first one the particle size was varied from 10 to 2000 nm whilst in the second from 50 to 100 nm. Particle sizes were randomly picked using a uniform random distribution. So, the first case represents a large variation in particle size (size parameter) whereas the second one a relatively small

variation in particle size. The concentration of ethanol was of interest. RMSECV statistics was drawn from 800 samples. The RMSECV curves of PLS calibration models built on the two μ_a datasets are compared in figure 7.2.

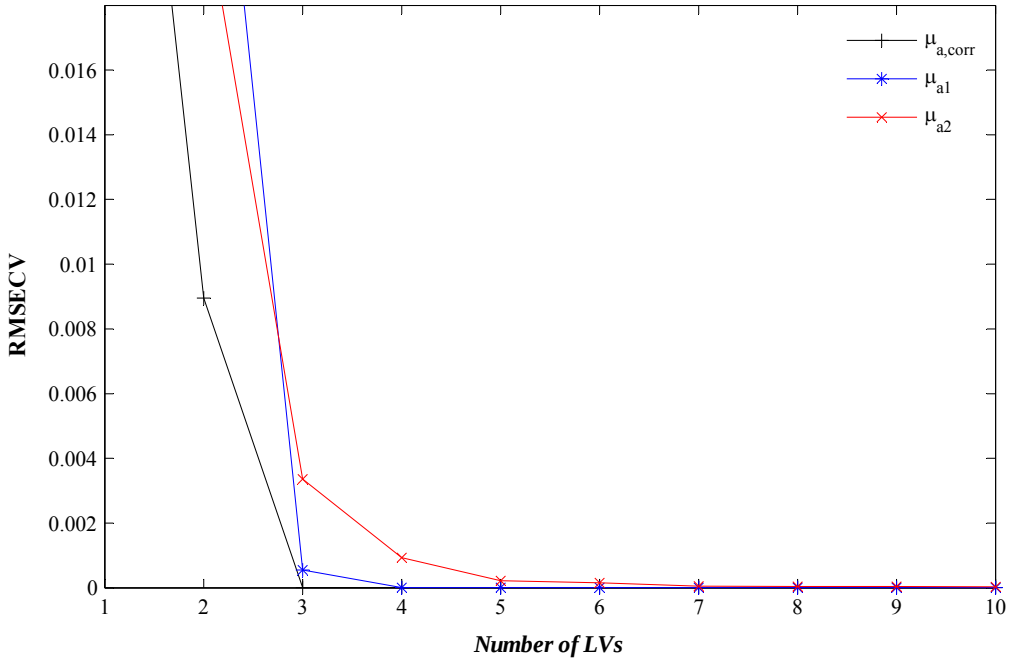

Figure 7.2. RMSECV curves of PLS calibration models built on μ_a where particle size varied from 50 to 100 nm (μ_{a1}) and from 10 to 2000 nm (μ_{a2}) and on $\mu_{a,corr}$ (corrected μ_a).

There is also the RMSECV curve of the corrected μ_a ($\mu_{a,corr}$) given in fig. 7.2, i.e. μ_a with μ_{ap} term removed. It represents the theoretical full correction, in which case, as one can expect, three latent variables explain 100 % of the variation in X and Y, since there are three independent concentrations (the fourth is completely correlated with those three due to the closure condition), and we have 100 % prediction accuracy. Note that since there is no noise in the simulated μ_a measurements the perfect accuracy should be achieved given a sufficient number of latent variables. As figure 7.2 shows, in the case when particle size varied little four components were needed to give a nearly perfect accuracy. This means that variation in R was successfully modelled by one latent variable which conforms to our implication that the nonlinear effect of R when the size parameter is varying little is close to univariate. When the particle size varies considerably the multivariate effect of nonlinearities is apparent as one can see from the figure. More than seven latent variables were required in this case to explain 100 % of variance in the concentration of ethanol i.e. to model the nonlinear effects of R. As a result, the rank of the matrix **A** increases as the multivariate nonlinear effects of μ_{ap} get stronger.

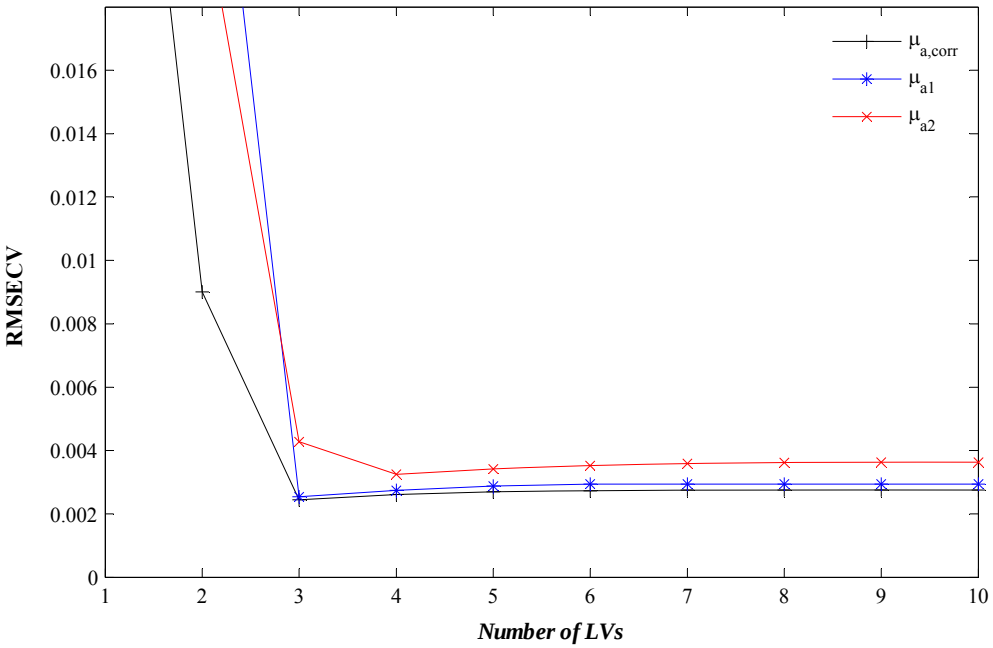

Figure 7.3. RMSECV curves when 1% noise was added to the μ_a datasets: μ_{a1} particle size varied from 50 to 100 nm, μ_{a2} from 10 to 2000 nm and $\mu_{a,corr}$ (corrected μ_a).

Figure 7.3 shows how this reflected on the prediction accuracy when some noise was added to the three datasets of μ_a. The performance of the PLS calibration model in the case of nearly univariate nonlinearities was close to the best possible theoretically i.e. the case of $\mu_{a,corr}$. The full correction of nonlinear effects in such case is not reasonable because the maximum possible improvement/gain in the prediction accuracy is not really significant whereas the complexity of the correction methodology and the time required doing it increases considerably. In this case, the partial correction only is reasonable. However, the performance of the PLS model in the case of more pronounced multivariate nonlinearities was notably worse i.e. lower accuracy with more LVs (four), in comparison with the theoretical performance that can be achieved if the nonlinear effects of μ_{ap} were completely removed from μ_a. In this case, full correction approach may be reasonable since the potential improvement in the prediction accuracy is significant.

As simulation shows the nonlinear multivariate effects of μ_{ap} on the bulk absorption coefficient can be reasonably strong when the size of particles is varying extensively. Consequently, this may have a significant negative impact on the calibration results in which case the full correction approach has a potential to improve them. It is worth noting that μ_{ap} can be even more nonlinear in the presence of particle interactions. To illustrate that the dataset taken from Thennadil's work [33], which was simulated with particle interactions taken into account by using PY-HS model, was used, see figure 7.4.

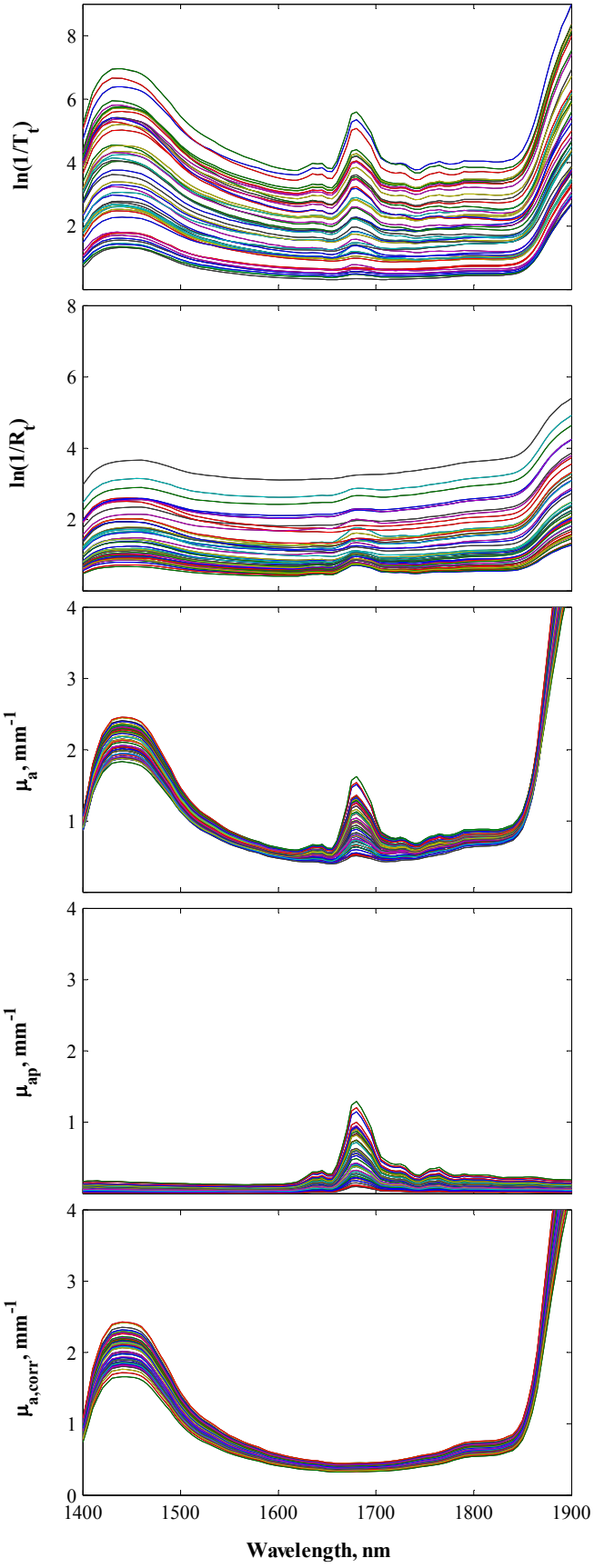

Figure 7.4. T_t, R_t, μ_a, absorption coefficient of particles $\mu_{a,p}$ and bulk absorption coefficient after correction $\mu_{a,corr}$ i.e. after subtraction of $\mu_{a,p}$.

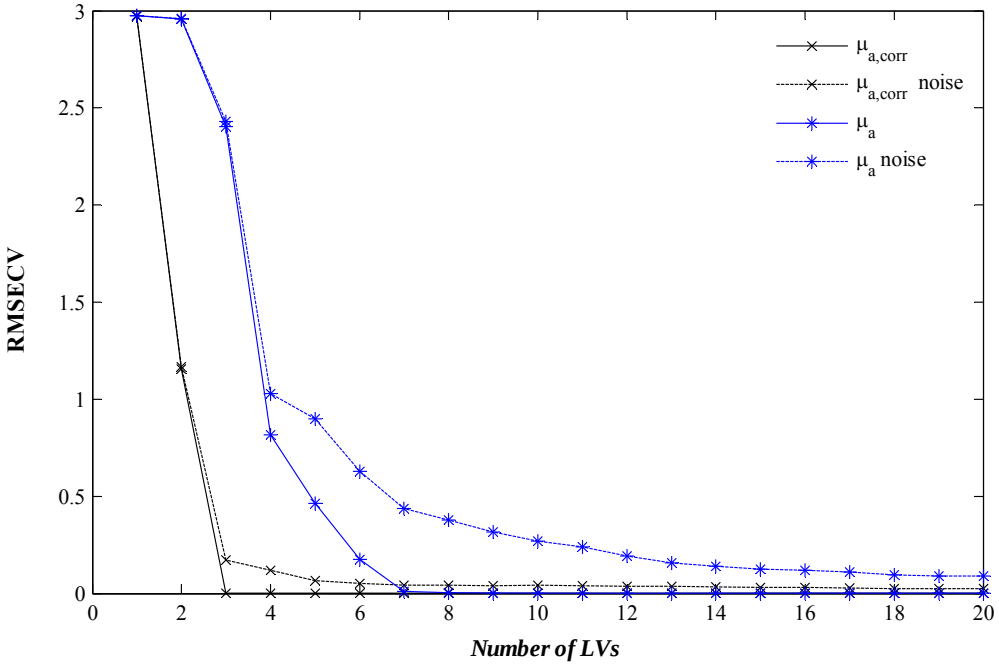

Figure 7.5. RMSECV curves for μ_a and $\mu_{a,corr}$; solid line with noise, dashed line no noise.

Fig. 7.4 shows the simulated measurements, the extracted bulk absorption coefficient and how it is partitioned into the absorption coefficient of particles and the absorption of the absorbing only species which is $\mu_{a,corr}$. The RMSECV curves for corrected and uncorrected μ_a with and without noise are plotted in fig. 7.5. As one can see, the difference between the performance of PLS with μ_a and $\mu_{a,corr}$ is really significant in this case. Therefore, in such cases, application of full correction approaches is rational.

7.2. OBJECTIVE FUNCTION IN ESTIMATION OF PARTICLE SIZE DISTRIBUTION

As discussed in chapter 4 any of the three optical properties can be used in the objective function to invert Mie solution and acquire the values of the mean, the standard deviation and the concentration of particles that are needed for estimation of μ_{ap} and subsequent correction of μ_a. So there are seven possible combinations i.e. seven different objective functions. The choice of the objective function turns out to be important and it is the object of this chapter.

For a given system, the optical properties of particles μ_s, μ_{ap} and g are functions of wavelength only since the complex refractive indices and the size parameter are both wavelength dependent. The constants that parameterise these functions are the size and the concentration of particles. In the case of normal particle size distribution we have three constants: the mean (M_R) and the standard deviation (d_R) of particle radius distribution and

particle concentration c_p. Finding them is a nonlinear least squares fit problem, which is solved using nonlinear optimisation. Traditionally, values of the bulk scattering coefficient at multiple wavelengths have been used for the fitting eq. (4.1). Even in the absence of noise finding the actual solution may not be a trivial problem for nonlinear optimisation, especially when a narrow wavelength range is used for the fitting. To illustrate that, an example of μ_s surfaces at two different wavelengths for an arbitrary grid of mean and standard deviation values of the particle radius is given in figure 7.6.

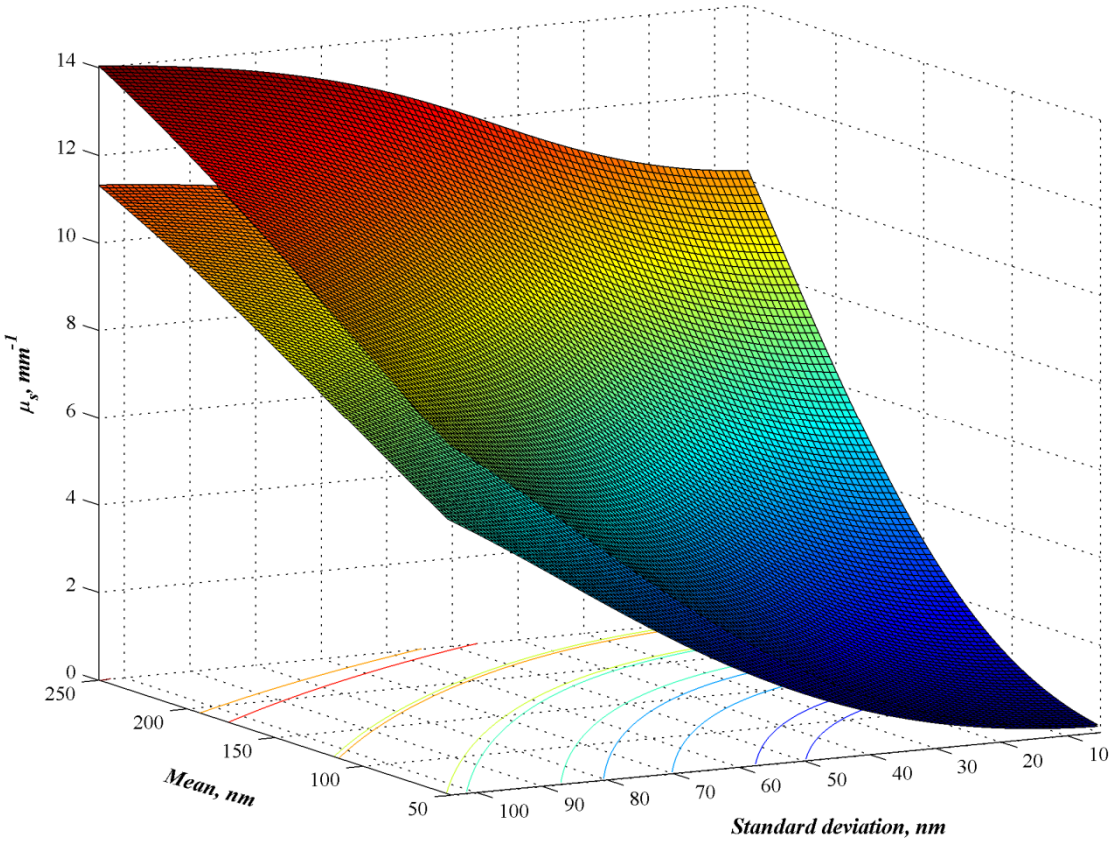

Figure 7.6. Two surfaces of μ_s at λ_1 = 1660 nm and at λ_2 = 1800 nm.

As one can see, the two surfaces and their isolines are quite similar/parallel. Solutions are where the isolines of the two surfaces cross. Figure 7.7 shows a pair of crossing isolines of two μ_s surfaces at neighbouring wavelengths i.e. the isoline of the surface of μ_s at 400 nm at the value of μ_s equal to 218.9 mm^{-1} and the isoline of the surface of μ_s at 401 nm at the value of μ_s equal to 217.9 mm^{-1} crossing at the value of the mean of the radius of the particles equal to 150 nm and the value of the standard deviation of the radius of the particles equal to 54 nm. Whilst, figure 7.8 shows a pair of crossing isolines of two μ_s surfaces at far apart wavelengths i.e. the isoline of the surface of μ_s at 400 nm at the value of μ_s equal to 218.9 mm^{-1} and the isoline of the surface of μ_s at 1800 nm at the value of μ_s

equal to 4.9 mm^{-1} crossing at the same values of the mean and standard deviation of the particle radius. As one can notice from these figures, the closer the wavelengths the more parallel the crossing isolines are, fig. 7.7, and vice versa, fig. 7.8. The more parallel the isolines are the harder it is for nonlinear optimisation to converge to the solution and the more sensitive it is to the errors in μ_s values. In the limit if λ_2 approached λ_1 the two surfaces and their isolines would merge into one and we would have an infinite number of solutions.

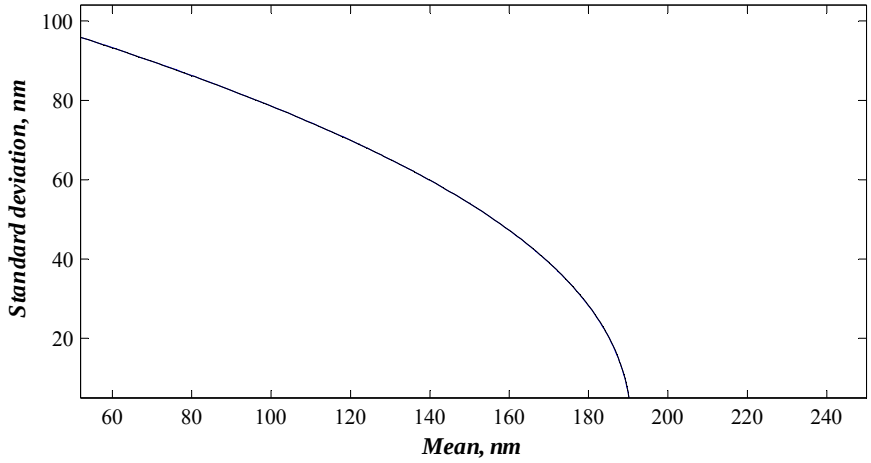

Figure 7.7. Two isolines of μ_s surfaces at neighbouring wavelengths λ = 400 nm (blue) and λ = 401 nm (black) which cross at the values of mean and standard deviation of particle radius 150 and 54 nm respectively.

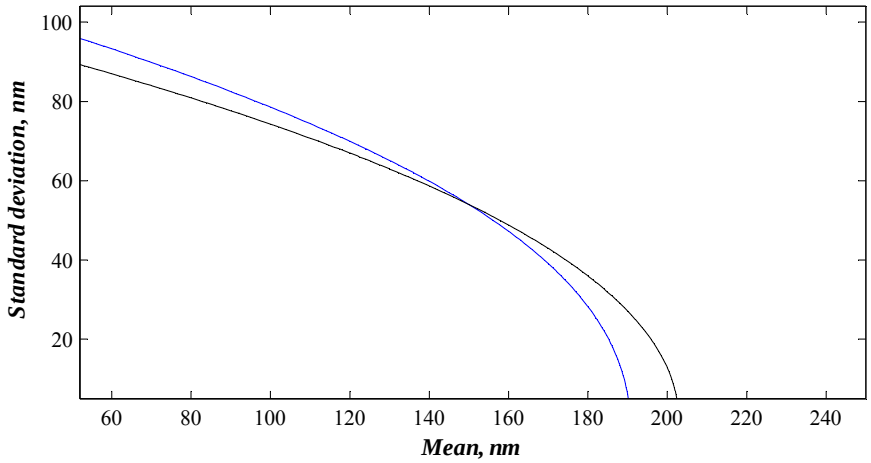

Figure 7.8. Two isolines of μ_s surfaces at far apart wavelengths λ = 400 nm (blue) and λ = 1800 nm (black) which cross at the values of mean and standard deviation of particle radius 150 and 54 nm respectively.

Solution search in nonlinear optimisation is based on the iterative steepest descent (i.e.

negative gradient) principle. Thus, in order to find it effectively we need to have a sufficient descent at any point in the field of the objective function (i.e. greater than the round off errors of Mie code or optimisation tolerances) apart from the true minimum. Because the isolines of the scattering coefficients are very similar at close wavelengths when a narrow wavelength range is used we get a shallow valley in the objective function following those isolines, fig. 7.9.

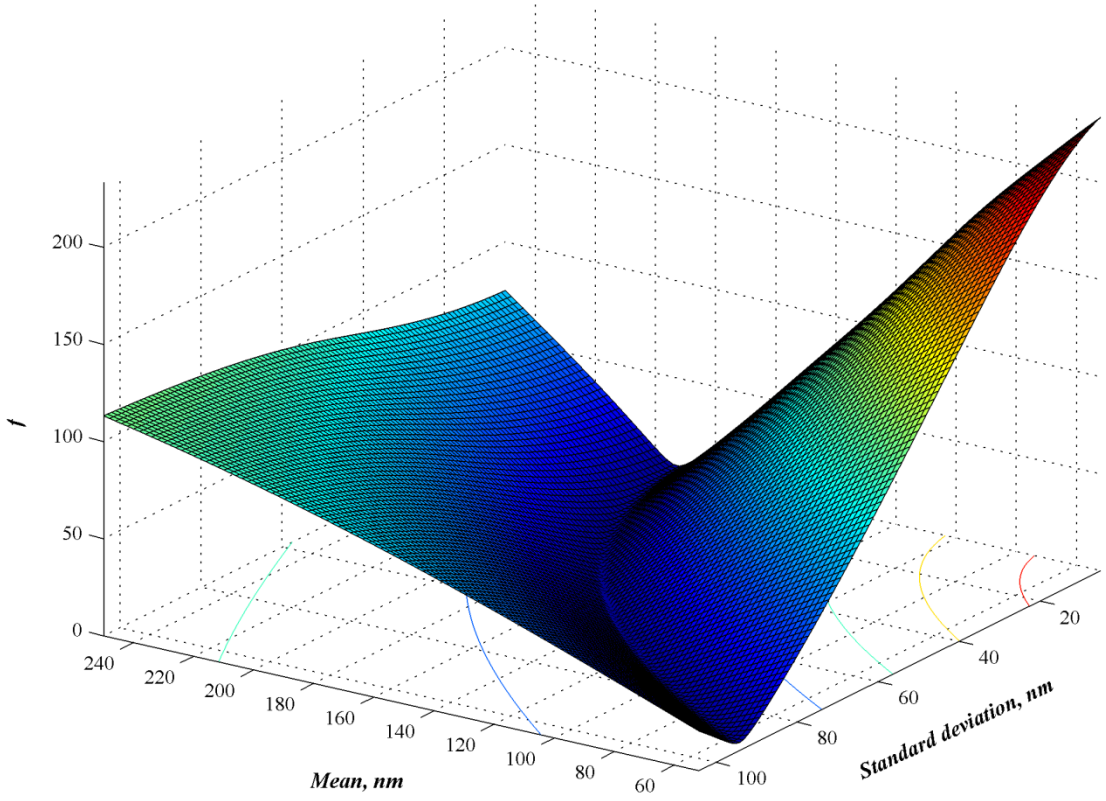

Figure 7.9. The objective function for μ_s in 400-1800 nm range (11 values at each 140 nm).

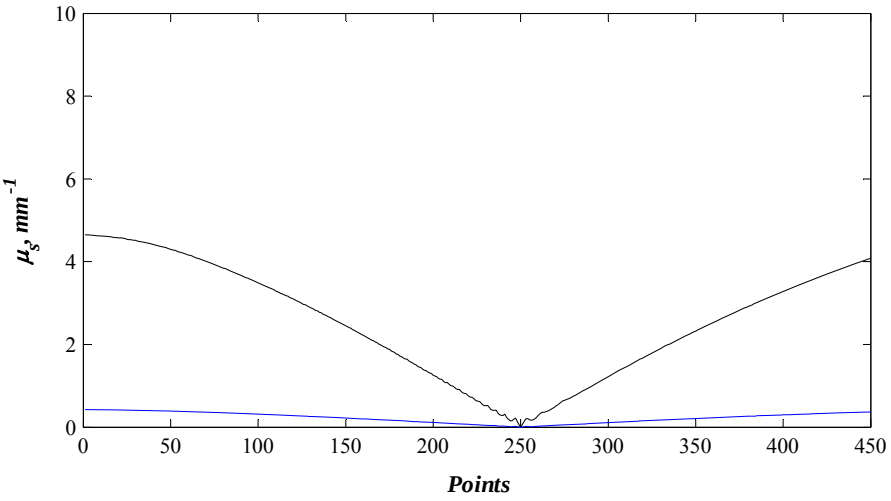

Figure 7.10. Change in objective function along the valley: (black) for μ_s in 400-1800 nm range and (blue) in 400-410 nm range (11 values of μ_s at 11 wavelengths in each case).

The negative gradient in that valley may become very small and therefore convergence may become an issue (similarly to the IAD case discussed in chapter 5). To illustrate the problem two cases are compared in figure 7.10, which depicts the change in the objective function along the valley. The black line marks the objective function formed from μ_s values at 11 wavelengths 140 nm apart (covering 400-1800 nm wavelength range). The blue line marks the objective function formed from 11 μ_s values too, but in this case values are taken at wavelengths only 1 nm apart (covering 400-410 nm wavelength range). As one can notice, the valley is much shallower in the second case therefore it might take more iterations to find the solution and it would be more sensitive to the error in μ_s. The sensitivity of the actual solution (i.e. its accuracy) to the error in the extracted μ_s values can be illustrated as follows:

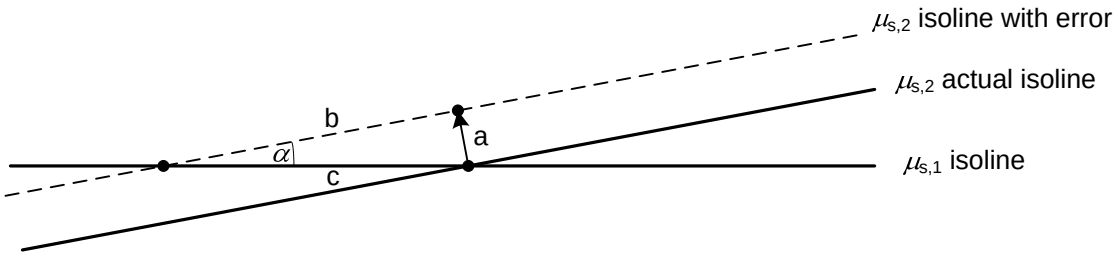

Figure 7.11. The influence of the error in μ_s on the accuracy of the solution.

According to the drawing in fig. 7.11, how much the solution will change with the error or in other words its sensitivity to the error can be simply calculated as:

$$c = \frac{a}{\sin(\alpha)} \tag{7.7}$$

As we can see from this equation, the sensitivity of the accuracy of PSD estimates (M_R and d_R) to the error in μ_s values is determined by the factor $1/\sin(\alpha)$. Thus, the smaller the angle (i.e. the more parallel the isolines are) the higher the sensitivity. This suggests that we should use a broader wavelength range in order to have quicker convergence and less sensitivity to the error. This is true irrespective of which optical property is used in the objective function.

In the ideal case (accurate values, no noise) it does not actually matter which objective function is used, nonlinear optimisation should give the same unique solution with all of them as long as the number of data points is greater than the number of unknowns (in our case three) and the wavelength range is not too narrow, since the descent would usually be sufficiently steep at any point in the field of any of these functions in this

case. However, in the presence of noise it does matter which objective function is used. To compare different objective functions simulations using Mie code for poly-disperse particles were carried out. Again, the refractive indices of the same four chemical components as those used in the experiments (water, deuterium oxide, ethanol and polystyrene particles) were taken to model the samples. The concentrations of ethanol, polystyrene and deuterium oxide were varied from 0 to 0.1, from 0 to 0.2 and from 0 to 0.5 in fractions of mass respectively. The concentration of water was taken such that the closure condition was satisfied i.e. $c_w + c_{hw} + c_{eth} + c_{pst} = 1$. The mean of the radii of particles was varied from 50 to 2000 nm and the standard deviation from 1 to 50 nm. The values of the mean and standard deviation were drawn randomly in the predefined ranges. The wavelength range used was 400-1880 nm. Figures 7.12, 7.13 and 7.14 show the objective functions for μ_s, g and μ_a respectively (a smaller grid of M_R and d_R values was used for the figures in order to get a good resolution). The actual solution was arbitrarily chosen at M_R = 518 nm and d_R = 30 nm, it is where the white ball is positioned.

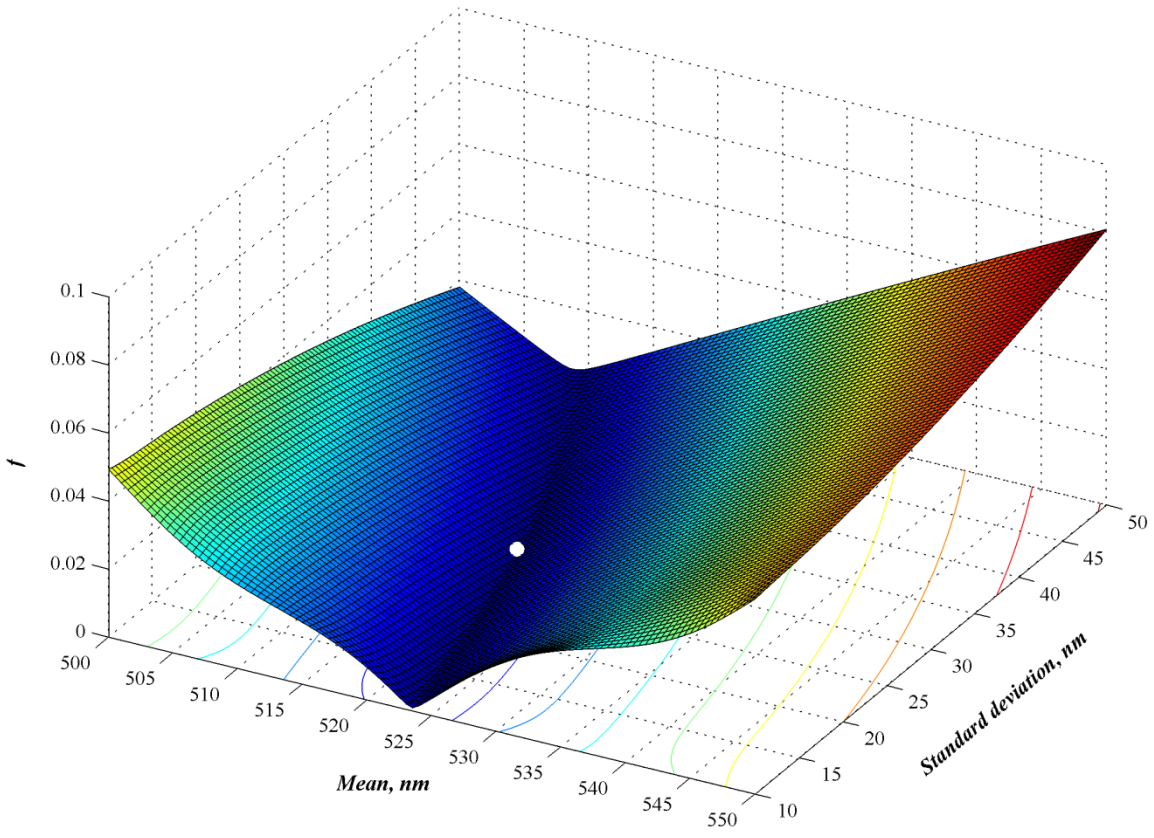

Figure 7.12. The surface of the objective function f based on fitting the values of μ_s for inversion of Mie solution.

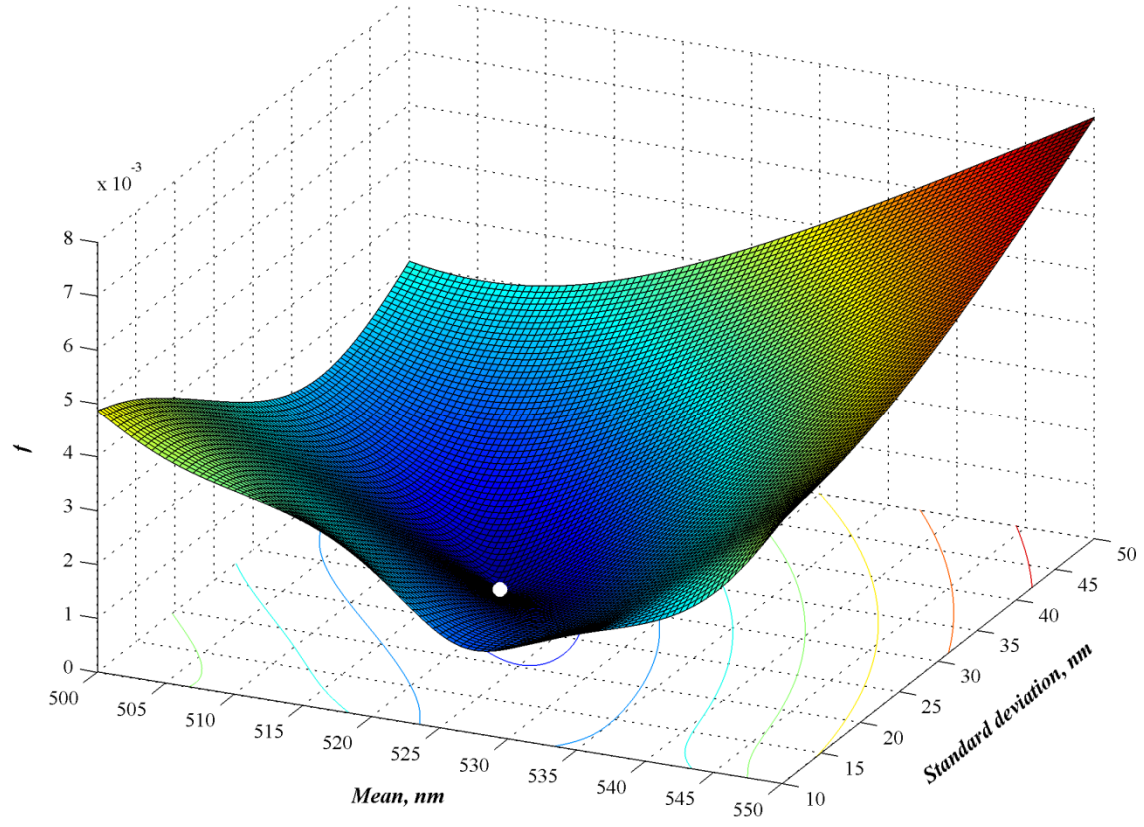

Figure 7.13. Surface of *f* based on fitting values of *g* for inversion of Mie solution.

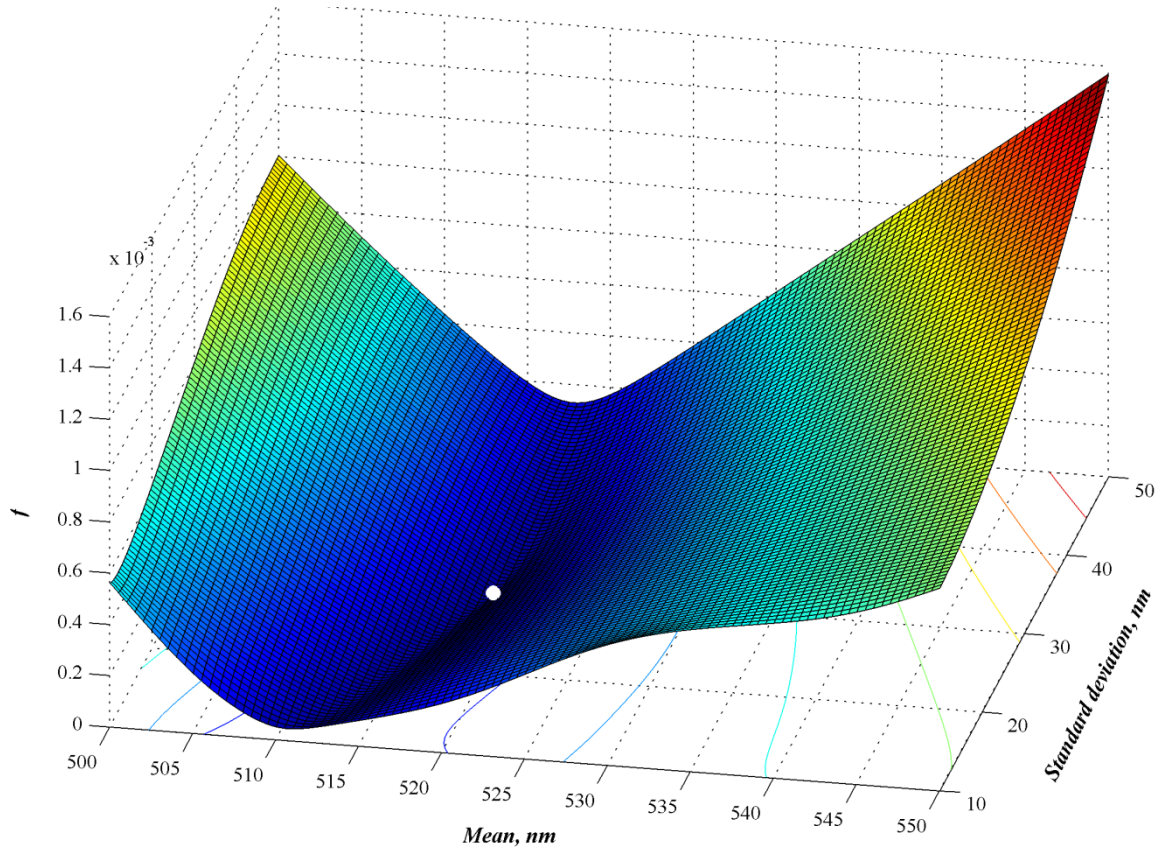

Figure 7.14. Surface of *f* based on fitting values of μ_a for inversion of Mie solution.

The global minimum is reasonably well defined for all three cases in the absence of noise, the best one being that of g in this particular case. However, noise smooths the fields of the objective functions making the gradient lower at every point in the field i.e. making them flatter, as one can see in figures 7.15, 7.16 and 7.17. The higher the noise the smoother the fields of the objective functions are and the more difficult it is to search for the global minimum. Then as in every least squares fitting problem, the confidence intervals for model parameters, in other words the accuracy of M_R, d_R and c_p estimates, depend on the number of data points fitted and the variance of the predictor variable i.e. the wavelength range, which is actually related to how well the global minimum is defined. The use of more than one optical property in the objective function addresses both factors: it increases the number of data points that have to be fitted by Mie model (twice if two optical properties are used and three times if all three of them are used) and it improves the definiteness of the global minimum. The two fold or three fold increase in the number of data points can give a significant improvement in the accuracy of M_R, d_R and c_p estimates. For instance, in the given simulation, the estimates of M_R and d_R obtained with different objective functions when noise was added were as follows in table 7.1.

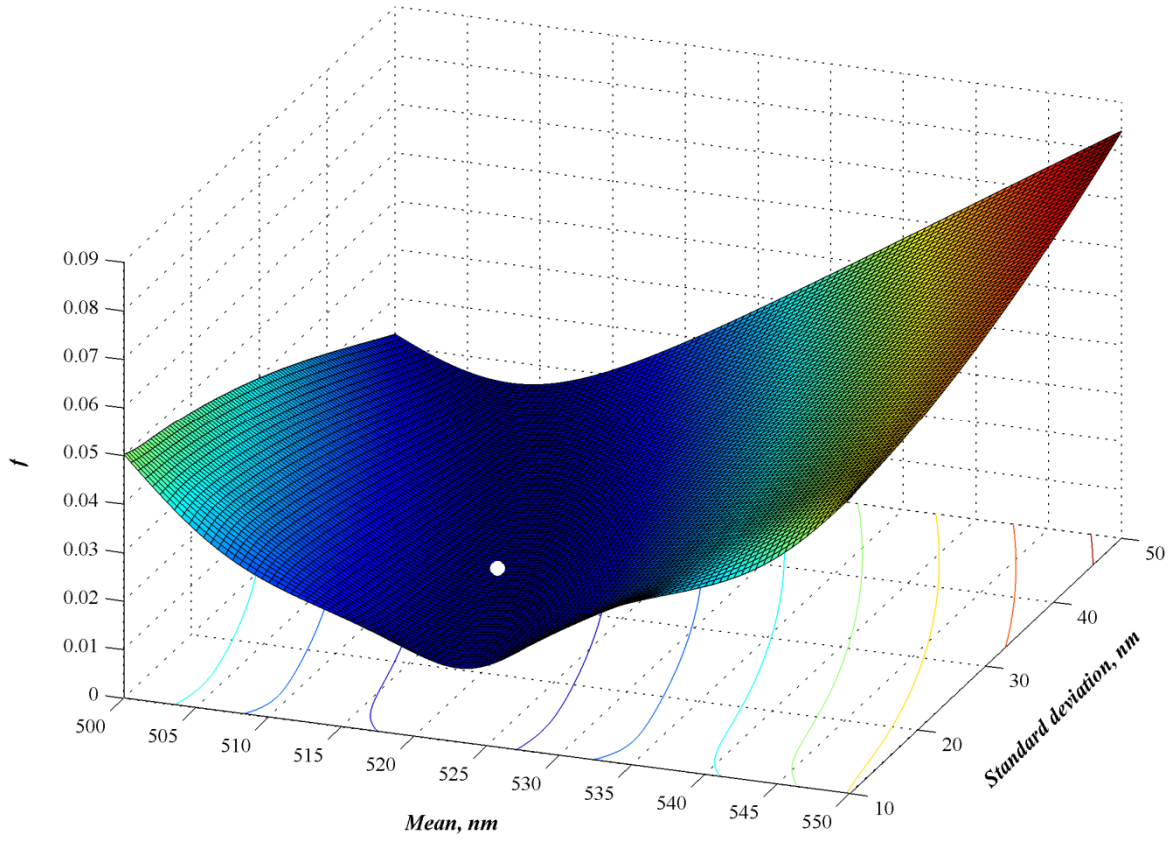

Figure 7.15. Surface of f based on fitting values of μ_s in the presence of noise.

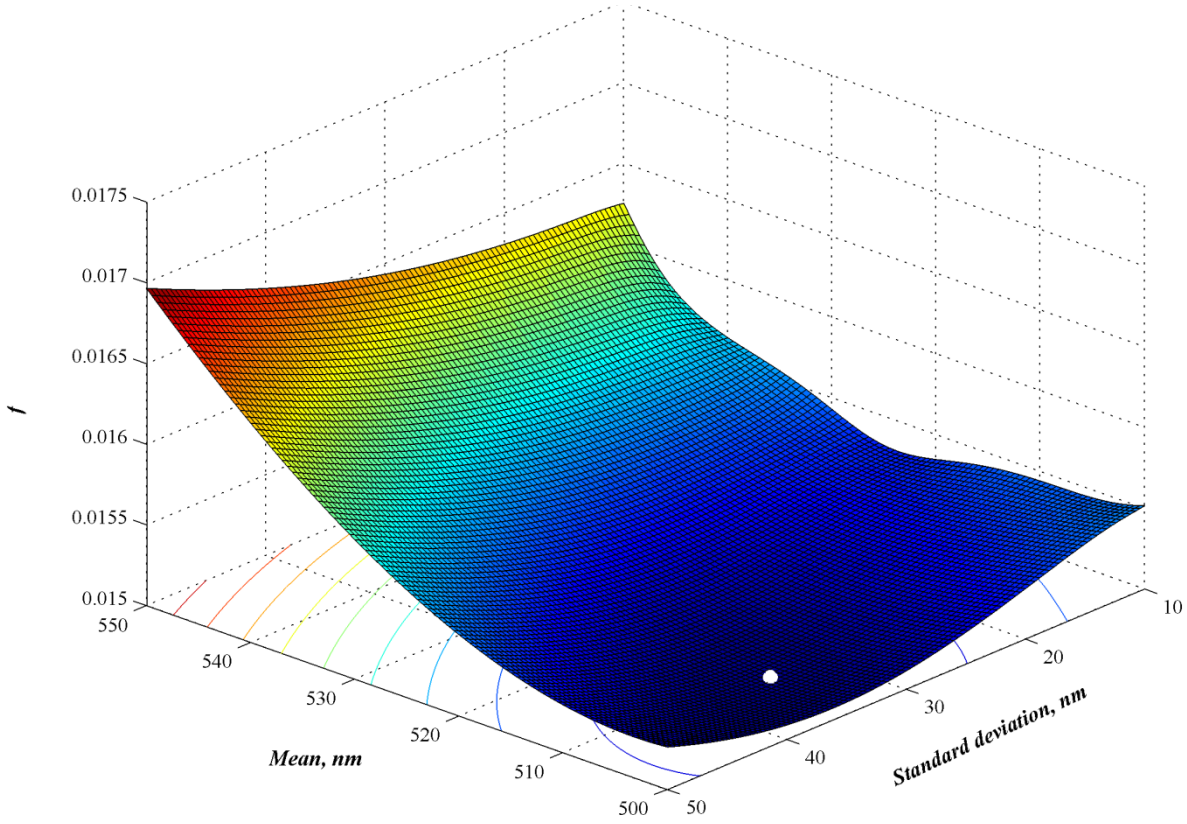

Figure 7.16. Surface of *f* based on fitting values of *g* in the presence of noise.

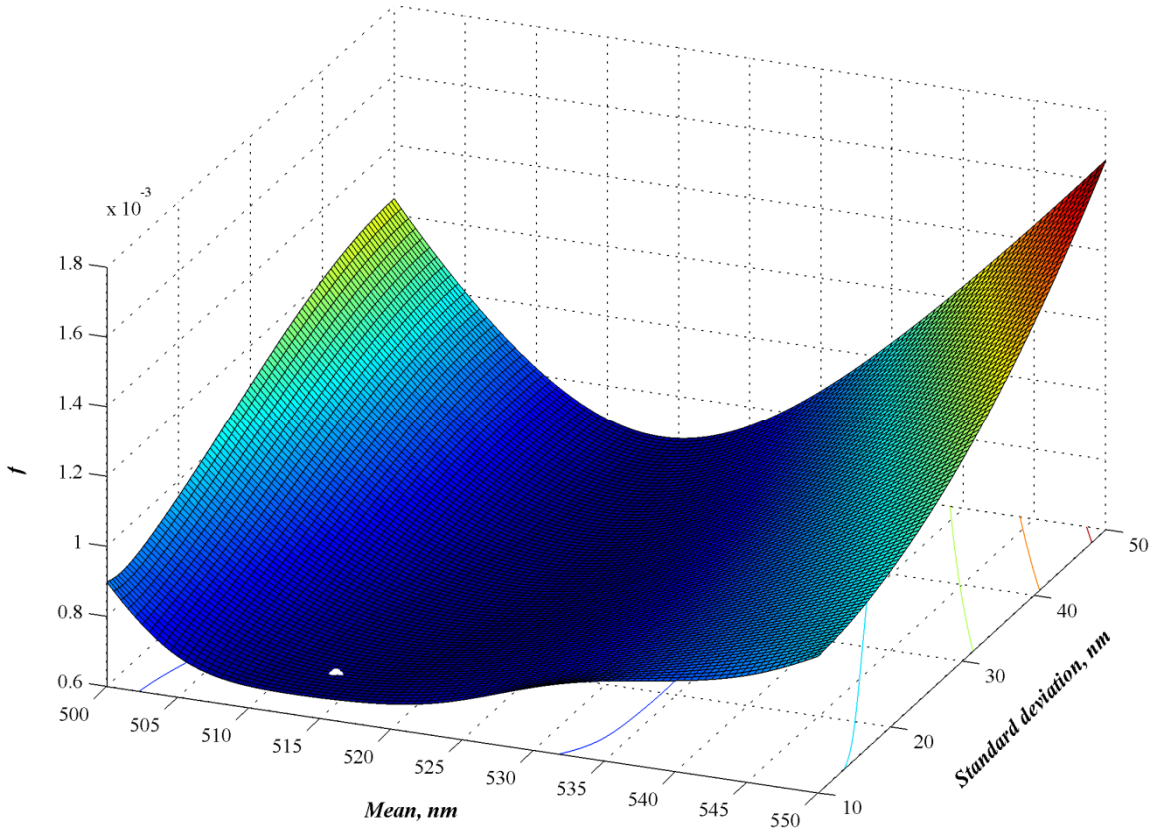

Figure 7.17. Surface of *f* based on fitting values of μ_a in the presence of noise.

Table 7.1. Estimates of mean and standard deviation of particle size distribution obtained using different objective functions

Objective function, f	M_R	d_R
$\sqrt{\sum(\mu_s - \hat{\mu}_s)^2}$	519	24.4
$\sqrt{\sum(g_s - \hat{g}_s)^2}$	508	34.4
$\sqrt{\sum(\mu_s - \hat{\mu}_s)^2} + \sqrt{\sum(g_s - \hat{g}_s)^2}$	517	30.8
Actual values	518	30

The objective function with two optical properties included gave better accuracy, as we would expect, since it is likely to obtain a more reliable estimate from more data points.

Apart from the advantage of having more data points the definiteness of the global minimum of the objective function with two or three optical properties may be better as well. As it can be seen from fig. 7.12-7.17 the fields of the objective functions of the three properties are tangibly different especially that of g in this particular case. Thus, the objective function combining all three optical properties is likely to have a better defined global minimum. The field of the combined objective function can also be altered by putting appropriate weights on each term in the eq. (4.9). In principal one could use the values of the three optical parameters at one wavelength to find the solution like in IAD. But, differently from IAD where the isolines of the surfaces of T_t and R_t are nearly perpendicular at any wavelength, the isolines of the surfaces of μ_s, g and μ_a in some wavelength ranges can be nearly parallel therefore the use of more wavelengths would be more appropriate in many practical situations. It was also noticed that the surfaces of μ_s and g are more distinct where the size parameter is varying around 1 i.e. where the particle size and the wavelength are comparable, e.g. in fig. 7.18 and 7.19 the surfaces of μ_s at 700 and 800 nm are shown (noise free). It can be seen that they are notably different. But, at longer wavelengths starting from around 800 nm they all get very similar to that given in fig. 7.19. This implies that the selection of wavelengths might be important as well. It is important to note that normalisation of μ_s and g to unit vectors not only brings them to the same scale but also transforms their surfaces. The effect of this transform requires a more detailed analysis. It is also worth noting that by normalising μ_s spectra to the unit length we basically make it independent from c_p, which means that the estimates of just mean and standard deviation could be obtained by using the normalised μ_s in the objective function.

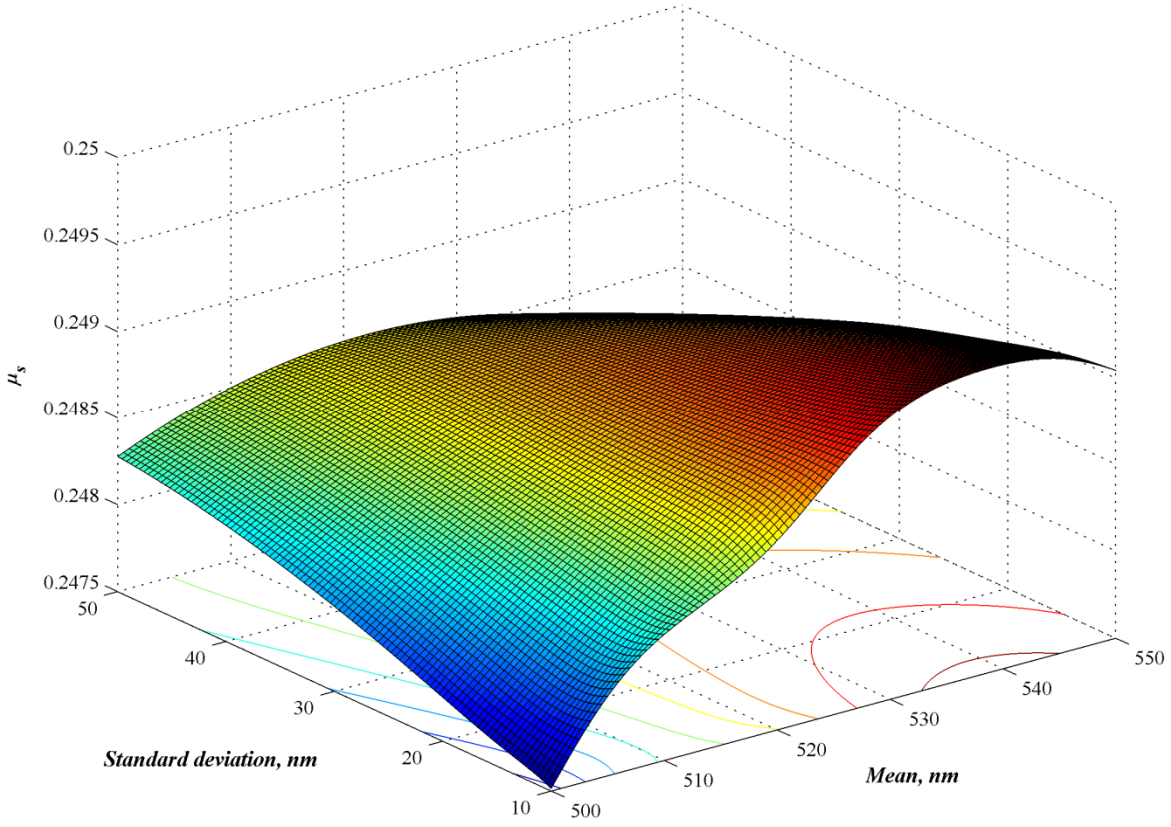

Figure 7.18. Surface of μ_s at 700 nm as a function of M_R and d_R.

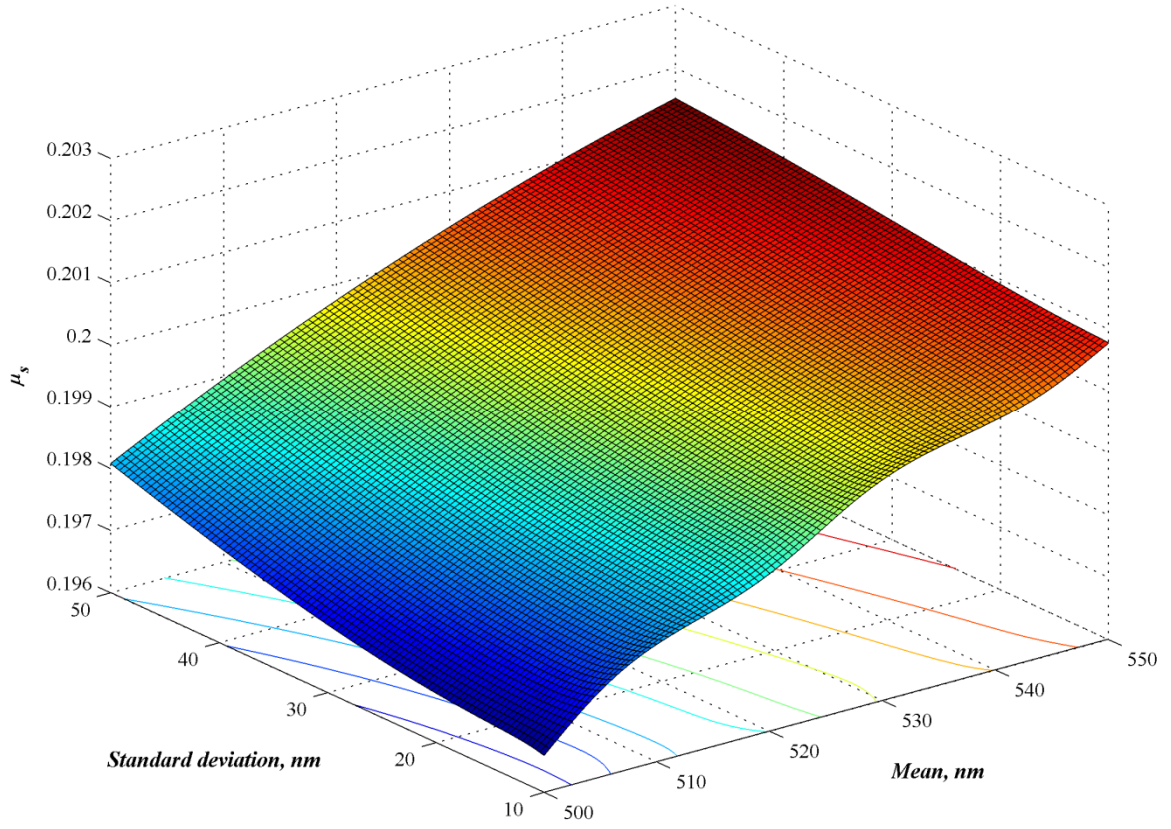

Figure 7.19. Surface of μ_s at 800 nm as a function of M_R and d_R.

This can also be done by using g, which is intrinsically independent from the concentration of particles, or μ_s and g, eq. (4.2).

It can be concluded that the use of all three optical properties i.e. maximum available information, in the inversion of Mie solution is likely to give us more accurate estimates of M_R, d_R and c_p and fewer iterations may be required to find them. Therefore the objective function given in eq. (4.9) was used in the full correction applications.

7.3. APPLICATION ON SIMULATED DATA

The full correction method was first applied on the simulated data generated in section 7.2 in order to test whether it improves the performance of the calibration model compared to the partial correction method in the presence of noise. The analysis in the section 7.1 suggests that the maximum possible improvement that one can get out of the full correction is usually relatively small in comparison with the improvement that can be obtained over the other pre-processing techniques when applying partial correction method. Therefore, the theoretical feasibility of getting any actual improvement is of interest.

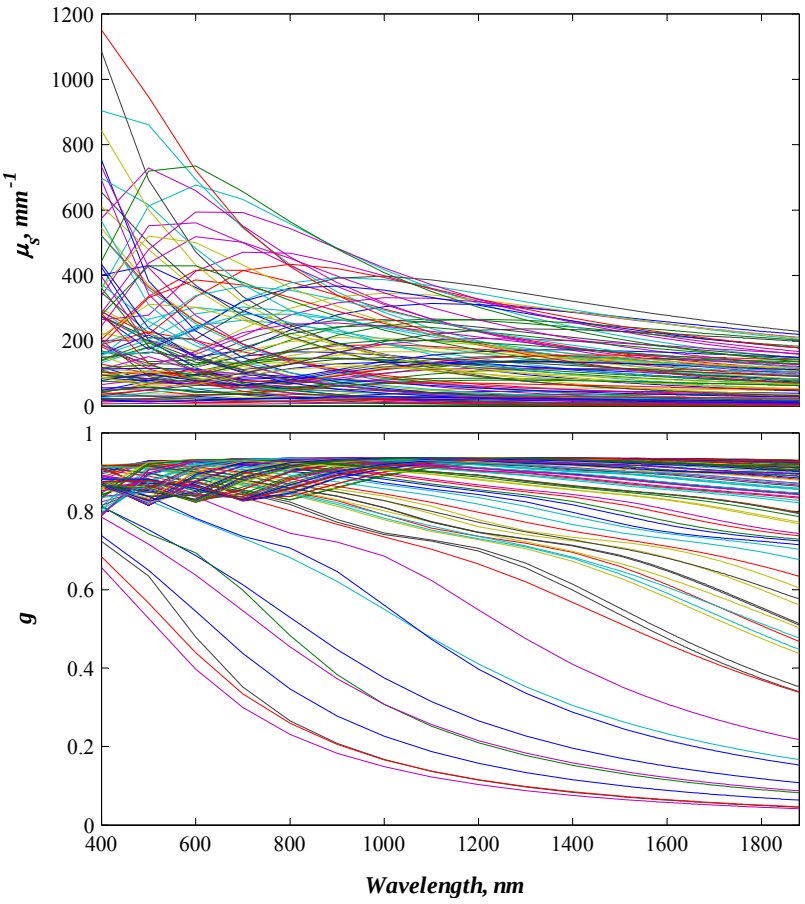

Figure 7.20. Simulated data for μ_s and g.

The simulated dataset closely resembles the four component experimental dataset only the size parameter and the concentration of particles vary more in the simulated dataset. The two optical properties (μ_s and g) related to scattering are shown in the figure 7.20. As one can notice the values of μ_s are very high due to high concentrations of particles and large size parameters. In real life to extract the optical properties from highly concentrated suspension using IAD we would have to either dilute it if we are to use T_t, R_t and T_c measurements or use alternative measurements such as diffuse reflectance at several angles. The bulk absorption coefficient and the bulk absorption coefficient corrected using the proposed methodology are shown in the figure 7.21 (only 1500-1880 nm wavelength range is shown in this figure, because the peaks of ethanol and polystyrene that we are interested in appear in this region). The peak in the absorption band 1650-1720 nm, which can be clearly seen in μ_a, is the nonlinearly varying peak of μ_{ap} i.e. polystyrene. As one can notice this peak disappeared in $\mu_{a,corr}$ i.e. it has been removed in the full correction step.

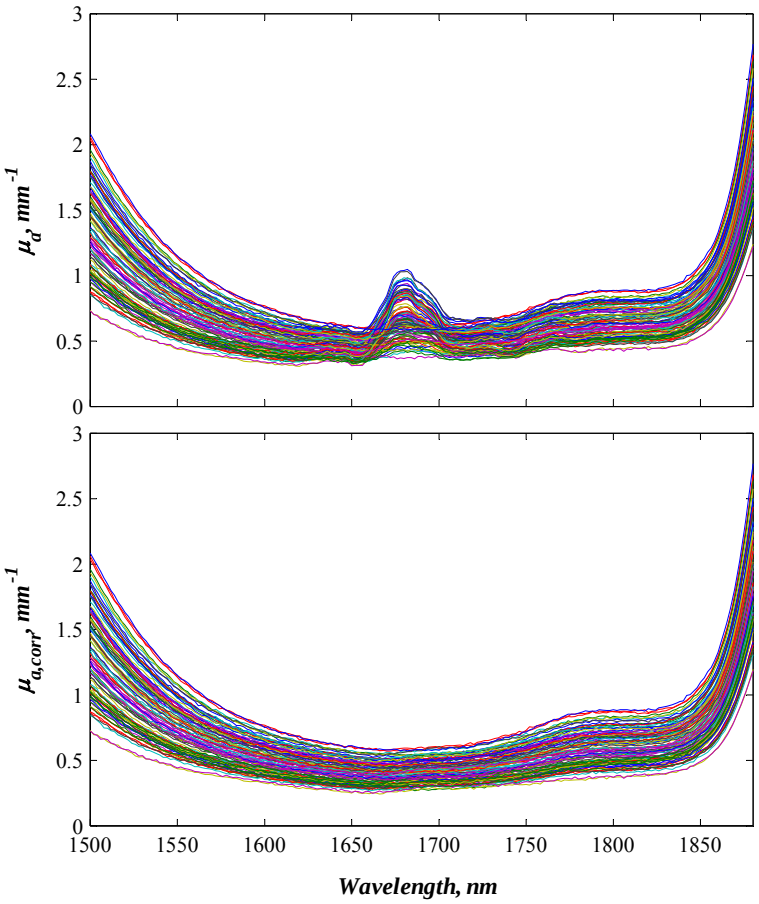

Figure 7.21. Uncorrected and corrected bulk absorption coefficients (simulation).

The projection matrix required for acquisition of μ_{ap} estimates and subsequent correction of μ_a was made out of the pure components in this case, for details see chapter 4.2.

The dataset comprising 400 samples in total was divided into the training set and the validation set. The training dataset was used for building the PLS calibration model whilst the validation dataset was used for obtaining the unbiased statistics of the accuracy of the predictions of ethanol concentrations i.e. root mean square error of prediction (RMSEP). Three calibration models were compared: PLS model built on μ_a, PLS model built on the estimated corrected bulk absorption coefficient $\hat{\mu}_{a,corr}$ (which was extracted using the proposed methodology) and PLS model built on the actual corrected bulk absorption coefficient $\mu_{a,corr}$. The leave-one-out cross validation method was used to obtain the RMSECV statistics. Their curves for all three cases are presented in figure 7.22. The cross validation results show that the performance of PLS calibration model built on $\hat{\mu}_{a,corr}$ is marginally better than the performance of PLS model built on uncorrected μ_a. Approximately the same RMSECV values were achieved with one less latent variable.

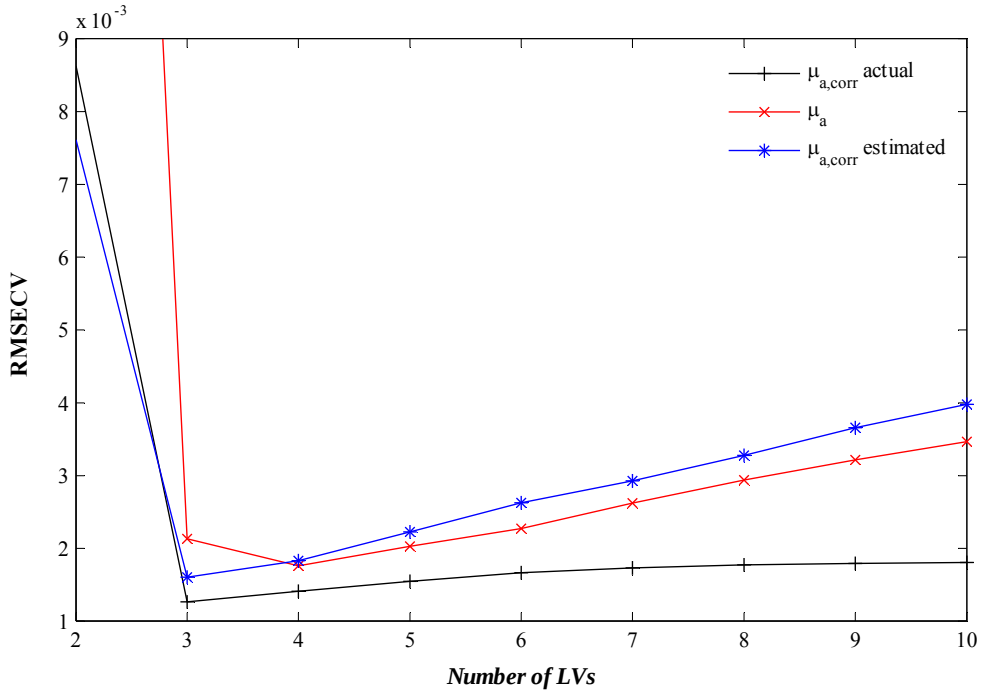

Figure 7.22. RMSECV curves for bulk absorption coefficients: not corrected μ_a, corrected theoretical (actual) $\mu_{a,corr}$ and corrected estimated (extracted) $\hat{\mu}_{a,corr}$.

The calculated RMSEP statistics, given in the table 7.2, confirmed the same. The conclusion can be drawn that some improvement can be achieved using full correction approach as long as the noise levels in the extracted optical properties are not high (the absolute error used in this case was generated using normal distribution with 0 mean and standard deviation of 0.005).

Table 7.2. Performance of calibration models for estimating the concentration of absorbing only species (i.e. ethanol) in the simulated data-set of the four-component system.

Predictions of concentration of absorbing only species (ethanol)				
Dataset which PLS was built on	Pre-processing	LVs	Calibration RMSECV (% vol.)	Test RMSEP (% vol.)
Calibration model built on μ_a	None	4	0.18	0.17
Calibration model built on $\hat{\mu}_{a,corr}$	None	3	0.17	0.17
Calibration model built on $\mu_{a,corr}$	None	3	0.13	0.12

It is interesting to note that if the peak of μ_{ap} happens not to overlap with the peaks of the component of interest, in this case ethanol, than we could just throw away the wavelength region where the nonlinearly varying μ_{ap} peak is, from the calibration. But, if they do overlap, as it is in this case, this approach is not adequate.

7.4. APPLICATION ON EXPERIMENTAL DATA

7.4.1. Acquisition of the projection matrix

The formation of the projection matrix is straightforward when the bulk absorption of a multi-component sample is a linear sum of absorption coefficients of all components. Whilst this is true for most of the liquid mixtures it is not true for every mixture as it is the case in our four-component experiment. This additive law does not hold if molecules of different species form some additional physical bonds between each other e.g. hydrogen bonds, due to attraction forces like electrostatic or Van der Waals. This causes new molecular vibration modes in the mixture [128, 129] therefore new absorption peaks appear in the NIR region that do not feature in spectra of pure components. As shown in section 6.2.2.3 we have a new peak in the spectra of the samples due to interaction between the molecules of water and deuterium oxide in the four-component experiment. In this case, the spectra of the mixtures cannot be modelled as some linear combination of the spectra of the pure species. That is the dimension of the column space of $\mathbf{A_p}$ (see section 4.1.2) consisting of spectra of different mixtures is higher than the number of pure species. In such case, Principal Component Analysis can be used to find the basis (i.e. principal axes) for the column space which is spanned by spectra of all possible mixtures of pure

species. The number of principal components that should be used to find the projection matrix can be determined from the cross validation.

The dataset consisting of spectra of mixtures of absorbing only species (water, deuterium oxide and ethanol) required for the Principal Component decomposition was collected from the samples prepared according to the same design of experiment given in the table 6.3 but without polystyrene particles. The absorption was measured using the collimated transmittance. The collected spectral data is shown in figure 7.23.

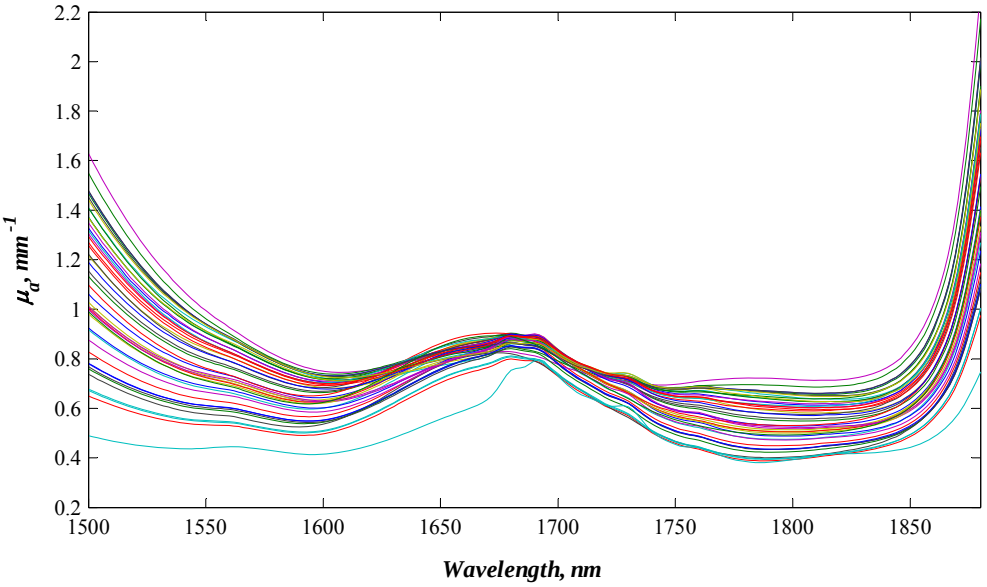

Figure 7.23. Absorption spectra of the set of non-scattering samples representing the same samples as in the four component experiment, but without the scattering component (i.e. polystyrene particles).

It actually represents the fully corrected bulk absorption coefficient $\mu_{a,corr}$ i.e. the best correction that can be achieved. This dataset should presumably give the best prediction performance, which will be presented in the following section. The cross-validation results are plotted in figure 7.24. Although a clear breakpoint is at four principal components the fifth PC still explains a fair part of variation in the measurement matrix and so it was included into the calculation of the projection matrix too. These principal components (eigenvectors) are shown in figure 7.25. One can recognise all peaks of pure chemical components there including the one occurring due to molecular interaction between water and deuterium oxide. Thus, any spectrum of a mixture of absorbing only species should be quite accurately modelled as some linear combination of these five principal components. The more accurate the correction of μ_a the less will be the error **e** given in eq. (4.8).

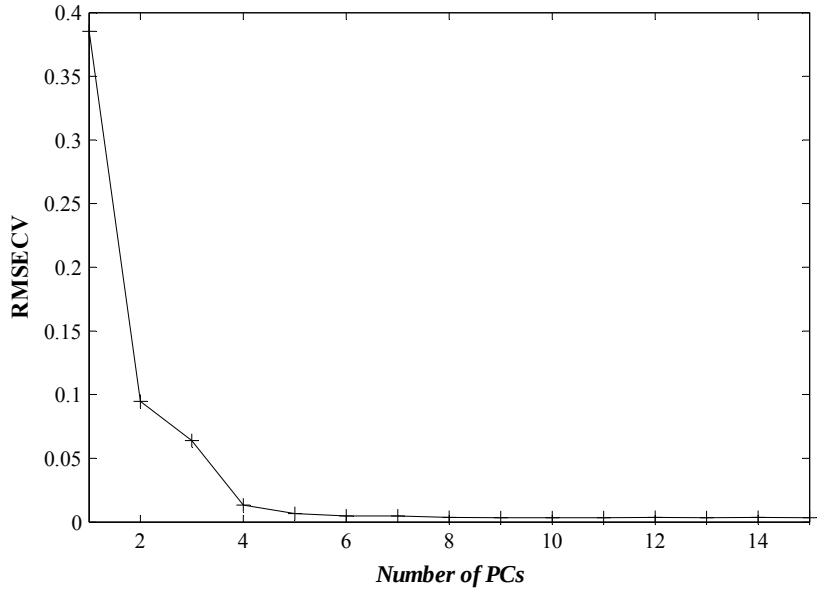

Figure 7.24. Cross-validation results for non-scattering dataset.

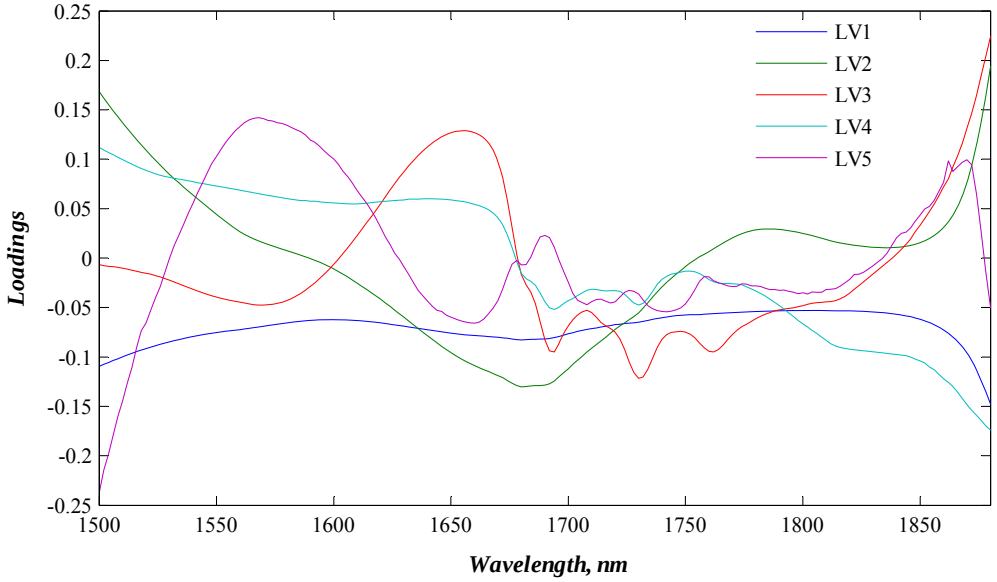

Figure 7.25. The loadings of the five principal components of the PCA model built on the non-scattering dataset.

7.4.1. Results and discussion

The developed full correction methodology was finally tested on the experimental dataset. The same dataset, comprising 45 four-component samples in total, was used for that. The raw measurements of total transmittance, total reflectance and collimated transmittance and the extracted optical properties of the samples have been given in appendixes A and B. Because the extracted values of anisotropy factor had a relatively large error/noise a smaller weight (0.8) was used for it in the objective function eq. (4.9),

whereas the weight for μ_a was increased (5) since its values were presumably most accurate i.e. least sensitive to the errors in the measurements.

The spectra of the estimated absorption coefficient of polystyrene particles obtained using the inverse Mie routine with the objective function (4.9) are illustrated in the figure 7.26. They were subtracted from the corresponding spectra of the bulk absorption coefficient of the samples to obtain the corrected spectra of μ_a for each sample.

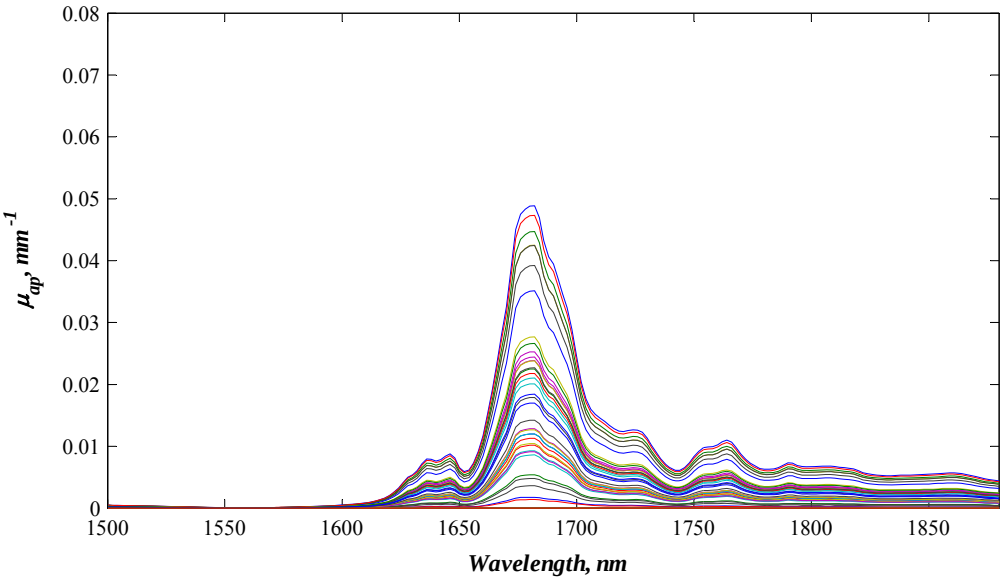

Figure 7.26. Spectra of estimated absorption coefficient of polystyrene particles.

The estimated values of the mean and the standard deviation of particle radius distribution and the concentration of particles and their actual values are compared in the figure 7.27. The mean diameter of polystyrene particles in the first nine samples is 100 nm, in the samples 10 to 18 – 200 nm, in the samples 19 to 27 – 300 nm, in the samples 28 to 35 – 430 nm and in the samples 36 to 45 – 500 nm. The green line is the actual value the blue line is the estimated value. To speed the inversion the initial guesses for the mean and the standard deviation were chosen close to the actual values of M_R and d_R, since the primary goal here is to see whether this approach is feasible. Further analysis should be done regarding the strategies for guessing initial values. As we can see from the figure, the estimated values of M_R match the actual ones well for 100, 200 and 300 nm particles (in diameter). But, nonlinear optimisation failed to converge to the solution for a number of samples with 500 nm particles. This is most probably due to the same reasons that are accountable for the mismatches seen in the comparison of the actual and simulated measurements and optical properties discussed in chapter 6, section 6.2.2.3.

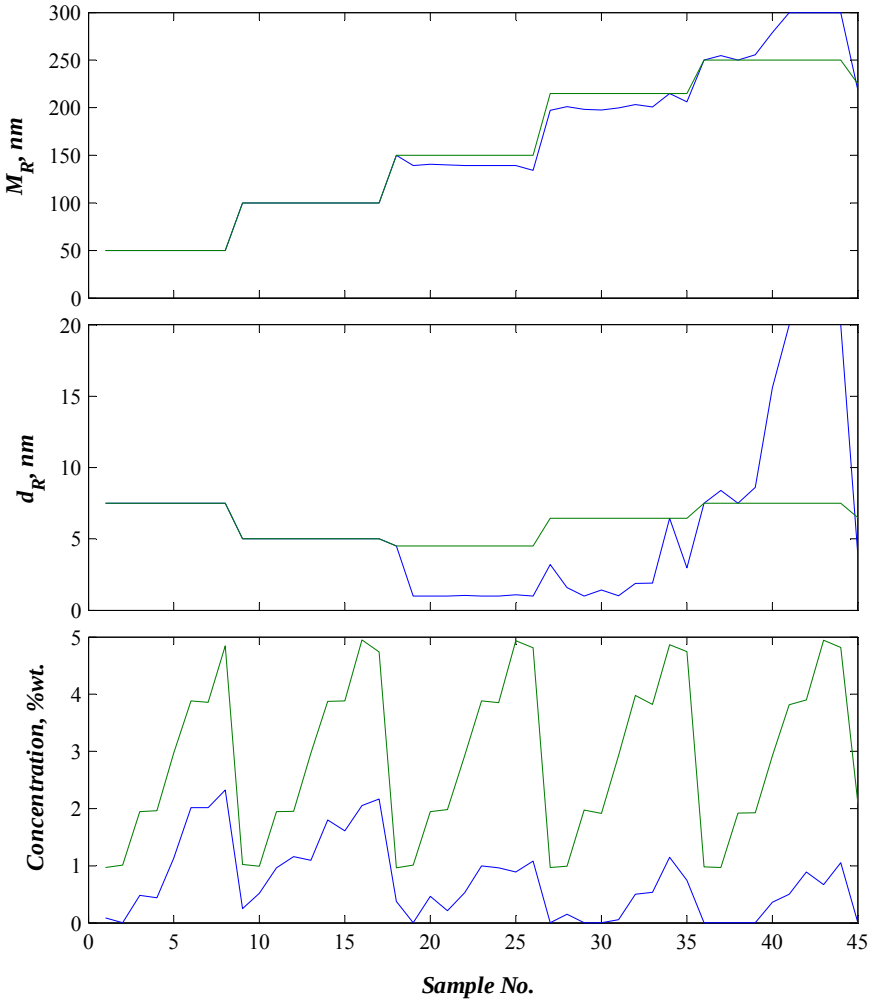

Figure 7.27. Comparison of actual (green) and extracted (blue) values of M_R, d_R and c_p.

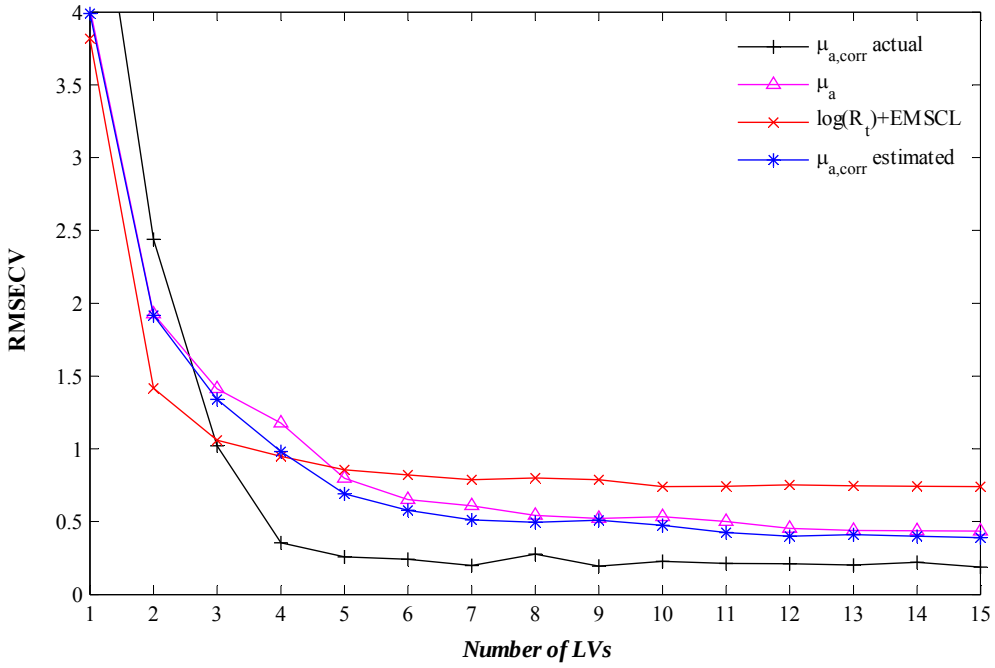

Figure 7.28. RMSECV curves for R_t, μ_a, $\mu_{a,corr}$ and $\hat{\mu}_{a,corr}$.

While the relative errors in the estimated values of the standard deviation are worse than the relative errors in the estimated means in terms of absolute errors they are similar. The notable difference i.e. offset, between the actual and the estimated concentrations of particles, which increases with the particle size, is probably due the light losses and particle interactions that are discussed in more detail in section 6.2.2. However, it is important to emphasise that the accuracy of the PSD and particle concentration estimates is not the primary goal here. The primary goal is to improve the accuracy of the predictions of the absorbing only species.

In this case, four calibration models were compared: PLS model built on the total reflectance pre-processed using EMSCL, PLS model built on μ_a, PLS model built on the corrected estimated bulk absorption coefficient $\hat{\mu}_{a,corr}$ (extracted using the proposed methodology of full correction of multiple scattering effects) and PLS model built on the actual corrected bulk absorption coefficient $\mu_{a,corr}$ which was obtained from the non-scattering dataset. The leave-one-out cross validation method was used to obtain the RMSECV statistics. RMSECV curves for all four cases are presented in figure 7.28. The cross validation results show that despite all errors the performance of PLS calibration model built on $\hat{\mu}_{a,corr}$ is again marginally better than the performance of PLS model built on uncorrected μ_a. The black line marks the best possible prediction performance which would be achieved if the full correction was perfect. The difference between the blue line and the black line represents the potential for further improvement of the full correction method. Cross validation results are summarised in table 7.3. It is important to note that the availability of accurate values of the complex refractive index of particles is crucial for the full correction of multiple scattering effects.

Table 7.3. Performance of calibration models for estimating the concentration of absorbing only species (i.e. ethanol) in the experimental data-set of the four-component system.

Dataset which PLS was built on	Pre-processing	LVs	RMSECV (% vol.)
R_t	EMSCL	7	0.79
μ_a	None	7	0.61
$\hat{\mu}_{a,corr}$	None	7	0.51
$\mu_{a,corr}$	None	5	0.26

CHAPTER VIII

CONCLUSIONS AND FUTURE WORK

1. The estimation of the concentration of a chemical species that (a) purely absorbs and (b) both absorbs and scatters light are two different types of problems from the point of view of multivariate calibration.
2. The following conclusions from the analysis of convergence conditions and optimisation error for IAD, when total transmittance, total reflectance and collimated transmittance are used to invert RTE, have been drawn:
   - There is always a unique global minimum in the objective function of the IAD. But, at high turbidity and low *albedo* we have a long valley with a very low gradient going through the actual minimum in the objective function. Thus, if the termination tolerances are not sufficiently low optimisation can terminate somewhere in the valley far from the actual solution giving us a large error.
   - Nonlinear optimisation may also have convergence issues, when searching for inverse adding-doubling solution using T_t, R_t and τ as inputs, if it hits $a = 0$ limit where the gradient of the objective function is also extremely small. Lowering termination tolerances can help to get rid of this problem, but this will not have an effect if termination tolerances get lower than the numerical accuracy/precision of the adding-doubling. Also, lower tolerances mean longer search time. Thus, in practical situations, one has to look for the optimum.
   - The error of optimisation varies with the values of a, τ and g, especially with the first two. The error becomes larger as the turbidity increases and *albedo* decreases. Therefore, it may be needed to adjust the termination tolerances accordingly in order to keep the optimisation error at the same level.
3. Simulation results indicated that applying the proposed methodology of partial correction of multiple scattering effects an appreciable improvement in the prediction performance can be obtained compared to applying empirical scatter correction techniques to single measurements. In the case of predicting scattering-absorbing species the RMSEP value obtained by using μ_a was more than 1.7 times lower than that obtained using the total reflectance and was achieved with half the number of latent variables. In the case of predicting absorbing only species the RMSEP value obtained by using μ_a was nearly three times lower than the best

result from the empirical pre-processing, which belonged to the total reflectance pre-processed with EMSCL followed by the first derivative, and was achieved with three latent variables less. Another interesting finding is that the accuracy of predictions drops with the increasing concentration of particles when it is being predicted. It is because although μ_a is free from nonlinear photon path length variations, it still has some intrinsic variation not related to the chemical information in cases when particles both scatter and absorb light.

4. The two-component experiment showed that the extraction algorithm using the RTE to obtain the bulk absorption spectra is successful in effectively removing path length variations and providing essentially a path length normalised absorption spectra. PLS model built on the extracted bulk absorption coefficient performed better than the one built on the empirically pre-processed total reflectance. However, it was outperformed by the calibration model built on the total transmittance, but only because the latter benefited from the correlation with water which is only possible with binary mixtures due to the closure condition. Whereas, the model built using μ_a was almost fully based on the actual polystyrene signal. Therefore, these results suggested that the models based on the direct measurements would lead to significantly larger errors when applied to a multi-component system where the secondary correlation will not exist. On the other hand, a model based on μ_a was expected to have less deterioration if at all when applied to multiple component systems provided the bulk absorption spectra could be extracted with similar levels of accuracy as in the two-component experiment.
5. According to the results from the four-component experiment for prediction of non-scattering species, PLS model built on μ_a gave the best accuracy RMSECV = 0.47 with the least number of latent variables 6 i.e. with the simplest calibration model. It is worth noting that the best performance on μ_a was achieved without pre-processing, which should be the case theoretically if bulk absorption is determined sufficiently accurately. Whilst applying EMSCL on the total reflectance and transmittance yielded an appreciable improvement in the performance of PLS model. An important result is that basically the same predicting performance was achieved with μ_a^w extracted using the refractive index of water as the refractive index of the medium for all samples. It can be conclude thus that fixing the real refractive index of the medium at a constant value in analogical situations should

not deteriorate the performance of the calibration model significantly.

6. As in the case with absorbing only species, the best predictive performance in estimation of the concentration of the scattering-absorbing species was achieved by PLS calibration model built on the extracted bulk absorption coefficient. However, in this case, it was achieved with one latent variable more i.e. 7 LVs.
7. Simulations showed that the nonlinear multivariate effects of μ_{ap} on the bulk absorption coefficient can be reasonably strong when the size of particles is varying extensively. Consequently, this may have a significant negative impact on the calibration results in which case the full correction approach has a potential to improve them. It is worth noting that μ_{ap} can be especially nonlinear in the presence of particle interactions.
8. The analysis of various forms of the objective function for estimation of particle size distribution (mean and standard deviation) through the inversion of Mie solution indicated that the use of all three optical properties i.e. maximum available information, in the inversion of Mie solution as proposed in the full correction methodology is likely to give more accurate estimates of mean, standard deviation and concentration of particles and fewer iterations may be required to find them.
9. The application of the proposed methodology of full correction of multiple scattering effects on the simulated data showed that the performance of PLS calibration model built on the corrected bulk absorption coefficient $\hat{\mu}_{a,corr}$ is marginally better than the performance of PLS model built on uncorrected μ_a. Approximately the same RMSECV values were achieved with one less latent variable. The calculated RMSEP statistics confirmed the same. Thus, results indicated that some improvement can be achieved using full correction approach as long as the noise levels in the extracted optical properties are not high (the absolute error used in this case was generated using normal distribution with 0 mean and standard deviation of 0.005).
10. The proposed full correction approach was finally tested on the four-component experimental dataset. Four calibration models were benchmarked: PLS model built on the total reflectance pre-processed using EMSCL, PLS model built on μ_a, PLS model built on the corrected estimated bulk absorption coefficient $\hat{\mu}_{a,corr}$ (extracted using the proposed methodology of full correction of multiple scattering effects) and PLS model built on the actual corrected bulk absorption coefficient $\mu_{a,corr}$

which was obtained from the non-scattering dataset. The cross validation results showed that despite all errors the performance of PLS calibration model built on $\hat{\mu}_{a,corr}$ was marginally better than the performance of PLS model built on uncorrected μ_a. Finally, the benchmarking analysis revealed that there is still a significant potential for an improvement in the prediction performance in the quantitative analysis of turbid samples.

Future work

The accurate measurement of the optical depth i.e. the transmitted unscattered part of the light, is a significant problem since with increasing turbidity of a sample the collimated transmittance gets quickly „contaminated" with the multiply scattered light. According to the results of this work, the mismatch between the optical depth estimated from the T_c measurement and the actual one becomes significant when the value of μ_s gets higher than approximately 2 mm^{-1} (see fig. A.3, A.6, A.9, A.12 and A.15). The error in the measured optical depth results in significant errors in the extracted optical properties or even in failure of IAD to converge to the solution. Therefore, it is important to investigate possible improvements of this measurement, e.g. employing polarization techniques, or the use of alternative measurements such as diffuse reflectance at different angles in the inversion of RTE.

At very low turbidity the error in the measured values of total transmittance and total reflectance may become significant due to light losses through the sides of a sample according to the results of this work. This loss cannot be accounted by the adding-doubling method therefore it is worth considering alternative methods for solving the radiative transfer equation that can account for that such as those based on Monte Carlo techniques.

It is also important to extend the proposed methodologies (or to develop new ones) to cases when the refractive index of the medium varies substantially. In the experiments carried out in this work the variation in the refractive index of the medium was relatively small and therefore fixing the refractive index did not have an adverse effect on the extraction and subsequently calibration results, but this may not be true in cases when the refractive index of the medium varies a lot.

APPENDIX A.

COMPARISON OF ACTUAL MEASUREMENTS WITH SIMULATED

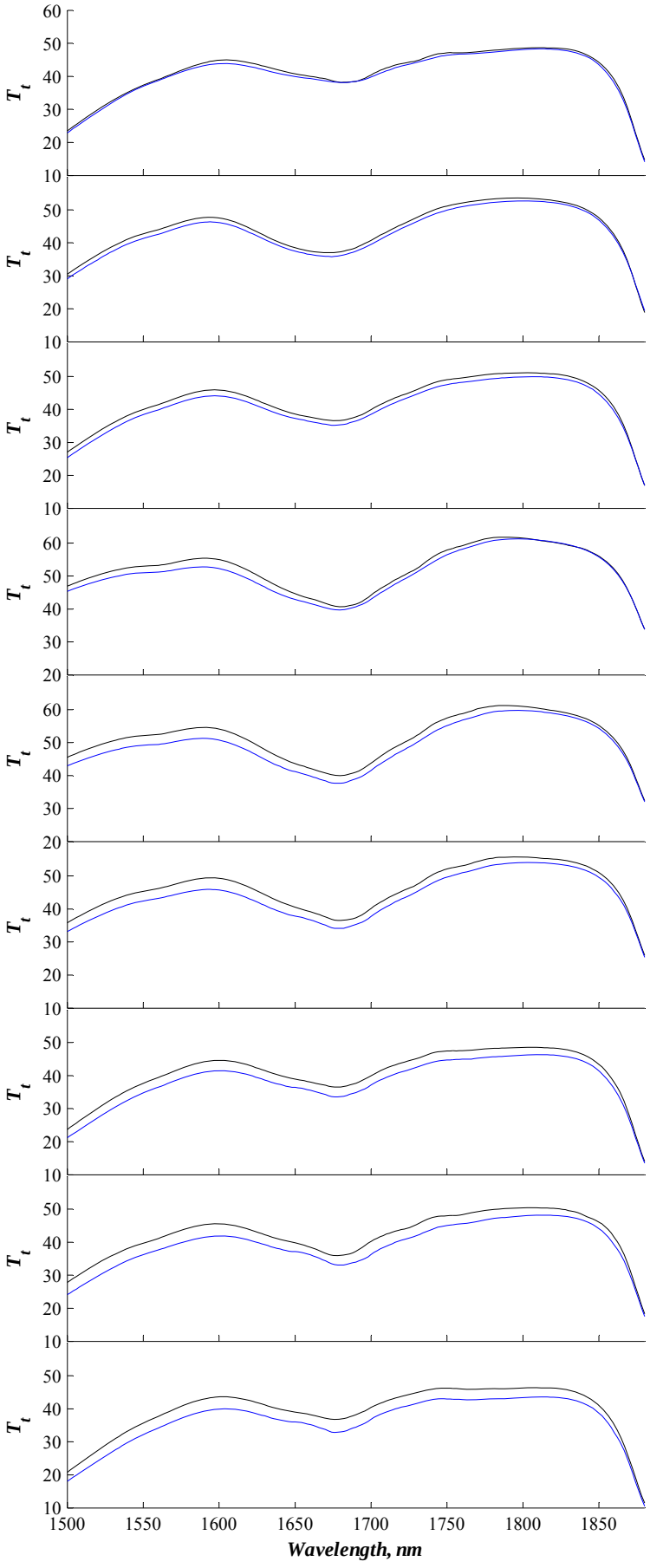

Figure A.1. Measured (black) and simulated (blue) spectra of T_t for particle size Ø 100 nm.

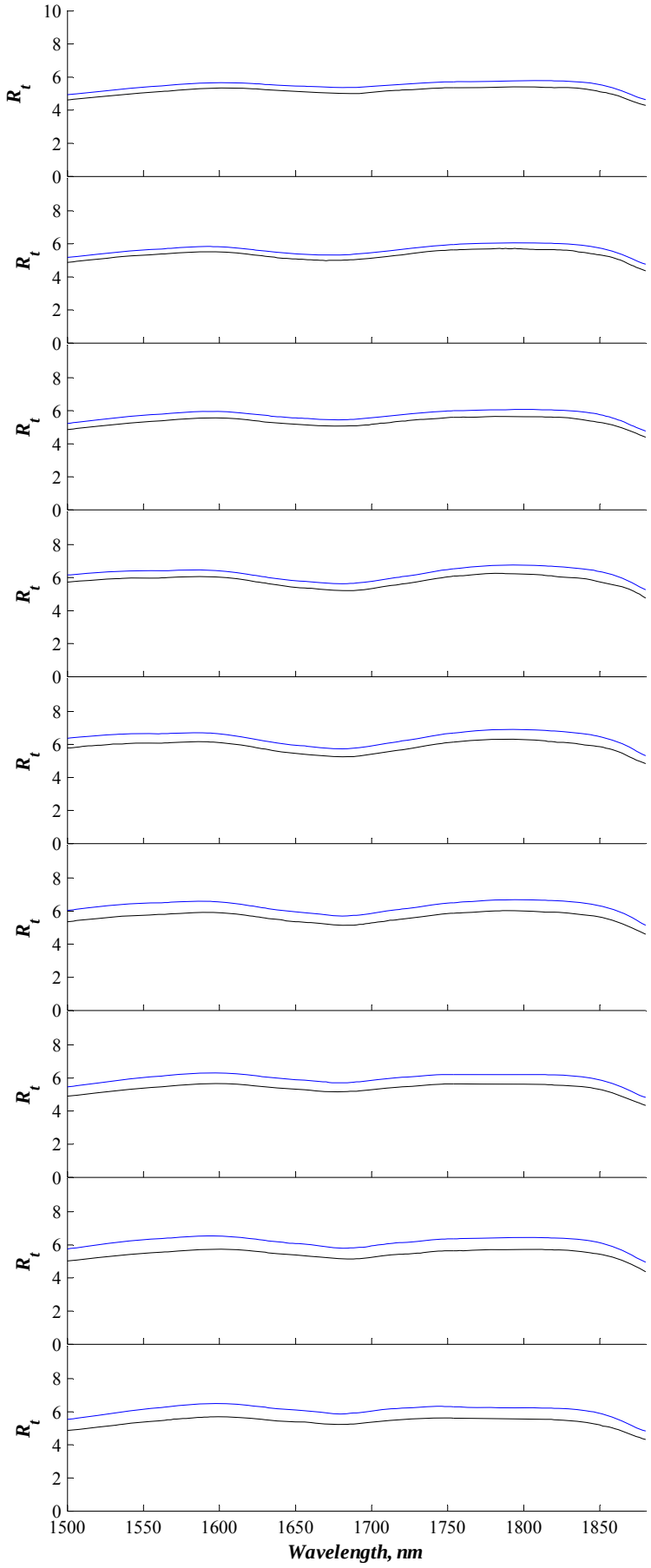

Figure A.2. Measured (black) and simulated (blue) spectra of R_t for particle size Ø 100 nm.

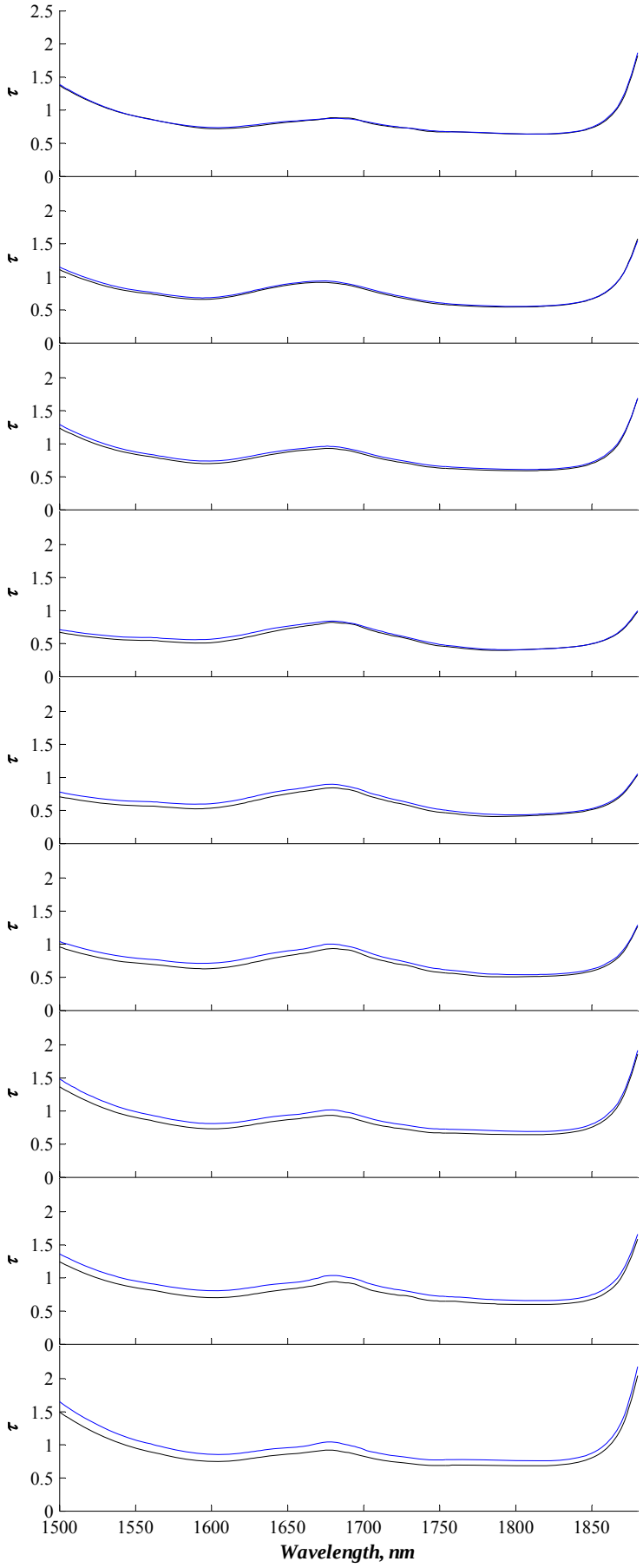

Figure A.3. Measured (black) and simulated (blue) spectra of τ for particle size Ø 100 nm.

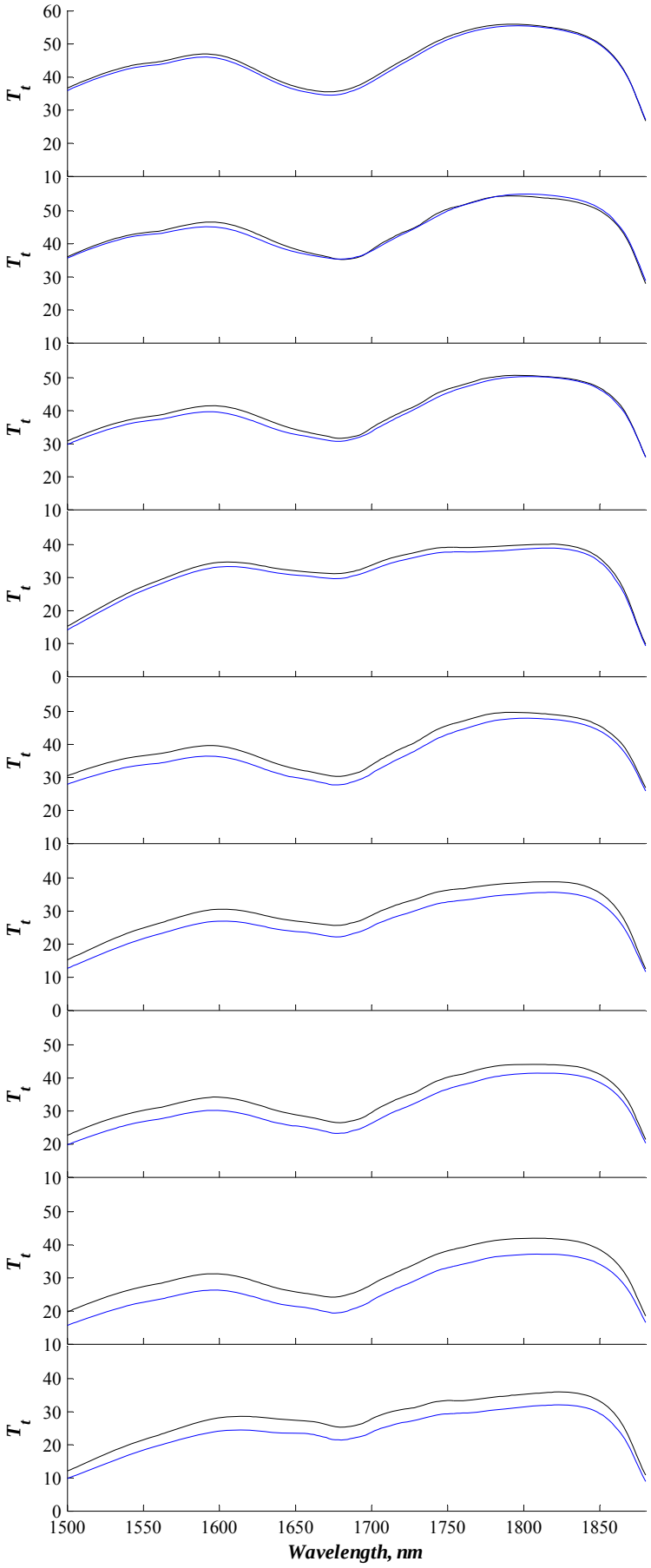

Figure A.4. Measured (black) and simulated (blue) spectra of T_t for particle size Ø 200 nm.

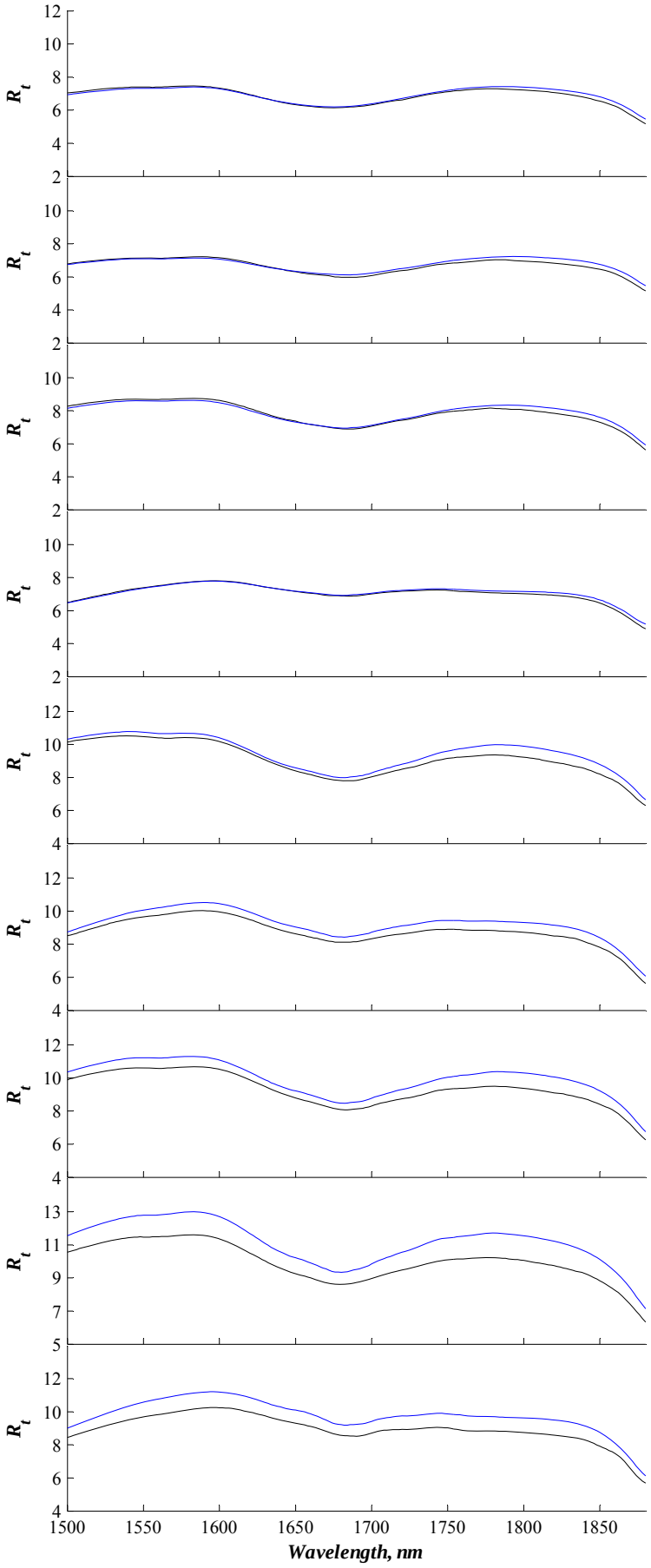

Figure A.5. Measured (black) and simulated (blue) spectra of R_t for particle size Ø 200 nm.

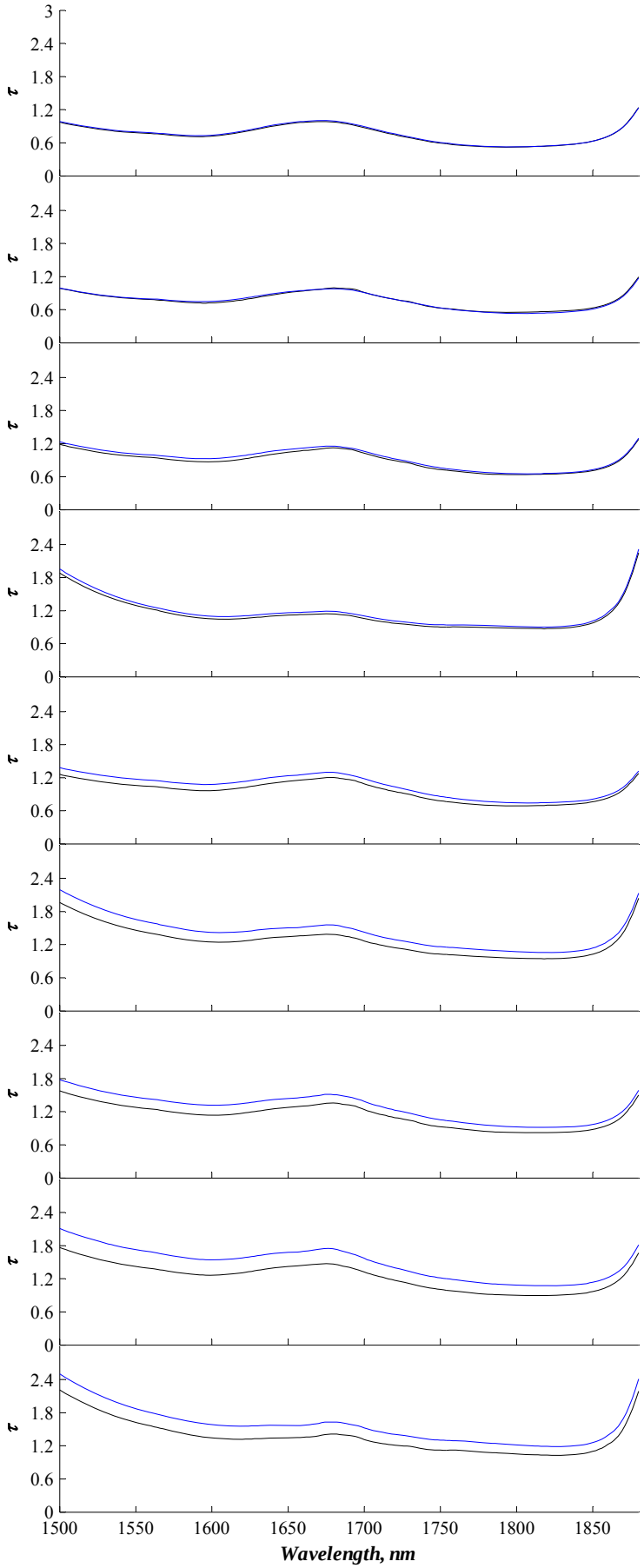

Figure A.6. Measured (black) and simulated (blue) spectra of τ for particle size Ø 200 nm.

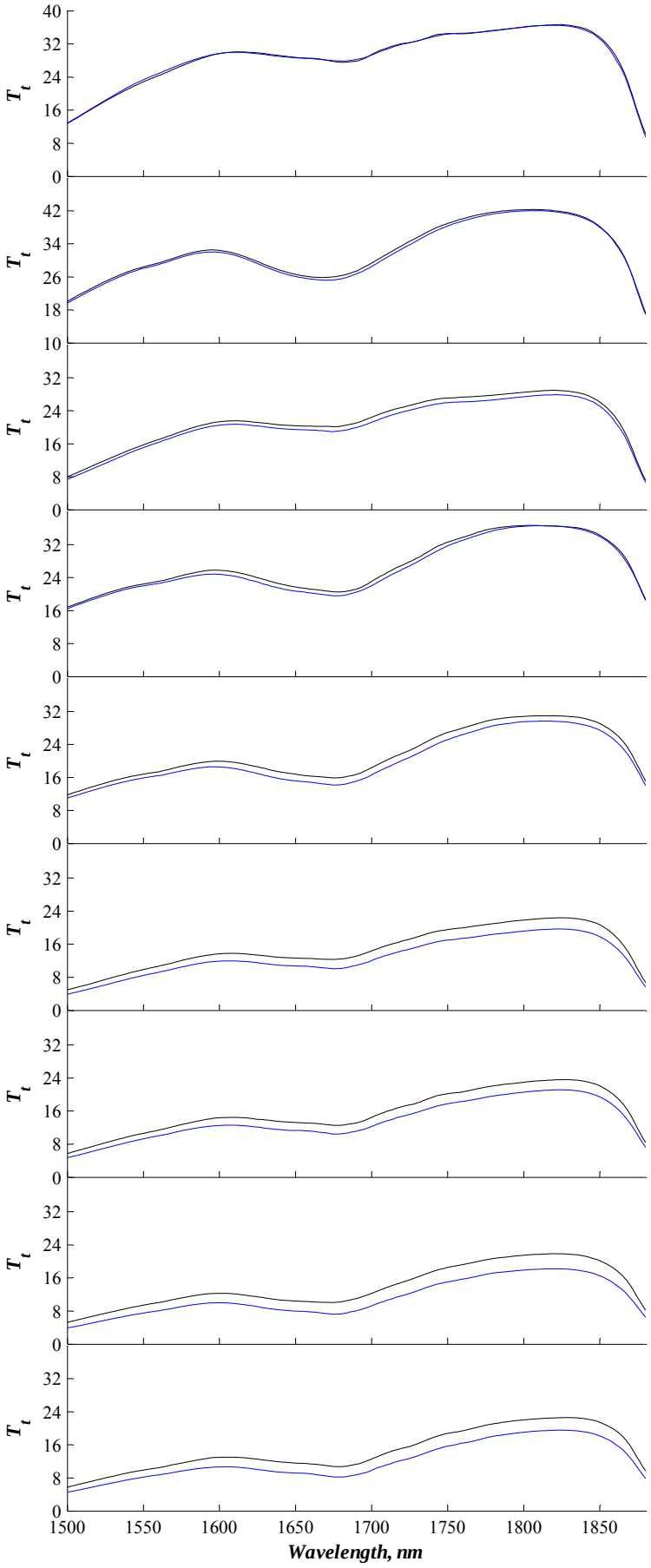

Figure A.7. Measured (black) and simulated (blue) spectra of T_t for particle size Ø 300 nm.

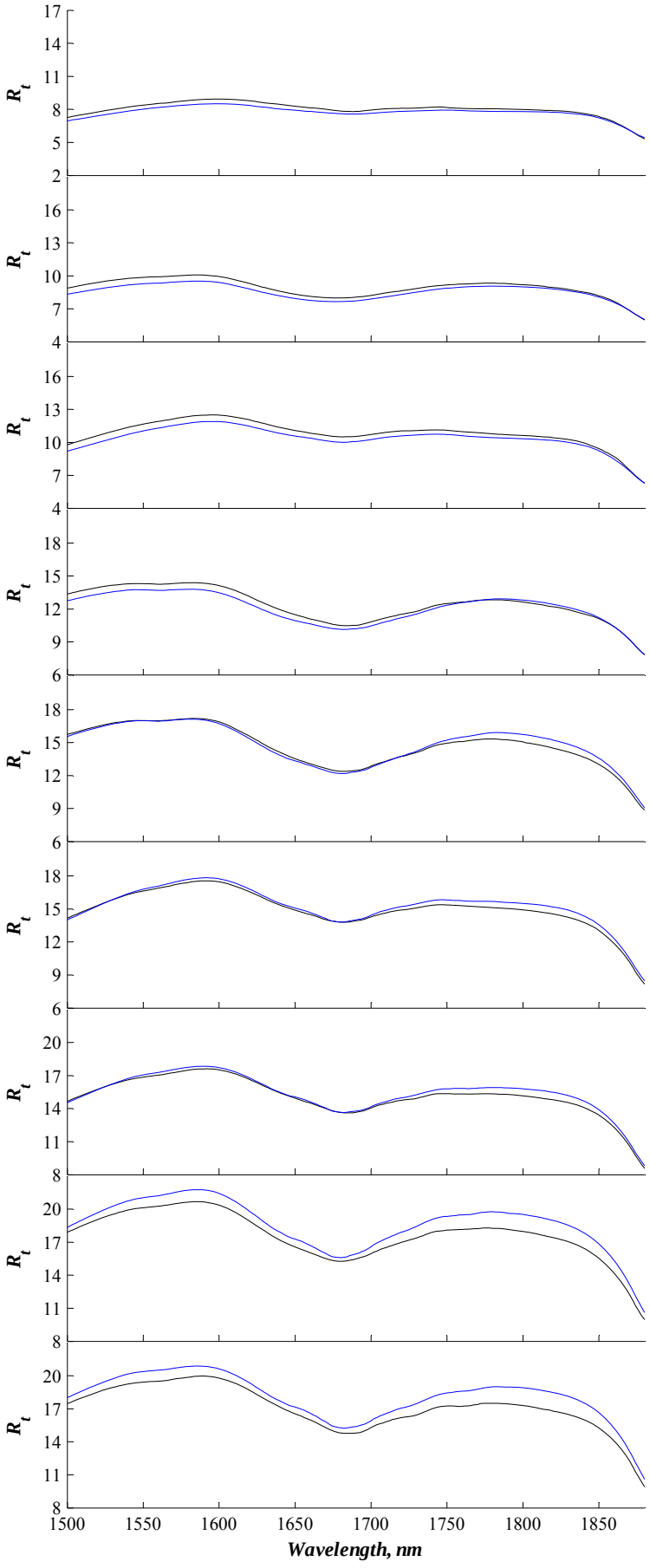

Figure A.8. Measured (black) and simulated (blue) spectra of R_t for particle size Ø 300 nm.

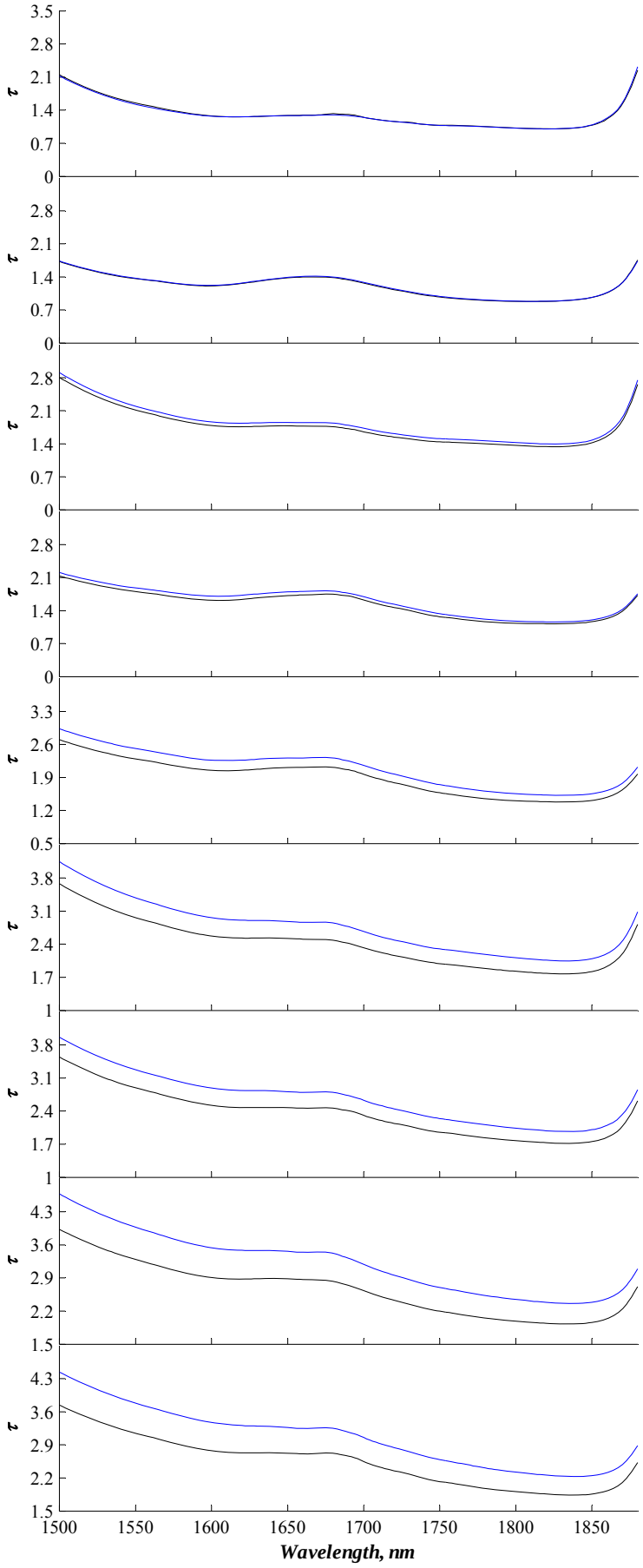

Figure A.9. Measured (black) and simulated (blue) spectra of τ for particle size Ø 300 nm.

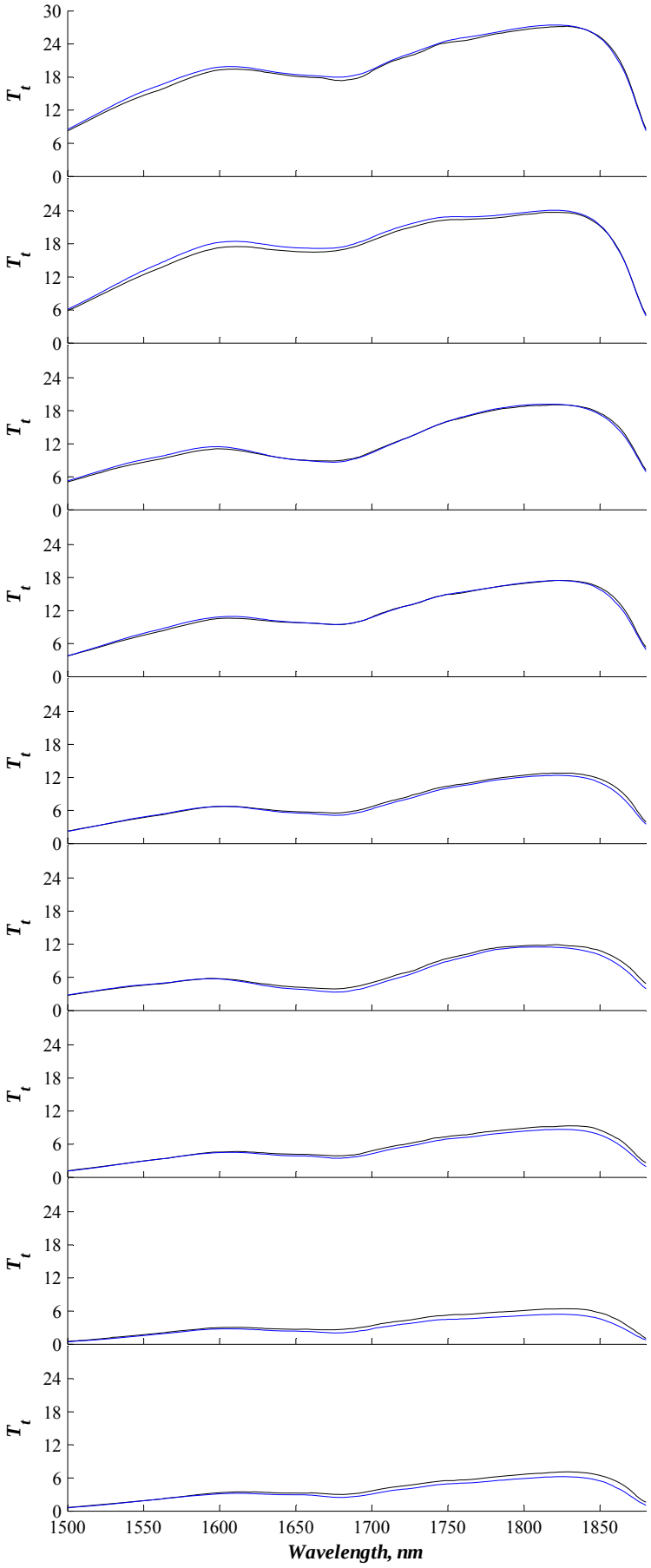

Figure A.10. Measured (black) and simulated (blue) spectra of T_t for particle size Ø430nm.

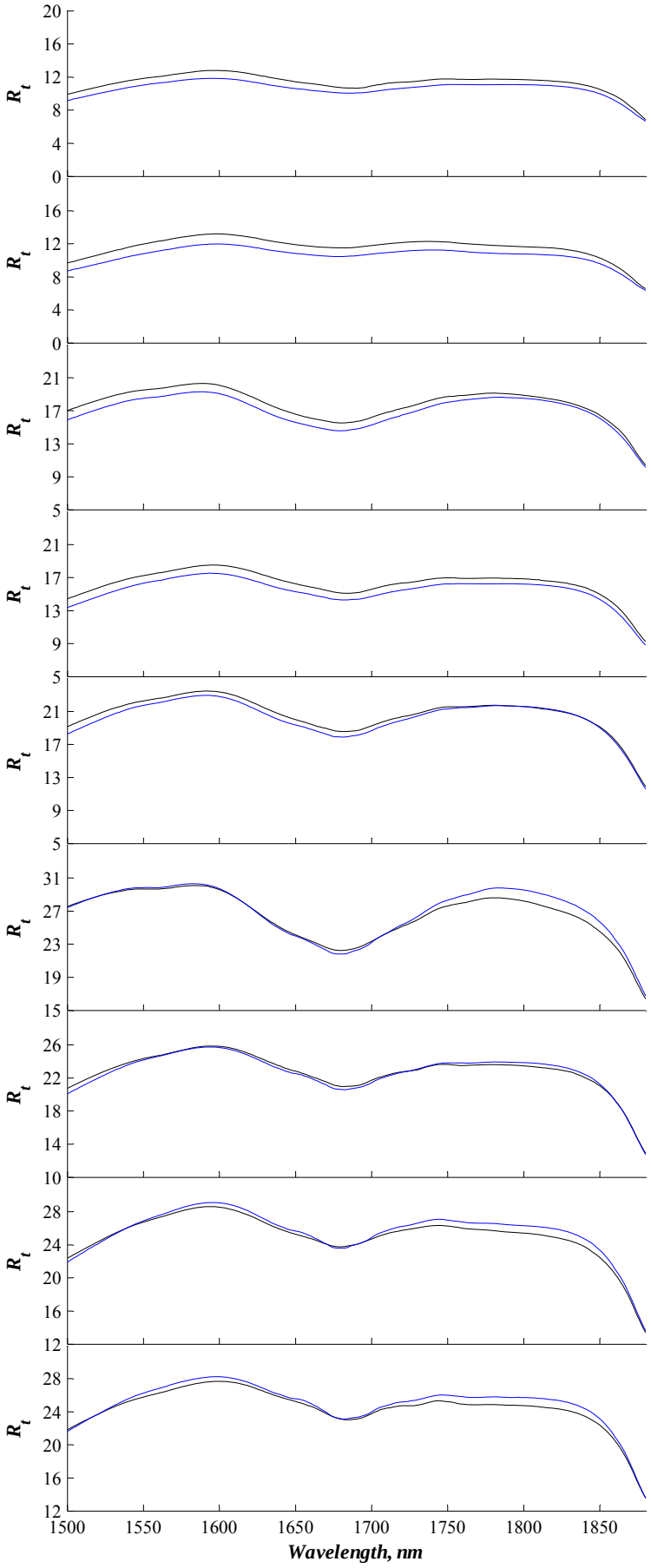

Figure A.11. Measured (black) and simulated (blue) spectra of R_t for particle size Ø430nm.

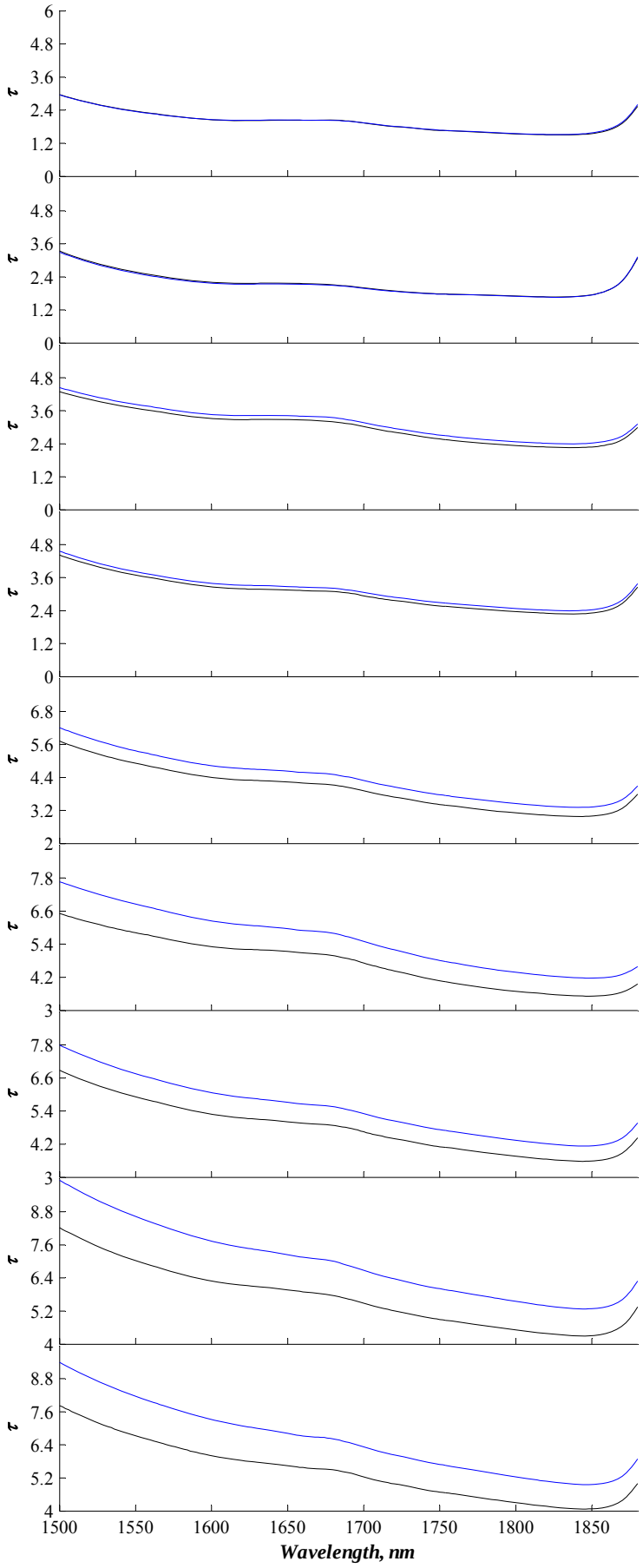

Figure A.12. Measured (black) and simulated (blue) spectra of τ for particle size Ø 430nm.

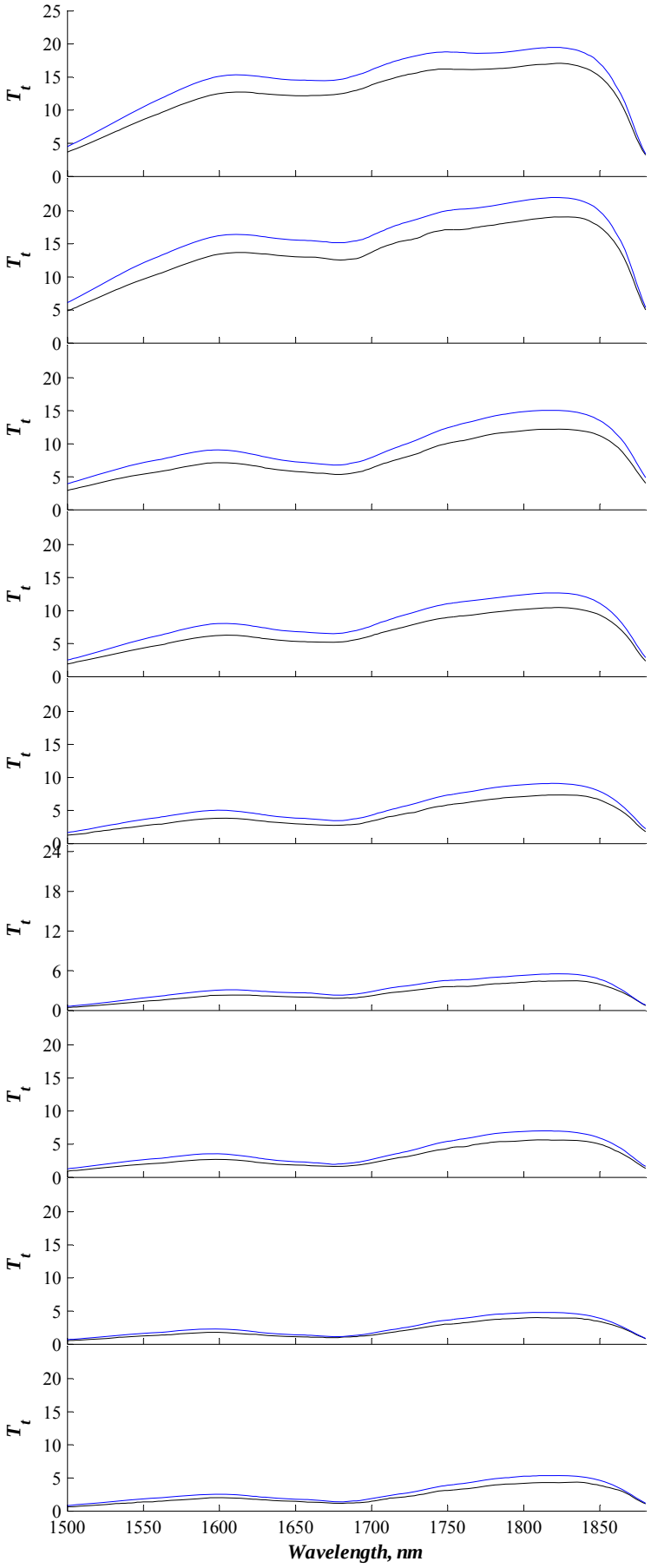

Figure A.13. Measured (black) and simulated (blue) spectra of T_t for particle size Ø500nm.

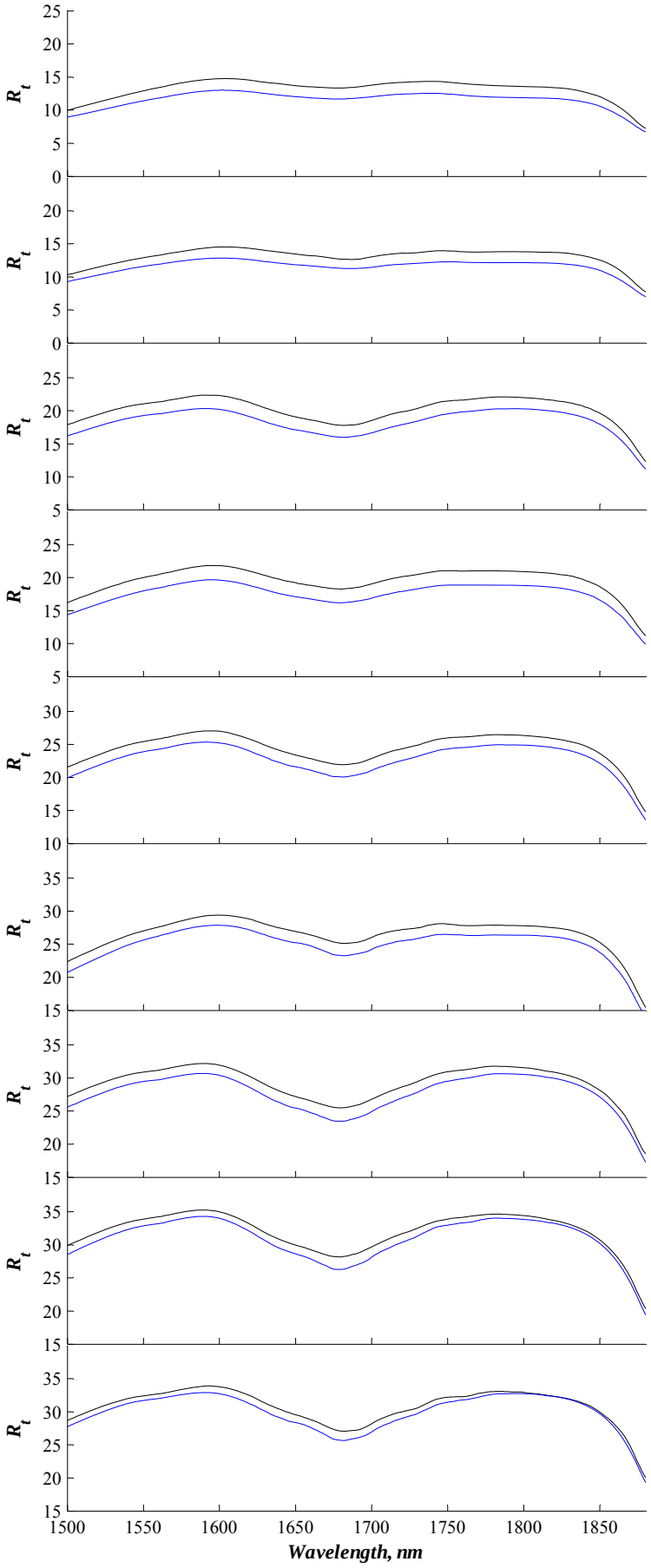

Figure A.14. Measured (black) and simulated (blue) spectra of R_t for particle size Ø500nm.

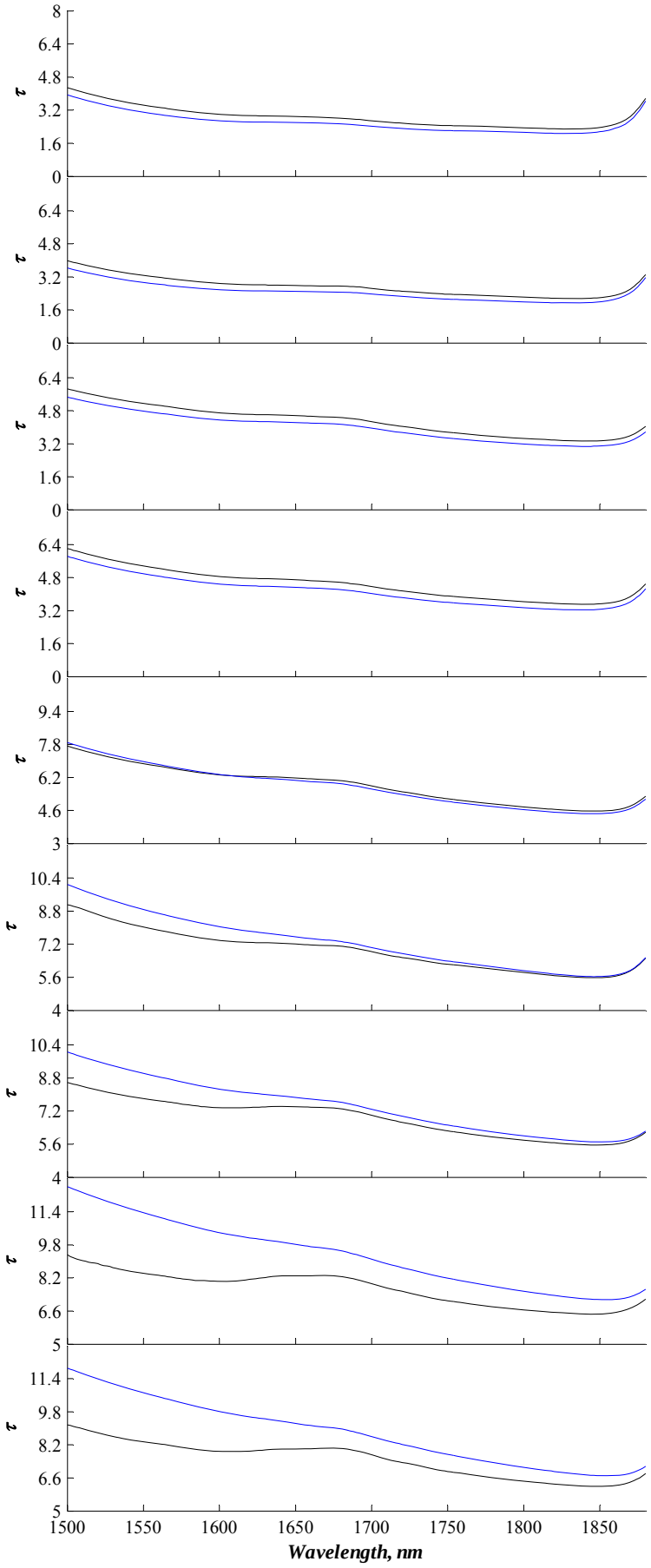

Figure A.15. Measured (black) and simulated (blue) spectra of τ for particle size Ø 500nm.

APPENDIX B.

COMPARISON OF EXTRACTED OPTICAL PROPERTIES WITH SIMULATED

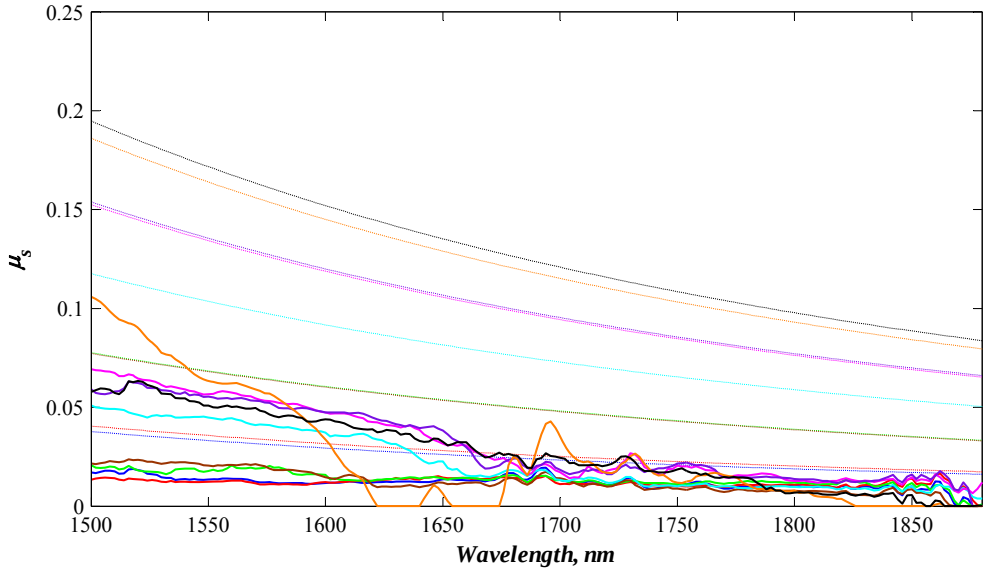

Figure B.1. Comparison of extracted (solid line) and simulated (dashed line) spectra of μ_s for particle size Ø 100 nm: 1 % wt., 1 % wt., 2 % wt., 2 %wt., 3 % wt., 4 % wt., 4 % wt., 5 % wt. and 5 % wt.

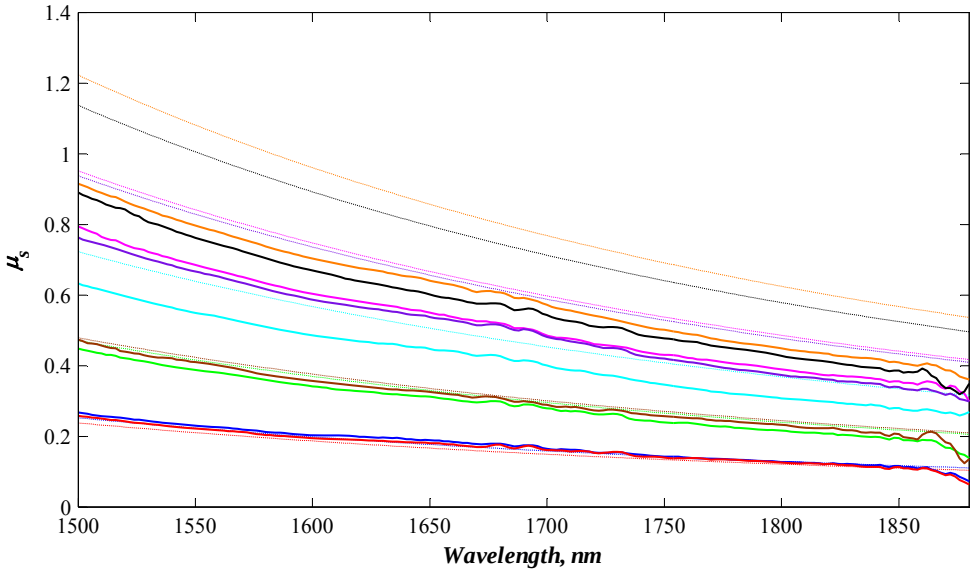

Figure B.2. Comparison of extracted (solid line) and simulated (dashed line) spectra of μ_s for particle size Ø 200 nm: 1 % wt., 1 % wt., 2 % wt., 2 %wt., 3 % wt., 4 % wt., 4 % wt., 5 % wt. and 5 % wt.

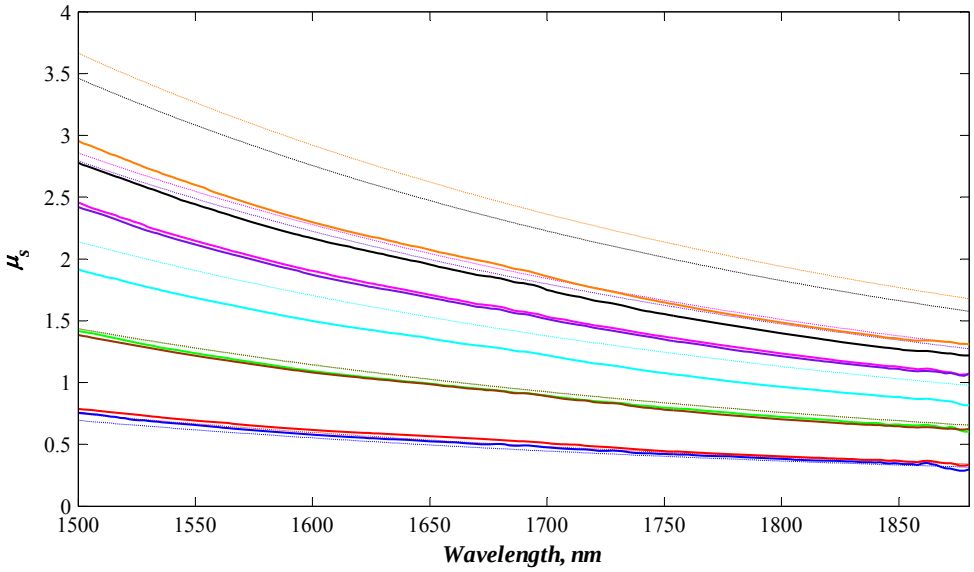

Figure B.3. Comparison of extracted (solid line) and simulated (dashed line) spectra of μ_s for particle size Ø 300 nm: 1 % wt., 1 % wt., 2 % wt., 2 %wt., 3 % wt., 4 % wt., 4 % wt., 5 % wt. and 5 % wt.

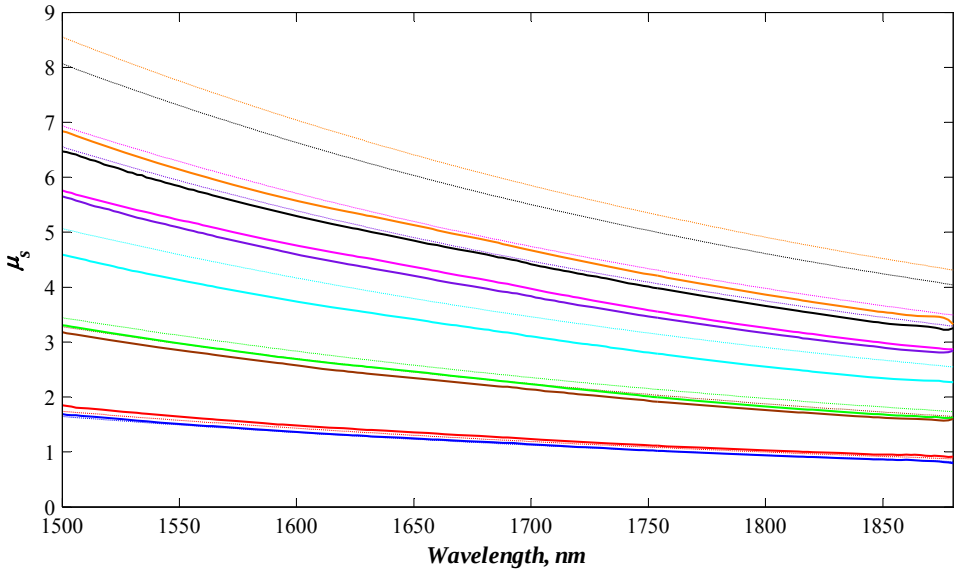

Figure B.4. Comparison of extracted (solid line) and simulated (dashed line) spectra of μ_s for particle size Ø 430 nm: 1 % wt., 1 % wt., 2 % wt., 2 %wt., 3 % wt., 4 % wt., 4 % wt., 5 % wt. and 5 % wt.

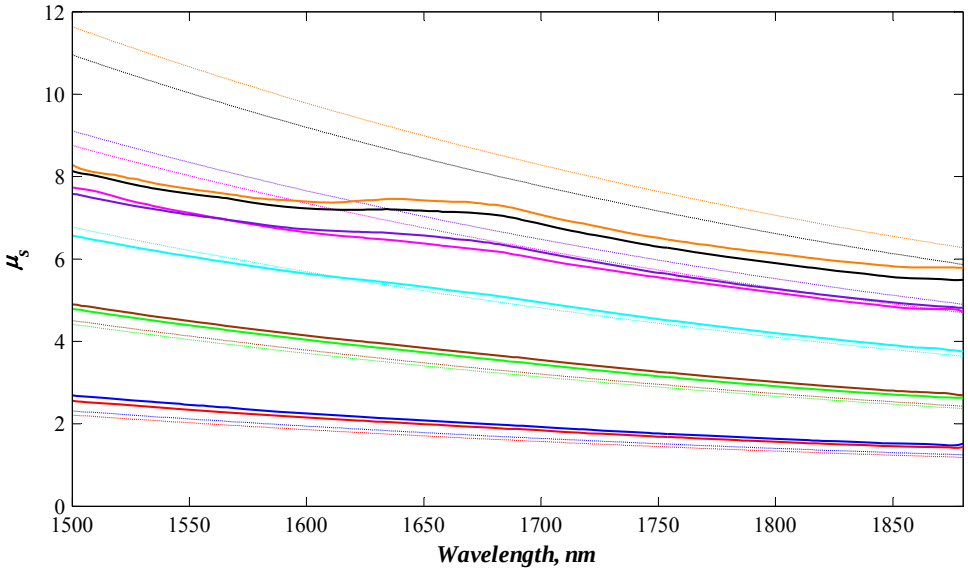

Figure B.5. Comparison of extracted (solid line) and simulated (dashed line) spectra of μ_s for particle size Ø 500 nm: 1 % wt., 1 % wt., 2 % wt., 2 %wt., 3 % wt., 4 % wt., 4 % wt., 5 % wt. and 5 % wt.

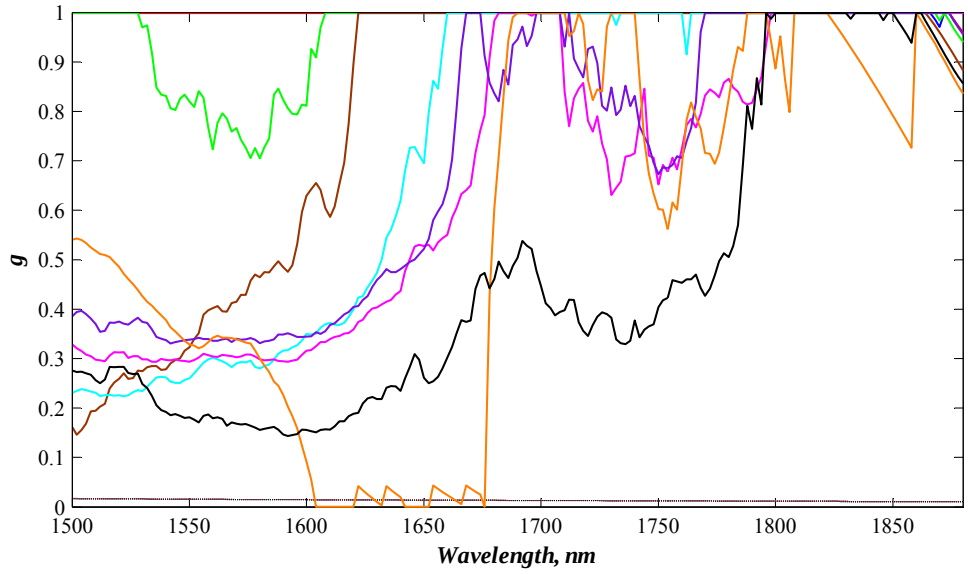

Figure B.6. Comparison of extracted (solid line) and simulated (dashed line) spectra of g for particle size Ø 100 nm: 1 % wt., 1 % wt., 2 % wt., 2 %wt., 3 % wt., 4 % wt., 4 % wt., 5 % wt. and 5 % wt.

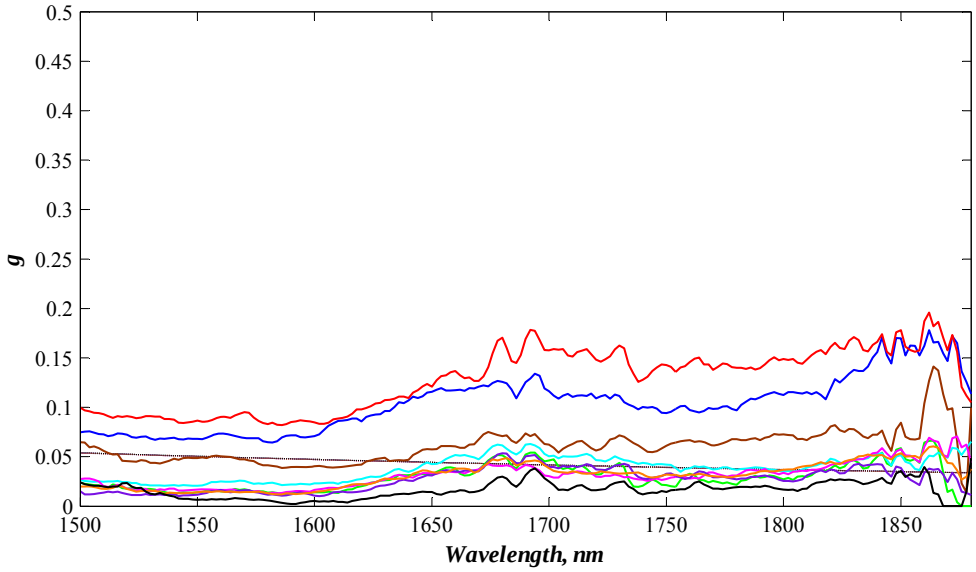

Figure B.7. Comparison of extracted (solid line) and simulated (dashed line) spectra of *g* for particle size Ø 200 nm: 1 % wt., 1 % wt., 2 % wt., 2 %wt., 3 % wt., 4 % wt., 4 % wt., 5 % wt. and 5 % wt.

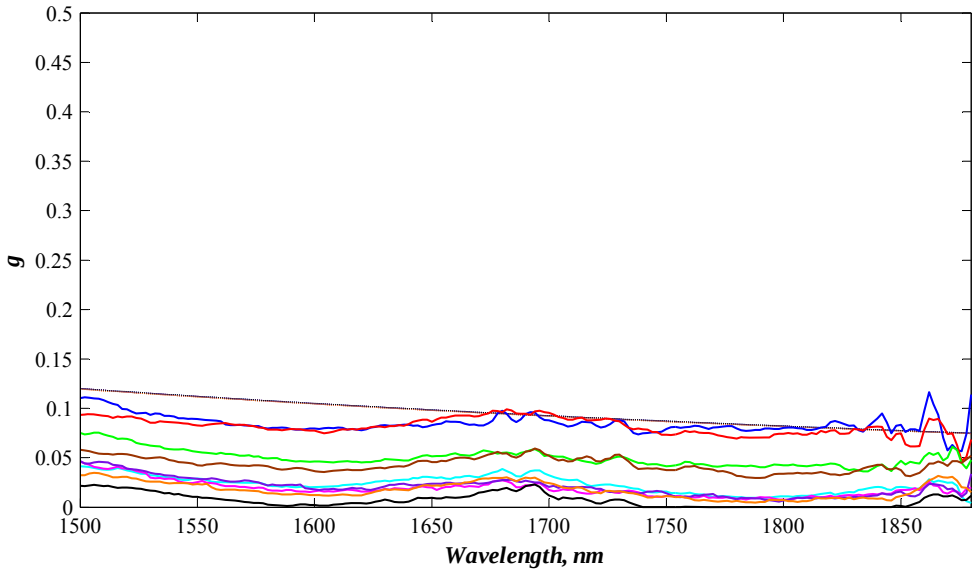

Figure B.8. Comparison of extracted (solid line) and simulated (dashed line) spectra of *g* for particle size Ø 300 nm: 1 % wt., 1 % wt., 2 % wt., 2 %wt., 3 % wt., 4 % wt., 4 % wt., 5 % wt. and 5 % wt.

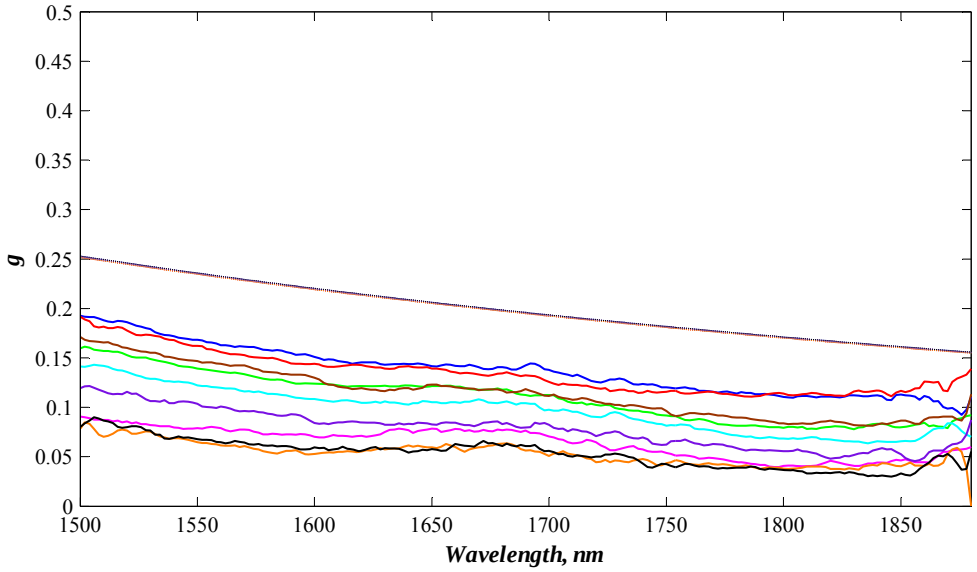

Figure B.9. Comparison of extracted (solid line) and simulated (dashed line) spectra of *g* for particle size Ø 430 nm: 1 % wt., 1 % wt., 2 % wt., 2 %wt., 3 % wt., 4 % wt., 4 % wt., 5 % wt. and 5 % wt.

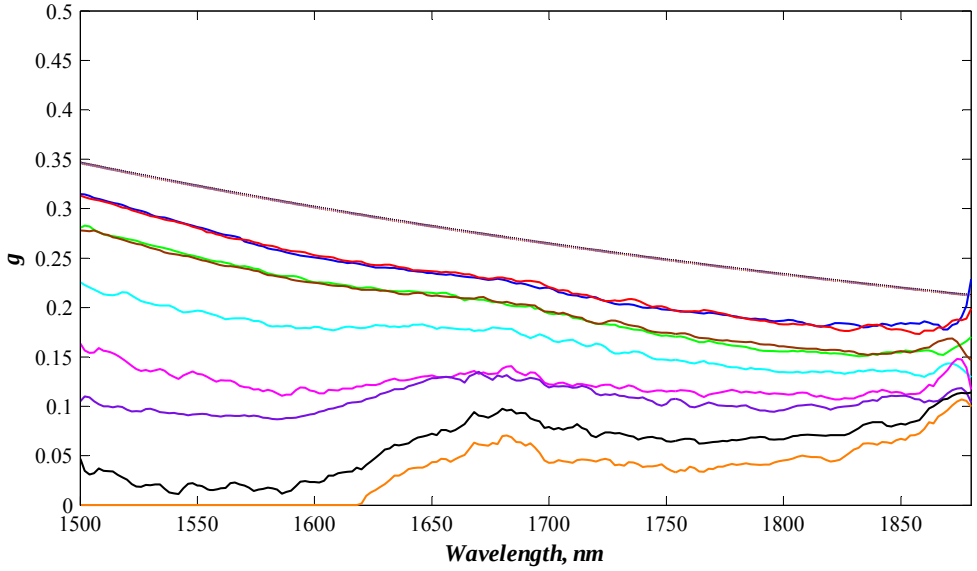

Figure B.10. Comparison of extracted (solid line) and simulated (dashed line) spectra of *g* for particle size Ø 500 nm: 1 % wt., 1 % wt., 2 % wt., 2 %wt., 3 % wt., 4 % wt., 4 % wt., 5 % wt. and 5 % wt.

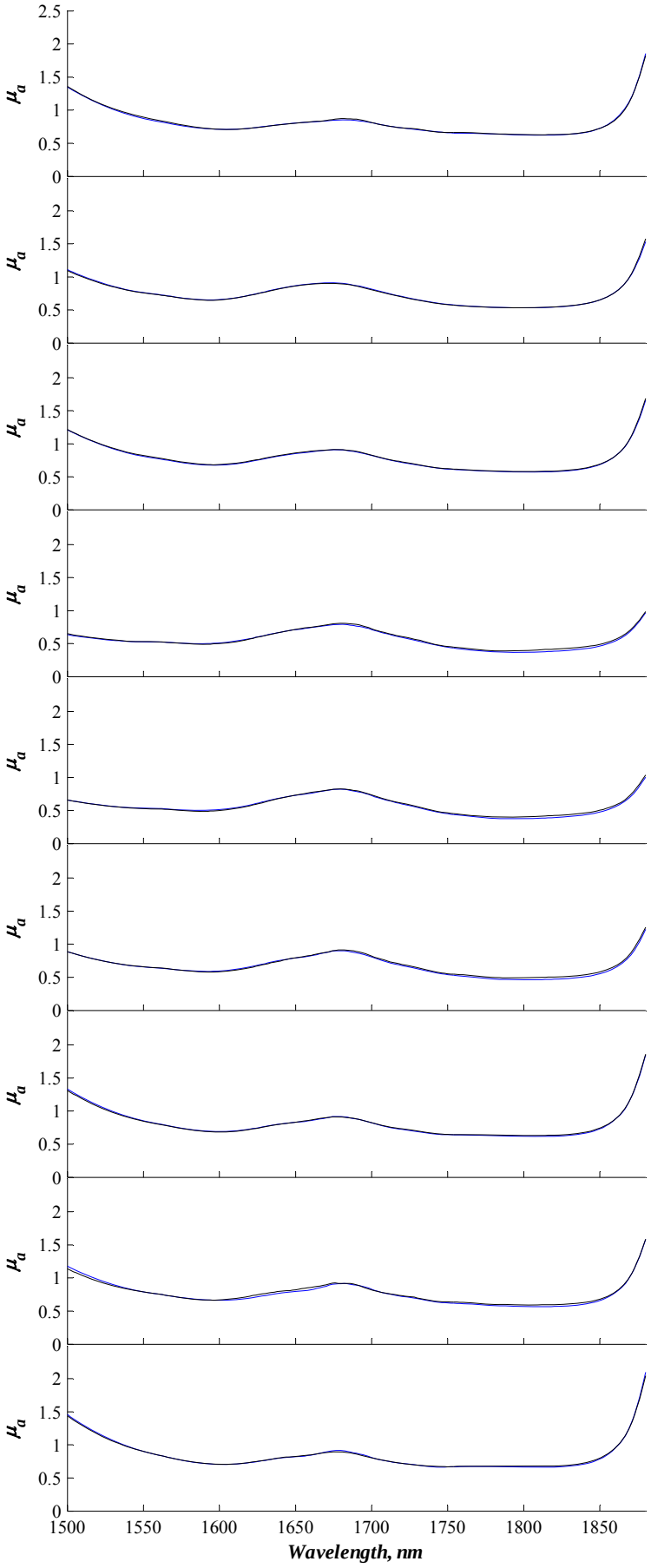

Figure B.11. Extracted (black) and simulated (blue) spectra of μ_a for particle size Ø100nm.

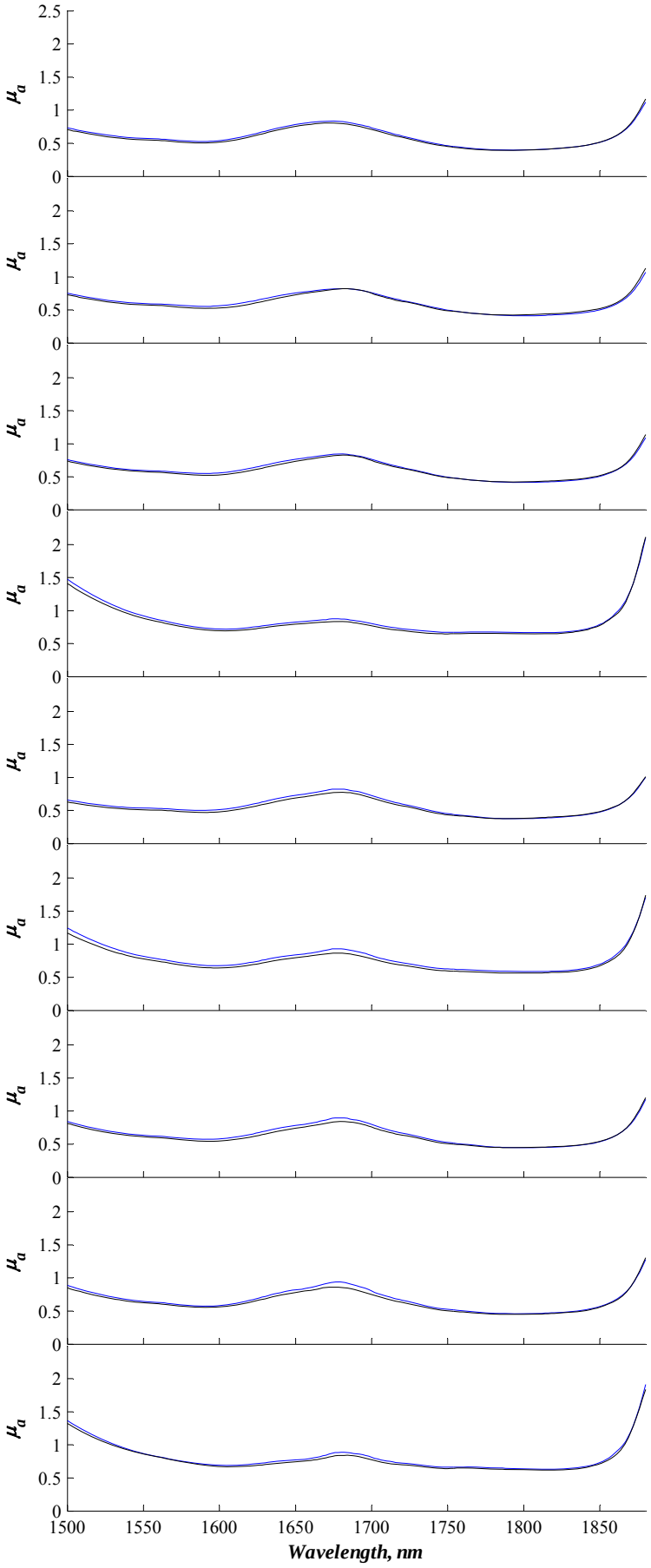

Figure B.12. Extracted (black) and simulated (blue) spectra of μ_a for particle size Ø200nm.

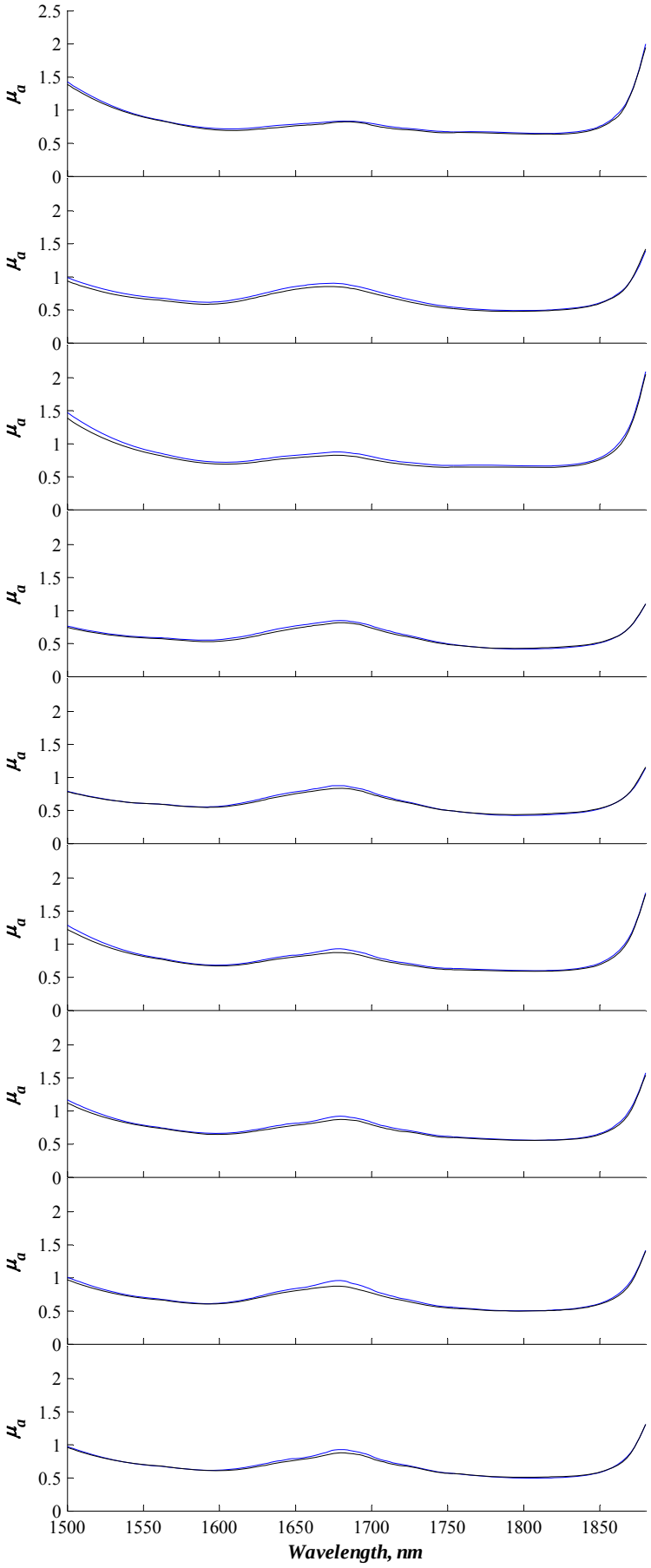

Figure B.13. Extracted (black) and simulated (blue) spectra of μ_a for particle size Ø300nm.

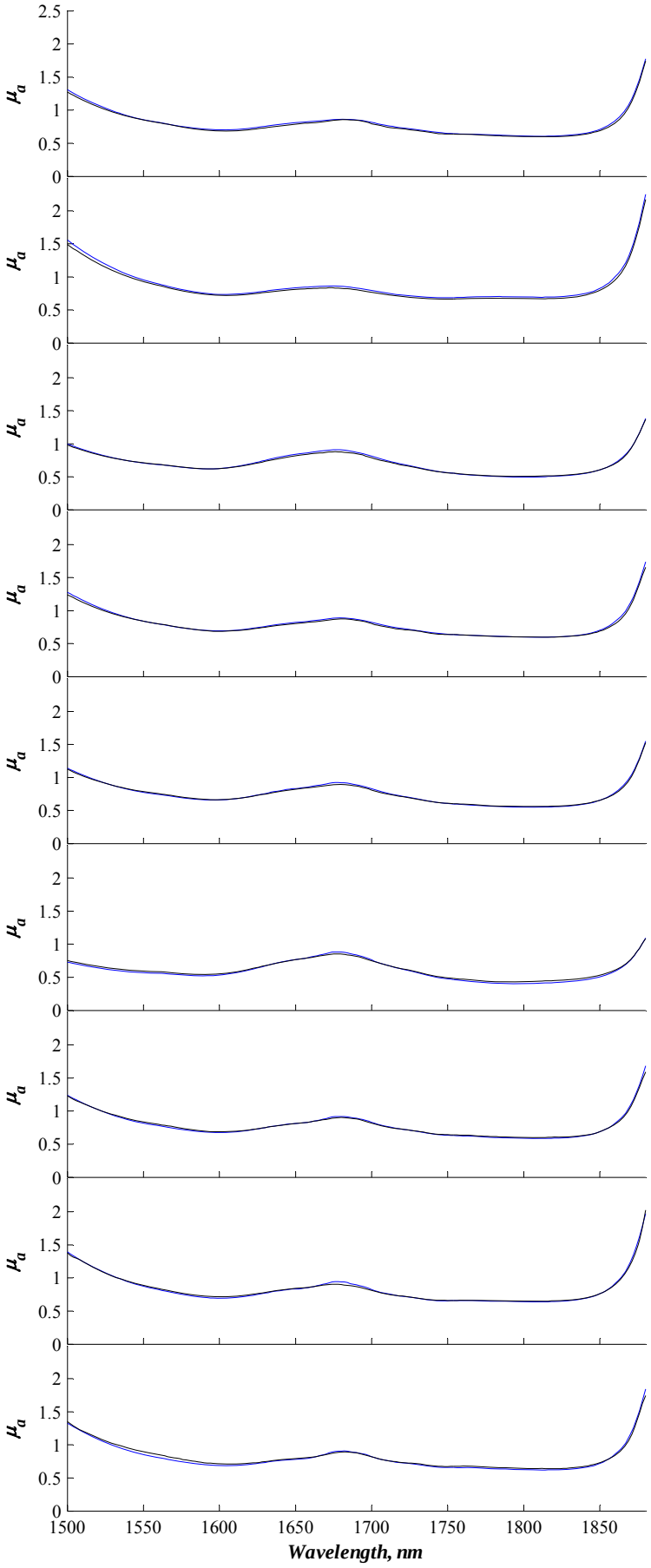

Figure B.14. Extracted (black) and simulated (blue) spectra of μ_a for particle size Ø430nm.

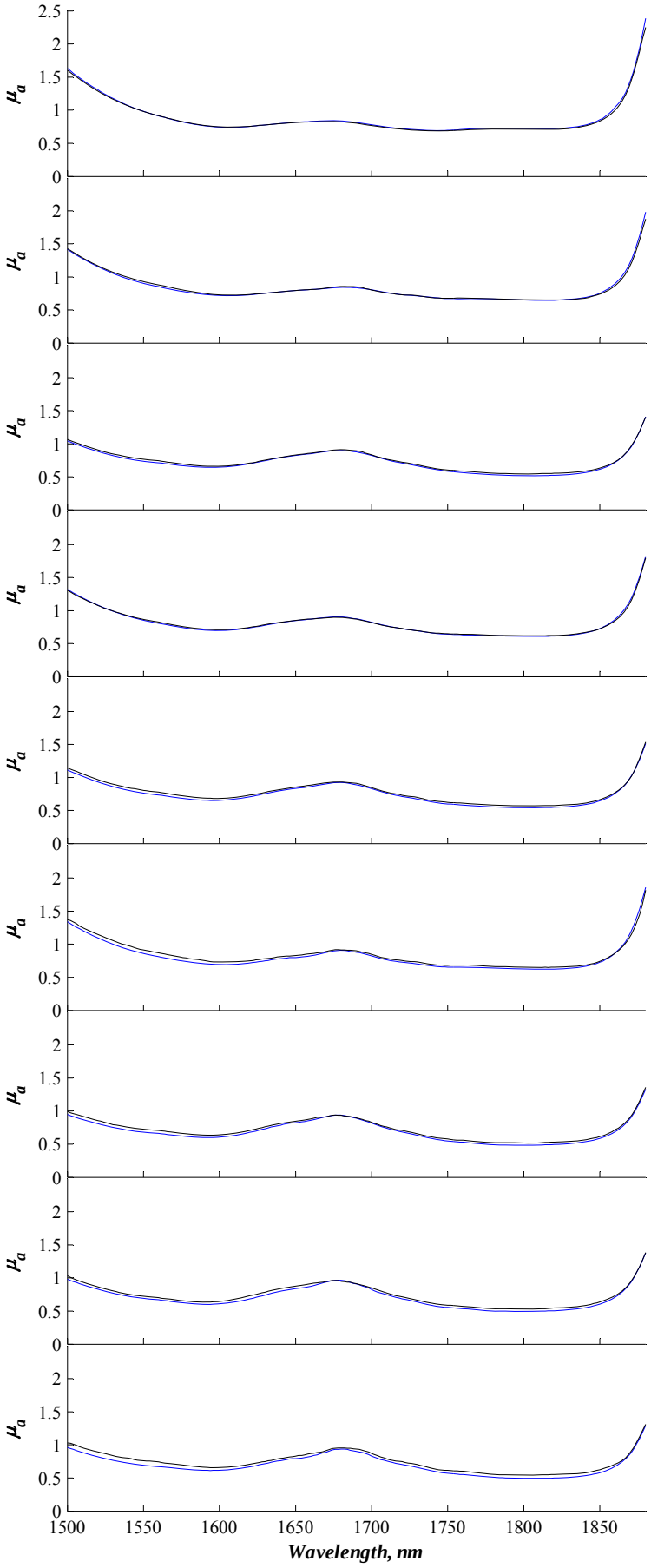

Figure B.15. Extracted (black) and simulated (blue) spectra of μ_a for particle size Ø500nm.

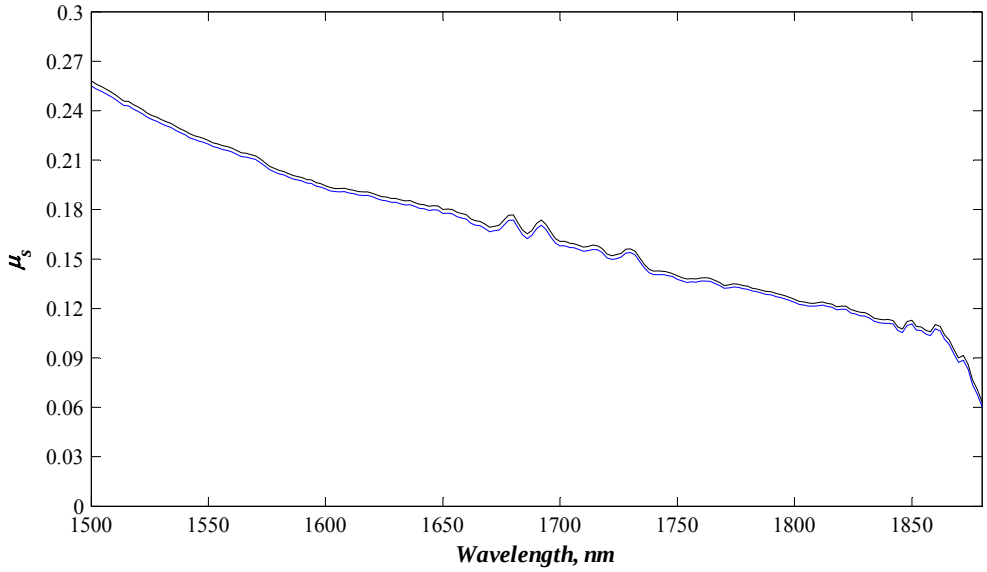

Figure B.16. Comparison of μ_s extracted using true refractive index of the medium and the refractive index of water for the 11th sample in table 6.4.

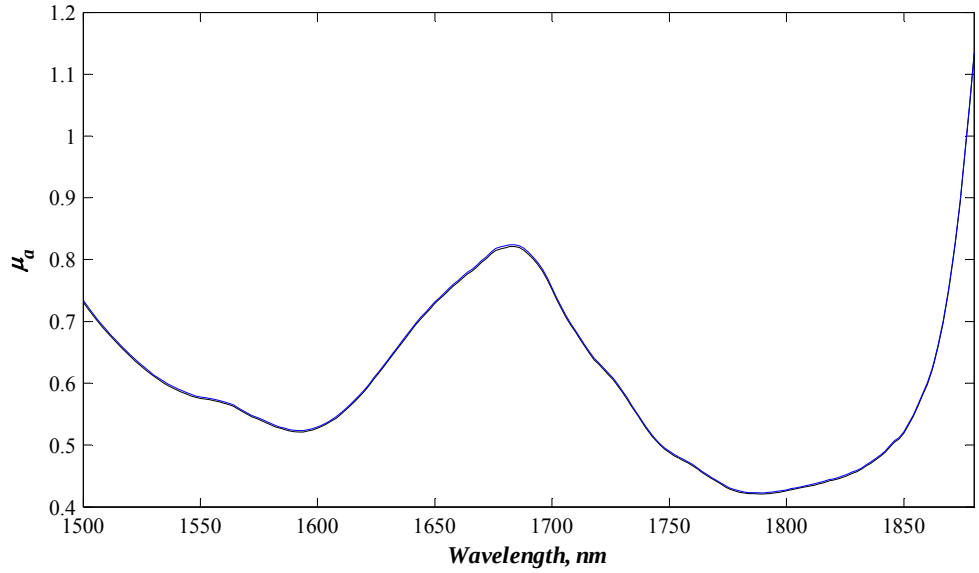

Figure B.17. Comparison of μ_a extracted using true refractive index of the medium and the refractive index of water for the 11th sample in table 6.4.

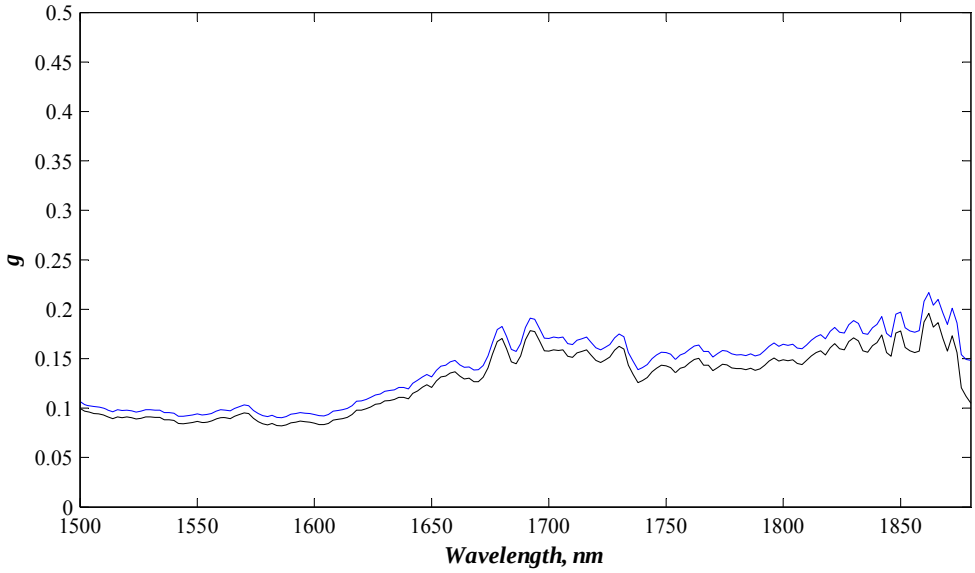

Figure B.18. Comparison of g extracted using true refractive index of the medium and the refractive index of water for the 11th sample in table 6.4.

APPENDIX C.

SEM PICTURES OF POLYSTYRENE PARTICLES

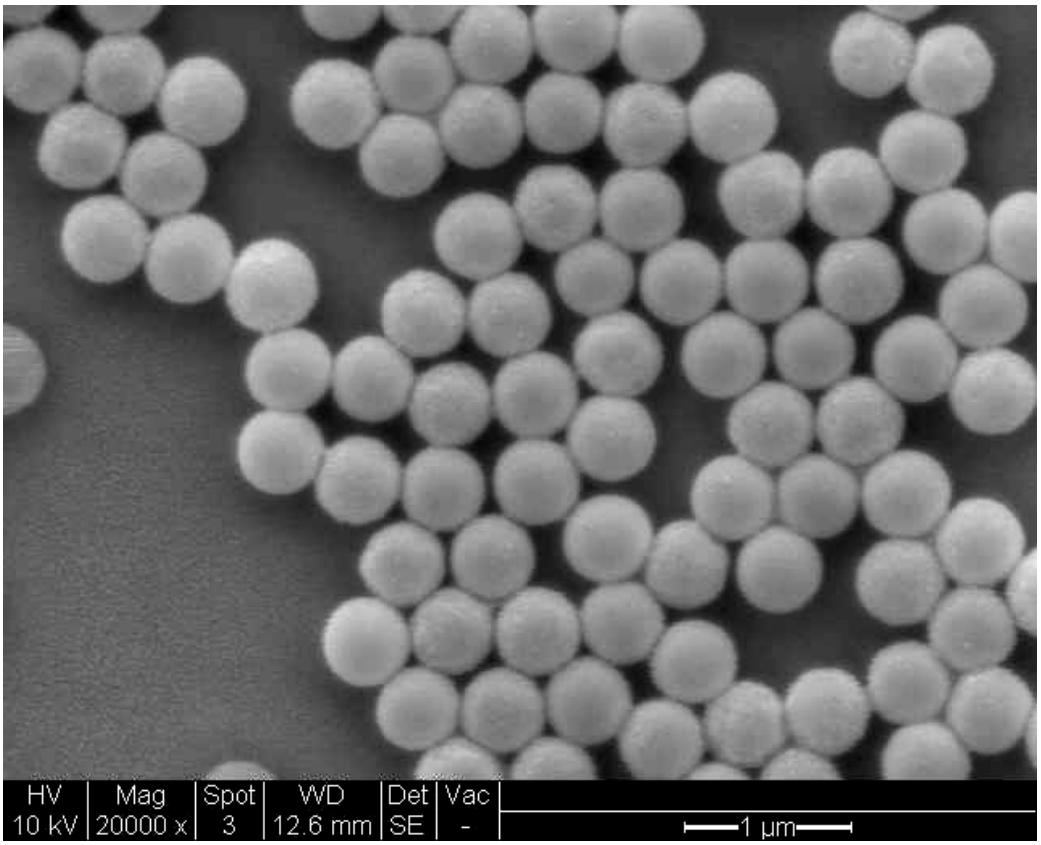

Figure C.1. 500 nm polystyrene latex particles bought from Duke Scientific.

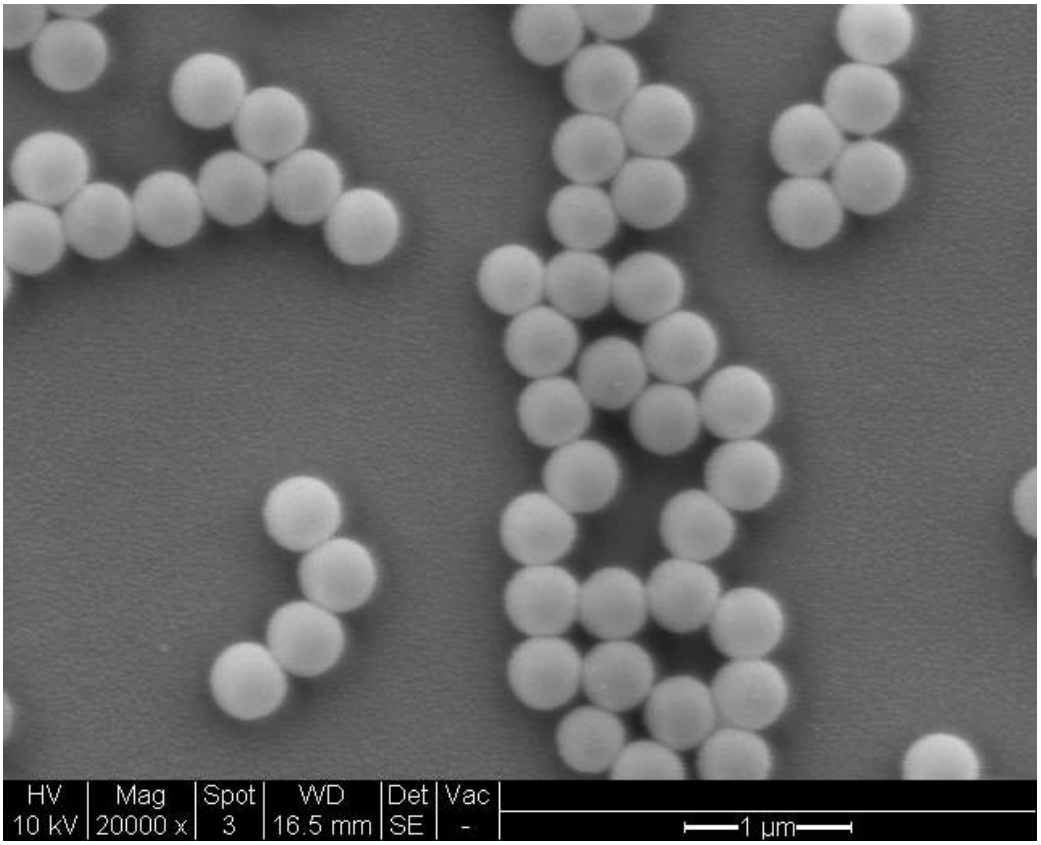

Figure C.2. 430 nm polystyrene latex particles bought from Duke Scientific.

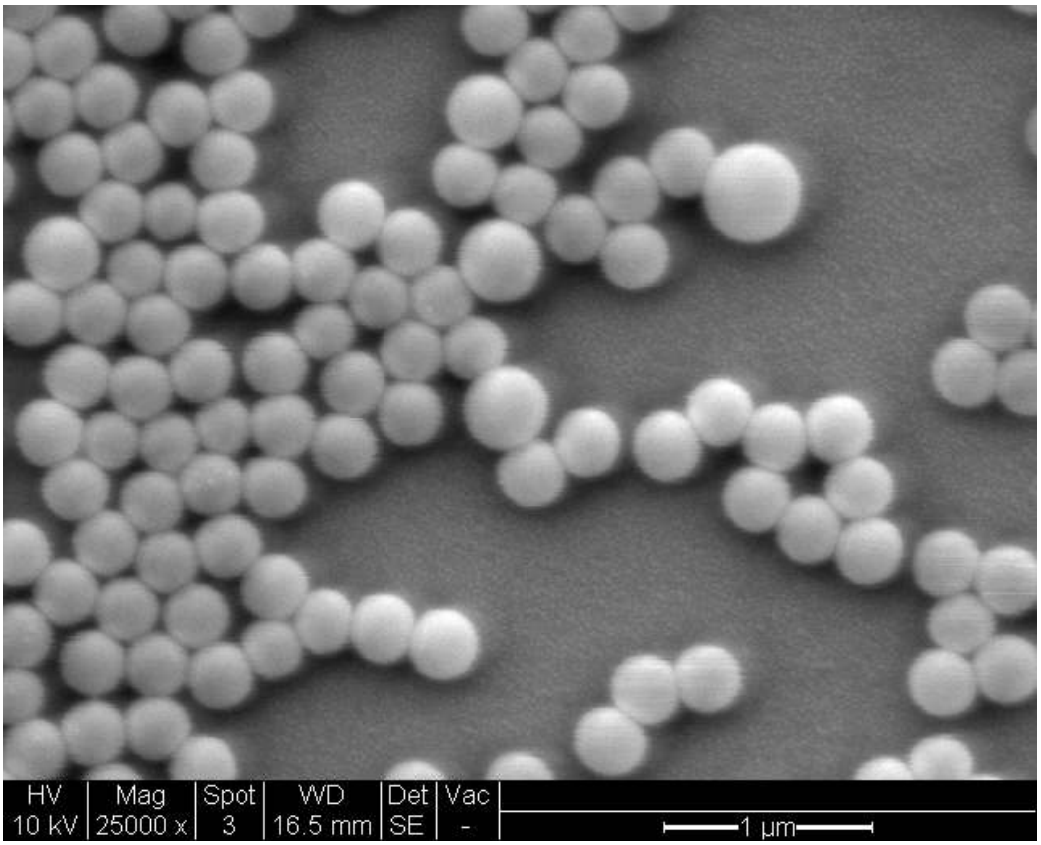

Figure C.3. 300 nm polystyrene latex particles bought from Duke Scientific.

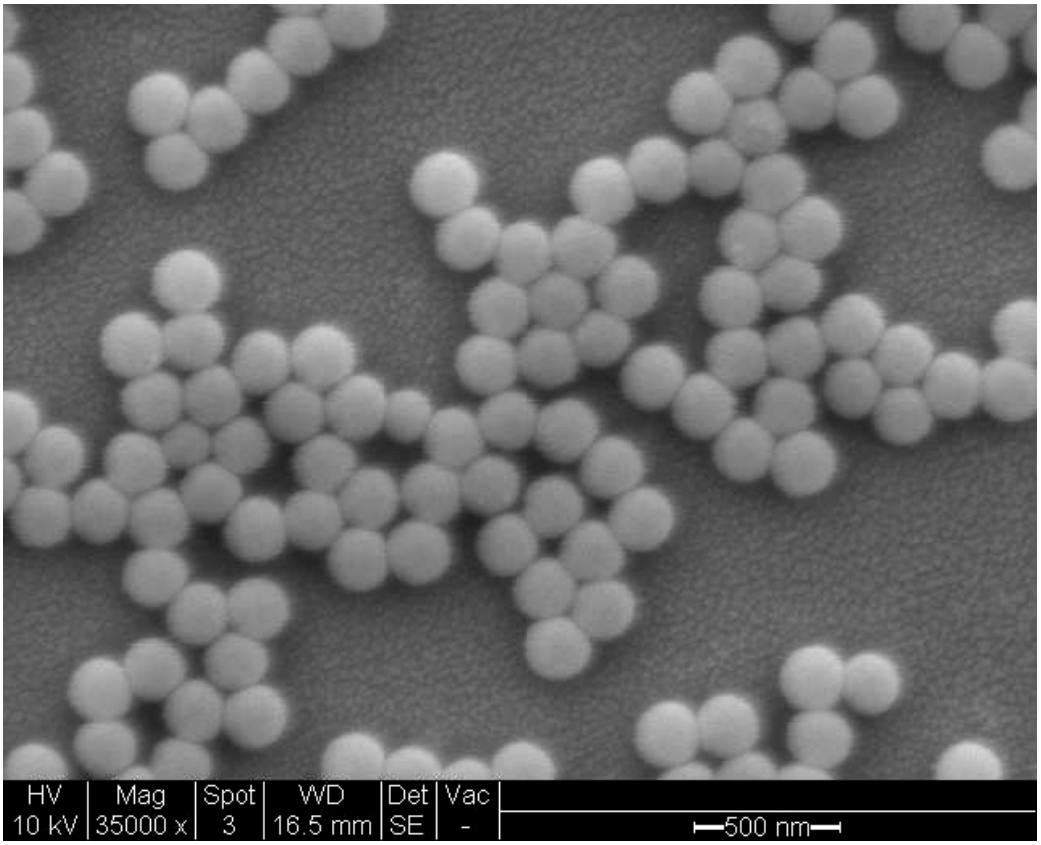

Figure C.4. 200 nm polystyrene latex particles bought from Duke Scientific.

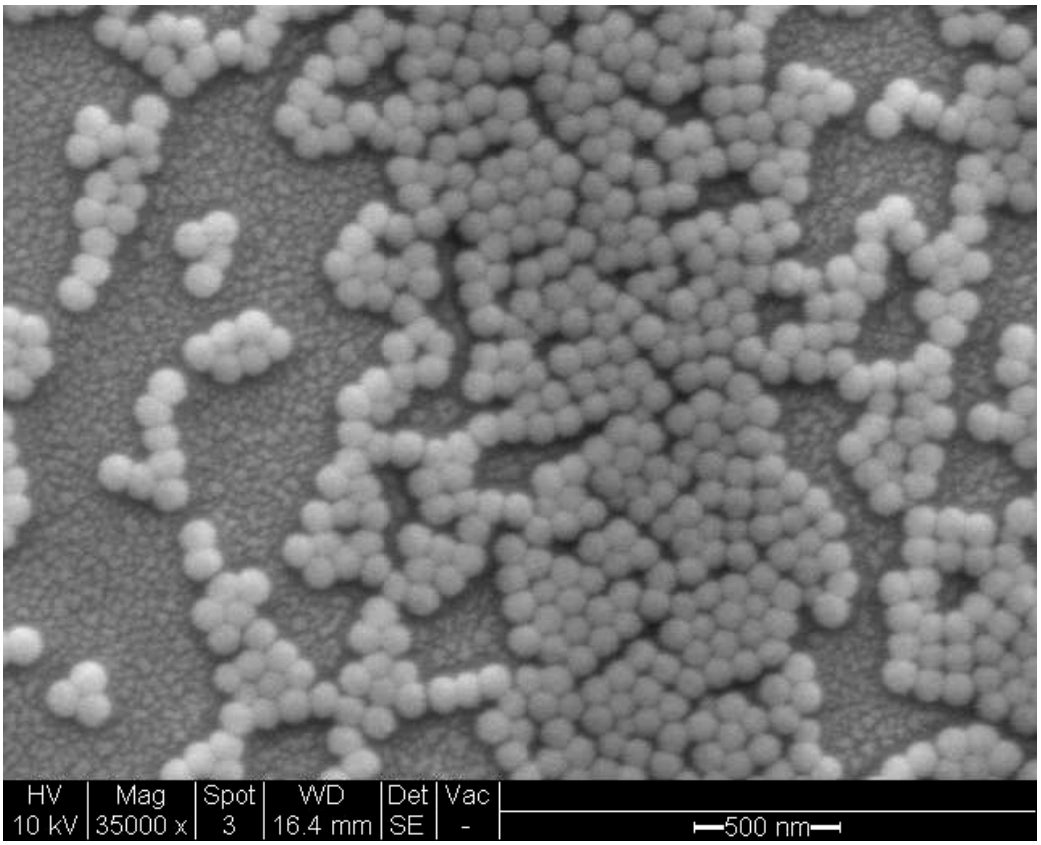

Figure C.5. 100 nm polystyrene latex particles bought from Duke Scientific.

REFERENCES

1. Reis, M.M., et al., *Spectroscopic on-line monitoring of reactions in dispersed medium: Chemometric challenges.* Analytica Chimica Acta, 2007. **595**(1-2): p. 257-265.
2. Alb, A.M., M.F. Drenski, and W.F. Reed, *Automatic continuous online monitoring of polymerization reactions (ACOMP).* Polymer International, 2008. **57**(3): p. 390-396.
3. Alb, A.M. and W.F. Reed, *Simultaneous monitoring of polymer and particle characteristics during emulsion polymerization.* Macromolecules, 2008. **41**(7): p. 2406-2414.
4. Reis, M.M., et al., *In situ near-infrared spectroscopy for simultaneous monitoring of multiple process variables in emulsion copolymerization.* Industrial and Engineering Chemistry Research, 2004. **43**(23): p. 7243-7250.
5. Chicoma, D., et al., *In line monitoring of VAc-BuA emulsion polymerization reaction in a continuous pulsed sieve plate reactor using NIR spectroscopy.* Macromolecular Symposia, 2010. **289**(1): p. 140-148.
6. Dzhongova, E., C.R. Harwood, and S.N. Thennadil, *Changes in the Absorption and Scattering Properties in the Near-Infrared Region During the Growth of Bacillus subtilis in Liquid Culture.* Applied Spectroscopy, 2009. **63**(1): p. 25-32.
7. Cervera, A.E., et al., *Application of near-infrared spectroscopy for monitoring and control of cell culture and fermentation.* Biotechnology Progress, 2009. **25**(6): p. 1561-1581.
8. Petersen, N., et al., *In situ near infrared spectroscopy for analyte-specific monitoring of glucose and ammonium in Streptomyces coelicolor fermentations.* Biotechnology Progress, 2010. **26**(1): p. 263-271.
9. Wong, C.W.L., et al., *The integration of spectroscopic and process data for enhanced process performance monitoring.* Canadian Journal of Chemical Engineering, 2008. **86**(5): p. 905-923.
10. Bunaciu, A.A., H.Y. Aboul-Enein, and S. Fleschin, *Application of fourier transform infrared spectrophotometry in pharmaceutical drugs analysis.* Applied Spectroscopy Reviews, 2010. **45**(3): p. 206-219.

11. Ma, C., et al., *On-line monitoring of pharmaceutical production processes by means of near infrared spectrum with hidden Markov model.* Control and Intelligent Systems, 2010. **38**(1): p. 8-15.
12. Mark, J., et al., *Online process control of a pharmaceutical intermediate in a fluidized-bed drier environment using near-infrared spectroscopy.* Analytical Chemistry, 2010. **82**(10): p. 4209-4215.
13. Vanarase, A.U., et al., *Real-time monitoring of drug concentration in a continuous powder mixing process using NIR spectroscopy.* Chemical Engineering Science, 2010.
14. Wu, H. and M.A. Khan, *Quality-by-design (QbD): An integrated process analytical technology (PAT) approach for real-time monitoring and mapping the state of a pharmaceutical coprecipitation process.* Journal of Pharmaceutical Sciences, 2010. **99**(3): p. 1516-1534.
15. Martens, H. and T. Naes, *Multivariate calibration*. 1989, New York: Wiley. 419p.
16. Malinowski, E.R., *Factor analysis in chemistry*. 2nd. ed. 1991, New York: Wiley. 368p.
17. Lai, X., et al., *Determination of Adsorbed Protein Concentration in Aluminum Hydroxide Suspensions by Near-Infrared Transmittance Spectroscopy.* Appl. Spectrosc., 2008. **62**(7): p. 784-790.
18. Savitzky, A. and M.J.E. Golay, *Smoothing and differentiation of data by simplified least-squares procedures.* Analytical Chemistry, 1964. **36**(8): p. 1627-1639.
19. Norris, K.H. and P.C. Williams, *Optimization of Mathematical Treatments of Raw near-Infrared Signal in the Measurement of Protein in Hard Red Spring Wheat .1. Influence of Particle-Size.* Cereal Chemistry, 1984. **61**(2): p. 158-165.
20. Tan, H.W. and S.D. Brown, *Wavelet analysis applied to removing non-constant, varying spectroscopic background in multivariate calibration.* Journal of Chemometrics, 2002. **16**(5): p. 228-240.
21. Gossen, P.D., J.F. MacGregor, and R.H. Pelton, *Composition and Particle Diameter for Styrene/Methyl Methacrylate Copolymer Latex Using UV and NIR Spectroscopy*, in *Applied Spectroscopy*. 1993. p. 1852-1870.
22. Wu, C., et al., *Remote in-line monitoring of emulsion polymerization of styrene by short-wavelength near-infrared spectroscopy. Part I. Performance during normal runs.* Process Control and Quality, 1996. **8**(1): p. 1-23.

23. Vieira, R.A.M., et al., *In-line and in situ monitoring of semi-batch emulsion copolymerizations using near-infrared spectroscopy.* Journal of Applied Polymer Science, 2002. **84**(14): p. 2670-2682.
24. Santos, A.F., et al., *Monitoring and control of polymerization reactors using NIR spectroscopy.* Polymer - Plastics Technology and Engineering, 2005. **44**(1): p. 1-61.
25. Geladi, P., D. Macdougall, and H. Martens, *Linearization and Scatter-correction for Near-Infrared reflectance spectra of meat.* Applied Spectroscopy, 1985. **39**(3): p. 491-500.
26. Barnes, R.J., M.S. Dhanoa, and S.J. Lister, *Standard Normal Variate Transformation and De-Trending of near-Infrared Diffuse Reflectance Spectra.* Applied Spectroscopy, 1989. **43**(5): p. 772-777.
27. Dhanoa, M.S., et al., *The link between multiplicative scatter correction (MSC) and standard normal variate (SNV) transformations of NIR spectra.* J. Near Infrared Spectrosc., 1994. **2**(1): p. 43-7.
28. Dhanoa, M.S., S.J. Lister, and R.J. Barnes, *On the Scales Associated with near-Infrared Reflectance Difference Spectra.* Applied Spectroscopy, 1995. **49**(6): p. 765-772.
29. Isaksson, T. and B. Kowalski, *Piece-Wise Multiplicative Scatter Correction Applied to near-Infrared Diffuse Transmittance Data from Meat-Products.* Applied Spectroscopy, 1993. **47**(6): p. 702-709.
30. Windig, W., J. Shaver, and R. Bro, *Loopy MSC: A Simple Way to Improve Multiplicative Scatter Correction.* Applied Spectroscopy, 2008. **62**(10): p. 1153-1159.
31. Martens, H. and E. Stark, *Extended Multiplicative Signal Correction and Spectral Interference Subtraction - New Preprocessing Methods for Near-Infrared Spectroscopy.* Journal of Pharmaceutical and Biomedical Analysis, 1991. **9**(8): p. 625-635.
32. Martens, H., J.P. Nielsen, and S.B. Engelsen, *Light scattering and light absorbance separated by extended multiplicative signal correction. Application to near-infrared transmission analysis of powder mixtures.* Analytical Chemistry, 2003. **75**(3): p. 394-404.

33. Thennadil, S.N. and E.B. Martin, *Empirical preprocessing methods and their impact on NIR calibrations: a simulation study.* Journal of Chemometrics, 2005. **19**(2): p. 77-89.
34. Ottestad, S., et al., *Scattering Correction by Use of a Priori Information.* Applied Spectroscopy, 2010. **64**(7): p. 795-804.
35. Thennadil, S.N., H. Martens, and A. Kohler, *Physics-based multiplicative scatter correction approaches for improving the performance of calibration models.* Applied Spectroscopy, 2006. **60**(3): p. 315-321.
36. Chen, Z.P., J. Morris, and E. Martin, *Extracting chemical information from spectral data with multiplicative light scattering effects by optical path-length estimation and correction.* Analytical Chemistry, 2006. **78**(22): p. 7674-7681.
37. Helland, I.S., T. Naes, and T. Isaksson, *Related Versions of the Multiplicative Scatter Correction Method for Preprocessing Spectroscopic Data.* Chemometrics and Intelligent Laboratory Systems, 1995. **29**(2): p. 233-241.
38. Pedersen, D.K., et al., *Near-infrared absorption and scattering separated by extended inverted signal correction (EISC): Analysis of near-infrared transmittance spectra of single wheat seeds.* Applied Spectroscopy, 2002. **56**(9): p. 1206-1214.
39. Decker, M., P.V. Nielsen, and H. Martens, *Near-infrared spectra of Penicillium camemberti strains separated by extended multiplicative signal correction improved prediction of physical and chemical variations.* Applied Spectroscopy, 2005. **59**(1): p. 56-68.
40. Watari, M. and Y. Ozaki, *Application of Near Infrared Spectroscopy and Chemometrics to On-Line Analysis for Polymer Process.* Bunseki Kagaku, 2010. **59**(4): p. 379-397.
41. Zhang, Q.X., G.J. Zhang, and Q.B. Li, *A path-length correction method on biochemical parameter nondestructive measuring of folium.* Guang Pu Xue Yu Guang Pu Fen Xi/Spectroscopy and Spectral Analysis, 2010. **30**(5): p. 1310-1314.
42. Rinnan, A., F. van den Berg, and S.B. Engelsen, *Review of the most common pre-processing techniques for near-infrared spectra.* Trac-Trends in Analytical Chemistry, 2009. **28**(10): p. 1201-1222.
43. Wold, S., et al., *Orthogonal signal correction of near-infrared spectra.* Chemometrics and Intelligent Laboratory Systems, 1998. **44**(1-2): p. 175-185.

44. Andersson, C.A., *Direct orthogonalization.* Chemometrics and Intelligent Laboratory Systems, 1999. **47**(1): p. 51-63.
45. Trygg, J. and S. Wold, *Orthogonal projections to latent structures (O-PLS).* Journal of Chemometrics, 2002. **16**(3): p. 119-128.
46. Zeaiter, M., J.M. Roger, and V. Bellon-Maurel, *Dynamic orthogonal projection. A new method to maintain the on-line robustness of multivariate calibrations. Application to NIR-based monitoring of wine fermentations.* Chemometrics and Intelligent Laboratory Systems, 2006. **80**(2): p. 227-235.
47. Goicoechea, H.C. and A.C. Olivieri, *A comparison of orthogonal signal correction and net analyte preprocessing methods. Theoretical and experimental study.* Chemometrics and Intelligent Laboratory Systems, 2001. **56**(2): p. 73-81.
48. Westerhuis, J.A., S. de Jong, and A.K. Smilde, *Direct orthogonal signal correction.* Chemometrics and Intelligent Laboratory Systems, 2001. **56**(1): p. 13-25.
49. Svensson, O., T. Kourti, and J.F. MacGregor, *An investigation of orthogonal signal correction algorithms and their characteristics.* Journal of Chemometrics, 2002. **16**(4): p. 176-188.
50. Blanco, M., et al., *Orthogonal signal correction in near infrared calibration.* Analytica Chimica Acta, 2001. **434**(1): p. 125-132.
51. Miller, C.E. and T. Naes, *A Pathlength Correction Method for near-Infrared Spectroscopy.* Applied Spectroscopy, 1990. **44**(5): p. 895-898.
52. Blanco, M., et al., *Calibration in non-linear near infrared reflectance spectroscopy: a comparison of several methods.* Analytica Chimica Acta, 1999. **384**(2): p. 207-214.
53. Gemperline, P.J., J.R. Long, and V.G. Gregoriou, *Nonlinear Multivariate Calibration Using Principal Components Regression and Artificial Neural Networks.* Analytical Chemistry, 1991. **63**(20): p. 2313-2323.
54. Bertran, E., et al., *Handling intrinsic non-linearity in near-infrared reflectance spectroscopy.* Chemometrics and Intelligent Laboratory Systems, 1999. **49**(2): p. 215-224.
55. Delpy, D.T. and M. Cope, *Quantification in tissue near-infrared spectroscopy.* Philosophical Transactions of the Royal Society B-Biological Sciences, 1997. **352**(1354): p. 649-659.

56. Hebden, J.C., S.R. Arridge, and D.T. Delpy, *Optical imaging in medicine .1. Experimental techniques.* Physics in Medicine and Biology, 1997. **42**(5): p. 825-840.

57. Chaiken, J. and J. Goodisman, *On probing human fingertips in vivo using near-infrared light: model calculations.* Journal of Biomedical Optics, 2010. **15**(3): p. 037007.

58. Chance, B., et al., *Comparison of Time-Resolved and Time-Unresolved Measurements of Deoxyhemoglobin in Brain.* Proceedings of the National Academy of Sciences of the United States of America, 1988. **85**(14): p. 4971-4975.

59. Andersson-Engels, S., et al., *Time-Resolved Transillumination for Medical Diagnostics.* Optics Letters, 1990. **15**(21): p. 1179-1181.

60. Ijichi, S., et al., *Quantification of cerebral hemoglobin as a function of oxygenation using near-infrared time-resolved spectroscopy in a piglet model of hypoxia.* Journal of Biomedical Optics, 2005. **10**(2): p. 9.

61. Doornbos, R.M.P., et al., *The determination of in vivo human tissue optical properties and absolute chromophore concentrations using spatially resolved steady-state diffuse reflectance spectroscopy.* Physics in Medicine and Biology, 1999. **44**(4): p. 967-981.

62. Hjalmarsson, P. and S.N. Thennadil, *Determination of glucose concentration in tissue-like material using spatially resolved steady-state diffuse reflectance spectroscopy - art. no. 685508*, in *Complex Dynamics and Fluctuations in Biomedical Photonics V*, V.V. Tuchin and L.V. Wang, Editors. 2008, Spie-Int Soc Optical Engineering: Bellingham. p. 85508-85508.

63. Pickering, J.W., et al., *Double-Integrating-Sphere System for Measuring the Optical-Properties of Tissue.* Applied Optics, 1993. **32**(4): p. 399-410.

64. Prahl, S.A., M.J.C. Vangemert, and A.J. Welch, *Determining the Optical-Properties of Turbid Media by Using the Adding-Doubling Method.* Applied Optics, 1993. **32**(4): p. 559-568.

65. Prahl, S.A., *The adding-doubling method*, in *Optical-thermal response of laser irradiated tissue*, A.J. Welch and M.J.C. van Gemert, Editors. 1995, Plenum Press: New York. p. 101-129.

66. Li, C., et al. *Improved double-integrating-spheres system for multi-wavelength optical properties measurement: Investigation and application*. in *Proceedings of SPIE - The International Society for Optical Engineering*. 2009. San Jose, CA.

67. Abrahamsson, C., et al., *Scatter correction of transmission near-infrared spectra by photon migration data: Quantitative analysis of solids.* Applied Spectroscopy, 2005. **59**(11): p. 1381-1387.

68. Leonardi, L. and D.H. Burns, *Quantitative constituent measurements in scattering media from statistical analysis of photon time-of-flight distributions.* Analytica Chimica Acta, 1997. **348**(1-3): p. 543-551.

69. Leonardi, L. and D.H. Burns, *Quantitative measurements in scattering media: Photon time-of-flight analysis with analytical descriptors.* Applied Spectroscopy, 1999. **53**(6): p. 628-636.

70. Abrahamsson, C., et al., *Time-resolved NIR spectroscopy for quantitative analysis of intact pharmaceutical tablets.* Analytical Chemistry, 2005. **77**(4): p. 1055-1059.

71. Crowe, J., et al., *Quantitative spectrophotometry of scattering media via frequency-domain and constant-intensity measurements.* Journal of the Optical Society of America a-Optics Image Science and Vision, 2007. **24**(7): p. 1969-1974.

72. Stockford, I.M., et al., *Reduction of error in spectrophotometry of scattering media using polarization techniques.* Applied Spectroscopy, 2007. **61**(12): p. 1379-1389.

73. Leger, M.N., *Alleviating the Effects of Light Scattering in Multivariate Calibration of Near-Infrared Spectra by Path Length Distribution Correction.* Applied Spectroscopy, 2010. **64**(3): p. 245-254.

74. Mishchenko, M.I., L.D. Travis, and A.A. Lacis, *Scattering, absorption, and emission of light by small particles*. 2002, Cambridge: Cambridge University Press. xv, 445 p., [16]p. of plates.

75. Ishimaru, A., *Wave propagation and scattering in random media*. 1997, New York, USA: IEEE Press. 574p.

76. Bohren, C.F. and D.R. Huffman, *Absorption and scattering of light by small particles*. 1983, New York, USA: Wiley. 530p.

77. Mie, G., *Beitrage zur Optik truber Medien, speziell kolloidaler Metallosungen.* Annalen der Physik, 1908. **25**(3): p. 377-445.

78. Doicu, A., T. Wriedt, and Y. Eremin, *Light scattering by systems of particles : null-field method with discrete sources : theory and programs*. 2006, Berlin ; [London]: Springer. xiii, 322 p.

79. Deirmendjian, D., *Electromagnetic Scattering on Spherical Polydispersions*. 1969, New York, USA: Elsevier Scientific Publishing. 290p.

80. Velazco Roa, M.A., *Estimation of optical constants of particles in suspension from multiple- scattered light*, in *School of Chemical Engineering and Advanced Materials*. 2008, Newcastle University: Newcastle upon Tyne. p. 180.
81. Case, K.M. and P.F. Zweifel, *Linear transport theory*. 1967, Reading, Mass. ; London: Addison-Wesley. 351p.
82. Wilson, B.C. and G. Adam, *A Monte-Carlo Model for the Absorption and Flux Distributions of Light in Tissue.* Medical Physics, 1983. **10**(6): p. 824-830.
83. Prahl, S.A., et al., *A Monte Carlo model of light propagation in tissue*, in *SPIE Proceedings of Dosimetry of Laser Radiation in Medicine and Biology*, G.J. Muller and D.H. Sliney, Editors. 1989, SPIE Optical Engineering Press. p. 102–111.
84. Orchard, S.E., *Reflection and transmission of light by diffusing suspensions.* J Opt Soc Amer, 1969. **59**(12): p. 1584-1597.
85. Chandrasekhar, S., *Radiative Transfer*. 1960, New York, USA: Dover.
86. Egan, W.G., T. Hilgeman, and J. Reichman, *Determination of Absorption and Scattering Coefficients for Nonhomogeneous Media .2. Experiment.* Applied Optics, 1973. **12**(8): p. 1816-1823.
87. Reichman, J., *Determination of Absorption and Scattering Coefficients for Nonhomogeneous Media .1. Theory.* Applied Optics, 1973. **12**(8): p. 1811-1815.
88. Kubelka, P., *New contributions to the optics of intensely light-scattering materials. Part I.* Journal of the Optical Society of America, 1948. **38**: p. 448–457.
89. Van de Hulst, H.C., *Multiple light scattering: tables formulas and applications*. Vol. 1. 1980, USA: USA Academic.
90. Plass, G.N., G.W. Kattawar, and Catching.Fe, *Matrix Operator Theory of Radiative Transfer .1. Rayleigh-Scattering.* Applied Optics, 1973. **12**(2): p. 314-329.
91. Wiscombe, W.J., *Doubling Initialization Revisited.* Journal of Quantitative Spectroscopy & Radiative Transfer, 1977. **18**(2): p. 245-248.
92. Wiscombe, W.J., *Initialization, Error and Flux Conservation in Doubling Method.* Journal of Quantitative Spectroscopy & Radiative Transfer, 1976. **16**(8): p. 637-658.
93. Prahl, S.A., *Light Transport in Tissue*. 1988, University of Texas at Austin.
94. Wold, S., H. Martens, and H. Wold, *The Multivariate Calibration-Problem in Chemistry Solved by the Pls Method.* Lecture Notes in Mathematics, 1983. **973**: p. 286-293.

95. Geladi, P. and B.R. Kowalski, *Partial least-squares regression: a tutorial.* Analytica Chimica Acta, 1986. **185**(C): p. 1-17.

96. Höskuldsson, A., *PLS regression methods.* Journal of Chemometrics, 1988. **2**: p. 211-228.

97. Keranen, V.T.J. and A.J. Makynen. *Double integrating sphere system for optical parameter determination of industrial suspensions*. in *Proceedings of SPIE - The International Society for Optical Engineering*. 2008. Levi.

98. Keranen, V.T.J., et al., *A Scattering Measurement System to Determine the Optical Characteristics of Industrial Suspensions.* I2mtc: 2009 Ieee Instrumentation & Measurement Technology Conference, Vols 1-3, 2009: p. 551-554.

99. Saeys, W., et al., *Optical properties of apple skin and flesh in the wavelength range from 350 to 2200 nm.* Applied Optics, 2008. **47**(7): p. 908-919.

100. Zollars, R.L., *Turbidimetric method for on-line determination of latex particle number and particle size distribution.* Journal of Colloid and Interface Science, 1980. **74**(1): p. 163-172.

101. Zollars, R.L., *Turbidimetric Method for Determination of Latex Particle-Size Distribution.* Journal of Dispersion Science and Technology, 1981. **2**(2-3): p. 331-344.

102. Melik, D.H. and H.S. Fogler, *Turbidimetric determination of particle size distributions of colloidal systems.* Journal of Colloid and Interface Science, 1983. **92**(1): p. 161-180.

103. Garcia-Rubio, L.H., *Averages from turbidity measurements.* Particle Size Distribution, 1987: p. 161-178.

104. Glatter, O. and M. Hofer, *Interpretation of elastic light scattering data. III. determination of size distributions of polydisperse systems.* Journal of Colloid and Interface Science, 1988. **122**(2): p. 496-506.

105. Elicabe, G.E. and L.H. Garcia-Rubio, *Latex particle size distribution from turbidimetry using inversion techniques.* J. Colloid Interface Sci., 1989. **129**(1): p. 192-200.

106. Brandolin, A. and L.H. Garcia-Rubio. *On-line particle size distribution measurements for latex reactors*. in *Polymeric Materials Science and Engineering, Proceedings of the ACS Division of Polymeric Materials Science and Engineering*. 1990.

107. Brandolin, A., et al. *Latex particle size distribution from turbidimetry using inversion techniques; experimental validation*. in *Polymeric Materials Science and Engineering, Proceedings of the ACS Division of Polymeric Materials Science and Engineering*. 1990.

108. Elicabe, G. and L.H. Garcia-Rubio, *Latex particle size distribution from turbidimetry using a combination of regularization techniques and generalized cross validation.* Polymer Characterization, 1990: p. 83-104.

109. Gordon, S., et al., *In-process particle characterization by spectral extinction.* Chemical Engineering Research and Design, 2000. **78**(8): p. 1147-1152.

110. Lai, X., et al., *Particle Size Determination in Aluminum Hydroxide Suspensions Using Near-Infrared Transmittance Spectroscopy.* Appl. Spectrosc., 2007. **61**(11): p. 1184-1190.

111. Khlebtsov, B.N., V.A. Khanadeev, and N.G. Khlebtsov, *Spectroturbidimetric Determination of the Size, Concentration, and Refractive Index of Silica Nanoparticles.* Optics and Spectroscopy, 2008. **105**(5): p. 732-738.

112. Pariset, C. and S.N. Thennadil. *Evaluation of cross-validation formulas for choosing the regularization parameter for inversion of Fredholm integral of the first kind with non-negativity constraints*. in *The 3rd International Conference on Sensing Technology*. 2008.

113. Pariset, C. and S.N. Thennadil. *Inversion of spectroscopic measurements for extracting particle size distribution*. in *The 6th International Multi-Conference on Systems, Signals and Devices,* . 2009.

114. Strang, G., *Linear algebra and its applications*. 3rd ed. ed. 1988, San Diego: Harcourt, Brace, Jovanovich, Publishers.

115. *Optimization Toolbox 4 User's Guide*. 2008, MathWorks Inc.

116. Han, S.P., *Globally Convergent Method for Nonlinear-Programming.* Journal of Optimization Theory and Applications, 1977. **22**(3): p. 297-309.

117. Powell, M.J.D., *A Fast Algorithm for Nonlinearly Constrained Optimization Calculations*, in *Numerical Analysis*, G.A. Watson, Editor. 1978, Springer Verlag.

118. de Vries, G., et al., *The effect of light losses in double integrating spheres on optical properties estimation.* Ieee Journal of Selected Topics in Quantum Electronics, 1999. **5**(4): p. 944-947.

119. Zhu, D., et al., *Effect of light losses of sample between two integrating spheres on optical properties estimation.* Journal of Biomedical Optics, 2007. **12**(6).

120. Kradgel, C. and K.A. Lee, in *Handbook of Near Infrared Analysis*, D.A. Burns and E.W. Ciurczak, Editors. 2008, CRC Press: Boca Raton, FL. p. 529-568.
121. Velazco-Roa, M.A. and S.N. Thennadil, *Estimation of complex refractive index of polydisperse particulate systems from multiple-scattered ultraviolet-visible-near-infrared measurements.* Applied Optics, 2007. **46**(18): p. 3730-3735.
122. Segelstein, D.J., *The complex refractive index of water*. 1981, University of Missouri-Kansas City.
123. Celis, M., *Studies of the Initial Conditions in Emulsion Polymerization Reactors*, in *Department of Chemical Engineering*. 2000, University of South Florida: Tampa, FL. p. 167.
124. Mokhtari, T., C.M. Sorensen, and A. Chakrabarti, *Multiple-scattering effects on static light-scattering optical structure factor measurements.* Applied Optics, 2005. **44**(36): p. 7858-7861.
125. Mehra, R., *Application of refractive index mixing rules in binary systems of hexadecane and heptadecane with n-alkanols at different temperatures.* Proceedings of the Indian Academy of Sciences: Chemical Sciences, 2003. **115**(2): p. 147-154.
126. Sharma, S., et al., *Density and comparative refractive index study on mixing properties of binary liquid mixtures of eucalyptol with hydrocarbons at 303.15, 308.15 and 313.15K.* E-Journal of Chemistry, 2007. **4**(3): p. 343-349.
127. *Refractive index database* available at http://refractiveindex.info
128. Fredin, L., B. Nelander, and G. Ribbegard, *Infrared spectrum of the water dimer in solid nitrogen. I. Assignment and force constant calculations.* The Journal of Chemical Physics, 1977. **66**(9): p. 4065-4072.
129. Engdahl, A. and B. Nelander, *On the relative stabilities of H- And D-bonded water dimers.* The Journal of Chemical Physics, 1986. **86**(4): p. 1819-1823.
130. Devlin, J.P., *Preferential deuterium bonding at the ice surface: A probe of surface water molecule mobility.* Journal of Chemical Physics, 2000. **112**(13): p. 5527-5529.